# PHYSICAL, METABOLIC, AND ENERGETIC INVESTIGATIONS OF METHANE-METABOLIZING MICROBIAL COMMUNITIES

Thesis by
Jeffrey Marlow

In Partial Fulfillment of the Requirements for the degree of
Doctor of Philosophy


CALIFORNIA INSTITUTE OF TECHNOLOGY
Pasadena, California
2016
(Defended June 5th, 2015)

# ACKNOWLEDGEMENTS

Whatever information of consequence that may be encompassed by this compilation is a testament to the generous network of support I have enjoyed during its completion. Most fundamentally, my family and dear friends, scattered across time zones, have provided critical grounding that has bolstered my faith in both the importance and limits of my scientific pursuits. Administration, staff members, and other researchers across the Caltech campus have helped in ways both seen and unseen to enable a frictionless scientific experience. I greatly appreciate the personal encouragement and scientific insight of all members of the Orphan Lab past and present – especially Jan Haskell, Stephanie Connon, Shana Goffredi, Joshua Steele, Greg Wanger, Connor Skennerton, Anne Dekas, Jennifer Glass, David Case, Derek Smith, Shawn McGlynn, Alexis Pasulka, and Roland Hatzenpichler – as well as other colleagues, most notably Joel Scheingross, Megan Newcombe, James Hemp, Sebastian Kopf, Ryan Hunter, Ajay Limaye, Doug LaRowe, Bethany Ehlmann, and Andrew Thurber. I am very grateful for the logistical, financial, and scientific support of John Grotzinger, Wiebke Ziebis, Lisa Levin, Peter Girguis, and Michael Roukes. Jan Amend has witnessed and shepherded my development as a scientist, from a dishwashing freshman at Washington University to a continuing collaborator in the study of microbial ecosystems. Countless scientific conversations with all of the remarkable colleagues above have shaped my scientific identity and set the groundwork for my future investigations. Financial support from the National Science Foundation's Graduate Student Fellowship Program, Caltech's Center for Environmental Microbial Interactions, and the National Research Council have made this work and its dissemination possible. My thesis advisory committee – Doug Rees, Woodward Fischer, Tori Hoehler, Dianne Newman, and Victoria Orphan – has provided generous guidance, overcoming busy schedules to discuss results and prioritize ballooning investigatory ambitions. In particular, Dianne Newman kindled my scientific drive through insightful interrogation and encouraged me to follow empirically testable questions with a focused tenacity. Victoria Orphan led and taught by the most effective means possible, through the quiet stimulation of wonder and awe rather than a fear of insufficiency or unworthiness. Her appreciation that, in its purest form, the curiosity that constitutes the most essential seed of a scientist's soul knows no bounds, allowed me to cultivate a wide range of interests that has – inevitably – enabled unforeseen scientific opportunities and broadened their ultimate impact. This list is a poor approximation of my indebtedness, but the deep support and prodding intellectual stimulation I have received from the vivacious scientific community in which I find myself inspires a brimless excitement for future questions we will engage and answers we will chase, together.

# ABSTRACT

Understanding the roles of microorganisms in environmental settings by linking phylogenetic identity to metabolic function is a key challenge in delineating their broad-scale impact and functional diversity throughout the biosphere. This work addresses and extends such questions in the context of marine methane seeps, which represent globally relevant conduits for an important greenhouse gas. Through the application and development of a range of culture-independent tools, novel habitats for methanotrophic microbial communities were identified, established settings were characterized in new ways, and potential past conditions amenable to methane-based metabolism were proposed. Biomass abundance and metabolic activity measures – both catabolic and anabolic – demonstrated that authigenic carbonates associated with seep environments retain methanotrophic activity, not only within high-flow seep settings but also in adjacent locations exhibiting no visual evidence of chemosynthetic communities. Across this newly extended habitat, microbial diversity surveys revealed archaeal assemblages that were shaped primarily by seepage activity level and bacterial assemblages influenced more substantially by physical substrate type. In order to reliably measure methane consumption rates in these and other methanotrophic settings, a novel method was developed that traces deuterium atoms from the methane substrate into aqueous medium and uses empirically established scaling factors linked to radiotracer rate techniques to arrive at absolute methane consumption values. Stable isotope probing metaproteomic investigations exposed an array of functional diversity both within and beyond methane oxidation- and sulfate reduction-linked metabolisms, identifying components of each proposed enzyme in both pathways. A core set of commonly occurring unannotated protein products was identified as promising targets for future biochemical investigation. Physicochemical and energetic principles governing anaerobic methane oxidation were incorporated into a reaction transport model that was applied to putative settings on ancient Mars. Many conditions enabled exergonic model reactions, marking the metabolism and its attendant biomarkers as potentially promising targets for future astrobiological investigations. This set of inter-related investigations targeting methane metabolism extends the known and potential habitat of methanotrophic microbial communities and provides a more detailed understanding of their activity and functional diversity.

# TABLE OF CONTENTS

# *Introduction*

Over the last several decades, as exploratory range has broadened and analytical tools have sharpened, our conception of the biosphere's extent has expanded dramatically. Much of the newly characterized habitat is the province of microorganisms: from the deep subsurface (Whitman et al. 1998) to the upper atmosphere (Wainwright et al. 2003), microbes are increasingly viewed as a pervasive force permeating Earth's habitable volume. These microscopic denizens are not merely passive footnotes in the saga of planetary evolution and elemental cycling; rather, microbial communities frequently drive such transformations, marshaling their metabolic versatility to produce oxygen (Farquhar et al. 2011), fix nitrogen (Burris & Roberts 1993), degrade organic matter (Middelburg et al. 1993), and access rock-bound metals (Haferburg & Kothe 2007).

Researchers have developed a healthy appreciation for microbes' range, but a wide gap between presence and functional relevance persists, and developing a more detailed understanding of the activity-based roles and relationships of these communities remains an important frontier. The most reliable methods of linking microbial identity to function, which require pure cultures of isolated species, are largely impotent when applied to environmental systems, where the vast majority of organisms are recalcitrant to culturing attempts (e.g., Rappé & Giovannoni 2003; Pace et al. 1986). What's more, the seemingly critical role of inter-species interactions (Pham & Kim 2012; West et al. 2007) renders pure culture studies imprecise at best and dangerously misleading at worst.

In response to the "culturability bottleneck," two paths have emerged in the quest to understand microbial roles in environmental contexts: characterizing evidence of

biochemical processes (largely through geochemical or isotopic means), and pursuing evidence of biochemical machinery (using a range of omics-based methods). When combined, these approaches enable researchers to cross-reference net environmental transformations with a library of potential (DNA) or actual (protein) biomachinery. While this theoretical framework for disentangling a complex milieu of microbial and chemical constituents is robust, its enactment is rife with complication. Cryptic elemental cycles can mask truly important biochemical substrates (Holmkvist et al. 2011), omics coverage limitations can obscure functionally critical components (e.g., Schneider & Riedel 2010), and reliance on annotations derived from a small subset of organisms can bias subsequent interpretation. Constantly improving analytical methods, as well as the creative combination of distinct approaches, offer a promising path forward.

The work presented here applies a range of culture-independent measures of microbial community activity and function to an environment that plays a key role in global biogeochemical processes: marine methane seeps. At an increasingly diverse set of geological settings, methane percolates upward from depth into the shallow subsurface, where the majority of the methane is biologically consumed through the anaerobic oxidation of methane (AOM). Given the radiative forcing power of methane (Denman et al. 2007), the subseafloor sink constitutes an important bulwark against climate change (Reeburgh 2007). AOM has been attributed to intimately linked microbial partnerships performing methane oxidation and sulfate reduction (Boetius et al. 2000; Orphan et al. 2002), and while this core functionality is well established, the full range, structure, and functional diversity of seep communities remain widely unconstrained.

Chapter 1 demonstrates methanotrophic activity within authigenic carbonate rock structures that shape seafloor seep environments. Given the volumetrically dominant role that such mounds play at seeps, endolithic AOM represents a previously unrecognized and globally relevant methane sink. Chapter 2 presents a novel method for measuring methane consumption rates that was developed during the assessment of carbonate-hosted methanotrophy. Using singly deuterated methane as substrate, the D/H ratio of the aqueous phase is measured; consistent scaling factors link this approach with more established methods, enabling both relative and absolute methane consumption measurements. Chapter 3 explores the determinants of microbial abundance and community diversity at seep environments, considering both the nature of the physical substrate and the degree of seepage activity. Carbonate rocks from actively seeping locations were found to possess more abundant microbial biomass, and bacterial and archaeal diversity patterns were shaped most significantly by substrate type and seepage activity, respectively.

Chapter 4 broadens the scope of culture-independent analysis of methane seep settings through the use of stable isotope probing metaproteomics, a broad method that offers important strategic advantages in low-activity settings. Thousands of proteins were detected, including a wide diversity of methane- and sulfur-metabolizing orthologs, some of which exhibited newly detected post-translational modifications. Chapter 5 examines the possibility of AOM on ancient Mars, using energetic relationships and environmental parameters gleaned from terrestrial methane seeps to develop a reaction transport model for a martian context. The metabolism appears to be exergonic under many likely past conditions, and sites of investigatory interest were proposed based on mineralogical signatures. Several appendices are also included, offering supplementary information in

support of corresponding chapters, as well as spin-off studies prompted by results in the main text.

As a whole, this work broadens our understanding of methane seep environments and related metabolisms through a range of culture-independent microbiological approaches. The methods and results presented herein expand the range – both potential and realized – of anaerobic methane oxidation and provide a more nuanced view of diversity controls and functional metabolic diversity in seep environments. As the investigation of microbial constituents in environmental systems moves from presence to activity and function, such interdisciplinary efforts will play increasingly prominent roles.

References:

Boetius A, Ravenschlag K, Schubert CJ, Rickert D, Widdel F, Gleseke A, et al. (2000). A marine microbial consortium apparently mediating anaerobic oxidation of methane. Nature 407.

Burris RH, Roberts G. (1993). Biological nitrogen fixation. Annual review of nutrition 13:317–335.

Denman KL, Brasseur G, Chidthaisong A, Ciais P, Cox PM, Dickinson RE, et al. (2007). Couplings between changes in the climate system and biogeochemistry. In:Climate Change 2007: The Physical Science Basis, Contribution of Working Group I to the Fourth Assessment Report of the Intergovernmental Panel on Climate Change, Cambridge University Press: Cambridge.

Farquhar, James, Aubrey L. Zerkle, and Andrey Bekker. "Geological constraints on the origin of oxygenic photosynthesis." *Photosynthesis research* 107.1 (2011): 11-36.

Haferburg G, Kothe E. (2007). Microbes and metals: interactions in the environment. Journal of basic microbiology 47:453–467.

Holmkvist L, Ferdelman TG, Jørgensen BB. (2011). A cryptic sulfur cycle driven by iron in the methane zone of marine sediment (Aarhus Bay, Denmark). Geochimica et Cosmochimica Acta 75:3581–3599.

Middelburg JJ, Vlug T, Jaco F, Van Der Nat W. (1993). Organic matter mineralization in marine systems. Global and Planetary Change 8:47–58.

Orphan VJ, House CH, Hinrichs K-U, McKeegan KD, DeLong EF. (2002). Multiple archaeal groups mediate methane oxidation in anoxic cold seep sediments. Proceedings of the National Academy of Sciences 99:7663–7668.

Pace NR, Stahl DA, Lane DJ, Olsen GJ. (1986). The analysis of natural microbial populations by ribosomal RNA sequences. In:Advances in microbial ecology, Springer, pp. 1–55.

Pham VH, Kim J. (2012). Cultivation of unculturable soil bacteria. Trends in biotechnology 30:475–484.

Rappé MS, Giovannoni SJ. (2003). The uncultured microbial majority. Annual Reviews in Microbiology 57:369–394.

Reeburgh WS. (2007). Oceanic Methane Biogeochemistry. Chem. Rev. 107:486–513.

Schneider T, Riedel K. (2010). Environmental proteomics: analysis of structure and function of microbial communities. Proteomics 10:785–798.

Wainwright M, Wickramasinghe NC, Narlikar J, Rajaratnam P. (2003). Microorganisms cultured from stratospheric air samples obtained at 41 km. FEMS Microbiology Letters 218:161–165.

West SA, Diggle SP, Buckling A, Gardner A, Griffin AS. (2007). The social lives of microbes. Annual Review of Ecology, Evolution, and Systematics 53–77.

Whitman WB, Coleman DC, Wiebe WJ. (1998). Prokaryotes: the unseen majority. Proceedings of the National Academy of Sciences 95:6578–6583.

*C h a p t e r  1*

# CARBONATE HOSTED METHANOTROPHY REPRESENTS AN UNRECOGNIZED METHANE SINK IN THE DEEP SEA

Jeffrey J. Marlow[1], Joshua A. Steele[1], Wiebke Ziebis[2], Andrew R. Thurber[3], Lisa A. Levin[4], Victoria J. Orphan[1*]

[1]Division of Geological and Planetary Sciences, California Institute of Technology, Pasadena, CA, 91125 USA
[2]Department of Biological Science, University of Southern California, Los Angeles, CA, 90089 USA
[3]College of Earth, Ocean, and Atmospheric Sciences, Oregon State University, Corvallis, OR, 97331 USA
[4]Center for Marine Biodiversity and Conservation and Integrative Oceanography Division, Scripps Institution of Oceanography, University of California, San Diego, La Jolla, CA, 92037 USA

*Adapted from Marlow, Jeffrey J., et al. "Carbonate-hosted methanotrophy represents an unrecognized methane sink in the deep sea." Nature communications 5 (2014). DOI: http://doi.org/10.1038/ncomms6094

**Abstract**

The atmospheric flux of methane from the oceans is largely mitigated through microbially mediated sulphate-coupled methane oxidation, resulting in the precipitation of authigenic carbonates. Deep-sea carbonates are common around active and paleo-methane seepage, and have primarily been viewed as passive recorders of methane oxidation; their role as active and unique microbial habitats capable of continued methane consumption has not been examined. Here we show that seep-associated carbonates harbor active microbial communities, serving as dynamic methane sinks. Microbial aggregate abundance within the carbonate interior exceeds that of seep sediments, and molecular diversity surveys reveal methanotrophic communities within protolithic nodules and well-lithified carbonate pavements. Aggregations of microbial cells within carbonate matrix actively oxidize methane as indicated by stable isotope FISH-nanoSIMS experiments and $^{14}CH_4$ radiotracer rate measurements. Carbonate-hosted methanotrophy extends the known ecological niche of these important methane consumers and represents a previously unrecognized methane sink that warrants consideration in global methane budgets.

**Introduction**

Methane has played an important role in global climate change in the past and remains the fourth most significant contributor to greenhouse forcing[1], motivating the characterization of methane's sources, sinks, and fluxes. Biologically mediated, sulphate-coupled anaerobic oxidation of methane (AOM) is the dominant sink for methane in the oceans, consuming an estimated 382 Tg $CH_4$ per year in seafloor sediments, a quantity equivalent to approximately 88% of the methane released from subsurface reservoirs[2].

Microbiological study of AOM at methane seeps has focused almost exclusively on sediment-based habitats, where the most energetically favorable geochemical horizon, the sulphate-methane transition zone, typically occurs in the top several centimeters[3]. However, sediment accounts for only a portion of the seafloor cover at methane seep structures: based on sidescan sonar imagery and seafloor video observations, substantial portions of actively seeping areas are capped by carbonate rock precipitate[4–7]. The presence and potential activity of extant microbial communities within these carbonate rocks, and their impact on global methane dynamics, has gone unexplored.

In anoxic sediments at methane seeps, advection-driven methane-rich fluids come into contact with sulphate-rich seawater[8]. At these sites, biological AOM is mediated through an enigmatic metabolic partnership involving methanotrophic archaea (ANME) and sulphur-metabolizing deltaproteobacteria that operates at a low predicted Gibbs energy yield[9–11]. The overall reaction of combined AOM and sulphate reduction increases carbonate alkalinity, promoting the precipitation of authigenic carbonate[12]. An estimated 14% of biologically oxidized methane at active seep settings precipitates in this manner[13], leading to a range of carbonate minerals[14]. The resulting precipitation products may vary in size, ranging from microcrystals[15] to extensive structures of pavements, slabs, and mounds produced by upward growth (known as chemoherms) or post-formation winnowing[14,16,17]. Carbonate volumes have been estimated for a few regions of active seepage and may exceed a million cubic meters at areas such as Costa Rica[4], Hydrate Ridge[6], and the Chilean subduction zone[5], suggesting that these methane-derived structures have the potential to serve as a significant habitat within the seep ecosystem.

The association of anaerobic methanotrophic microbial biomass with authigenic carbonates has been previously discussed in specialized environments. Most prominently, methane-fueled 'reefs' composed of porous carbonates and thick mats of ANME archaea and sulphate-reducing bacteria (SRB) were discovered at sites of vigorous methane venting in the euxinic bottom waters of the Black Sea[18]. Organic geochemical analysis of microbial mats within cm–scale void spaces within carbonate chemoherms from the Black Sea were found to contain lipids indicative of ANME and SRB; it was proposed that these carbonate structures formed through AOM-mediated carbonate precipitation in the sediment and, after sufficient accumulation, expanded into the overlying anoxic water column[19]. While the discovery of the Black Sea AOM ecosystem has expanded our view of anaerobic methanotrophy and carbonate precipitation, the unique geochemical setting of this euxinic basin makes it difficult to extrapolate associated findings to the more globally relevant carbonate precipitation associated with AOM along continental margins. At such locations, carbonate slabs and pavements range from outcrops of vuggy, highly porous rock to lower-permeability massive structures[6,16]. Sr-isotope data and the presence of carbonate precipitation products favored under high-bicarbonate, low-sulphate conditions suggest that carbonate is largely precipitated within the sediment, and is subsequently exposed through uplift and/or erosion[16]. There is no large-scale visible surficial manifestation of ANME / sulphate-reducing bacteria biomass, as observed in the Black Sea[18], and the potential for carbonate-associated methanotrophic activity by extant endoliths (organisms living within the pore spaces of rocks) has not been examined.

In select seep settings along continental margins and submarine mud volcanoes, archaeal 16S rRNA gene surveys and lipid biomarker analyses of carbonate crusts provided

evidence of methanotrophic microbial biosignatures[20]. Within porous Hydrate Ridge chemoherms experiencing focused fluid flow, isotopic links between AOM and carbonates were reported, as were putative fossilized microbial filaments[6]. In both cases, the potential occurrence of intact, viable microorganisms and active methane oxidation within the carbonate matrix was not determined.

The conditions in which microbial AOM has been suggested to occur alongside carbonate precipitation products[18–21] represent an end-member of potential endolithic habitats: settings with high connectivity to metabolic reactants (e.g., methane and sulphate) and seemingly minor physicochemical or energetic obstacles to sulphate-dependent AOM. Well-lithified massive carbonate rocks that pave substantial areas of the seafloor associated with present and past methane seepage, as well as those precipitates found in areas of low seepage activity, represent unique endolithic habitats more constrained by permeability limitations and/or methane supply; the potential of methanotrophic activity in such settings warrants investigation.

When subseafloor environments are considered, well-lithified rock constitutes the volumetrically dominant physical substrate at seep-associated mounds[4–6,14]. While some endolithic organisms appear to gain nutrients from their host rock[22], the self-sealing effect of microbially accelerated authigenic carbonate formation implies that the supply of energy and nutrients may be limited in the seep-associated endolithic habitat, offering a valuable comparison with the better studied sediment-hosted methane seep communities. Carbonate mounds like those at Hydrate Ridge, Oregon, are made up of several different lithologies, the most prominent being gray micrite-cemented massive carbonates and white aragonitic

breccias that exhibit a range of porosities[6,14]. These rocks form extensive cohesive structures at seep sites, often extending hundreds of meters beneath the seafloor[5,23].

Endoliths are likely pervasive within rocks at the Earth's surface[22] and have been observed within basaltic oceanic crust on the seafloor[24] and in deep subseafloor samples[25]. Endoliths are more formally divided into chasmo-, crypto-, and eu-endoliths depending on their mode of rock colonization[26]; the microorganisms referred to in this study with the more general term "endolith" belong to a separate subset of organisms that precipitate authigenic rock around them in a process of gradual self-entombment. Geobiological studies that have examined authigenic carbonate mounds have primarily pursued biomarker characterization rather than modern endolithic activity. $^{13}$C-depleted lipids such as crocetane and archaeol at Aleutian margin seeps[27], lipids and ANME 16S rRNA genes at Gulf of Cadiz structures[28], and an ANME-2-derived extended sn-2-hydroxyarchaeol found in multiple seep carbonate mounds[29] are all suggestive of methanotrophic archaeal involvement, but offer limited insight on contemporary metabolic activity. The presence of biomarkers within mounds is often used forensically in an effort to reconstruct antecedent microbial communities and past conditions of carbonate precipitation[30]; such studies have offered evidence of AOM and methanogenesis in association with authigenic carbonates during and potentially after their formation[31]. The suggestion of microbial involvement with carbonate crust formation[20], predicated on the detection of low-abundance ANME 16S rRNA gene sequences and $^{13}$C depleted archaeal lipids, challenged the interpretation of carbonate precipitation products as exclusively fossil deposits. However, the viability of the microbial community and sustained endolithic AOM activity within the authigenic carbonate matrix was not demonstrated.

Seafloor and sediment-hosted authigenic carbonates have not historically been considered to be dynamic living ecosystems whose biological activity significantly impacts seafloor methane fluxes; the findings presented here suggest that is precisely the case. We use molecular diversity surveys and fluorescence *in situ* hybridization (FISH) to demonstrate that methane derived authigenic carbonates, including sediment-hosted protolithic nodules and exhumed carbonate rocks from both actively venting and low methane flux environments, are viable habitats for abundant methanotrophic microorganisms. Stable isotope analyses of carbonate-associated microorganisms by nanoscale secondary ion mass spectrometry (NanoSIMS) and $^{14}CH_4$ radiotracer studies confirmed aerobic and anaerobic methanotrophic activity, revealing seafloor carbonate habitats as important, previously unrecognized methane sinks.

**Results**

*Characterizing the Endolithic Habitat*

Twenty-four samples were collected for study from methane seep sites at Hydrate Ridge, Eel River Basin, and the Costa Rica Margin (Supplementary Table 1.1, Supplementary Figs. 1.1 and 1.2; all supplementary tables and figures can be found in Appendix 1). Porosity and permeability values of representative samples were empirically measured using core plug analysis to quantify the fluid flow potential through the physical substrates and characterize putative microbial habitats (Supplementary Table 1.2). Active massive carbonate samples (A.Carb-4588E3 and A.Carb-5152) had permeabilities of $1.7x10^{-15}$ to $4.9x10^{-15}$ $m^2$, while low-activity massive carbonates (L.Carb-5473, L.Carb-5028, L.Carb-2719, and L.Carb-2787; Supplementary Fig. 1.2g) were two orders of

magnitude less permeable, averaging $1.3x10^{-17}$ $m^2$ +/- $1x10^{-17}$ $m^2$ SE. Active porous carbonates analogous to chemoherm samples reported in Bahr et al.[19] (e.g., A.Carb-5305 and A.Carb-3439; Supplementary Fig. 1.2e) were too friable for core plug analysis, but likely exhibit even higher permeabilities given their macroscale vugs and conduits. Petrographic thin sections provide microscopic evidence of less developed pore-filling aragonite fans and less dense micritic matrix in active porous carbonates compared with lithified structures from low-activity seep areas (Supplementary Fig. 1.3).

Microbial 16S rRNA gene analysis revealed abundant methane seep-associated archaeal and bacterial phylotypes with an apparent shift in community composition with lower seep activity (Supplementary Data 1.1-1.3). Among Archaea, ANME lineages were the predominant sequences recovered at sites within active seep areas, including sediment (92.9%, n=170 total clones), sediment hosted carbonate nodule (85%; n=113) and exhumed carbonate slab (70.9%; n=206) environments, while a carbonate sample from a region of low methane flux contained a much smaller percentage of ANME representatives (12.9%; n=139; Supplementary Data 1.1). Members of the ANME-1 group comprised nearly all of the recovered ANME sequences within the low-activity seafloor carbonate (83.7%), compared with <40% in active samples (12.7%, 39.6%, and 20.6% of ANME sequences in sediment, nodules, and carbonates, respectively). The presence of ANME-1 within low-activity carbonate rock was confirmed with FISH, using an ANME-1 specific oligonucleotide probe[32]. *Deltaproteobacteria*, including representatives closely related to sulphate-reducing genera that associate with ANME in seep environments, accounted for large percentages of the bacterial clones from active sediment (27.3%; 45 sequences) and nodules (53.6%; 75 sequences) but represented a lower proportion of recovered sequences

within the carbonates from active and low activity areas (15.2% and 22.7%, respectively, 74 total sequences). Known aerobic methanotrophic sequences were not recovered in 16S rRNA gene bacterial surveys (Supplementary Data 1.2), but *Methylococcales* sequences were identified in 454 pyrotag sequencing of the A.Carb-3439 carbonate (14 of n=7124 reads; Supplementary Data 1.3). Genes encoding particulate methane monooxygenase (*pmoA*), the enzyme responsible for the first step of aerobic methane oxidation, were detected by PCR and sequenced from active seep sediment (A.Sed-3452, 3-6 cm depth horizon) and a carbonate sample recovered off-seep (L.Carb-3414; data not shown).

Cell aggregates of Archaea and sulphate-reducing *deltaproteobacteria* were observed by catalyzed reporter deposition fluorescence *in situ* hybridization (CARD-FISH) using the general archaeal probe Arch915 and *Desulfosarcina*/*Desulfococcus* specific probe DSS658 in all carbonates examined, revealing the presence of endolithic microorganisms with intact ribosomes. Quantification of DAPI-stained cells and cell clusters showed that microbial aggregates within the interior of active carbonates were more abundant and larger, but less densely packed, than sediment- and nodule-hosted aggregates (Table 1.1; Supplementary Fig. 1.4). A "pair correlation statistic"[33] supported this packing density trend, suggesting that cells from sediment-hosted microbial aggregates favored a shorter inter-cellular distance (0.59 +/- 0.02 μm) than aggregates from nodules, active porous, and active massive carbonates (~1 μm). The vast majority of observed biomass was in aggregate form: microscopic analysis of microorganisms concentrated on 0.22 μm filters showed that <1% of DAPI-stained cells were in single or few-celled arrangements in active rocks, sediment, and nodules, while a larger proportion (~10-15%)

was observed in low-activity sediment and carbonate rock samples (Supplementary Table 3).

| | Average Aggregate Diameter, µm (SE; n) | Aggregates per mg (SE) | Aggregate biovolume relative to sediment (SE) | Pair Correlation Peak, µm (SE) | Aggregate biomass relative to sediment (per mg) |
|---|---|---|---|---|---|
| **Active Sediment** | 6.51 (0.69; 3) | 319 (2.7) | 1 (0.08) | 0.59 (0.02) | 1 |
| **Active Nodule** | 6.48 (0.87; 3) | 406 (2.4) | 0.46 (0.01) | 1.09 (0.05) | 0.58 |
| **Active Porous Carbonate** | 10.2 (1.6; 2) | 511 (8.9) | 0.23 (0.03) | 1.04 (0.04) | 1.41 |
| **Active Massive Carbonate** | 9.94 (0.98; 3) | 481 (7.4) | 0.20 (0.04) | 0.98 (0.02) | 1.05 |
| **Low Act. Sediment** | 6.12 (1.1; 2) | 177 (3.2) | NM | NM | NM |
| **Low Act. Massive Carbonate** | 5.56 (1.0; 3) | 205 (2.4) | NM | NM | NM |

**Table 1.1**. The average diameter, abundance, biovolume, and pair correlation peak of DAPI-stained aggregates across all sample types. Estimated relative overall biomass is also provided for sediment, nodule, active porous carbonate, active massive carbonate, low activity sediment, and low activity massive carbonate samples. Aggregate diameter and abundance values are from the following samples: A.Sed-3098, A.Sed-3452, A.Sed-5128, A.Nod-2518, A.Nod-2688, A.Nod-3099, A.Carb-3439, A.Carb-5305, A.Carb-2871, A.Carb-4588E3, A.Carb-5152, L.Sed-2939, L.Sed-5043, L.Carb-2874, L.Carb-3604, and L.Carb-5028. Biovolume and pair correlation peak calculations were obtained with DAIME software for the following samples: A.Sed-3098 aggregates 5, 6, 12, 15, and 19 (sediment); A.Nod-3099 aggregates 2, 5, 6, 14, and 16 (nodule); A.Carb-3439 aggregates 18, 19, 22, 26, and 33 (active porous carbonate); A.Carb-5152 aggregates 5, 6, 12, 17, and 18 (active massive carbonate). Relative biomass values were calculated from diameter, abundance, and biovolume values. Biovolume and pair correlation peaks were only measured for active samples in order to appropriately compare ecosystems most influenced by methane seepage.

Combining measurements of aggregates' abundance, size, and biovolume within the different habitats surveyed in this study, we calculated that active carbonate habitats had greater aggregate-based microbial abundances per unit dry mass than active methane seep sediment and nodules. Porous carbonates and massive carbonates from active methane seeps hosted 41% and 5% more aggregate-based cells than active seep sediment

(per unit mass), respectively, and 143% and 81% more than sediment-hosted carbonate nodules, respectively (Table 1.1).

*Methanotrophic Metabolic Activity*

To verify whether the carbonate-hosted communities were active in methane oxidation, a $^{14}CH_4$ radiotracer method was used to directly demonstrate net methane consumption by endolithic microorganisms. Methane oxidation was highest in active methane seep sediment (A.Sed-5128, 0-12 cm depth horizon) incubated under anoxic conditions, consuming 193.6 +/- 20.4 nmol $CH_4$ $cm^{-3}$ $d^{-1}$ after a 7-day incubation at 4ºC (n=3). Porous (A.Carb-5305) and massive (A.Carb-5152) carbonates from active seep sites oxidized methane at rates approximately 42% and 27% of the sediment AOM rate, or 80.9 +/- 9.2 nmol $CH_4$ $cm^{-3}$ $d^{-1}$ and 52.5 +/- 8.0 nmol $CH_4$ $cm^{-3}$ $d^{-1}$, respectively. When scaled by relative DAPI-stained aggregate biomass (Table 1.1), porous carbonates consumed methane at 30% of the rate of active seep-associated sediment per unit biomass, and massive carbonates were 26% as active. Sediment and carbonate samples from the lower methane flux sites (L.Sed-5043 and L.Carb-5028) both demonstrated low, but detectable, levels of AOM activity (7.5 +/- 1.8 nmol $CH_4$ $cm^{-3}$ $d^{-1}$ and 11.8 +/- 2.0 nmol $CH_4$ $cm^{-3}$ $d^{-1}$, respectively). Rates of methane oxidation under oxic conditions were also measured using parallel incubations amended with $CH_4$ (2.2 mM) and $O_2$ (420 μM). Aerobic methane oxidation rates were approximately 31% that of their anaerobic counterparts for both sediments and carbonates among active methane seep samples and 60% among low-activity samples. In all data presented here, rates derived from killed control incubations were subtracted (1.2 and 0.6 nmol $CH_4$ $cm^{-3}$ $d^{-1}$ for anaerobic sterilized active sediment and

active porous carbonate, respectively; 3.1 and 2.9 nmol $CH_4$ $cm^{-3}$ $d^{-1}$ for oxic sterilized active sediment and active porous carbonate, respectively); (Fig. 1.1).

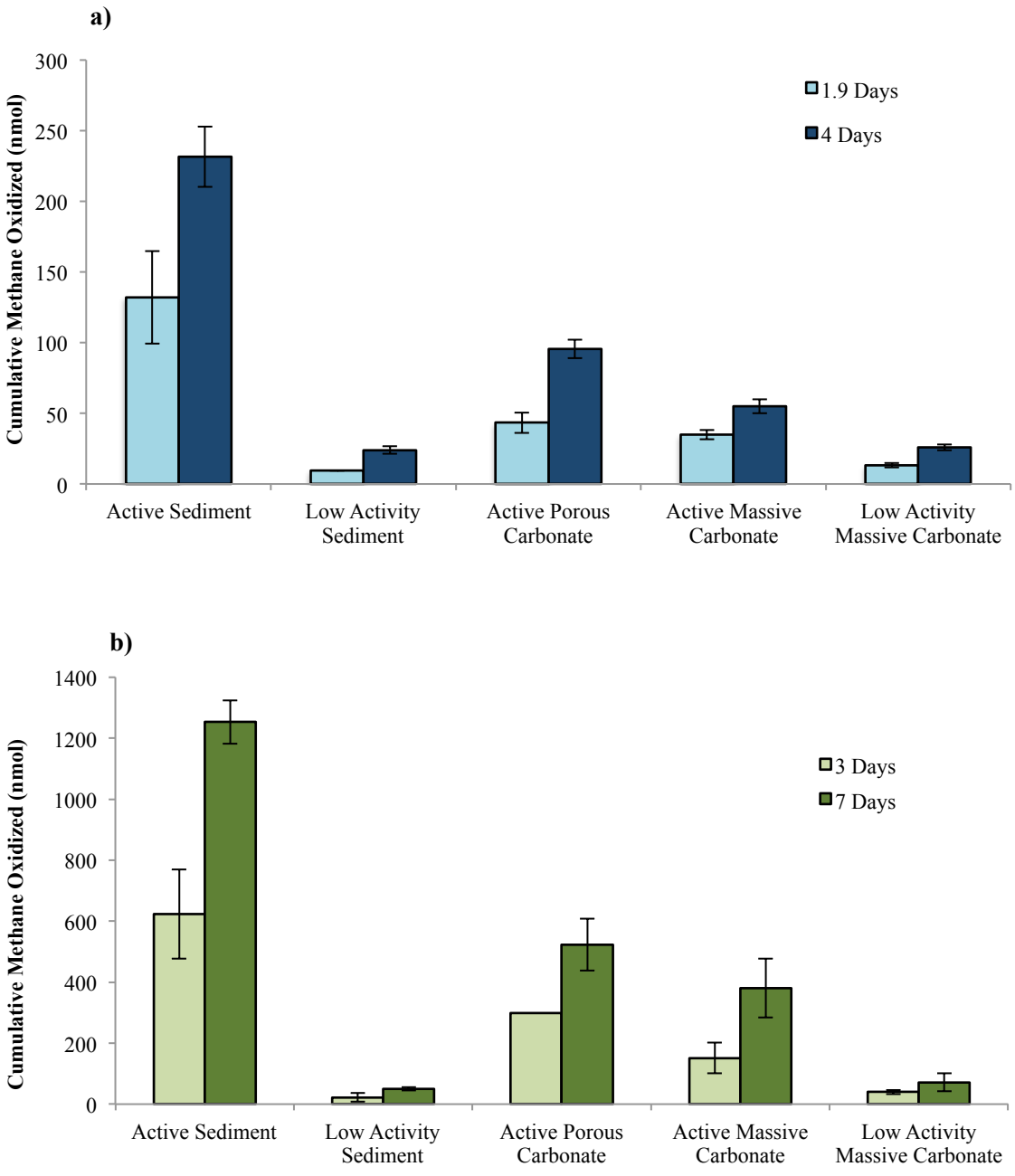


**Fig. 1.1**. Methane oxidation rates derived from $^{14}CH_4$ radiotracer experiments. Rates under **(A)** oxic and **(B)** anoxic conditions are shown, using active sediment (A.Sed-5128), low-activity sediment (L.Sed-5043), and intact pieces of active porous carbonate (A.Carb-

5305), active massive carbonate (A.Carb-5152), and low-activity massive carbonate (L.Carb-5028) from Hydrate Ridge. Each bar represents nmol methane oxidized at a particular time point, with values from killed control experiments subtracted; error bars show standard errors for triplicate incubations (the 1.875-day aerobic low activity sediment and 3-day anaerobic active porous carbonate data points represent only one replicate).

To confirm the viability and anabolic activity of carbonate-associated archaea and bacteria, targeted FISH-nanoSIMS analyses were conducted using samples from an active porous carbonate (A.Carb-3439; Supplementary Fig. 1.2e), collected from Hydrate Ridge. Following amendment of intact interior pieces of carbonate (~5 cm diameter pieces, ~300 g total mass) with 2 mM $^{15}NH_4Cl$ and 0.44 mM $CH_4$ (50% $^{13}CH_4$) at 4 °C for 27 months, three endolithic archaea and *Desulfosarcina/Desulfococcus* (*DSS*) aggregates were identified by CARD-FISH and their $^{13}C/^{12}C$ and $^{15}N/^{14}N$ ratios measured by nanoSIMS. All three consortia showed maximum levels of $^{15}N$ incorporation ranging from 83.3 – 87.9 atom % (Fig. 1.2a-c), demonstrating consistent overall growth rates over an extended incubation period. Carbonate-hosted aggregates had maximum $^{13}C$ values of 1.11-1.36 atom % after 27 months, which was approximately double that of the $^{13}C/^{12}C$ ratios measured from unlabeled control aggregates (0.48-0.66 atom %; Table S 1.4).

FISH-nanoSIMS analysis of $^{15}NH_4^+$ assimilation by ANME/SRB aggregates recovered from intact sediment-hosted carbonate nodules (~15 mm diameter) also demonstrated significant enrichment after 9 months, reaching $^{15}N$ values of 76 atom % (Fig. 1.2d) while aggregates from parallel unlabeled control incubations had $^{15}N$ values of approximately 0.5 atom %. Additionally, nanoSIMS analysis of a five-day shipboard incubation experiment with an intact active carbonate sample (A.Carb-3439, ~10 cm diameter subsample) amended with 0.44 mM $CH_4$ (50% $^{13}CH_4$) and $O_2$ (air) revealed that

half of the DAPI-stained microbial aggregates analyzed (n=10) showed slightly elevated levels of $^{13}C$ in biomass relative to the parallel unlabeled controls (n=3 aggregates) (Fig. 1.3).

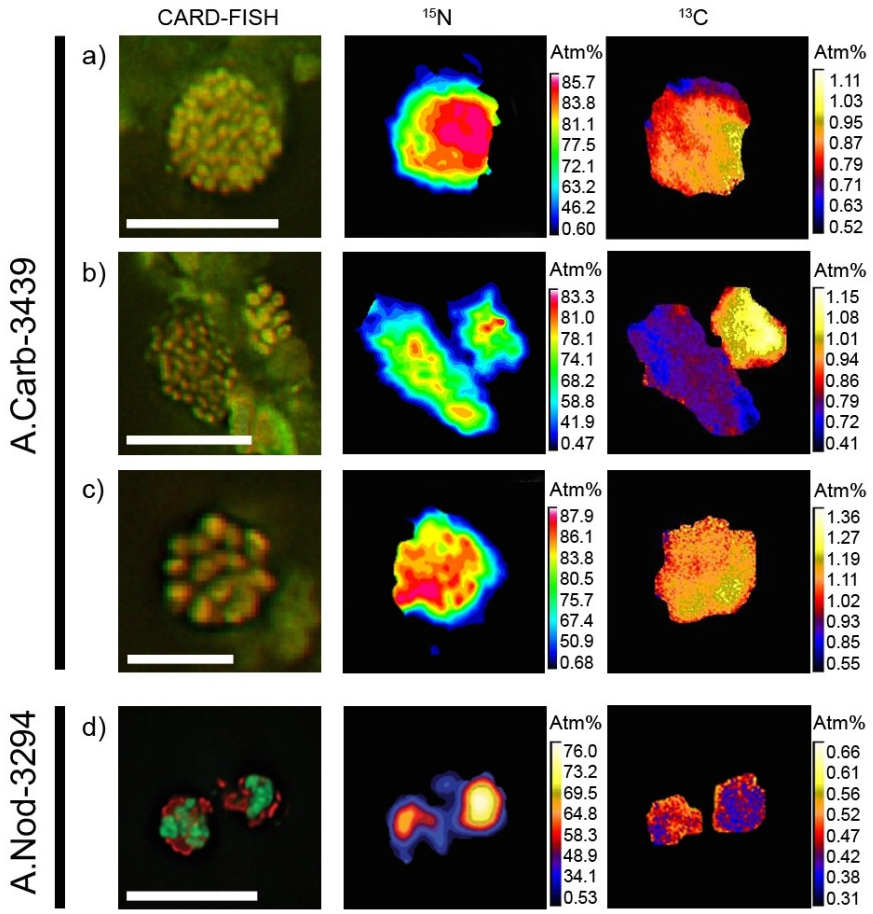


**Fig. 1.2.** Anabolic incorporation of isotopically-labeled substrate by endolithic microbial aggregates. Paired CARD-FISH and nanoSIMS results of samples A.Carb-3439 **(A)-(C)** and A.Nod-3294 **(D)** are provided. A.Carb-3439 was incubated at 4 °C for 27 months under anoxic conditions with 2 mM $^{15}NH_4Cl$ and 1.48 mM $CH_4$ (50% $^{13}CH_4$); A.Nod-3294 was incubated at 4 °C for 9 months under anoxic conditions with 1mM $^{15}NH_4$ and 1.12 mM $^{12}CH_4$. In A.Carb-3439 CARD-FISH images, red signal indicates Arch 915 hybridization and green indicates DSS 658 hybridization; the colors are reversed for A.Nod-3294 hybridizations. $^{15}N$ and $^{13}C$ atom % nanoSIMS images are derived from $^{15}N^{12}C^-$ / $^{14}N^{12}C^-$ and $^{13}C$ / $^{12}C$ ion count ratios, respectively, and represent mean values from multiple planes of analysis. Scale bars apply to CARD-FISH and nanoSIMS images, and are 10 μm for **(A)** and **(B)**, and 5 μm for **(C)** and **(D)**. Control A.Carb-3439 aggregates (n=3) incubated with unlabeled chemical substrate exhibited average $^{15}N$ and $^{13}C$ atm % values of 0.35 and 0.54, respectively.

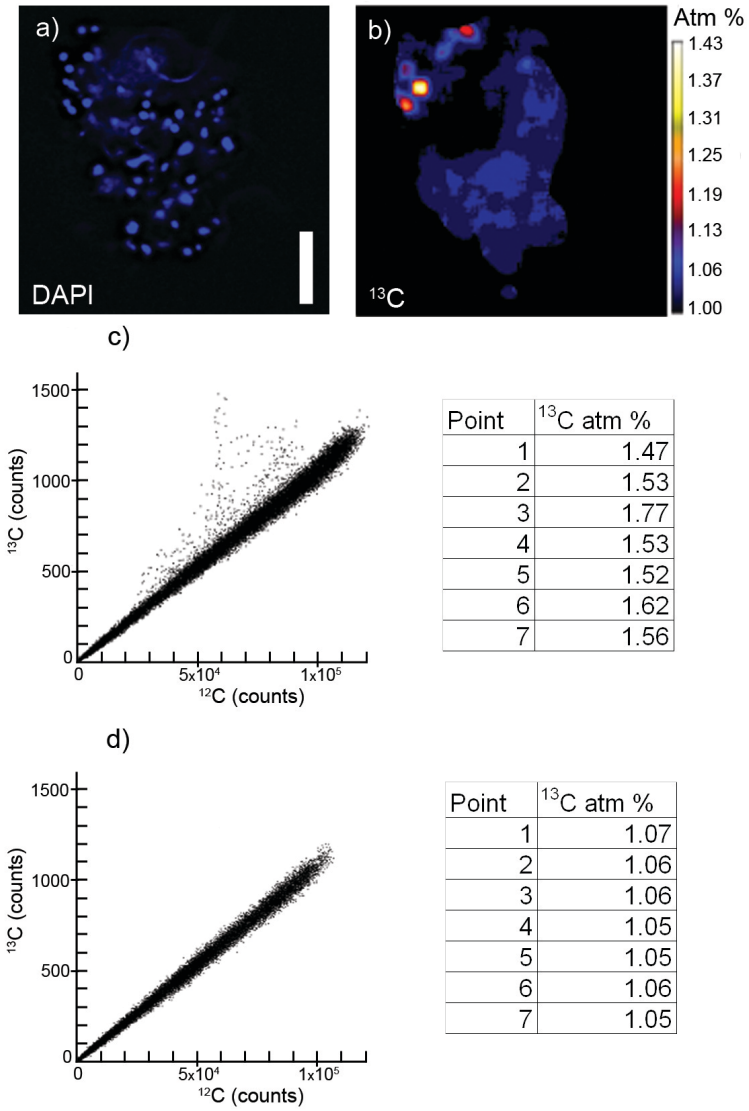


| Point | $^{13}$C atm % |
|---|---|
| 1 | 1.47 |
| 2 | 1.53 |
| 3 | 1.77 |
| 4 | 1.53 |
| 5 | 1.52 |
| 6 | 1.62 |
| 7 | 1.56 |

| Point | $^{13}$C atm % |
|---|---|
| 1 | 1.07 |
| 2 | 1.06 |
| 3 | 1.06 |
| 4 | 1.05 |
| 5 | 1.05 |
| 6 | 1.06 |
| 7 | 1.05 |

**Fig. 1.3**. Anabolic incorporation of isotopically-labeled substrate after brief incubation. **(A)** DAPI and **(B)** $^{13}$C atom % NanoSIMS images of aggregate 27 from sample A.Carb-3439 are shown following a 5-day incubation with $^{13}CH_4$ and air headspace. **(C)** A scatter plot of individual pixels' $^{13}$C and $^{12}$C counts from nanoSIMS analysis shows that many pixels skew heavy for the incubated aggregate while **(D)** none skew away from the mode ratio in a control A.Carb-3439 aggregate incubated without labeled chemical substrates (corresponding control aggregate images not shown). Tables in **(C)** and **(D)** provide $^{13}$C atom percent values for several cell-sized regions of interest acquired from various nanoSIMS cycles during analysis of the experimental and control aggregate, respectively. Scale bar = 5 μm.

**Discussion**

The data presented above demonstrate that methane derived authigenic carbonates, including sediment-hosted nodules and well-lithified carbonate rocks and pavements at the seabed, host substantial active microbial biomass capable of methane oxidation under both oxic and anoxic conditions. Porosity and permeability heavily influence the microbial habitability of rock-hosted environments by determining both the habitable volume and the dynamics of chemical substrate delivery ($CH_4$, $SO_4^{2-}$, nutrients) and end product removal ($H_2S$, $HCO_3^-$). The measured permeability values, which indicate connected pore spaces within rock (Supplementary Table 1.2), ranged over three orders of magnitude. Permeability values of active massive carbonates are within the range of values observed for seep sediments[34], indicating that fluid flow through the carbonate interior is sufficient to support biological activity. It was not possible to determine the porosity and permeability of active porous carbonates, but their macroscopic vugs and fractures likely confer even higher values; indeed, similar porous structures are reported to harbor localized microbial mats[19], biomarkers, and depleted carbon isotopic signatures[6] in chemoherms. Such enhanced fluid supply is an important environmental variable, particularly in surface-exposed porous carbonates unencumbered by lower-permeability overlying sediment, and may influence microbial aggregate size, abundance, and spatial structure. The massive carbonates recovered off-seep from low activity sites demonstrate much lower permeabilities, likely due to the time-integrated accumulation of biologically produced carbonate[13]. Similar permeability decreases occur within modeled mid-ocean ridge basaltic crust, as anhydrite and sulfide precipitation limit fluid flow[35], and these physical constraints, which could limit methane and nutrient flux, may curtail *in situ* microbial

growth. Active massive carbonates exhibit permeability values similar to those of seafloor basalts, which have been shown to host endolithic chemolithoautotrophic microorganisms[24]. In comparison, permeabilities of massive carbonates from low activity areas are analogous to those of basalts several hundreds of meters below the seafloor[36]. The organisms we detected in this hydrologic regime may exhibit adaptations to limited chemical substrate delivery; studying these unique ecosystems may provide insight into survival strategies under physical constraints (see Appendix 2 for a more detailed treatment of carbonate-hosted AOM and endolithic microbial lifestyles).

The methanotrophic communities identified within carbonate rocks appeared to differ across the sampled range of seepage activities and habitat types. In archaeal 16S rRNA gene clone libraries, ANME lineages were decreasingly prominent from active seep sediment (92.9%) to active carbonate nodule (85%) to active seep carbonate (70.9%) habitats; this progressive decrease may point to a physical substrate-based influence on community structure in which additional niches develop in lithified carbonates. The ANME contingent of the carbonate sample from a low activity site not only comprised a smaller percentage of total archaeal sequences (12.9%), but was also dominated by ANME-1, in contrast to the ANME-2-rich assemblages found at actively venting seeps. ANME-1 archaea may be capable of methanogenesis[37] and have been found to live independently of bacterial partners, indicating that they may not require the close spatial association of syntrophic bacteria[38]. It is possible that ANME-1 in low-activity carbonates adopt multiple configurations, from bacteria-independent monospecific aggregates to ANME-1-deltaproteobacterial consortia.

Low-activity carbonates recovered from outside the seep area retained significant microbial biomass in the carbonate interior, much of which appeared to be unrelated to seep-associated microorganisms and suggests a secondary colonization after methane flux wanes. Nonetheless, the occurrence of methanotrophic activity upon the addition of methane indicates the presence and viability of anaerobic and aerobic methane-oxidizing microorganisms, an observation supported by our FISH detection of ANME-DSS aggregates in these samples.

Endolithic aggregates recovered from active carbonates were larger and more diffusely packed than those described from active seep sediments (Table 1.1, Supplemenatry Fig. 1.4), exhibiting mixed or clustered species distributions. When modeling large aggregates (25 μm), Orcutt and Meile found that consortia partners in shell-type aggregates were too distant for electron carrying intermediates to diffuse out of the archaea-dense inner core at metabolically feasible rates[39]. The observed patchy arrangement of syntrophic partners within large aggregates suggests that their diffusive regimes may be similar to those of smaller aggregates. The diffuse cell packing we observe in endolithic aggregates may represent a transition to a more biofilm-like mode of growth, in which secreted polymeric substances offer a community-wide competitive advantage[40] despite higher localized diffusion coefficients[41].

The rates of AOM measured by $^{14}CH_4$ radiotracer were within the range of previously reported rates from Hydrate Ridge and other seep sites (Table 1.2). Porous and massive carbonates from active seep sites performed AOM at rates commensurate with active seep sediment[42–44], while sediment and carbonate rates from off-seep, low-activity areas were similar to those reported from continental shelves[10,45,46].

| Study | | Sample | Methane Oxidation Rate (nmol C / $cm^3$ day) |
|---|---|---|---|
| This Study | Oxic | Active Sediment A.Sed-5128 | 64.1 (11.3) |
| | | Low Activity Sediment L.Sed-5043 | 4.7 (0.5) |
| | | Active Porous Carbonate A.Carb-5305 | 23.5 (2.4) |
| | | Active Massive Carbonate A.Carb-5152 | 16.2 (2.1) |
| | | Low Activity Massive Carbonate L.Carb-5028 | 6.8 (0.6) |
| | Anoxic | Active Sediment A.Sed-5128 | 193.6 (20.4) |
| | | Low Activity Sediment L.Sed-5043 | 7.5 (1.8) |
| | | Active Porous Carbonate A.Carb-5305 | 80.9 (9.2) |
| | | Active Massive Carbonate A.Carb-5152 | 52.5 (8.0) |
| | | Low Activity Massive Carbonate L.Carb-5028 | 11.8 (2.0) |
| Treude et al. (2003) | | Hydrate Ridge Active Seep Sediment | 32 – 2358 |
| Wegener et al., (2008) | | North Sea Active Seep Sediment | 25 - 450 |
| Joye et al. (2004)[92] | | Gulf of Mexico Active Seep Sediment | 121 - 501 |
| Girguis et al. (2003) | | Monterey Bay Active Seep Sediment | 82.3 |
| Hansen et al. (1998) | | Norsminde Fjord Inner Shelf Sediment | 14.3 |
| Hoehler et al. (1994) | | Cape Lookout Bight Inner Shelf Sediment | 14 - 18 |
| Reeburgh (1980) | | Skan Bay Outer Shelf Sediment | 4.9 - 9.3 |

**Table 1.2**. Comparison of methane oxidation rates. Results for the ten sample types tested in this study are provided alongside several previously published rates of AOM for a range of seafloor geologic environments. All cited values are maximum rate measurements for a sedimentary column under anoxic conditions, correlating with the sulphate-methane transition zone. Values from this study are derived from the experiments presented in Fig. 1; all control-subtracted rate values from the two time points (n=6 bottles) were divided by the incubation times to calculate the daily rate. These values were averaged, and standard error values are in parentheses.

Within the comparative context of FISH-nanoSIMS analysis, active porous carbonate-hosted Archaea-*DSS* aggregates under anoxic conditions display substantial $^{15}N$ incorporation compared with aggregates from unlabeled incubations, confirming significant anabolic activity associated with cells residing in carbonate interiors. $^{15}N$ enrichment values were consistent with those of ANME/DSS aggregates measured from six-month

$^{15}NH_4^+$-amended seep sediment incubations[47] and roughly half of those reported in time series analyses by Orphan et al.[48]. $^{13}CH_4$ incorporation into AOM biomass has been reported to be approximately 1% of the total methane oxidized[49], and thermophilic AOM aggregates have been shown to derive most of their biomass from inorganic carbon sources[50]. Our results were consistent with these observations and the related prediction of substantially lower methane-derived $^{13}C$ enrichment than $NH_4$-based $^{15}N$ uptake (Supplementary Table 1.4). $^{15}NH_4^+$ uptake was also observed in active nodule-hosted consortia after nine months (Fig. 1.2d), with enrichment levels suggestive of approximately two or three doublings, similar to estimated growth rates reported from incubations of sediment samples from an active methane seep[47].

NanoSIMS analysis of carbonate-hosted communities was suggestive of aerobic methane oxidation potential, though known bacterial methanotrophs were not recovered in 16S rRNA gene clone libraries. Observable $^{13}C$ enrichment from AOM requires extended incubations, considering that ANME-SRB consortia have doubling times of several months[49]. Thus, the enrichment observed in our five-day incubation is likely attributable to aerobic methanotrophs, consistent with the aerobic methane oxidation measured by $^{14}CH_4$ radiotracer experiments. The detection of genes encoding particulate methane monooxygenase in active seep sediment (A.Sed-3452, 3-6 cm depth horizon) and a low-activity carbonate sample (L.Carb-3414), coupled with the observation of *Methylococcales* sequences from 454 pyrotag sequencing of A.Carb-3439 (Supplementary Data 1.3), suggests that aerobic methanotrophs are associated with both sediment and exhumed carbonate habitats. However, 16S rRNA gene sequences from known bacterial methanotrophs were not recovered in clone libraries (n=705 across four sample types;

Supplementary Data 1.2), indicating that they may be exceedingly rare members of the community, or that there may be uncharacterized aerobic methanotrophs within the seep carbonate environment. Alternatively, the activity detected under oxic conditions may be due, at least in part, to AOM occurring in anoxic niches, where putative extracellular polymeric substances may confer protection against oxygen exposure.

Methane oxidation rates under oxic conditions were approximately 31% +/-1.2% SE that of their anaerobically incubated counterparts for both sediments and carbonates among active methane seep samples and 60% +/- 2.8% SE among samples from low-activity, seep-adjacent sites. The consistent proportions of aerobic to anaerobic methanotrophic activity among different sample types, demonstrated by the low standard errors, contrasts the samples' varying microbial community assemblages. These findings suggest that low-abundance microorganisms, both anaerobic and aerobic, maintain viability under quiescent periods of methane flux and are able to initiate activity soon after the introduction of stimulating conditions. It appears that waning methane supply does not necessitate ecosystem shutdown, but rather represents a selective force that presents alternative niches and promotes the successional development or persistence of an endolithic microbial assemblage that retains the capacity for continued methane consumption.

The observation of actively metabolizing methanotrophic organisms within carbonate rocks at sites of active and low-activity methane seepage furthers previous studies linking methanotrophic microorganisms with authigenic carbonate formation and shifts the geobiological perception of seep-associated authigenic carbonates. The association of methanotrophic organisms with active porous chemoherms at Hydrate Ridge

has been previously postulated[6], but the associated petrographic, isotopic, and microfossil evidence from porous carbonate lithologies (like that represented by A.Carb-3439 panels in Supplementary Fig. 1.3) stopped short of demonstrating contemporary endolithic activity and net methane consumption. In contrast to such studies of porous chemoherms and carbonate-associated ANME biofilms in the euxinic Black Sea, which cover outer surfaces of carbonate reefs[18] or line cm-scale cavities[19], some of the active AOM assemblages described here persist within pore spaces of highly lithified, low-permeability structures that pave the seafloor and are volumetrically dominant at active and dormant seep sites. We report active and abundant methanotrophic microorganisms not only in porous carbonates at seepage sites with high $CH_4$ flux, but indeed within carbonates from all investigated seafloor environments, including the abundant low-permeability massive carbonate pavements covering regions of low-seepage activity. These findings suggest that such endolithic communities may be broadly distributed across a wide range of methane- and sulphate-infused carbonates.

Endolithic aerobic and anaerobic methanotrophic communities occupy a previously undescribed niche, replete with distinct physicochemical challenges such as potential nutrient limitation or metabolic product accumulation. There are fundamental similarities in community structure and aggregate morphology between endolithic and sediment-hosted methanotrophic communities, but the distinct parameters of rock-hosted habitats likely promote a unique set of metabolic responses or interspecies spatial relationships, as revealed by our recovery of larger, less cohesive endolithic aggregates (Supplementary Fig. 1.4). Understanding the full metabolic repercussions of the endolithic methanotrophic lifestyle – and how it differs from the more familiar sediment-based mode in terms of

methane processing or environmental interaction – is a compelling direction of future work. Endolithic methanotrophs within authigenic cold seep mounds may also serve as a useful point of comparison with communities associated with chemically precipitated carbonates at warmer chemolithotrophic habitats like Lost City.

Endolithic methanotrophs likely play an integral role within the larger context of global methanotrophy and methane cycling. While the extents of both methane seepage and associated authigenic carbonates on a global scale are poorly constrained, targeted studies from select regions indicate that methane seeps and vents are significant contributors to net methane oxidation and are frequently accompanied by substantial carbonate formation[e.g.,15,27]. Along the Costa Rica Margin, multibeam bathymetry, side-scan sonar imagery, TV-sled observations, and sampling revealed more than 100 previously unknown seep sites, typified by authigenic carbonate mounds rising up to 100 m above the seafloor[23]. At better characterized sites, published side scan sonar results, seafloor photographic images, and descriptions of seep sites indicate that approximately 46% of active methane seep sites at the seabed are paved by authigenic carbonates[4–6] (surveyed sites include Hydrate Ridge, the Costa Rica Margin, Santa Monica Basin, and the Chilean Subduction Zone). Assuming methanotrophy at active sites that would otherwise occur in overlying sediment takes place endolithically, we estimate that endolithic AOM in surface-exposed carbonates may account for 12.5% (using massive carbonate rates) to 19.2% (using porous carbonate rates) of the overall methane consumption estimated to take place at active seeps. The endolithic contribution to AOM at low-activity settings and adjacent marine sediment sites is more difficult to quantify.

The carbonate samples collected for this study were, by necessity, from exhumed seafloor carbonate pavements, and the extent to which our findings translate to deeper carbonate lenses and platforms requires targeted study. Authigenic carbonates account for the vast majority of mound volume at methane seep complexes: 85.7% at the Costa Rica margin[4], 99.8% at Hydrate Ridge South Pinnacle and SE Knoll[6], 99.2% at Chilean seeps[5] and, in regions like the Florida escarpment, carbonates can pave extensive areas of the seafloor[51]. The high permeability values measured from carbonates at actively venting sites and the emergence of methane-rich fluids above carbonate pavements[52] imply that large carbonate mounds (10s to ~100 meters tall) are supplied with abundant methane. Sulphate supply within the carbonate interior may be enhanced by downward fluid circulation, which has been attributed to tidal forcing and/or negative pressure generated by focused fluid discharge[34], and hydrologic recharge of carbonate masses, previously suggested at the base of methane seep sites including Hydrate Ridge[6] and the Florida Escarpment[51]. With extensive methane and sulphate perfusion of mound carbonates[6,34,51], and the recognition that sulphate concentration far below that of ambient seawater can sustain AOM[53], the potential for endolithic methanotrophy is substantial, and may exceed that of surface associated seep sediments.

Hidden sources of endolithic AOM, where either methane availability and/or carbonates have no seafloor surface expression, could further enhance the global contribution of carbonate-hosted communities to methane budgets. Thin carbonate crusts may cut off methane supply to overlying sediments within hundreds of years[54]: this self-sealing effect limits methanotrophy in the upper sediment column but may increase

methane concentrations in the underlying carbonate layers[55] and sustain AOM activity, provided sufficient electron acceptor availability.

The recognition of seep-associated carbonates as active and dynamic habitats across a range of geochemical conditions also challenges the treatment of such structures as passive recorders of historical methane seepage. The persistence of actively metabolizing communities in seafloor mound structures makes the deconvolution of modern and fossil microbial assemblages difficult without phylogenetically linked isotopic tracer incubation studies or well-constrained biomarker isotopic relationships. However, any perturbation, including methane-perfused incubations, may stimulate dormant microbial lineages and thus erroneously characterize the metabolic activity and relative abundances of *in situ* microbial constituents. The extent to which microbial communities in low-activity carbonates are diagnostic of previous seep activity and the rate of community succession between active and inactive seep areas has ramifications for the interpretation of biomarker analysis in ancient seeps[56]. Biomarkers within ancient seep structures[57] are thus time-integrated reflections of a range of physicochemical environments, likely weighted toward particularly productive or recent regimes, and tempered by remineralization, succession, and competition among microbial communities.

The demonstration of abundant, active methanotrophic microorganisms within authigenic methane seep-associated carbonates reveals a dynamic ecosystem able to adapt to changing environmental conditions and methane fluxes. Given the broad distribution of methane- and sulphate-infused carbonates at and below the seafloor, carbonate-hosted methanotrophy likely represents a globally relevant sink for methane. The discovery of substantial methane consumption by these carbonate-associated microbial communities

also marks an important step in our understanding of the extent of viable habitats for anaerobic methanotrophs and associated methane turnover within the marine environment.

## Methods

*Sample Collection and Characterization*

Samples for the study of endolithic AOM were collected from three convergent boundary cold seep sites: an erosional subduction zone near Costa Rica (Mound 12, 1000 m depth; 8°55.8'N, 84°18.8'W), Eel River Basin (Northern Ridge, 525 m; 40°48.70'N, 124°36.68'W), and an accretionary prism at Hydrate Ridge, Oregon (Hydrate Ridge South, 800 m; 44°34.09'N, 125°09.14'W and SE Knoll, 620 m; 44°26.99'N, 125°01.97'W).

These sites have been previously established as areas of active methane seepage and sediment-based AOM at which methane from seep structures enters the water column at concentrations ranging from 100 nM (Costa Rica)[58] and 200 nM (Eel River Basin)[59] up to 4400 nM (Hydrate Ridge)[60]. Authigenic carbonates have been shown to adsorb methane and create localized sites of heightened concentrations[61], and pore water geochemical measurements from selected sediment push cores confirm elevated methane levels and reveal signs of AOM metabolism (pore water extrusion and geochemical analyses from push core sediments were conducted following protocols outlined in Orphan et al., 2004[63]; and House et al., 2009[70]). For example, sediment porewater measurements associated with the Eel River Basin seep (6-9 cm below seafloor) from which A.Nod-2688 was collected exhibited high levels of sulfide (8.5 mM), depleted sulphate (19.2 mM) and elevated methane (950 μM) and dissolved inorganic carbon (23 mM) with a $\delta^{13}C_{DIC}$ that is highly negative (-36.1‰), indicative of active methane oxidation. More limited geochemical

measurements associated with the Costa Rica methane seep sample from which A.Nod-3294 was recovered also were consistent with active seepage, with pore waters containing 1.23 mM $CH_4$, while the Hydrate Ridge seep sediments from which A.Nod-2518 was obtained contained 2.74 mM $CH_4$ and a $\delta^{13}C_{DIC}$ of -38.64‰.

Sediments, nodules, and carbonates were sampled with the *DSV Alvin* during R/V Atlantis legs AT-15-11 (Hydrate Ridge and Eel River Basin; September-October, 2006), AT-15-44 (Costa Rica; February, 2009), AT-15-59 (Costa Rica; January 2010), AT-15-68 (Hydrate Ridge; August, 2010), and with *ROV Jason* during AT-18-10 (Hydrate Ridge; September, 2011). Samples included 6 sediment cores, 4 sediment-entrained nodules, and 14 carbonates naturally exposed at the seafloor; all samples were kept at ambient bottom water temperatures (~4 °C) during recovery. Supplementary Table 1.1 provides a more detailed accounting of the origin, activity, and degree of lithification of all samples referenced below via serial number, and Supplementary Fig. 1.2 presents images of representative samples. Average $\delta^{13}C_{carbonate}$ values from both active (A.Carb-2840: -48.3‰; A.Carb-2871: -27.5‰; A.Carb-3439: -38.5‰) and low- activity carbonates (L.Carb-2874: -28.5‰; L.Carb-3414: -38.2‰) indicate the incorporation of $^{13}C$-depleted, methane-derived carbon.

The “active” designation refers to sites where methane seepage was manifested by seafloor ecosystems known to be fueled by subsurface methane (mussel beds, tubeworm bushes, clam beds, provannid snails, bacterial mats) or methane bubble ebullition (Supplementary Fig. 1.1a-b). Authigenic carbonate precipitates, whose calcium carbonate mineralogy was confirmed with X-ray diffraction, form loosely consolidated protoliths heretofore referred to as “nodules” within active sediments. With further precipitation and

compaction in a methane-perfused regime, larger, carbonate rocks (or, "active carbonates") form, which can be uplifted and exhumed, generating extensive pavements around methane-seeps[62,63]. The term "low activity" references sampling sites that did not exhibit any clear signs of methane seepage or chemosynthetic communities, though methane supply cannot be entirely ruled out, as subsurface advective flow can shift with time[43,64]. Low activity sites were comparatively barren, yet $\delta^{13}C_{carbonate}$ values and the carbonate mineralogy of such samples suggest that they formed in "active" seep settings. In all experiments involving carbonates, interior portions (> 5 cm from the surface) were used in order to ensure that properties exhibited were representative of bulk rock material and not a reflection of surface-based adherent cells or entrained material. At seep-associated mounds, carbonate rocks form extensive pavements and are often overlaid by thin veneers of sediment and/or microbial mats (Supplementary Fig. 1.1c-d). The thickest layers of sediment associated with active seep areas often occur between carbonate blocks in depressions that may have formed as a result of localized faulting. At low activity sites, carbonate surface expression is less pronounced, though deposits of unsedimented carbonates are apparent (Supplementary Fig. 1.1e-f).

*X-Ray Diffraction*

Two samples of sediment (A.Sed-3098, A.Sed-3452), nodule (A.Nod-3099, A.Nod-3294), active carbonate exterior (A.Carb-4588E3, A.Carb-5305), active carbonate interior (A.Carb-4588E3, A.Carb-5305), low activity carbonate exterior (L.Carb-2874, L.Carb-3604), and low activity carbonate interior (L.Carb-2874, L.Carb-3604) were powdered with a sterilized ceramic mortar and pestle. The relative intensity of X-ray reflections as a function of beam incidence angle was measured with a Phillips X'Pert

Multi Purpose X-Ray Diffractometer. $SiO_2$ was used as a standard, and best-fit analyses (with peak-shifting permitted) were conducted with the X'Pert HighScore software and its library of diffractograms.

*Porosity and Permeability*

Porosity and permeability tests were conducted by Weatherford Laboratories (Humble, TX) on 2.54 cm diameter core plugs between 5-7.5 cm in length. Porosity was determined with Boyle's Law Single Cell Method, a non-destructive technique that quantifies porosity directly without the need for disaggregation. Permeability was calculated using Darcy's Law and incorporated measured flow rates through the core plug under a range of pressures. Details on porosity and permeability methodology can be found in the American Petroleum Institute's Recommended Practices for Core Analysis[65].

*Petrographic Analysis*

Five thin sections – representing three active (A.Carb-2840, A.Carb-3439, and A.Carb-3460) and two low activity carbonates (L.Carb-2874 and L.Carb-3414) – were prepared by Spectrum Petrographics (Vancouver, WA) with blue epoxy embedding and visualized across a range of magnifications with a Leica DM 2500P microscope and Nikon DXM 1200F camera. All thin sections were prepared with a thickness of 30 μm.

*Phylogenetic Analysis*

To acquire 16S rRNA gene sequences, the following workflow was performed for active sediment (sample A.Sed-3730), carbonate nodule (A.Nod-2518), active carbonate (A.Carb-3439), and low-activity carbonate (L.Carb-3604). DNA was extracted from ~0.5 g of material using the UltraClean Soil DNA isolation kit (Mo Bio Laboratories, Carlsbad, CA). Bacterial and archaeal 16S rRNA genes were amplified in separate polymerase chain

reactions (PCR) as described in Appendix 1. Cleaned amplified DNA product was cloned into chemically competent *E. coli* with the TOPO TA Cloning Kit (Invitrogen, Carlsbad, CA). Restriction fragment length polymorphism was performed for bacterial sequences using HaeIII and Sau96I enzymes and for archaeal sequences using RsaI and HaeIII enzymes; all enzymes were acquired from NEB (Ipswich, MA), and one or two representatives of each unique restriction digest pattern were sequenced by Laragen, Inc. (Culver City, CA). Resulting sequences were aligned, checked for chimeras, and plotted as described in Appendix 1.

454 pyrotag sequencing was performed using the Roche 454 GS-FLX Titanium platform (Roche Diagnostics, Castle Hill, NSW, Australia) at the Australian Centre for Ecogenomics. See Appendix 1 for details on PCR conditions and amplicon processing.

*Cell Visualization*

Upon recovery from the seafloor, carbonate and sediment samples for microscopy analysis were fixed in 2% formaldehyde and stored at 4 °C overnight; the next day, the formaldehyde was washed from the samples with sterile PBS buffer and then transferred into 100% ethanol and stored at -80 °C. In the case of carbonate rocks, interior portions were isolated for analysis by sterile mortar and pestle and razor blade manipulation to minimize the role of surface-based communities. This method of mechanical separation was replicated on sediments; resulting samples, when compared with unprocessed sediment samples, confirmed that the diffuse aggregate morphology, cell abundance, and aggregate size found in carbonate samples are not artifacts of mortar and pestle treatment. Aggregate counts were performed using catalyzed reporter deposition fluorescence *in situ* hybridization (CARD-FISH) and DAPI (4',6-diamidino-2-phenylindole) staining on 3 μm

polycarbonate filters. To examine the proportion of single cells, sonicated sample material (sonicated on ice 3x 10 seconds at 8 W; Branson sonifier 150) was concentrated on a 0.22 μm polycarbonate filter and stained with DAPI. 25 fields of view were surveyed to determine the proportion of cells present as single cells. Cell and aggregate counts were normalized per unit dry mass for all sample types.

Samples for CARD-FISH were prepared as follows. To concentrate cell aggregates, a percoll density separation was performed according to Orphan et al.[38]. Fixed, crushed sample was permeabilized by mixing 60 μl sample with 1290 μl TE (pH = 9) and heated for 3 minutes at 60 °C. The sample tubes were put on ice for 5 minutes; 4.5 μl of 30% $H_2O_2$ was then added (to deactivate peroxidase) and incubated at room temperature for 10 minutes. Tubes were put back on ice, and 150 μl sodium pyrophosphate were introduced. Sample mixtures were sonicated on ice 3 times at 8 W for 10 seconds each time and applied to the density gradient vials. The vials were then centrifuged at 4,800 rpm for 15 minutes at 4 °C. The supernatant was filtered through a 3 μm filter, which was then rinsed with 2 ml PBS and dehydrated with 2 ml 1:1 ethanol:PBS.

For samples intended for nanoSIMS analysis, percoll prepared aggregates were concentrated onto a 3-μm pore sized polycarbonate filter and inverted onto an indium tin oxide-coated glass slide to transfer biomass as described in Orphan et al. (2002)[38]. For samples only visualized with DAPI, the above protocol was followed with the exception of the permeabilization and peroxidase deactivation steps.

CARD-FISH reactions on slides and filters were performed as in Dekas et al.[47] (see Appendix 1 for additional details). All visualizations and cell counts described above were

conducted with epifluorescence microscopy using a 60x objective lens (Olympus BX51 microscope, Olympus, Melville, NY).

*Aggregate Spatial Analysis*

Aggregate architecture was examined with the DAIME image analysis and 3D visualization program[33]. By recognizing fluorescent biomass within manually set aggregate boundaries throughout a z-stack of images, DAIME is able to calculate biovolume and the pair correlation function. Biovolume is determined by dividing the 3D integrated volume of cells by the overall aggregate volume. To derive the pair correlation function, the program rasters across the entire aggregate, deploying dipole lines of varying lengths in all directions at each pixel. If each end of the dipole contacts a distinct object (i.e., a cell), a hit is recorded at that dipole length. By ratioing the dipole hits to total dipoles as a function of dipole length and normalizing by cell density, the pair correlation statistic is obtained; its peak value corresponds to the most favored cell-cell distance. Biovolume and pair correlation values were obtained from five representative aggregates from each environment; cell sizes were consistent for all samples.

*$^{14}CH_4$ Rate Measurements*

Methane oxidation rates at two times points were measured for each of seven samples: A.Sed-5128, A.Carb-5305, A.Carb-5152, L.Sed-5043, L.Carb-5028, and sterilized control aliquots of A.Sed-5128 and A.Carb-5305. All incubations contained 10 ml physical substrate (compressed sediment or carbonate rock) and 20 ml filtered Hydrate Ridge bottom water. Carbonate rock samples were fragmented in order to fit through the 28-mm diameter bottle opening (SVG-50 gaschro vials, Nichiden Riku Glass Co, Kobe, Japan); pieces were kept as large as possible to minimize the increase in surface area-to-

volume ratio and maintain conditions as representative of the *in situ* environment as possible. Following several minutes of flushing with $N_2$ (g), 60 ml of gas was injected into the 30 ml headspace, generating a pressure of approximately 2 atm. Anaerobic incubation headspace was 100% $CH_4$; aerobic incubation headspace was 30 ml $CH_4$, 20 ml $N_2$, and 10 ml $O_2$. All incubation set-up prior to gas flushing and injection took place in an anaerobic chamber.

Triplicate incubations for each sample / headspace combination (which represented subsamples of the sample type population) were set up for each of two time points, with the exception of sterilized controls, which were sampled only at the second time point. In total, 72 incubations were prepared and maintained with a $CH_4$ headspace at 4 °C for two weeks prior to radiolabel addition in order to establish consistent environmental conditions.

Rates of methane oxidation were measured following the methods of Treude et al.[66]; details are provided in Appendix 1. The rate of methane oxidation can then be determined by the equation

$$Methane\ Oxidation = \frac{^{14}CO_2 \bullet CH_4}{(^{14}CH_4 + ^{14}CO_2) \bullet v \bullet t}$$

in which $^{14}CH_4$ is the combusted unreacted radiolabeled methane, $^{14}CO_2$ represents the quantity of acidified oxidation product, $CH_4$ signifies the initial quantity of methane in the experiment, v is the volume of sediment or carbonate rock, and t is the time over which the incubation was active. Methane oxidation rates from control incubations were attributed to abiotic activity, and these values (3.1 nmol $CH_4$ $cm^{-3}$ $d^{-1}$ for aerobic sediment, 2.9 for

aerobic carbonate, 1.2 for anaerobic sediment, and 0.6 for anaerobic carbonate) were subtracted from experimental treatments to yield the final biological oxidation rate values.

*NanoSIMS Measurements*

Target aggregates from CARD-FISH analysis were mapped on the indium tin oxide-coated glass squares using both epifluorescence and transmitted light microscopy with a DeltaVision RT (Applied Precision Inc., WA) according to Dekas et al.[47]. The Cameca nanoSIMS 50L was used to collect high-resolution data on isotopic uptake in nodule and carbonate rock incubations; $^{15}N^{12}C^-$, $^{14}N^{12}C^-$, $^{13}C^-$, and $^{12}C^-$ ions were collected. For our analyses, a 2.5 pA cesium beam with a spot size of 100-200 nm was used. The beam rastered over areas dependent on the size of the aggregates selected (generally between 5-20 μm) with a 256 x 256 pixel resolution, a dwell time of 5-10 ms per pixel, and a resolving power of ~5,000. Multiple frames, each lasting approximately 30 minutes, were taken per aggregate (between 5 and 60 frames), as the beam sputtered away layers of material.

NanoSIMS images were processed with L'image (developed by L. Nittler, Carnegie Institution of Washington, Washington D.C.). Each set of frames was corrected for drift and detector dead time. Discrete regions of interest (ROIs) were drawn manually on the ion images based on the corresponding CARD-FISH data; isotope ratios were subsequently calculated for these regions.

The following samples were analyzed: A.Nod-3294 incubated for nine months amended with 1 mM $^{15}NH_4Cl$ and an unlabeled methane headspace in a 125 ml vial; A.Carb-3439 incubated under air for five days in an air-tight mylar bag (~800 ml) with the addition of 0.74 mM $^{12}CH_4$ and 0.74 mM $^{13}CH_4$; A.Carb-3439 incubated for 27 months

under anoxic conditions with 2 mM $^{15}NH_4Cl$, 0.74 mM $^{12}CH_4$, and 0.74 mM $^{13}CH_4$. Parallel incubations of aliquots treated with unlabeled $NH_4$ and $CH_4$ chemical substrates served as controls. All incubations were set up shipboard, within hours of sample recovery from the seafloor (after several minutes of Ar sparging in the case of anoxic experiments). The extended incubations, during which methane was not replenished and the water was not flushed, likely influenced the composition and activity of resident microbial communities as the methane-sourced carbon may transition through multiple pools prior to analysis. However, when dealing with organisms that grow at such low rates (doubling times in excess of a month), such long anabolism-based incubations are necessary. Understanding these limitations, growth rates derived from nanoSIMS data should be viewed as conservative estimates; the primary utility of the method is to definitively demonstrate anabolic activity through the isotopic enrichment of cell material. Sterilized control incubations were not measured by nanoSIMS analysis, but isotopic enrichment was exclusively observed in association with Archaea-SRB aggregates (as established by CARD-FISH), indicating that abiotic isotopic incorporation was not statistically significant. All incubations were conducted in anoxic filtered Hydrate Ridge bottom water at 4 °C. *Clostridia* spores with known $^{13}C/^{12}C$ and $^{15}N/^{14}N$ ratios (measured by conventional EA-IRMS) were used as a standard and measured before and after sample analysis to track instrumental mass fractionation and drift over the course of the nanoSIMS analysis session. The $^{13}C$ and $^{15}N$ ratios of *Clostridia* spores analyses bracketing our samples were consistent throughout the run. The $^{13}C/^{12}C$ ratios of the unlabeled control archaeal – *DSS* aggregates were below natural abundance and can be attributed to the incorporation of $^{13}C$-depleted carbon from the methane seep environment[48], instrument-associated fractionation[67], or

biological matrix effects[68]. While the accuracy of the natural abundance $\delta^{13}C$ values for aggregates in control incubations is poorly constrained, these samples serve as a comparative reference for our $^{13}CH_4$ amended samples.

*pMMO Analysis*

Particulate methane monooxygenase genes *(pmoAC)* were amplified from extracted DNA using the MISA PCR assay as described previously by Tavormina et al.[69]. Products were cloned into pSMARTGC LK-kan (Lucigen Corp, Middleton, WI) following the manufacturer's guidelines. Forty-two colonies from sample L.Carb-3414 and 46 from A.Sed-3452 were picked and amplified with SL1f (5'–CAG TCC AGT TAC GCT GGA GTC–3') and SR2r (5'–GGT CAG GTA TGA TTT AAA TGG TCA GT–3'); the product DNA was digested with restriction enzyme RsaI. Representative restriction fragment patterns were selected and the corresponding DNA was sequenced by Laragen, Inc. (Culver City, CA). Resulting sequences were processed and aligned using the Sequencher software and chimeras were removed. *Pmo* sequences recovered in this study have been submitted to Genbank under accession numbers KF616507-KF616827.

*Estimates of Carbonate Volume and Ground Cover*

The relative volumes of carbonate rock and overlying sediment at several cold seep sites were estimated by compiling side scan sonar data, photographs, and descriptions from previously published studies. The proportion of mound volumes attributable to carbonate rock was determined by side scan sonar images of vent fields, in which high backscatter is interpreted as carbonate rock and from which depths of carbonate extent can be estimated[4]. The average thickness of the overlying sediment layer is known from published reports[4–6], allowing for the calculation of the proportion of active methane seep mound volume

occupied by potentially habitable carbonate rock. (This calculation approach fails to detect carbonate nodules within sediment, thereby minimally underestimating the volume of potentially habitable endolithic habitat.) The estimate of actively seeping surface area covered by carbonate rock is derived from side scan sonar surface expression data and schematic maps based on extensive *in situ* observation[4–6].

**References**


1. Denman, K. L. et al. in Climate Change 2007: The Physical Science Basis, Contribution of Working Group I to the Fourth Assessment Report of the Intergovernmental Panel on Climate Change (Cambridge University Press, 2007).
2. Reeburgh, W. S. Oceanic Methane Biogeochemistry. Chem. Rev. **107,** 486–513 (2007).
3. Dale, A. W., Van Cappellen, P., Aguilera, D. R. & Regnier, P. Methane efflux from marine sediments in passive and active margins: Estimations from bioenergetic reaction–transport simulations. Earth and Planetary Science Letters **265,** 329–344 (2008).
4. Klaucke, I., Masson, D. G., Petersen, C. J., Weinrebe, W. & Ranero, C. R. Multifrequency geoacoustic imaging of fluid escape structures offshore Costa Rica: Implications for the quantification of seep processes. Geochemistry, Geophysics, Geosystems **9,** Q04010 (2008).
5. Klaucke, I., Weinrebe, W., Linke, P., Kläschen, D. & Bialas, J. Sidescan sonar imagery of widespread fossil and active cold seeps along the central Chilean continental margin. Geo-Mar Lett **32,** 489–499 (2012).
6. Teichert, B., Bohrmann, G. & Suess, E. Chemoherms on Hydrate Ridge—Unique microbially-mediated carbonate build-ups growing into the water column. Palaeogeography, Palaeoclimatology, Palaeoecology **227,** 67–85 (2005).
7. Paull, C. K., Normark, W. R., Ussler III, W., Caress, D. W. & Keaten, R. Association among active seafloor deformation, mound formation, and gas hydrate growth and accumulation within the seafloor of the Santa Monica Basin, offshore California. Marine Geology **250,** 258–275 (2008).
8. Masuzawa, T., Handa, N., Kitagawa, H. & Kusakabe, M. Sulfate reduction using methane in sediments beneath a bathyal 'cold seep' giant clam community off Hatsushima Island, Sagami Bay, Japan. Earth and Planetary Science Letters **110,** 39–50 (1992).
9. Boetius, A. et al. A marine microbial consortium apparently mediating anaerobic oxidation of methane. Nature **407,** (2000).
10. Hoehler, T. M., Alperin, M. J., Albert, D. B. & Martens, C. S. Field and laboratory studies of methane oxidation in an anoxic marine sediment: Evidence for a

methanogen-sulfate reducer consortium. Global Biogeochemical Cycles **8,** 451–463 (1994).
11. Milucka, J. et al. Zero-valent sulphur is a key intermediate in marine methane oxidation. Nature **491,** 541–546 (2012).
12. Ziebis, W. & Haese, R. R. in Interactions Between Macro- and Microorganisms in Marine Sediments 267–298 (American Geophysical Union, 2005). at <http://dx.doi.org/10.1029/CE060p0267>
13. Luff, R. & Wallmann, K. Fluid flow, methane fluxes, carbonate precipitation and biogeochemical turnover in gas hydrate-bearing sediments at Hydrate Ridge, Cascadia Margin: numerical modeling and mass balances. Geochimica et Cosmochimica Acta **67,** 3403–3421 (2003).
14. Greinert, J., Bohrmann, G. & Suess, E. in Natural Gas Hydrates: Occurrence, Distribution, and Detection **124,** 99–113 (AGU, 2001).
15. Aloisi, G., Pierre, C., Rouchy, J.-M., Foucher, J.-P. & Woodside, J. Methane-related authigenic carbonates of eastern Mediterranean Sea mud volcanoes and their possible relation to gas hydrate destabilisation. Earth and Planetary Science Letters **184,** 321–338 (2000).
16. Naehr, T. H. et al. Authigenic carbonate formation at hydrocarbon seeps in continental margin sediments: A comparative study. Deep Sea Research Part II: Topical Studies in Oceanography **54,** 1268–1291 (2007).
17. Eichhubl, P., Greene, H., Naehr, T. & Maher, N. Structural control of fluid flow: offshore fluid seepage in the Santa Barbara Basin, California. Journal of Geochemical Exploration **69,** 545–549 (2000).
18. Michaelis, W. et al. Microbial Reefs in the Black Sea Fueled by Anaerobic Oxidation of Methane. Science **297,** 1013–1015 (2002).
19. Bahr, A. et al. Authigenic carbonate precipitates from the NE Black Sea: a mineralogical, geochemical, and lipid biomarker study. International Journal of Earth Sciences **98,** 677–695 (2009).
20. Aloisi, G. et al. CH4-consuming microorganisms and the formation of carbonate crusts at cold seeps. Earth and Planetary Science Letters **203,** 195–203 (2002).
21. Treude, T., Knittel, K., Blumenberg, M., Seifert, R. & Boetius, A. Subsurface Microbial Methanotrophic Mats in the Black Sea. Applied and Environmental Microbiology **71,** 6375–6378 (2005).
22. Walker, J. J. & Pace, N. R. Endolithic Microbial Ecosystems. Annu. Rev. Microbiol. **61,** 331–347 (2007).
23. Sahling, H. et al. Fluid seepage at the continental margin offshore Costa Rica and southern Nicaragua. Geochemistry, Geophysics, Geosystems **9,** Q05S05 (2008).
24. Santelli, C. M. et al. Abundance and diversity of microbial life in ocean crust. Nature **453,** 653–656 (2008).
25. Lever, M. A. et al. Evidence for Microbial Carbon and Sulfur Cycling in Deeply Buried Ridge Flank Basalt. Science **339,** 1305–1308 (2013).
26. Golubic, S., Friedmann, E. I. & Schneider, J. The lithobiontic ecological niche, with special reference to microorganisms. Journal of Sedimentary Research **51,** 475–478 (1981).

27. Greinert, J., Bohrmann, G. & Elvert, M. Stromatolitic fabric of authigenic carbonate crusts: result of anaerobic methane oxidation at cold seeps in 4,850 m water depth. Int J Earth Sci (Geol Rundsch) **91,** 698–711 (2002).
28. Stadnitskaia, A. et al. Carbonate formation by anaerobic oxidation of methane: Evidence from lipid biomarker and fossil 16S rDNA. Geochimica et Cosmochimica Acta **72,** 1824–1836 (2008).
29. Stadnitskaia, A., Bouloubassi, I., Elvert, M., Hinrichs, K.-U. & Sinninghe Damsté, J. S. Extended hydroxyarchaeol, a novel lipid biomarker for anaerobic methanotrophy in cold seepage habitats. Organic Geochemistry **39,** 1007–1014 (2008).
30. Birgel, D., Himmler, T., Freiwald, A. & Peckmann, J. A new constraint on the antiquity of anaerobic oxidation of methane: Late Pennsylvanian seep limestones from southern Namibia. Geology **36,** 543–546 (2008).
31. Peckmann, J., Goedert, J. L., Thiel, V., Michaelis, W. & Reitner, J. A comprehensive approach to the study of methane-seep deposits from the Lincoln Creek Formation, western Washington State, USA. Sedimentology **49,** 855–873 (2002).
32. Pernthaler, J., Glöckner, F.-O., Schönhuber, W. & Amann, R. Fluorescence *in situ* hybridization (FISH) with rRNA-targeted oligonucleotide probes. Methods in microbiology **30,** 207–226 (2001).
33. Daims, H., Lücker, S. & Wagner, M. Daime, a novel image analysis program for microbial ecology and biofilm research. Environmental microbiology **8,** 200–213 (2006).
34. Tryon, M., Brown, K. & Torres, M. Fluid and chemical flux in and out of sediments hosting methane hydrate deposits on Hydrate Ridge, OR, II: Hydrological processes. Earth and Planetary Science Letters **201,** 541–557 (2002).
35. Fontaine, F. J., Rabinowicz, M. & Boulègue, J. Permeability changes due to mineral diagenesis in fractured crust: implications for hydrothermal circulation at mid-ocean ridges. Earth and Planetary Science Letters **184,** 407–425 (2001).
36. Fisher, A. T. Permeability within basaltic oceanic crust. Reviews of Geophysics **36,** 143–182 (1998).
37. Lloyd, K. G., Alperin, M. J. & Teske, A. Environmental evidence for net methane production and oxidation in putative ANaerobic MEthanotrophic (ANME) archaea. Environmental Microbiology **13,** 2548–2564 (2011).
38. Orphan, V. J., House, C. H., Hinrichs, K.-U., McKeegan, K. D. & DeLong, E. F. Multiple archaeal groups mediate methane oxidation in anoxic cold seep sediments. Proceedings of the National Academy of Sciences **99,** 7663–7668 (2002).
39. Orcutt, B. & Meile, C. Constraints on mechanisms and rates of anaerobic oxidation of methane by microbial consortia: process-based modeling of ANME-2 archaea and sulfate reducing bacteria interactions. Biogeosciences Discussions **5,** 1933–1967 (2008).
40. Xavier, J. B. & Foster, K. R. Cooperation and conflict in microbial biofilms. Proceedings of the National Academy of Sciences **104,** 876–881 (2007).
41. Petroff, A. P. et al. Reaction–diffusion model of nutrient uptake in a biofilm: Theory and experiment. Journal of Theoretical Biology **289,** 90–95 (2011).

42. Wegener, G. et al. Biogeochemical processes and microbial diversity of the Gullfaks and Tommeliten methane seeps (Northern North Sea). Biogeosciences Discussions **5,** 971–1015 (2008).
43. Treude, Boetius, Knittel, Wallmann & Jorgensen. Anaerobic oxidation of methane above gas hydrates at Hydrate Ridge, NE Pacific Ocean. Mar Ecol Prog Ser **264,** 1–14 (2003).
44. Girguis, P. R., Orphan, V. J., Hallam, S. J. & DeLong, E. F. Growth and Methane Oxidation Rates of Anaerobic Methanotrophic Archaea in a Continuous-Flow Bioreactor. Applied and Environmental Microbiology **69,** 5472–5482 (2003).
45. Hansen, L. B., Finster, K., Fossing, H. & Iversen, N. Anaerobic methane oxidation in sulfate depleted sediments: effects of sulfate and molybdate additions. Aquatic Microbial Ecology **14,** 195–204 (1998).
46. Reeburgh, W. S. Anaerobic methane oxidation: Rate depth distributions in Skan Bay sediments. Earth and Planetary Science Letters **47,** 345–352 (1980).
47. Dekas, A. E., Poretsky, R. S. & Orphan, V. J. Deep-Sea Archaea Fix and Share Nitrogen in Methane-Consuming Microbial Consortia. Science **326,** 422–426 (2009).
48. Orphan, V. J., Turk, K. A., Green, A. M. & House, C. H. Patterns of 15N assimilation and growth of methanotrophic ANME-2 archaea and sulfate-reducing bacteria within structured syntrophic consortia revealed by FISH-SIMS. Environmental Microbiology **11,** 1777–1791 (2009).
49. Nauhaus, K., Albrecht, M., Elvert, M., Boetius, A. & Widdel, F. In vitro cell growth of marine archaeal-bacterial consortia during anaerobic oxidation of methane with sulfate. Environmental Microbiology **9,** 187–196 (2007).
50. Kellermann, M. Y. et al. Autotrophy as a predominant mode of carbon fixation in anaerobic methane-oxidizing microbial communities. Proceedings of the National Academy of Sciences **109,** 19321–19326 (2012).
51. Paull, C. et al. Seawater circulation through the flank of the Florida Platform: evidence and implications. Marine geology **102,** 265–279 (1991).
52. Torres, M. E. et al. Gas hydrate growth, methane transport, and chloride enrichment at the southern summit of Hydrate Ridge, Cascadia margin off Oregon. Earth and Planetary Science Letters **226,** 225–241 (2004).
53. Beal, E. J., Claire, M. W. & House, C. H. High rates of anaerobic methanotrophy at low sulfate concentrations with implications for past and present methane levels. Geobiology **9,** 131–139 (2011).
54. Luff, R., Wallmann, K. & Aloisi, G. Numerical modeling of carbonate crust formation at cold vent sites: significance for fluid and methane budgets and chemosynthetic biological communities. Earth and Planetary Science Letters **221,** 337–353 (2004).
55. Hovland, M. On the self-sealing nature of marine seeps. Continental Shelf Research **22,** 2387–2394 (2002).
56. Thiel, V. et al. Highly isotopically depleted isoprenoids: molecular markers for ancient methane venting. Geochimica et Cosmochimica Acta **63,** 3959–3966 (1999).
57. Peckmann, J., Birgel, D. & Kiel, S. Molecular fossils reveal fluid composition and flow intensity at a Cretaceous seep. Geology **37,** 847–850 (2009).
58. Mau, S. et al. Estimates of methane output from mud extrusions at the erosive convergent margin off Costa Rica. Marine Geology **225,** 129–144 (2006).

59. Valentine, D. L., Blanton, D. C., Reeburgh, W. S. & Kastner, M. Water column methane oxidation adjacent to an area of active hydrate dissociation, Eel river Basin. Geochimica et Cosmochimica Acta **65,** 2633–2640 (2001).
60. Heeschen, K. U. et al. Methane sources, distributions, and fluxes from cold vent sites at Hydrate Ridge, Cascadia Margin. Global Biogeochemical Cycles **19,** GB2016 (2005).
61. Ijiri, A. et al. Enrichment of adsorbed methane in authigenic carbonate concretions of the Japan Trench. Geo-Mar Lett **29,** 301–308 (2009).
62. Greinert, J., Bohrmann, G. & Suess, E. Gas hydrate-associated carbonates and methane-venting at Hydrate Ridge: classification, distribution, and origin of authigenic lithologies. Geophysical Monograph Series **124,** 99–113 (2001).
63. Boetius, A. & Suess, E. Hydrate Ridge: a natural laboratory for the study of microbial life fueled by methane from near-surface gas hydrates. Chemical Geology **205,** 291–310 (2004).
64. Orphan, V. J. et al. Geological, geochemical, and microbiological heterogeneity of the seafloor around methane vents in the Eel River Basin, offshore California. Chemical Geology **205,** 265–289 (2004).
65. American Petroleum Institute. Recommended Practices for Core Analysis: Recommended Practice 40. (1998).
66. Treude, T., Krüger, M., Boetius, A. & Jørgensen, B. B. Environmental control on anaerobic oxidation of methane in the gassy sediments of Eckernfoerde Bay(German Baltic). Limnology and oceanography **50,** 1771–1786 (2005).
67. Slodzian, G. Challenges in localized high precision isotope analysis by SIMS. Applied surface science **231,** 3–12 (2004).
68. Herrmann, A. M. et al. Nano-scale secondary ion mass spectrometry—a new analytical tool in biogeochemistry and soil ecology: a review article. Soil Biology and Biochemistry **39,** 1835–1850 (2007).
69. Tavormina, P. L., Ussler, W., Joye, S. B., Harrison, B. K. & Orphan, V. J. Distributions of putative aerobic methanotrophs in diverse pelagic marine environments. The ISME journal **4,** 700–710 (2010).

*C h a p t e r  2*

# DEUTERATED METHANE: A NOVEL APPROACH FOR MEASURING RATES OF BIOLOGICAL METHANE OXIDATION

Jeffrey J. Marlow[1], Joshua A. Steele[1], Wiebke Ziebis[2], David Case[1], Silvan Scheller[1], Victoria J. Orphan[1]

[1]Division of Geological and Planetary Sciences, California Institute of Technology, Pasadena, CA, 91125 USA
[2]Department of Biological Science, University of Southern California, Los Angeles, CA, 90089 USA

## Introduction

Methane-consuming microbial processes represent an important component of natural biogeochemical cycles and human-impacted systems. In terrestrial soils, methane production in rice fields, anoxic wetlands, and thawing permafrost supports methanotrophic communities (Holzapfel-Pschorn et al. 1985; Mackelprang et al. 2011). In marine settings, an estimated 85 Tg of methane per year, derived from biogenic and thermogenic sources, enters the subseafloor, the vast majority of which is biologically consumed in anaerobic sediments (Reeburgh 2007). Much of what remains is taken up in microaerophilic or aerobic zones of the sediment or water column by aerobic methanotrophic microorganisms (Valentine et al. 2001). Methanotrophy is also of interest in a range of human-impacted contexts, including wastewater treatment plants (Ho et al. 2013), landfills (Scheutz et al. 2009), and oil spills (Crespo-Medina et al. 2014).

In addition to the climatic and economic implications of the methanotrophic process, its biochemical intricacies have attracted the attention of many investigators. The anaerobic oxidation of methane (AOM) has proven particularly challenging to understand, often involving a mutualistic relationship between anaerobic methanotrophic (ANME) Archaea and sulfate reducing Bacteria (SRB; Boetius et al. 2000). A consensus on the precise nature of the mutualism remains outstanding, but the net result of the process is typically the stoichiometric oxidation of methane coupled with sulfate reduction (Knittel & Boetius 2009). Alternative electron acceptors including nitrate (Haroon et al. 2013), and nitrite (Ettwig et al. 2010) have been demonstrated, while several studies have presented equivocal evidence for methane oxidation coupled directly to iron or manganese reduction (Beal et al. 2009; Sivan et al. 2014; Nauhaus et al. 2005).

Methanotrophy is both a biogeochemically relevant reaction that shapes climate forcing and a biochemical curiosity; given this dual role, there is substantial interest in measuring the rate of the process. AOM rate measurement has traditionally focused on a handful of techniques. Numerical models incorporating environmental sediment profiles of sulfate and methane concentrations can be used to back-calculate methane consumption rates (Jørgensen et al. 2001). Stable isotope $^{13}CH_4$ tracers can be used to probe longer-term rates in controlled conditions (Moran et al. 2008), but high levels of natural $^{13}C$ in marine dissolved inorganic carbon pools complicates the measurement (Pack et al. 2011). Gas chromatography quantification of dissolved (Girguis et al. 2003) or headspace (Carini et al. 2003) methane concentrations has also been demonstrated as a rate measurement tool, though low molarities make samples susceptible to exsolution if not processed quickly after collection, a requirement that may not be achievable in field settings. Perhaps the most sensitive approach uses radiolabeled $^{14}CH_4$ to track carbon movement into oxidized species (Alperin & Reeburgh 1985; Treude et al. 2003). Tritiated methane was introduced for water column (aerobic) methane oxidation measurements due to its improved specific activity and the logistical advantages of working with a water-phase product rather than gaseous products (Valentine et al. 2001). Logistical and health and safety regulations led Pack et al. (2011) to develop an accelerator mass spectrometry detection method that requires $10^3$-$10^5$ less radiolabel than previous $^{14}C$ and $^{3}H$ approaches, though the analytical procedure remains labor intensive.

Despite the range of procedural options, methanotrophy rate measurements remain cumbersome, and the demonstration of a precise, safe, and easily enacted approach would be a welcome contribution for a diverse field of researchers. Nearly all of the

aforementioned approaches are carbon-based; a hydrogen-based tracer would offer an additional dimension to investigations of methane biochemical dynamics. Here we introduce a novel method for biologically mediated methanotrophy rate measurement that utilizes singly deuterated methane ($CH_3D$) as a substrate and measures the D/H ratio of the aqueous solution.

We demonstrate, through methanotrophic cell cultures and microcosm incubations of seafloor sediment and carbonate rock fragments, that aqueous D/H values are consistently proportional to $^{14}C$-based rate measurements for a given environmental treatment. The resulting ratios, when viewed in the context of partial versus complete methane oxidation, represent a new tool with which to examine the reversibility and catabolic / anabolic partitioning of methanotrophic metabolisms. As a rate measurement protocol, this approach offers several advantages over current techniques: it does not require the logistical, safety, and administrative challenges associated with radiotracers such as $^{14}CH_4$ and $CH_3T$, it is less invasive than methane headspace measurements, and compares favorably in terms of equipment cost and portability. The deuterated methane protocol offers new flexibility for practitioners and represents a useful contribution to the array of methanotrophic rate measurement tools.

**Methods**

Experimental Set-Up

To demonstrate the precision and replicability of the deuterated methane approach, it was tested alongside the better-established $^{14}CH_4$ radiotracer protocol. Both techniques were applied to a) aerobic methanotrophic cultures of *Methylosinus trichosporium* and *Methyloprofundus sedimenti*, b) oxic incubations of methane seep sediment and carbonate

rocks, and c) anoxic incubations of methane seep sediment and carbonate rocks. Finally, the deuterated methane protocol was used in a comparative context to demonstrate the effect of heightened, environmentally relevant pressure on methane consumption rates in anoxic seep sediment samples. For a representation of all experiments conducted in this study, see Table 2.1.

| | | Oxic | | Anoxic | |
|---|---|---|---|---|---|
| | | $CH_3D$ | $^{14}CH_4$ | $CH_3D$ | $^{14}CH_4$ |
| Aerobic Methanotroph Cultures Experiment | | | | | |
| | *M. trichosporium* | | | | |
| | *M. sedimenti* | | | | |
| Seep Sediment Experiment | | | | | |
| | A.Sed-5128* | | | | |
| | L.Sed-5043 | | | | |
| Seep Carbonate Experiment | | | | | |
| | A.Carb-5305 | | | | |
| | A.Carb-5152 | | | | |
| | L.Carb-5028 | | | | |
| Pressure Experiment | | | | | |
| | A.Sed-3450 | | | | |

Table 2.1: A summary of the samples used for all experiments conducted in this study. Green boxes indicate that the experiment took place (with all relevant permutations and controls, as described in the text); red boxes indicate experiments that were not conducted. $CH_3D$ refers to methanotrophic rate experiments using the novel deuterated methane technique, while $^{14}CH_4$ refers to radiolabel-based experiments. The three-part codes for samples derived from environmental material are explained in the text. *Sample A.Sed-5128 was also used for NMR studies of methane headspace.

*Aerobic Methanotroph Cultures*

Cultures of *Methylosinus trichosporium* strain OB3b (Whittenbury et al. 1970) were grown using NMS medium at 30 °C. The newly characterized *Methyloprofundus sedimenti* strain WF1 was grown in a modified NMS medium at 25 °C (Tavormina et al. 2015). In both cases, cultures were grown up from stock in sealed 25 mL test tubes that contained 5 mL media and 50:50 air : methane by volume. When cultures were in

exponential growth phase (three sequential growth curves were evaluated to enable robust prediction of exponential phase timing), inoculum was passaged. 0.85 mL of inoculum was introduced to 8.5 mL media, and ten different experimental conditions were set up, each in triplicate (see Table 2.2). Briefly, condition #1 tested the $CH_3D$ approach, #2 was a $CH_3D$ killed control, #3 was a cell-free $CH_3D$ control, #4 was an oxygen-free $CH_3D$ control, and #5 was a $CH_3D$-free control, in which $CH_4$ served as the methane source. Conditions #6, #7, and #8 incorporated $^{14}CH_4$ to allow for three time points of destructive sampling; #9 was a radiolabel-free control, and #10 was a killed control with $^{14}CH_4$.

| | $p(CH_3D)$ | $p(CH_4)$ | $^{14}CH_4$ | $p(O_2)$ | p(Ar) | Inoculum Introduced | Killed Cells |
|---|---|---|---|---|---|---|---|
| #1 | 1 atm | | | 1 atm | | 10% v/v | |
| #2 | 1 atm | | | 1 atm | | 10% v/v | Yes |
| #3 | 1 atm | | | 1 atm | | | |
| #4 | 1 atm | | | | 1 atm | 10% v/v | |
| #5 | | 1 atm | | 1 atm | | 10% v/v | |
| #6 | 1 atm | | 13 kBq (T1) | 1 atm | | 10% v/v | |
| #7 | 1 atm | | 13 kBq (T2) | 1 atm | | 10% v/v | |
| #8 | 1 atm | | 13 kBq (T3) | 1 atm | | 10% v/v | |
| #9 | 1 atm | | | 1 atm | | 10% v/v | |
| #10 | 1 atm | | 13 kBq (T3) | 1 atm | | 10% v/v | Yes |

Table 2.2: Conditions for the aerobic methanotrophy experiments; all sample types were set up in triplicate.

Samples for D/H analysis were taken at seven time points – most concentrated around anticipated exponential growth phases – throughout 140-hour (*M. trichosporium*) and 476-hour (*M. sedimenti*) experiments. Samples for radiolabel processing were taken at 46, 102, and 166.5 hours for *M. trichosporium* cultures and 102, 166.5, and 432 hours for the slower-growing *M. sedimenti* cultures.

*Environmental Samples: Methane Seep Sediments and Carbonates*

Samples recovered from the Hydrate Ridge methane seep system were used to comparatively examine the novel $CH_3D$ approach alongside the $^{14}CH_4$ protocol with environmental microcosm samples. Hydrate Ridge, Oregon, is located along a convergent tectonic margin and is well established as a site of methane seepage and sediment-based AOM (e.g., Treude et al. 2003; Suess et al. 1999; Tryon et al. 2002). Methane concentrations within the most active seep sediments reach several mM, and have been measured and modeled at values up to 70 mM (Boetius & Suess 2004) and 50 mM (Tryon et al. 2002), respectively.

Samples used for methanotrophic rate experiments are specified in Table 2.1. All samples received a unique four-digit serial number. The "active" designation refers to sites where methane seepage was manifested by seafloor ecosystems known to be fueled by subsurface methane (mussel beds, tubeworm bushes, clam beds, provannid snails, bacterial mats) or methane bubble ebullition. The term "low activity" references sampling sites that did not exhibit any clear signs of methane seepage or chemosynthetic communities, though methane supply cannot be entirely ruled out, as subsurface advective flow can shift with time (Orphan et al. 2004; Treude et al. 2003). Low activity sites were comparatively barren, yet $\delta^{13}C_{carbonate}$ values and the carbonate mineralogy of such samples suggest that they formed in "active" seep settings. Sample types are abbreviated by the A.Sed (active sediment), A.Carb (active carbonate), L.Sed (low-activity sediment, and L.Carb (low-activity carbonate) designations. Seven samples were analyzed to examine a range of physical substrate type (sediment vs. carbonate rock) and seepage environments (active and low-activity): A.Sed-5128, A.Carb-5305, A.Carb-5152, L.Sed-5043, L.Carb-5028, and sterilized control aliquots of A.Sed-5128 and A.Carb-5305. Carbonate samples include

both porous materials with macroscale vugs and pore spaces, as well as massive lithologies with more homogenous structure.

Samples were collected with the *DSV Alvin* during *Atlantis* leg AT-16-68 in September 2010 and *ROV Jason* during *Atlantis* leg AT-18-10 in September 2011. During the depressurization associated with ascent to the surface, supersaturated methane may have degassed, as suggested by occasional gas pockets in core tubes. Shipboard, push cores and bottom water-submerged carbonates were immediately transferred to a 4 °C walk-in cold room and processed within several hours. To prepare material for future experimentation, compacted sediment and carbonate rocks were stored in anoxic, Ar-flushed mylar bags at 4 °C until use. In advance of experimental set-up, sediment and carbonate samples were prepared under anoxic conditions using 0.22 μm filtered, anoxic $N_2$-sparged Hydrate Ridge bottom water (at a 1:2 sediment/carbonate : bottom water ratio by volume) and maintained under a 30 psi $CH_4$ headspace for one month.

To set up the experimental incubations, 10 mL physical substrate (compressed sediment or carbonate rock) and 20 mL filtered Hydrate Ridge bottom water were placed in 60-mL glass bottles (SVG-50 gaschro vials, Nichiden Riku Glass Co, Kobe, Japan). In all experiments involving carbonates, interior portions (> 5 cm from the rock surface) were used in order to ensure that properties exhibited were representative of bulk rock material and not a reflection of surface-based adherent cells or entrained material. Carbonate rock samples were fragmented in order to fit through the 28-mm diameter bottle opening; pieces were kept as large as possible to minimize the increase in surface area-to-volume ratio and maintain conditions as representative of the *in situ* environment as possible. All bottles were sealed with butyl stoppers, and following several minutes of flushing with $N_2$ (g), 60

mL of gas was injected into the 30 mL headspace, generating a pressure of approximately 2 atm. Anoxic incubation headspace was 100% methane; oxic incubation headspace was 30 mL methane, 20 mL $N_2$, and 10 mL $O_2$. All incubation set-up prior to gas flushing and headspace injection took place in an anaerobic chamber.

Triplicate samples, including killed controls, were prepared for all sample types. Measurements were taken for both D/H and $^{14}C$ analysis at 1.9 and 4 days for oxic incubations, and 3 and 8 days for anoxic incubations. An additional triplicate set of anoxic A.Sed-5128 incubations with 60 mL $CH_3D$ initial headspace was run for 38 days and subsequently sampled for Nuclear Magnetic Resonance (NMR) studies.

*Pressurized samples*

In order to understand the effect of pressure on anaerobic methanotrophic rates, a set of experiments was established, using the deuterated methane technique to determine relative rate differences. Active sediment from Hydrate Ridge (A.Sed-3450) was collected, processed shipboard, and prepared for experimentation as described above. To set up the incubations, eight 100 mL mylar bags were prepared with the components shown in Table 2.3: identical sets of four compositionally distinct samples were established such that each could be subjected to low and high pressure. Prior to gas addition, each bag was flushed for 5 minutes with Ar.

Once the incubations were prepared, they were inserted into a stainless steel, custom-built pressure chamber with 3-cm thick walls and pressure valves rated to 6000 psi. The chamber was placed in a walk-in cold room (4 °C), and hydraulic fluid was pumped into the sealed chamber using a Star Hydraulics P1A-250 hand pump. The pressure was maintained at 8.96 MPa psi (equivalent to ~900 m water depth) during the course of the 38-

day experiment, with daily adjustments to account for thermal compression effects. At the conclusion of the experiment, mylar bags were removed from the chamber and checked for leaks (none were observed) and sampled for D/H ratio measurement.

| Sample # | Sediment | Labeled Nitrogen Source | Methane Source | Pressure (MPa) |
|---|---|---|---|---|
| | | | | |
| 1a | 50 mL | 500 uM $^{13}C$ $^{15}N$ Glycine | 40 mL $CH_3D$ | 0.1 |
| 2a | 50 mL | 500 uM $^{15}NH_4Cl$ | 40 mL $CH_3D$ | 0.1 |
| 3a | 50 mL | 500 uM $^{14}NH_4Cl$ | 40 mL $CH_4$ | 0.1 |
| 4a | 50 mL, killed control | 500 uM $^{13}C$ $^{15}N$ Glycine | 40 mL $CH_3D$ | 0.1 |
| | | | | |
| 1b | 50 mL | 500 uM $^{13}C$ $^{15}N$ Glycine | 40 mL $CH_3D$ | 8.96 |
| 2b | 50 mL | 500 uM $^{15}NH_4Cl$ | 40 mL $CH_3D$ | 8.96 |
| 3b | 50 mL | 500 uM $^{14}NH_4Cl$ | 40 mL $CH_4$ | 8.96 |
| 4b | 50 mL, killed control | 500 uM $^{13}C$ $^{15}N$ Glycine | 40 mL $CH_3D$ | 8.96 |

Table 2.3: The experimental set-up for methane seep sediment pressurized rate measurement incubations. The samples ran for 38 days at 4 °C, and each sample was contained in a sealed Mylar bag.

## Analytical Procedures

### *$CH_3D$ Rate Measurements*

At designated sampling times, ~1 mL of medium / water was collected from cultures or incubations in an anaerobic chamber with a sterile syringe. The liquid was then pushed through a 0.22 μm Durapore filter (EMD Millipore, Temecula, CA) and into a 1-mL GC vial. A LGR DLT-100 liquid water isotope analyzer (Los Gatos Research, Mountain View, CA) was used to determine the D/H ratio of each sample, with an injection volume of 700 nL at 1000 nL/s, four intra-injection flush strokes, and a flush time of 60 s between injections. Four rounds of ten injections per sample were performed in order to avoid memory effects; only the latter five injections were used in subsequent calculations. Sample runs were limited to ~250 injections in order to minimize salt precipitation, and

each analysis included an appropriate blank (i.e., autoclaved media for the cultures, or filter sterilized bottom water used during incubation set-up in the case of sediment and carbonate incubations) and two standards of known isotopic ratios (Deep Blue: δD = 0.5‰, and CIT: δD = -73.4‰). Data was removed if instrumental temperature or pressure parameters were flagged as sub-optimal (0.76% of all analyses).

To calculate methane consumption rates, known D/H ratios of the water standards were first used to generate a linear scaling factor that was applied to the corresponding sampling run's data. Using the experiment's overall water volume and the adjusted D/H values (averaging across the latter five injections of the four distinct injection rounds), the number of deuterium atoms in the culture / incubation was calculated. This value was multiplied by four given the 1:3 D:H stoichiometry of the $CH_3D$ substrate to derive the number of methane molecules consumed. The resulting proxy value was divided by the incubation time and volume to arrive at a rate of methane consumption.

(Note: the predicted scaling factor of four was used in the context of methane activation – the initial mobilization of the molecule through conversion to a methyl group – and may not be appropriate for all subsequent processing as hydrogen/deuterium atoms are removed or exchanged. However, a consistent scaling factor was necessary to link $^{14}C$-based results with those derived from the $CH_3D$ approach, and evaluating its "correct" value illuminates additional findings and further questions of methane metabolism systematics discussed at length below.)

*$^{14}CH_4$ Rate Measurements*

Methane oxidation rates using radiolabeled methane substrate were measured as described in detail by Treude et al. (2005) and Treude and Ziebis (2010). Radiolabeled

methane ($^{14}CH_4$ dissolved in seawater, corresponding to an activity of 13 kBq for culture experiments and 52 kBq in sediment and carbonate samples) was injected into each sample container, and samples were incubated at the appropriate temperatures for the designated amount of time (see above). To stop microbial activity and begin analysis, 2.5 ml of 2.5% (w/w) NaOH was injected. Each sample's headspace was purged with airflow through an 850 °C quartz tube furnace filled with Cu(II) oxide, combusting unused $^{14}CH_4$ to $^{14}CO_2$, which was collected in two sequential 23-ml scintillation vials pre-filled with 7 ml phenylethylamine and 1 ml 2-methoxyethanol. 10 ml of scintillation cocktail (Ultima Gold XR, PerkinElmer) was added, and the activity attributable to $^{14}CO_2$ was measured by scintillation counting 24 hours later (Beckman Coulter LS 6500 Multi-Purpose Scintillation Counter, 10 minute analysis per sample).

To quantify the $^{14}CO_2$ and $H^{14}CO_3^-$ produced during the incubation period, each sample was uncapped and the entire volume was transferred into a 250-ml Erlenmeyer flask along with 1 drop of antifoam. 5 ml of 6M HCl was added and the flask was immediately closed with a rubber stopper, two clamps, and parafilm to prevent gas escape. The flask was placed on a shaking table (60 rpm) at room temperature for 24 hours. A 7-ml scintillation vial, pre-filled with 1 ml of 2.5% NaOH and 1 ml of phenylethylamine, was suspended from the rubber stopper inside the flask to collect $^{14}CO_2$ generated by the acidification. 5 ml of scintillation cocktail was added, and the vial was measured by scintillation counting 24 hours later. This method has been shown to recover an average of 98% of $^{14}CO_2$ (Treude et al. 2003).

Finally, sterilized control samples (#10, see Table 2.2) were set aside after $^{14}CH_4$ addition for gas chromatography to determine the initial concentration of methane gas. 400

µl of headspace was injected into a gas chromatograph (Shimadzu GC-2014), equipped with a packed stainless steel Supelco Custom Column (50/50 mixture, 80/100 Porapak N support, 80/100 Porapak Q column, 6 ft x 1/8 in) and a flame ionization detector. The carrier gas was helium at a flow rate of 30 ml $min^{-1}$, and the column temperature was 60 °C. Results were scaled based on comparison with standards of known methane concentrations (10 and 100 ppm; Matheson Tri-Gas, Twinsburg, OH). The rate of methane oxidation was determined by the equation

$$Methane\ Oxidation = \frac{^{14}CO_2 \bullet CH_4}{(^{14}CH_4 + ^{14}CO_2) \bullet v \bullet t}$$

in which $^{14}CH_4$ is the combusted unreacted radiolabeled methane, $^{14}CO_2$ represents the quantity of acidified oxidation product, $CH_4$ signifies the initial quantity of methane in the experiment, v is the volume of sediment or carbonate rock, and t is the time over which the incubation was active.

*Nuclear Magnetic Resonance*

NMR was conducted on incubation headspace with a Varian 400 MHz Spectrometer using broadband auto-tune OneProbe. $^1H$ NMR spectra were recorded at 298 K without spinning; methane was passed through $CDCl_3$ with a fine needle to absorb the methane and measured with a 5 s relaxation delay (10 s repetition rate). Fitting of NMR spectra was carried out with the iNMR 4.1.7 software for the determination of the enrichment.

**Results and Discussion**

Aerobic Methanotroph Cultures

D/H ratios were acquired at eight points during the *M. trichosporium* growth curve and seven points of the *M. sedimenti* growth curve; three measurements of $^{14}C$ distributions were acquired for each strain, targeting exponential and stationary phases (Figs. 2.1, 2.2). *M. trichosporium* exhibited methane consumption rates more than an order of magnitude greater than those of *M. sedimenti*, yet the scaling factor relating the $CH_3D$- and $^{14}CH_4$-derived rates is remarkably consistent in both cases. Using data points from both $CH_3D$ and $^{14}CH_4$ experiments taken closest to the end of exponential growth phase (47.5 hours for *M. trichosporium*, 140 and 102 hours for *M. sedimenti* $CH_3D$ and $^{14}CH_4$ measurements, respectively) and in stationary phase (140 and 166.5 hours for *M. trichosporium* $CH_3D$ and $^{14}CH_4$ measurements; 476 and 432 hours for *M. sedimenti* $CH_3D$ and $^{14}CH_4$ measurements), the ratio of methane oxidation rates derived from each approach can be compared. This value, hereafter referred to as the $CH_3D$ : $^{14}CH_4$ ratio, can be used to evaluate the consistency of the novel deuterated methane method and as an investigatory tool in catabolic / anabolic processing of methane. Using averaged values of tubes #1a, #1b, and #1c for $CH_3D$ rates and the triplicate $^{14}CH_4$ tubes of the appropriate time point (#6, #7, or #8), $CH_3D$ : $^{14}CH_4$ ratio values were calculated and are shown in Table 2.4. The implications of this value in aerobic methanotrophs (~1.5 for both species) is addressed below, but its consistency is a promising indicator of the utility of the deuterated methane approach for ground-truthed rate measurements. By dividing rates derived from D/H values by 1.5, a reliable estimate of full-oxidation methanotrophy can be attained.

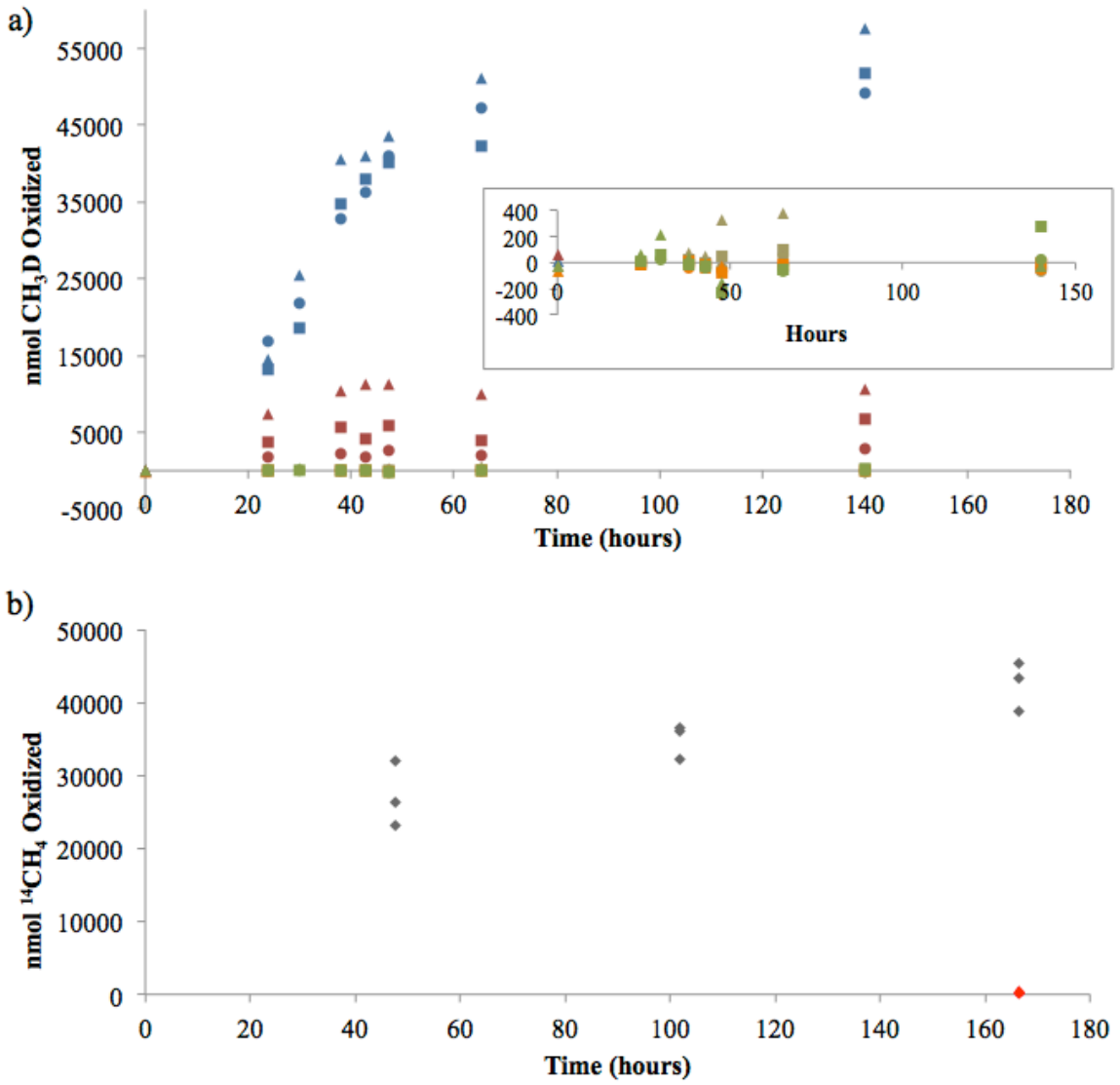


Fig. 2.1: Methane oxidation data for *M. trichosporium* cultures using a) the $CH_3D$ method, and b) the $^{14}CH_4$ method. Symbols correspond to sample types as follows (see Table 2.2 for further details). In a), blue = #1; brown = #2; orange = #3; red = #4; green = #5; different shapes represent biological replicates. In b), grey points = #6, #7, and #8; red point = #9.

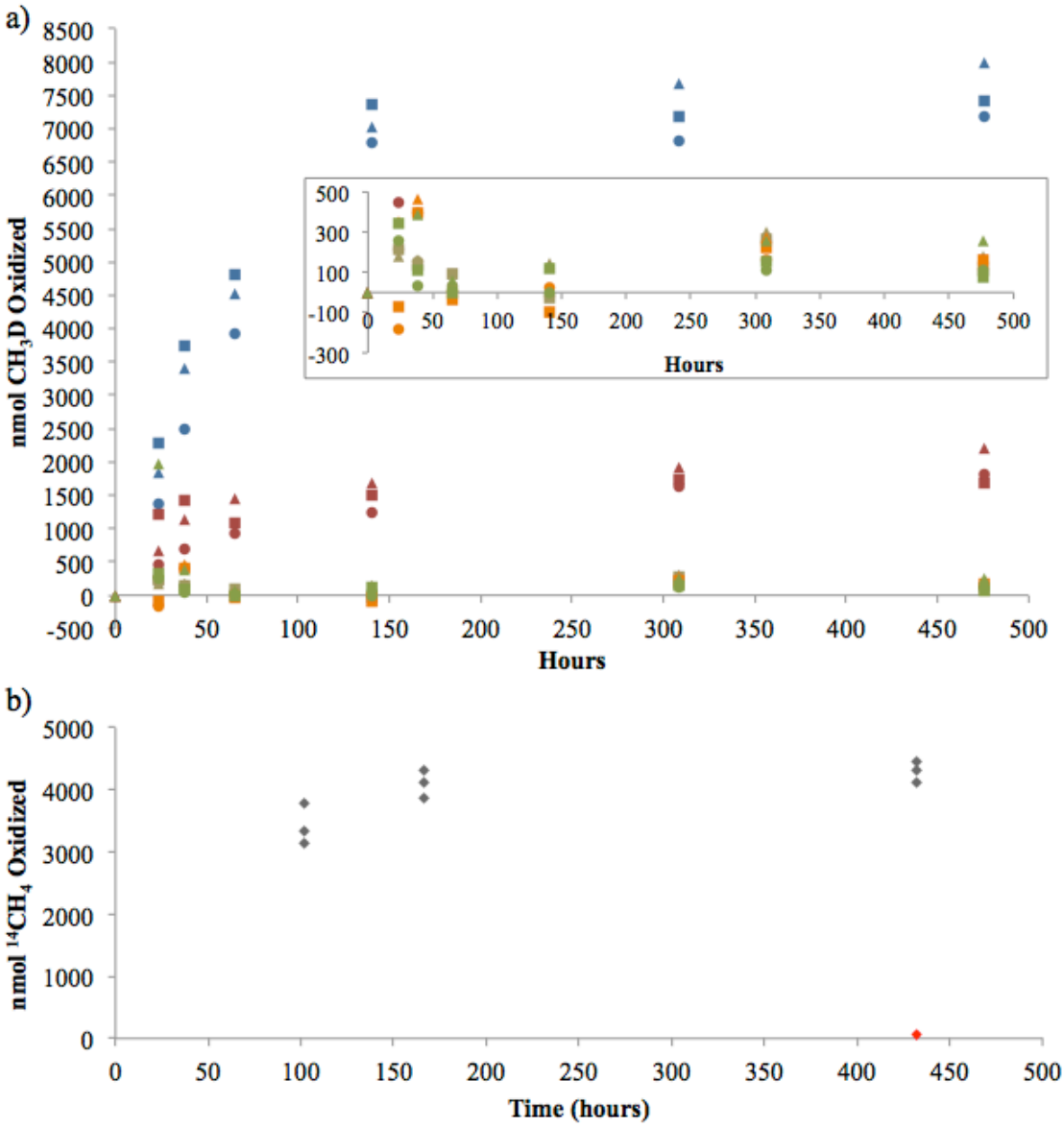


Fig. 2.2: Methane oxidation data for *M. sedimenti* cultures using a) the $CH_3D$ method, and b) the $^{14}CH_4$ method. See Fig. 2.1 for symbol key.

Environmental Samples: Methanotrophy Under Oxic and Anoxic Conditions

Oxidation rates under oxic conditions, derived from both $CH_3D$ and $^{14}CH_4$ measurements, are provided for all five sample types (active sediment, low-activity sediment, active porous carbonate, active massive carbonate, and low-activity massive

carbonate) in Fig. 2.3a. The corresponding values for anoxic conditions are shown in Fig. 2.3b. All values were calculated from the second time point (4d for oxic conditions, 8d for anoxic conditions); approximately linear activity rates were observed between the two observations (data not shown).

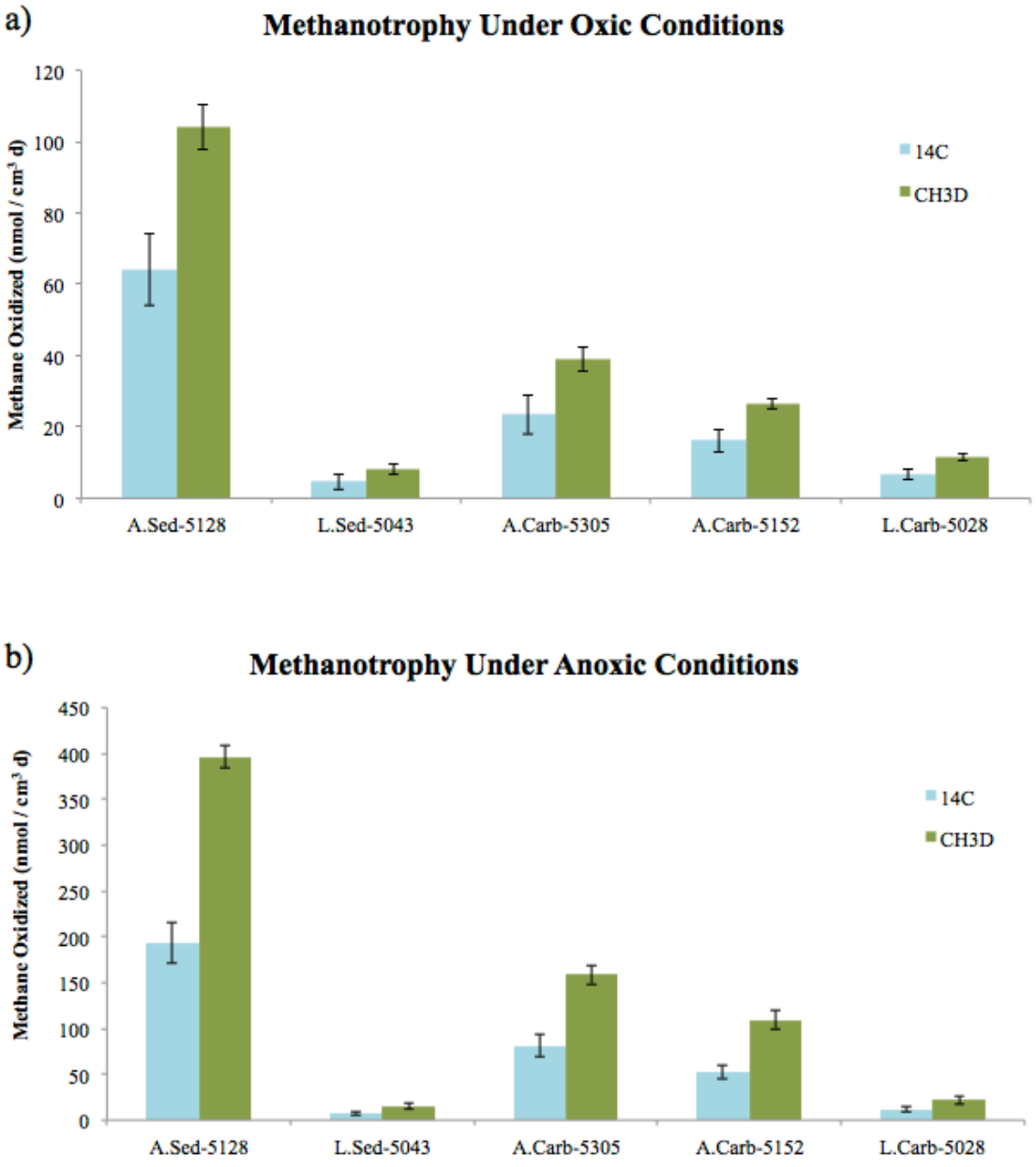


Fig. 2.3: Methane oxidation rates of a) oxic and b) anoxic incubations. Bars compare rates derived from the $^{14}CH_4$ (blue) and $CH_3D$ (green) experiments.

The $CH_3D$ : $^{14}CH_4$ ratio for the oxic incubations was 1.66 +/- 0.02 SE and 1.99 +/- 0.04 SE for anoxic conditions (Table 2.4). These relatively consistent values across physical substrate type (sediment and carbonates of varying lithology) and collection site activity level (active and low-activity) demonstrate the potential and limits of the deuterated methane technique and suggest an underlying metabolic basis of these $CH_3D$ : $^{14}CH_4$ ratios.

| **Aerobic Methanotroph Cultures** | | |
|---|---|---|
| | Exponential Phase | Stationary Phase |
| *M. trichosporium* | 1.5 | 1.48 |
| *M. sedimenti* | 1.54 | 1.59 |
| | | |
| **Methane Seep Sediments and Carbonates** | | |
| | Oxic Incubations | Anoxic Incubations |
| A.Sed-5128 | 1.62 | 2.05 |
| L.Sed-5043 | 1.71 | 2.01 |
| A.Carb-5305 | 1.65 | 1.96 |
| A.Carb-5152 | 1.63 | 2.08 |
| L.Carb-5028 | 1.69 | 1.86 |

Table 2.4: $CH_3D$ : $^{14}CH_4$ ratios for the experimental treatments addressed in this study.

Anaerobic Methanotrophy at Pressure

Material collected for microbiological studies of AOM is frequently obtained from marine settings of various depths that are subjected to distinct and substantial pressure regimes (Ruff et al. 2015). Pressure is not always rigorously incorporated into microcosm experiments, though evidence suggests it can be an important determinant of methanotrophic rates (Zhang et al. 2010; Nauhaus et al. 2005).

In order to evaluate the influence of *in situ* pressure on methanotrophic rates of Hydrate Ridge seep sediment microbial communities, parallel incubations were subjected to 0.1 MPa (atmospheric pressure) and 8.96 MPa (equivalent to ~900 m depth). Measured

rates, expressed in δD values derived from D/H ratios, are shown in Fig. 2.4. A significant increase in methane consumption was observed in both live conditions at heightened pressure, corresponding to sediment incubated with isotopically labeled glycine (samples 1a and 1b) and ammonium chloride (samples 2a and 2b). Controls lacking $CH_3D$ (samples 3a and 3b) and biological activity (samples 4a and 4b) showed no increase in D/H ratios. The simulation of *in situ* Hydrate Ridge pressures led to a 179.5% (+/- 6.5 SE) increase in relative methane oxidizing rates. Incubation with 500 uM glycine rather than ammonia at high and low pressures resulted in small but consistent rate increases of 12% +/- 4.1% SE, potentially reflecting the energetic and biosynthetic distinction between exogenous amino acids and unprocessed fixed nitrogen.

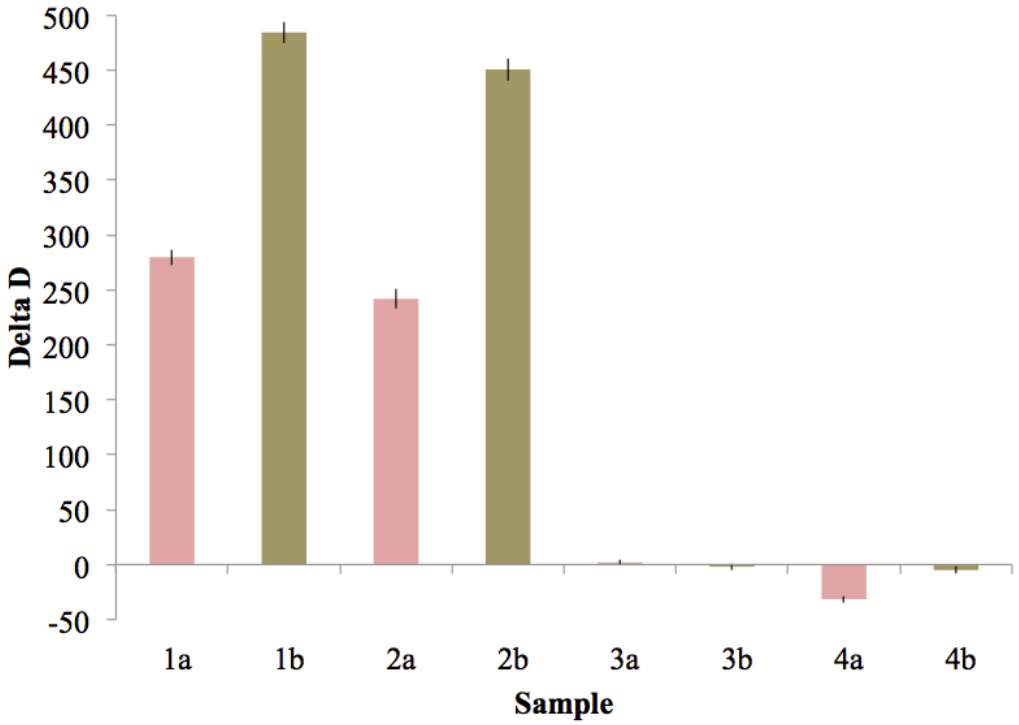


Fig. 2.4: Water δD values of seep sediment samples following 38-day incubations with $CH_3D$ at 8.96 MPa (brown bars, "b" samples) or 0.1 MPa (pink bars, "a" samples).

Other studies have found a wide range of pressure-related effects. In a sulfate-coupled AOM bioreactor, pressures were varied from 1 to 8 MPa and sulfide production approximately tripled, demonstrating Michaelis-Menten style kinetics with an apparent Km of 37 mM (Zhang et al. 2010). Methane partial pressures of 1.1 MPa led to a 5x increase in sulfate reduction rates with Hydrate Ridge sediments demonstrating methane-dependent sulfate reduction (Nauhaus et al. 2002).With methane seep sediment from the Japan Trench, however, methane-driven sulfate reduction rates did not correlate with changing pressure (Vossmeyer et al. 2012).

Nauhaus et al. (2005) suggested that the pressure-induced rate increases are due more to heightened methane solubility and bioavailability rather than physiological effects or enzyme kinetics. Bowles et al. (2011) presented a very different perspective by showing a six- to ten-fold AOM rate increase at 10 MPa when methane concentrations were held constant. Deconvolving these two influences and how they depend on community composition or physochemical parameters is feasible with pressure chamber experiments utilizing deuterated methane. Understanding the relative contributions of environmental and physiological effects to methane oxidation will help constrain methane fluxes across a larger envelope of the planet's methanotrophically active zones.

Understanding the $CH_3D$ : $^{14}CH_4$ Ratio

The $CH_3D$ and $^{14}CH_4$ approaches to rate measurements quantify different aspects of methanotrophy, and while our understanding of hydrogen and carbon atom distributions is currently insufficient to draw full equivalencies between the methods, each offers an important tool in understanding methane metabolism. The $^{14}CH_4$ technique quantifies the amount of $^{14}C$ – initially supplied as methane – that is fully oxidized and persists as soluble

species ($HCO_3^-$) or precipitation products ($CaCO_3$). The $CH_3D$ protocol, on the other hand, reports the extent to which methane-derived hydrogen atoms are found in the aqueous phase. Because methane is a stable molecule, its activation indicates enzymatic functionalization, but the fate of each hydrogen during methane oxidation is unclear.

The flow of methane-derived hydrogen atoms through anaerobic and aerobic methanotrophic metabolisms was examined in an attempt to predictively evaluate the consequence of deuterated methane reactions. Previously published reports were used to compile Figs. 2.5 (e.g., Thauer 2011; Vorholt & Thauer 1997; Hallam et al. 2004) and 2.6 (Lieberman & Rosenzweig 2004), which trace anaerobic and aerobic methane metabolisms, respectively, with a specific focus on hydrogen atoms.

*Anaerobic Methanotrophy*

AOM is depicted via the reverse methanogenesis pathway in Fig. 2.5, whereby methyl-coenzyme M reductase (Mcr) functionalizes a disulfide bond to activate methane. A tetrahydromethanopterin molecule supplants CoM, and two hydrogen atoms are sequentially shuttled to membrane-bound pumping enzymes by $F_{420}$. The final hydrogen atom is abstracted from formylmethanofuran in a two-electron oxidation that forms carbon dioxide. Ultimately, the number of methane-derived hydrogen atoms that enter water-exchangeable products dictates the physiological interpretation of waterborne D/H ratios. For example, if just one methane-derived hydrogen enters an intermediate and is freely exchangeable with water, then observed water-based deuterium must be multiplied by four to arrive at the actual quantity of activated methane molecules. (This example neglects kinetic isotope effects favoring initial C-H activation by a factor of 1.2.) In this context, the experimental $CH_3D$ : $^{14}CH_4$ ratio values may provide useful insight. A $CH_3D$ : $^{14}CH_4$ ratio

of 2 for the reverse methanogenesis pathway suggests that, for every methane molecule that is fully oxidized to $CO_2$, two hydrogen atoms enter water-exchangeable intermediates. ($CH_3D$ rate values were quantified by multiplying D atom excesses by 4; if they were instead multiplied by 2, the resulting values would correspond very closely with those determined by $^{14}CH_4$ measurements.) In the full methane oxidation pathway presented in Fig. 2.5, two hydrogens are pumped out of the cell ($H^2$ and $H^3$), while the other two appear to enter the aqueous phase within the cell; these latter atoms may enter biomolecules or go otherwise undetected by the filtered bulk water D/H analysis.

*Constraining Reversibility*

Back reactions of enzymatic processes involving hydrogen loss could represent an additional complication. For example, upon the activation of methane by Mcr, HS-CoB and $CH_3$-S-CoM form, with the thiol hydrogen likely exchanging with water-bound hydrogen. If the thiol-bound hydrogen were deuterium, then the re-formation of methane would result in a heightened D/H ratio but no net methane consumption (Fig. 2.5). It is possible to constrain the rate at which this occurs via nuclear magnetic resonance (NMR), an approach that can distinguish the isotopologues of methane headspace. Over the course of 43 days in triplicate seep sediment incubations prepared with exclusively $CH_3D$ headspace, $CH_4$ in the headspace increased from 0.33% +/- $2.5x10^{-3}$% SE to 4.48% +/- 0.27% SE. If this demonstrated reversibility only reflects the back reaction of Mcr, then the $CH_4$ increase must be multiplied by four to reflect the actual percentage of headspace methane that was re-formed by Mcr. However, if the reversibility reflects back reaction of the entire pathway, then no scaling factor is needed. Thus, the range of potential methane headspace percentage lohaaccounted for by methane reformed from initial $CH_3D$ is between 4.15 – 16.6%.

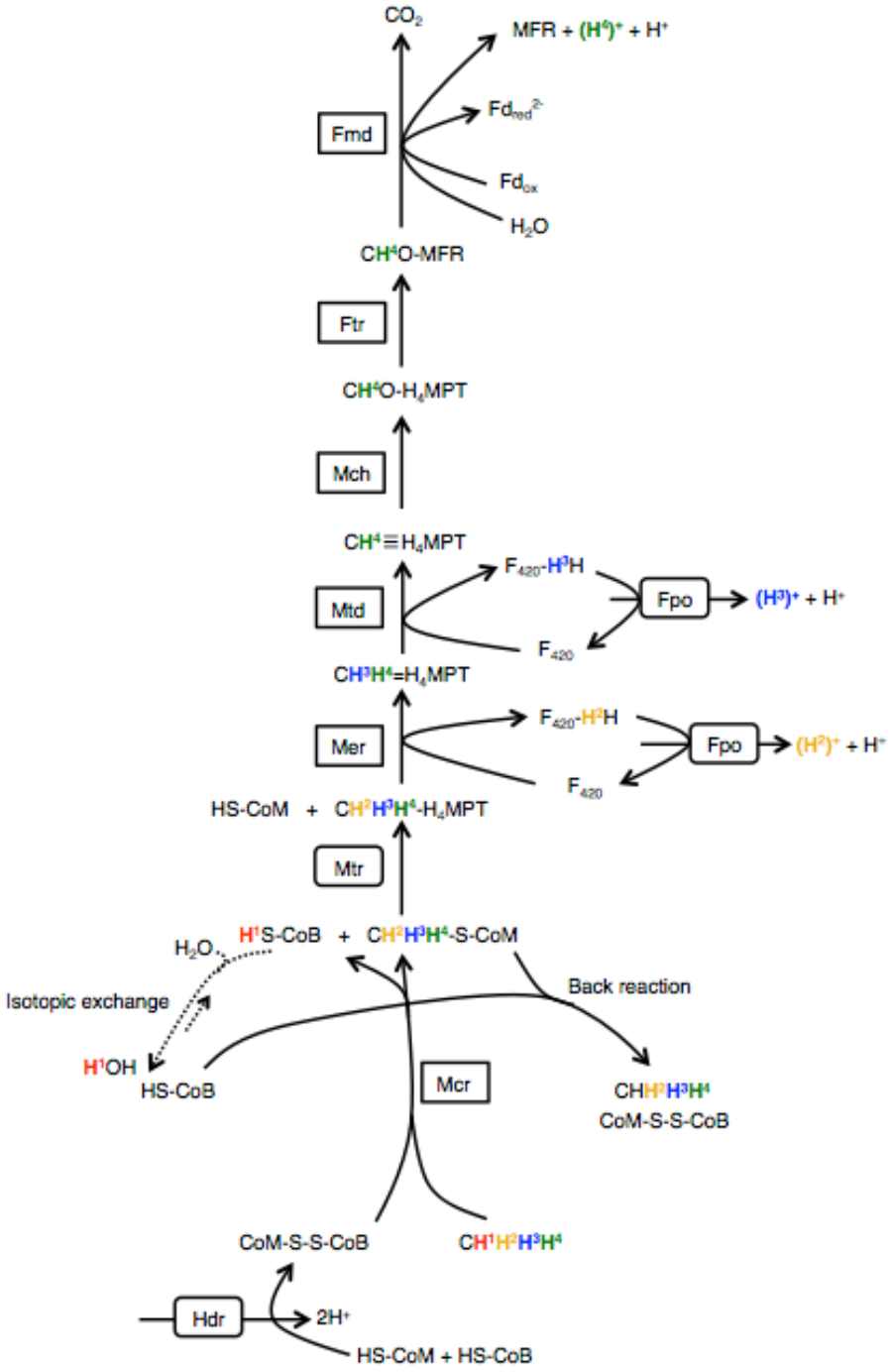


Fig. 2.5: A schematic diagram demonstrating the potential fate of methane's hydrogen atoms in the "reverse methanogenesis" pathway. Hydrogen atoms are distinguished by color and superscript number. Arrows are unidirectional to demonstrate the net methane-consuming direction of the pathway, but all enzymes have been shown to be reversible (Thauer, 2008), a situation that is shown explicitly only for Mcr.

This calculation assumes that the $CH_4$ formed in the incubations was not formed by methanogens in the sediment: this and other important constraints can be pursued through further experimentation. For example, partial reversibility can be evaluated by a) including a $^{13}CO_2$ signal in the water and measuring $^{13}CH_4$, and/or b) utilizing multiply deuterated methane as initial headspace and measuring all possible isotopologues. More precise quantification of methane headspace would be another important parameter to consider. Nonetheless, even the upper bound of partially and reversibly oxidized $CH_3D$ suggests that methanogenic back-reaction is only a minor contributor to the $CH_3D$ : $^{14}CH_4$ ratio, and that the majority of the D/H signal is attributable to reactions indicative of net methane consumption, if not complete oxidation.

*Aerobic Methanotrophy*

In aerobic methanotrophy, a $CH_3D$ : $^{14}CH_4$ ratio of ~1.5 was observed, suggesting that on average, 2.67 of the four methane-derived hydrogen atoms likely enter water-exchangeable products during the course of a full oxidation pathway. Intriguingly, this ratio was similar for both cultured organisms despite their distinct metabolic pathways. *M. tricosporium* is a type II methanotroph, a member of the *Alphaproteobacteria* that uses the serine pathway for carbon assimilation. *M. sedimenti* is a gammaproteobacterial type II methanotroph, using the ribulose monophosphate (RuMP) carbon assimilation pathway (Tavormina et al. 2015). The pathway data presented in Fig. 2.6 suggests that all methane-bound hydrogens are water exchangeable during the catabolic oxidation of methane to carbon dioxide. Thus, to achieve a $CH_3D$ : $^{14}CH_4$ ratio greater than 1, a substantial

proportion of methane-derived formaldehyde would need to proceed down the assimilatory pathway, a requirement that was likely met given the cultures' increase in cell density.

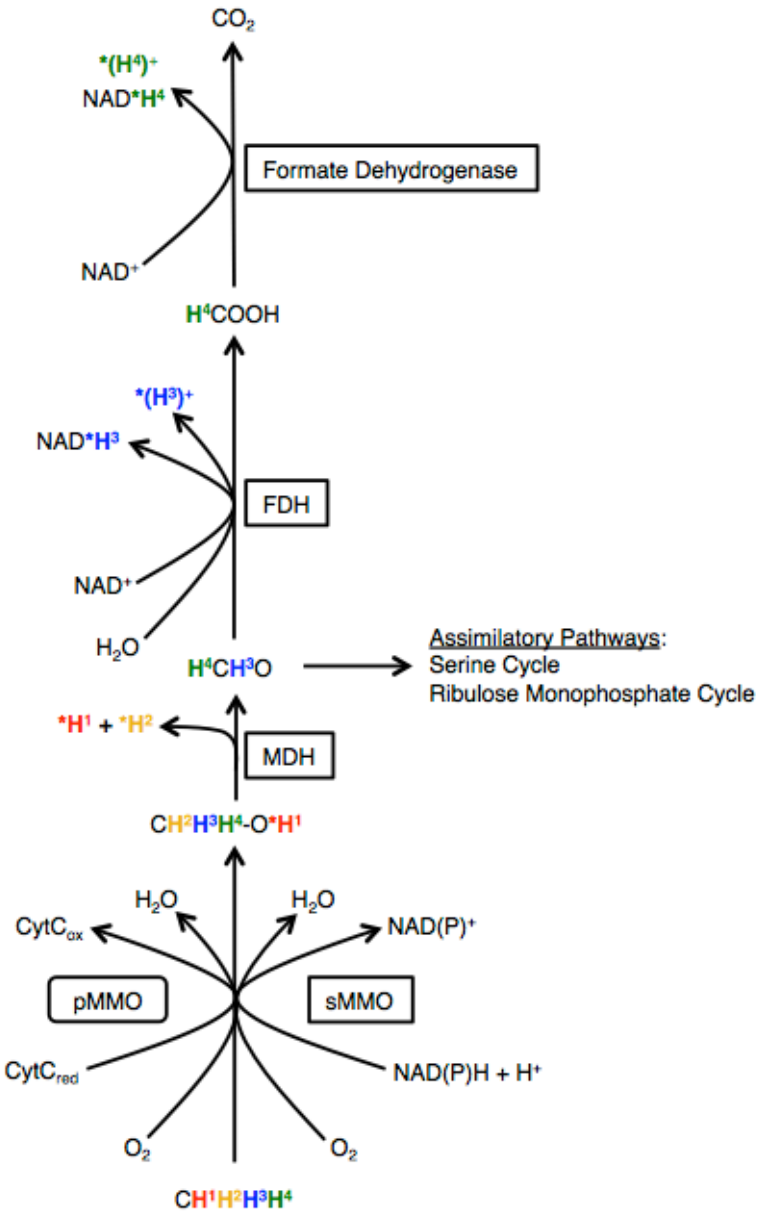


Fig. 2.6: A schematic diagram demonstrating the potential fate of methane's hydrogen atoms in the aerobic methanotrophy pathways. Hydrogen atoms are distinguished by color and superscript number. Mmo enzymes are not believed to perform reversible reactions.

The oxic incubations of methane seep sediment produced a $CH_3D$ : $^{14}CH_4$ ratio of 1.66 +/- 0.02 SE. Given that the known modes of biological methane oxidation – type I and type II aerobic methanotrophy and reverse methanogenesis anaerobic methanotrophy – bound this observed value, it appears likely that the oxic incubations represent a mixture of both aerobic and anaerobic methane oxidation processes. Aerobic methane oxidation likely dominated, based on the 10 psi partial pressure of $O_2$ and the closeness of the $CH_3D$ : $^{14}CH_4$ ratio to that of the aerobic methanotrophic cultures, but anoxic niches likely remained or developed in the static incubation bottles.

*$CH_3D$ as a Future Analytical Tool for Methane Biochemistry*

The $CH_3D$ : $^{14}CH_4$ ratios presented here are based on experimental data, and an underlying theoretical framework regarding the fate of methane-bound hydrogen atoms remains outstanding. From this perspective, deuterated methane could serve an important role in clarifying metabolic regulation, particularly when used in concert with the $^{14}CH_4$ rate measurement method. For example, quantification of aqueous D/H ratios, $^{14}CO_2$, and $CH_4$ : $CH_3D$ ratios (via NMR) could provide a better understanding of Mcr activation and reversibility under distinct energetic regimes. Evaluating $CH_3D$ : $^{14}CH_4$ ratios under more clearly defined growth and maintenance phases of aerobic methanotrophy would elucidate distinct $CH_3D$ : $^{14}CH_4$ ratios associated with catabolic, RuMP, and serine pathways, enabling future use of that parameter as an arbiter of relative anabolic and catabolic activity.

Deuterated Methane in Experimental Investigations

Based on the $^{14}CH_4$ ground-truthed experiments with aerobic methanotrophic cultures, oxic seep sediment, and anoxic seep sediment, as well as the proof-of-concept

pressurized experiments, we believe that the deuterated methane approach to methane oxidation rate measurement is a useful addition to the biogeochemist's arsenal. Compared with radiolabel approaches ($^{14}CH_4$, $CH_3T$, $^{34}SO_4^{2-}$), the method requires less processing, is more affordable, and requires less safety-oriented planning. It also appears to be more precise than the $^{14}CH_4$ protocol (based on the data spread in, e.g., Fig. 2.3), though comparisons are difficult because different aliquots of the same initial material were used and may have varied in important ways. Because the deuterated methane method focuses on methane-bound hydrogen atoms, it offers different information on methanotrophic systems than carbon-based techniques like methane or bicarbonate quantification. While this uncertainty complicates the interpretation of isolated D/H ratios, it can offer additional data for analysis of methane-derived intermediates in relevant metabolisms.

Given these caveats, we recommend three use cases for deuterated methane in methane oxidation rate measurement applications. First, the approach can be employed in a strictly comparative context using analogous inoculum exposed to a range of different conditions, as demonstrated with the pressure-based sediment incubations presented above. For example, evaluating the effect of different temperatures, chemical concentrations, or energetic landscapes on seep sediment methane oxidizing rates would all be promising applications. Comparative analysis of AOM rates at different seep sites would also be useful, provided anaerobic or aerobic methanotrophic processes could be isolated. Second, by conducting side-by-side deuterated methane and radiocarbon tests, a sample-specific $CH_3D$ : $^{14}CH_4$ ratio can be determined, and absolute rates can then be inferred based on D/H ratios alone. Finally, incorporating deuterated methane into systematic studies alongside other methods such as carbon- or sulfur-tracking procedures would enable a

multi-dimensional examination of anabolic and catabolic processes in a range of methane-based metabolisms.

**Conclusion**

The ability to accurately measure methane oxidation rates – both comparatively and in absolute values – is an important component of methanotrophic studies. Such measurements frequently depend on radiotracers or measurements of chemical species that are related to, but not directly indicative of, methane metabolism. The deuterated methane technique presented here represents a novel approach to methane oxidation rate measurements, notable for its logistical and analytical ease, as well as the added dimension provided by H-based, rather than C-based, information. $CH_3D$ gas is injected into the gas-tight experimental system, and the resulting D/H ratio of the water is measured. We have demonstrated that the D/H ratio is directly proportional to methane oxidation rates as measured in absolute terms by the well-established $^{14}CH_4$ method. The value of the proportionality constant differs based on the experimental system, likely dictated by relative proportions of aerobic and anaerobic methanotrophic metabolisms.

Methane biogeochemistry is a dynamic field of study with implications for carbon cycling, microbial ecology, and climate dynamics, though experimental challenges have slowed our understanding of methane-based biological reactions. With the $CH_3D$ approach as an added tool in the arsenal of rate-based examinations, a broader understanding of methane metabolism in environmental and anthropogenic systems is within reach.

## References


Alperin MJ, Reeburgh WS. (1985). Inhibition Experiments on Anaerobic Methane Oxidation. Applied and Environmental Microbiology 50:940–945.

Beal EJ, House Christopher H., Orphan Victoria J. (2009). Manganese- and Iron-Dependent Marine Methane Oxidation. Science 325:184–187.

Boetius A., Ravenschlag K, Schubert CJ, Rickert D, Widdel F., Gleseke A, et al. (2000). A marine microbial consortium apparently mediating anaerobic oxidation of methane. Nature 407.

Boetius Antje, Suess E. (2004). Hydrate Ridge: a natural laboratory for the study of microbial life fueled by methane from near-surface gas hydrates. Chemical Geology 205:291–310.

Bowles MW, Samarkin VA, Joye SB. (2011). Improved measurement of microbial activity in deep sea sediments at *in situ* pressure and methane concentration. Limnology and Oceanography: Methods 9:499–506.

Carini SA, Orcutt BN, Joye SB. (2003). Interactions between methane oxidation and nitrification in coastal sediments. Geomicrobiology Journal 20:355–374.

Crespo-Medina M, Meile C, Hunter K, Diercks A, Asper V, Orphan V, et al. (2014). The rise and fall of methanotrophy following a deepwater oil-well blowout. Nature Geoscience.

Ettwig KF, Butler MK, Le Paslier D, Pelletier E, Mangenot S, Kuypers MM, et al. (2010). Nitrite-driven anaerobic methane oxidation by oxygenic bacteria. Nature 464:543–548.

Girguis PR, Orphan Victoria J., Hallam SJ, DeLong EF. (2003). Growth and Methane Oxidation Rates of Anaerobic Methanotrophic Archaea in a Continuous-Flow Bioreactor. Applied and Environmental Microbiology 69:5472–5482.

Hallam SJ, Putnam N, Preston CM, Detter JC, Rokhsar D, Richardson PM, et al. (2004). Reverse methanogenesis: testing the hypothesis with environmental genomics. Science 305:1457–1462.

Haroon MF, Hu S, Shi Y, Imelfort M, Keller J, Hugenholtz P, et al. (2013). Anaerobic oxidation of methane coupled to nitrate reduction in a novel archaeal lineage. Nature 500:567–570.

Ho A, Vlaeminck SE, Ettwig KF, Schneider B, Frenzel P, Boon N. (2013). Revisiting methanotrophic communities in sewage treatment plants. Applied and environmental microbiology 79:2841–2846.

Holzapfel-Pschorn A, Conrad R, Seiler W. (1985). Production, oxidation and emission of methane in rice paddies. FEMS Microbiology Ecology 1:343–351.

Jørgensen BB, Weber A, Zopfi J. (2001). Sulfate reduction and anaerobic methane oxidation in Black Sea sediments. Deep Sea Research Part I: Oceanographic Research Papers 48:2097–2120.

Knittel K, Boetius Antje. (2009). Anaerobic Oxidation of Methane: Progress with an Unknown Process. Annu. Rev. Microbiol. 63:311–334.

Lieberman RL, Rosenzweig AC. (2004). Biological methane oxidation: regulation, biochemistry, and active site structure of particulate methane monooxygenase. Critical reviews in biochemistry and molecular biology 39:147–164.

Mackelprang R, Waldrop MP, DeAngelis KM, David MM, Chavarria KL, Blazewicz SJ, et al. (2011). Metagenomic analysis of a permafrost microbial community reveals a rapid response to thaw. Nature 480:368–371.

Moran JJ, Beal EJ, Vrentas JM, Orphan Victoria J., Freeman KH, House Christopher H. (2008). Methyl sulfides as intermediates in the anaerobic oxidation of methane. Environmental Microbiology 10:162–173.

Nauhaus K, Boetius Antje, Krüger M, Widdel Friedrich. (2002). In vitro demonstration of anaerobic oxidation of methane coupled to sulphate reduction in sediment from a marine gas hydrate area. Environmental Microbiology 4:296–305.

Nauhaus K, Treude T, Boetius Antje, Krüger M. (2005). Environmental regulation of the anaerobic oxidation of methane: a comparison of ANME-I and ANME-II communities. Environmental Microbiology 7:98–106.

Orphan V.J., Ussler III W, Naehr T., House C.H, Hinrichs K-U, Paull C. (2004). Geological, geochemical, and microbiological heterogeneity of the seafloor around methane vents in the Eel River Basin, offshore California. Chemical Geology 205:265–289.

Pack MA, Heintz MB, Reeburgh WS, Trumbore SE, Valentine DL, Xu X, et al. (2011). A method for measuring methane oxidation rates using lowlevels of 14C labeled methane and accelerator mass spectrometry. Limnology and Oceanography: Methods 9:245–260.

Reeburgh WS. (2007). Oceanic Methane Biogeochemistry. Chem. Rev. 107:486–513.

Ruff SE, Biddle JF, Teske AP, Knittel K, Boetius Antje, Ramette A. (2015). Global dispersion and local diversification of the methane seep microbiome. Proceedings of the National Academy of Sciences 201421865.

Scheutz C, Bogner J, De Visscher A, Gebert J, Hilger H, Huber-Humer M, et al. (2009). Microbial methane oxidation processes and technologies for mitigation of landfill gas emissions. Waste Management & Research.

Sivan O, Antler G, Turchyn AV, Marlow JJ, Orphan Victoria J. (2014). Iron oxides stimulate sulfate-driven anaerobic methane oxidation in seeps. Proceedings of the National Academy of Sciences 111:E4139–E4147.

Suess E, Torres M, Bohrmann G, Collier R, Greinert J, Linke P, et al. (1999). Gas hydrate destabilization: enhanced dewatering, benthic material turnover and large methane plumes at the Cascadia convergent margin. Earth and Planetary Science Letters 170:1–15.

Tavormina PL, Hatzenpichler R, McGlynn S, Chadwick G, Dawson KS, Connon SA, et al. (2015). Methyloprofundus sedimenti gen. nov., sp. nov., an obligate methanotroph from ocean sediment belonging to the ‘deep sea-1’clade of marine methanotrophs. International journal of systematic and evolutionary microbiology 65:251–259.

Thauer RK. (2011). Anaerobic oxidation of methane with sulfate: on the reversibility of the reactions that are catalyzed by enzymes also involved in methanogenesis from CO 2. Current opinion in microbiology 14:292–299.

Treude, Boetius, Knittel, Wallmann, Jorgensen. (2003). Anaerobic oxidation of methane above gas hydrates at Hydrate Ridge, NE Pacific Ocean. Mar Ecol Prog Ser 264:1–14.

Treude T, Krüger M, Boetius Antje, Jørgensen BB. (2005). Environmental control on anaerobic oxidation of methane in the gassy sediments of Eckernfoerde Bay(German Baltic). Limnology and oceanography 50:1771–1786.

Treude T, Ziebis W. (2010). Methane oxidation in permeable sediments at hydrocarbon seeps in the Santa Barbara Channel, California. Biogeosciences (BG) 7:3095–3108.

Tryon M., Brown K., Torres M. (2002). Fluid and chemical flux in and out of sediments hosting methane hydrate deposits on Hydrate Ridge, OR, II: Hydrological processes. Earth and Planetary Science Letters 201:541–557.

Valentine DL, Blanton DC, Reeburgh WS, Kastner M. (2001). Water column methane oxidation adjacent to an area of active hydrate dissociation, Eel river Basin. Geochimica et Cosmochimica Acta 65:2633–2640.

Vorholt JA, Thauer RK. (1997). The Active Species of 'CO2' Utilized by Formylmethanofuran Dehydrogenase from Methanogenic Archaea. European Journal of Biochemistry 248:919–924.

Vossmeyer A, Deusner C, Kato C, Inagaki F, Ferdelman TG. (2012). Substrate-specific pressure-dependence of microbial sulfate reduction in deep-sea cold seep sediments of the Japan Trench. Frontiers in Microbiology 3:253.

Whittenbury R, Phillips K, Wilkinson J. (1970). Enrichment, isolation and some properties of methane-utilizing bacteria. Journal of General Microbiology 61:205–218.

Zhang Y, Henriet J-P, Bursens J, Boon N. (2010). Stimulation of in vitro anaerobic oxidation of methane rate in a continuous high-pressure bioreactor. Bioresource Technology 101:3132–3138.

*Chapter 3*

# MICROBIAL ABUNDANCE AND DIVERSITY PATTERNS ASSOCIATED WITH SEDIMENTS AND CARBONATES FROM THE METHANE SEEP ENVIRONMENTS OF HYDRATE RIDGE, OR

Jeffrey J. Marlow[1], Joshua A. Steele[1], David H. Case[1], Stephanie A. Connon[1], Lisa A Levin[2], Victoria J. Orphan[1]

[1]Division of Geological and Planetary Sciences, California Institute of Technology, Pasadena, CA, 91125 USA
[2]Integrative Oceanography Division, Scripps Institution of Oceanography, University of California, San Diego, La Jolla, CA, USA

*Adapted from Microbial abundance and diversity patterns associated with sediments and carbonates from the methane seep environments of Hydrate Ridge, OR
DOI: http://doi.org/10.3389/fmars.2014.00044

**Abstract**

Methane seeps are among the most productive habitats along continental margins, as anaerobic methane-oxidizing euryarchaeaota and sulfur-metabolizing deltaproteobacteria form the biological base of a dynamic deep-sea ecosystem. The degree of methane seepage therefore represents one important variable in ecosystem dynamics, and the recent discovery of carbonate-hosted endolithic methanotrophy exposes another potentially discriminating factor: physical substrate type. Methanotrophic microbial communities have been detected within diverse seep-associated habitats, including unlithified sediments, protolithic carbonate nodules, and lithified carbonate slabs and chemoherms of distinct mineralogies. However, a systematic assessment of the diversity and community structure associated with these different habitats has been lacking. In this study, microbial aggregate analysis, microbial abundance quantification, mineralogical identification, and archaeal and bacterial 16S rRNA gene clone libraries were used to deconvolve the relationships between seepage activity, substrate type, and microbial community structure. We report prevalent methane-oxidizing archaeal lineages in both active and low-activity seep settings, and a strong community dependence on both seepage activity and substrate type. Statistical treatments of relative taxa abundances indicate that archaeal community structure is more dependent on the degree of methane seepage than physical substrate type; bacterial assemblages appear to be more strongly influenced by the type of colonization substrate than seepage activity. These findings provide a window into the determinants of community structure and function, improving our understanding of potential elemental cycling at seep sites.

## Introduction

The seafloor is a dynamic and varied environment whose biological communities are dependent upon organic detritus from surface waters and/or chemically reduced fluids emitted from the subseafloor. Benthic habitats cover a range of productivities; in all cases, microorganisms play critical roles in mobilizing chemical or organic energy sources and mediating elemental fluxes (Orcutt et al., 2011 and references therein). Many studies of seafloor microbial ecology have focused on near-surface sediment, examining, for example, methane generation (Claypool and Kvenvolden, 1983), dinitrogen production (Thamdrup and Dalsgaard, 2002), or organic matter remineralization with a range of electron acceptors (Reeburgh, 1983). As the full extent of benthic microbial activity comes into focus, clarifying the identities, distribution, and metabolic roles of constituent organisms in not only sediments, but also endolithic and deeper-seated habitats across a spectrum of energetic regimes, has emerged as a priority.

Methane seeps are among the most productive habitats on the sub-photic zone seafloor. In these regions, reduced, methane-rich fluids come into contact with oxidized seawater, fueling chemosynthetic communities such as anaerobic methanotrophic archaea (ANME) / Deltaproteobacteria consortia that mediate the sulfate-coupled anaerobic oxidation of methane (AOM). AOM is a globally significant process which consumes an estimated 80-90% of methane at the seafloor (Reeburgh, 2007). The cultivation-independent investigation of the microorganisms responsible for AOM has revealed two primary constituents: methane-oxidizing archaea and sulfur-metabolizing bacteria. ANME are believed to activate methane and transfer reducing equivalents to their syntrophic partners, sulfate-reducing or sulfur disproportionating bacteria (SRB; Nauhaus et al., 2002;

Hoehler et al., 1994; Milucka et al., 2012). The metabolic byproducts of methanotrophy support micro- and macrofaunal communities in the seep's food web, including sulfide-oxidizing bacteria (*Beggiatoa*, *Thioploca*), chemosynthetic clams (*Vesicomya*), mussels (*Bathymodiolus*), tube worms (Siboglinidae), and ampharetid polychaetes that serve as visual manifestations of $CH_4$ seepage on the seafloor (Van Dover et al., 2003; Levin, 2005; Niemann et al., 2013).

Detailed examination of microbial communities within methane seep sediments has further revealed the community composition and exposed relationships between constituent members. The archaeal group ANME-1 is currently divided into two subgroups (ANME-1a and ANME-1b) and represents a novel order within the Euryarchaeota (Hinrichs et al., 1999; Hallam et al., 2004; Meyerdierks et al., 2005). These anaerobic methane-oxidizing microorganisms have been observed as single cells, as monospecific aggregates, and in association with bacteria (Orphan et al., 2002; Treude et al., 2007; Holler et al., 2011). The Methanosarcinales-affiliated ANME-2 (divisible into three phylogenetic subgroups, ANME-2a, -2b, and -2c; Orphan et al., 2001) frequently form aggregates with members of the Desulfobacteraceae family (e.g., the Seep-SRB1 group; Boetius et al., 2000; Knittel et al., 2005; Schreiber et al., 2010) or Desulfobulbaceae (Pernthaler et al., 2008; Green-Saxena et al., 2014). Members of the ANME-3 clade have been shown to associate with Bacteria most closely related to another lineage within the Desulfobulbaceae (Lösekann et al., 2007; Green-Saxena et al., 2014).

Sulfate-coupled methane oxidation produces two units of alkalinity per unit of dissolved inorganic carbon, thereby promoting the precipitation of authigenic carbonate minerals (Aloisi et al., 2002). These precipitates form loosely consolidated protoliths,

hereafter referred to as "nodules," found below the sediment-water interface within methane-perfused sediments (Orphan et al., 2004; Watanabe et al., 2008). Larger, fully lithified carbonate rocks also form, likely within methane-perfused sediment (Stadnitskaia et al., 2008; Bian et al., 2013), and can be exposed at the seabed following episodes of uplift and winnowing (Ussler and Paull, 2008; Greinert et al., 2001; Naehr et al., 2007). AOM activity associated with methane seepage at the seabed results in a heterogeneous landscape of reduced sediments and carbonate pavements, chemoherms, and large mounds, covered by patches of chemosynthetic communities. Carbonate structures can be hundreds of meters tall and likely represent the time-integrated accretion of AOM-linked authigenic carbonate precipitation (Greinert et al., 2001). Subsurface advective methane flow can shift with time, turning "active" habitats, which exhibit gas bubbling and/or seafloor chemosynthetic communities, into "low-activity" sites with minimal or no apparent methane flux to the seabed (Boetius & Suess, 2004; Treude et al., 2003). These low-activity areas often contain carbonates with negative $\delta^{13}C$ values that are presumed to reflect previous AOM activity, yet it remains unclear how sediment and carbonate-hosted microbial communities differ between active and low-activity sites.

The recent quantification of active metabolic rates of methanotrophic microbial biomass living within the pore spaces of authigenic carbonates in active and low-activity areas further motivates the study of endolithic microbial communities (Marlow et al., 2014). Previous literature has characterized the common taxa associated with carbonates in methane-rich regimes such as cold seeps and mud volcanoes by examining lipid biomarkers (Blumenberg et al., 2004; Stadnitskaia et al., 2005, 2008; Gontharet et al.,

2009) and 16S rRNA gene signatures (Stadnitskaia et al., 2005; Reitner et al., 2005; Heijs et al., 2006; Stadnitskaia et al., 2008). These published findings have been used to discuss the paleo seepage record (Gontharet et al., 2009), as well as stages of carbonate formation (Stadnitskaia et al., 2005; Reitner et al., 2005; Bahr et al., 2009; Stadnitskaia et al., 2008). Microbial communities associated with carbonate crusts and sediments have been broadly compared in the euxinic Black Sea (Stadnitskaia et al., 2005) and the eastern Mediterranean Sea (Heijs et al., 2006), but the extent to which methanotrophic communities within partially and fully lithified habitats differ from adjacent sediment-hosted communities at continental margin seeps remains largely unconstrained. Given the influence of AOM in methane processing, the community structure of carbonate-based habitats may exert a significant influence on methane and sulfur biogeochemical processes in the deep sea.

This study examines microbial abundance and community diversity in six structural classes of methane seep habitats (active sediments, active nodules, active carbonates, low-activity sediments, low-activity carbonates, and off-seep background sediments); which integrate two key environmental variables: seepage activity and physical substrate type. We analyze mineralogy, 16S rRNA gene archaeal and bacterial sequence diversity, and cell abundances of 12 samples from six different deep-sea habitats associated with methane seepage at Hydrate Ridge, OR, USA (Table 3.1; Fig. 3.1). With this dataset, we characterize the microbial diversity and the potential importance of seepage activity and substrate as determinants of microbial community structure in and around methane seeps.

| Identification Number | Seep Activity Level | Sample Depth Horizon | Physical Substrate Type | Site | Location (Latitude, Longitude) | Water Depth (m) | Mineralogy |
|---|---|---|---|---|---|---|---|
| AS-3730 | Active | 0-6 cm | Sediment | HR South | 44°34.20', 125°8.87' | 775 | Quartz |
| AS-5119 | Active | 6-9 cm | Sediment | HR North, Site 7 | 44°40.02', 125°5.99' | 600 | Quartz |
| AN-3730N | Active | 0-6 cm | Nodule | HR South | 44°34.20', 125°8.87' | 775 | Q/C/A Mix |
| AN-5119N | Active | 6-9 cm | Nodule | HR North, Site 7 | 44°40.02', 125°5.99' | 600 | Q/C/A Mix |
| AC-3439 | Active | Seafloor* | Carbonate | HR South | 44°34.11', 125°9.17' | 774 | Aragonite |
| AC-5120 | Active | Seafloor* | Carbonate | HR North, Site 7 | 44°40.02', 125°6.00' | 601 | Dolomite |
| LS-3433 | Low Activity | 0-6 cm | Sediment | HR South | 44°34.23', 125°8.80' | 774 | Quartz |
| LS-5164 | Low Activity | 6-9 cm | Sediment | HR North, Site 8 | 44°40.05', 125°6.03' | 601 | Quartz |
| LC-3662 | Low Activity | Seafloor* | Carbonate | HR South | 44°34.09', 125°9.18' | 788 | Aragonite |
| LC-5189 | Low Activity | Seafloor* | Carbonate | HR North, Site 8 | 44°40.06', 125°6.04' | 604 | Q/C/A Mix |
| OS-3487 | Off-Seep | 0-5 cm | Sediment | Off-Seep | 44°35.27', 124°53.50' | 600 | Quartz |
| OS-3582 | Off-Seep | 10-15 cm | Sediment | Off-Seep | 44°35.28', 124°53.56' | 589 | Quartz |

**Table 3.1**. Identification numbers, site location details, and mineralogical identifications of carbonate, sediment, and nodule samples used in this study. Identification numbers are encoded with information regarding the seepage activity of the sample site ("A" for active, "L" for low-activity, "O" for off-seep) and the physical substrate type ("S" for sediment, "N" for nodule, "C" for carbonate rock). "QCA" refers to a mineralogical mixture of quartz, calcite, and aragonite. *All carbonate rocks were collected from the seafloor; samples used for mineralogical, cell count, and phylogenetic analysis were manually isolated from endolithic fractions >5 cm from the exposed surface.

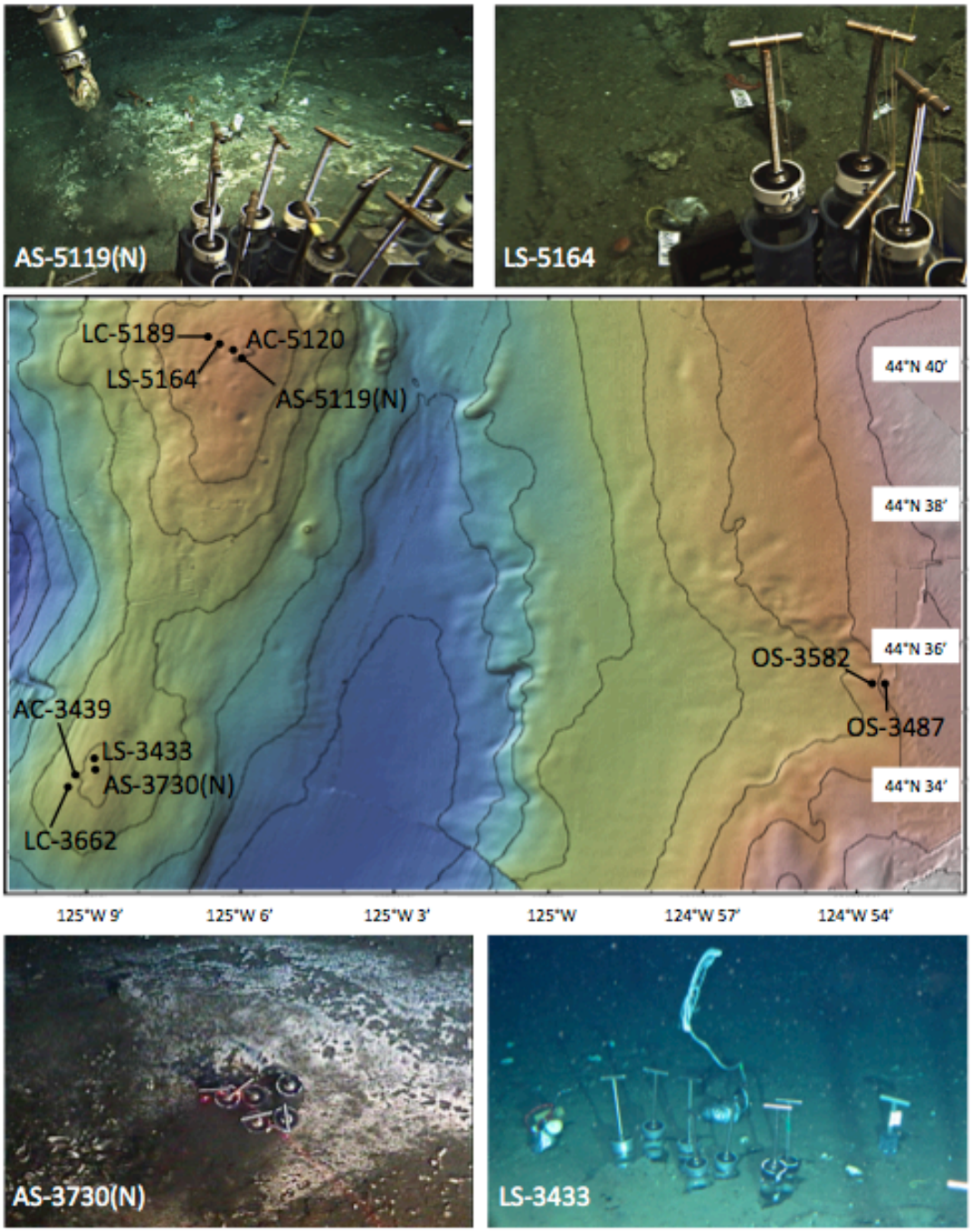


**Figure 3.1**. A map of Hydrate Ridge, showing the locations of origin of the samples used in this study, accompanied by images showing the general locations of sample collection. Samples LC-5189, LC-5164, AC-5120, AS-5119, and AS-5119N were collected from Hydrate Ridge north (mound summit ~600 m depth); samples AC-3439, LS-3433, LC-3662, AS-3730, and AS-3730N were collected from Hydrate Ridge south (mound top ~780 m depth); samples OS-3582 and OS-3487 were collected off-seep from a water depth of

~600 m. Hydrate Ridge north and south sampling sites were located approximately 12 km apart. Base map is derived from Global Multi-Resolution Topography (GMRT, Ryan et al., 2009; GeoMapApp); contour lines represent 100 m of depth, and each minute of latitude represents 1.85 km. In the images, push cores are 10 cm in diameter for scale.

## Methods

*Site Description*

Microbial DNA samples were collected from active and low-activity sites around Hydrate Ridge, Oregon, a convergent tectonic margin well established as a site of methane seepage and sediment-based AOM (e.g., Treude et al., 2003; Suess et al., 1999; Tryon et al., 2002). Samples were collected in consecutive years, with the *DSV Alvin* during R/V *Atlantis* leg AT-15-68 (September 2010), and with the *ROV Jason* during *Atlantis* leg AT-18-10 (September 2011). Two samples representative of each substrate-activity pairing were used in this study – one from Hydrate Ridge North (44°40.25'N, 125°06.30'W, ~600 m water depth), and one from Hydrate Ridge South (44°34.09'N, 125°09.14'W, ~780 m water depth), a separation distance of approximately 11.2 km. Sampling at two distinct seep-influenced locations at Hydrate Ridge confers interpretive power across a relatively broad spatial scale (km rather than meters). Active nodules were recovered from a corresponding active sediment push core (i.e., AN-3730N refers to a carbonate nodule found within the AS-3730 sediment core). Background sediment was collected from an off-seep site approximately 15 km east of Hydrate Ridge (Table 3.1, Fig. 3.1). The sulfate-methane transition zone (SMTZ) at Hydrate Ridge active seep sites has been reported to occur within the 2-9 cm below seafloor (cmbsf) depth horizon, corresponding to peak values of microbial aggregate abundance, methane oxidation, and sulfate reduction (Boetius and Suess, 2004; Boetius et al., 2000). Methane concentrations within the most

active seep sediments reach several mM, and have been measured and modeled at values up to 70 mM (Boetius and Suess, 2004) and 50 mM (Tryon et al., 2002), respectively.

*Sample Collection and Processing*

On the seafloor, sediment was collected in push cores (35 cm long) deployed by the *ROV Jason* or *DSV Alvin*. Individual carbonate rocks were collected with the manipulator arm and placed inside Plexiglas compartments in a subdivided, insulated biobox with a lid to minimize water column or cross-sample contamination during recovery. During ascent to the surface, supersaturated methane may have degassed during depressurization, as was apparent from gas pockets in core tubes. Shipboard, push cores and carbonates within their respective plexiglass containers were immediately transferred to a 4 °C walk-in cold room and processed within several hours. Samples intended for DAPI (4',6-diamidino-2-phenylindole) counts and fluorescence *in situ* hybridization (FISH) were fixed in 2% formaldehyde and stored at 4 °C overnight, while samples intended for DNA extraction were frozen at -80 °C. The next day, the formaldehyde was washed from the sample with sterile 1X PBS buffer and then replaced with 100% ethanol and transferred to a -80 °C freezer. In the case of carbonate rocks, interior portions (≥5 cm from an exposed surface) were isolated to ensure the analysis of endolithic communities; this was done by breaking the sample with an autoclaved ceramic mortar and pestle and removing the outer surface with a sterile razor blade. Similar mortar and pestle treatment of sediment and subsequent DAPI visualization confirmed that aggregate morphology is not an artifact of carbonate sample preparation.

*X-Ray Diffraction*

Samples for X-ray diffraction analysis (XRD) were powdered with an autoclaved ceramic mortar and pestle. The diffraction profiles were measured with a Phillips X'Pert Multi Purpose X-Ray Diffractometer housed in the Division of Materials Science at Caltech. $SiO_2$ was used as an internal standard, and best-fit analyses (with peak-shifting permitted) were conducted with the X'Pert HighScore software and its library of diffractograms.

The analysis of XRD data focused on four components: quartz ($SiO_2$), calcite ($CaCO_3$), dolomite ($CaMg(CO_3)_2$), and aragonite ($CaCO_3$). These minerals are the primary constituents of seep-associated carbonates (Greinert et al., 2001). The following peaks were used as diagnostic markers following peak-shifting: calcite (104) $2\theta = 30.0°$, dolomite (104) $2\theta = 31.2°$, aragonite (221) $2\theta = 46.0°$, and quartz (011) $2\theta = 27.0°$ (Kontoyannis & Vagenas, 2000; Zhang et al., 2010). Each of these peaks is the most prominent for its respective mineral type, allowing for qualitative compositional characterization by relative peak heights (Tennant and Berger, 1957; Bergmann, 2013). Minor constituents not accounted for by the four components described above cannot be ruled out, but these four peaks, as well as the additional peaks associated with each mineral, account for the majority of XRD features in all spectra.

*Microscopy determination of Relative Microbial Biomass*

Formaldehyde / ethanol fixed samples of carbonate and sediments were prepared for microbial aggregate characterization and FISH as follows. Nodules and interior carbonate pieces were pulverized with an autoclaved porcelain mortar and pestle. To concentrate biomass away from mineral and sediment particles, a percoll density separation was performed on all samples following a modified protocol outlined in Orphan et al.

(2001). Specifically, 60 µl sample was mixed with 1290 µl TE (pH = 9) and heated for 3 minutes at 60 °C to permeabilize cells. The sample tubes were placed on ice for 5 minutes; 4.5 µl of 30% $H_2O_2$ was then added (to deactivate native peroxidase for CARD-FISH) and incubated at room temperature for 10 minutes. Tubes were placed back on ice, and 150 µl sodium pyrophosphate was introduced. Sample mixtures were sonicated (Branson sonifier 150) on ice 3 times at 8 W (10 seconds each time) and overlaid on a percoll density gradient. The gradient tubes were then centrifuged at 4,800 rpm for 15 minutes at 4 °C (Allegra X-15R, Beckman Coulter, Indianapolis, IN). The percoll supernatant overlaying the sediment/ carbonate pellet was removed and concentrated by vacuum filtration through both a 3 µm and a 0.22 µm white polycarbonate filter (Millipore). Filtered samples were immediately rinsed with 2 ml 1X PBS and dehydrated with 2 ml of a 1:1 ethanol:PBS solution while on the filter tower. Dried filters were removed and stored in the dark at 4 °C prior to analysis. Cell counts were performed on an (Olympus BX51) epifluorescence microscope under 60x magnification (Plan Apo N objective) using the general DNA stain DAPI (4',6-diamidino-2-phenylindole). 25 fields of view were counted for each of the ten seep-linked samples (Table 2).

The architecture of DAPI-stained aggregates was examined by acquiring a z-stack of epifluorescence images with a DeltaVision RT microscope and the associated Softworx program (Applied Precision, Inc., Issaquah, WA). Subsequent image processing was conducted with the DAIME image analysis and 3D visualization program (Daims et al., 2006). By recognizing fluorescently stained cells within manually delineated aggregate boundaries throughout a z-stack of images, DAIME is able to calculate biovolume and the pair correlation function. Biovolume is determined by dividing the 3D integrated volume

of cells by the overall aggregate volume, and the peak pair correlation value corresponds to the most favored cell-cell distance (Daims et al., 2006). Biovolume and pair correlation values were obtained from five representative aggregates from each habitat; individual cell sizes were broadly consistent for all samples.

Relative microbial abundance within the 12 distinct samples was determined by calculating the cumulative aggregate volume per unit volume sample, dividing by a typical cell (1 μm diameter) volume, multiplying by the maximum possible spherical packing density (0.7405; Steinhaus, 1999), and scaling by the DAIME-determined biovolume aggregate factor. The abundance of single cells (recovered on the 0.22 μm filter) was then added to the aggregate value, and the sum of both aggregate-associated cells and single cells was divided by the largest cell abundance calculated for the dataset (sample AC-3439). Resulting values thus indicate the fraction of microbial cell abundance associated with each sample, relative to the sample with the highest cell count. This calculation did not distinguish between Archaea and Bacteria, and overall microbial abundance scaling factors (Table 3.2) were applied to both Domains' diversity charts (Figs. 3.2, 3.3).

*Phylogenetic Analysis*

To assess 16S rRNA gene diversity, the following workflow was performed for all 12 samples. DNA was extracted from ~0.5 g of sediment or pulverized nodule / carbonate material using the UltraClean Soil DNA isolation kit (Mo Bio Laboratories, Carlsbad, CA). Bacterial and archaeal 16S rRNA genes were amplified in separate Polymerase Chain Reactions (PCR) with 27F (5'-AGAGTTTGATCCTGGCTCAG-3') / 1492R (5'-GGYTACCTTGTTACGACTT-3') and 8F (5'-TCCGGTTGATCCTGCC-3') / 958R (5'-YCCGGCGTTGAMTCCAATT-3') primers, respectively (all primer concentrations were

0.4 μM, primers from Integrated DNA Technologies, Inc., Coralville, IA), New England BioLab's *Taq* DNA Polymerase (NEB, Ipswich, MA), 0.4 μM dNTP solution mix (NEB), and 1X ThermoPol Reaction Buffer (NEB). PCR was performed on an Eppendorf Mastercycler Ep Gradient S thermocycler with a two-minute 95 °C initialization, followed by 35 cycles of a 30 second 94 °C denaturation, 60 second 54 °C annealing, and 90 second 72 °C elongation. A final seven-minute 72 °C elongation completed the procedure, at which point the block was cooled to 4 °C until samples were retrieved (<15 hours). 16S rRNA gene amplicons were cleaned by filtration through a Millipore MultiScreen Filter Plate (Millipore Corp., Billerica, MA) and cloned using the TOPO TA Cloning Kit following the manufacturer's instructions (Invitrogen, Carlsbad, CA). For bacterial analysis, 288 transformants (colonies) were picked for each sample, an average of 233 of which contained appropriately sized inserts. For archaeal clone libraries, 192 colonies were picked for each analysis, and an average of 168 of these colonies contained the correctly sized insert. A random subset of clones in each library (Table S3.1) were selected and sequenced by Laragen, Inc. (Culver City, CA). Archaeal amplicons were sequenced in one direction (~900 bp), using the T3 primer (5'-ATTAACCCTCACTAAAGGG-3'), while bacterial inserts were sequenced bi-directionally, using the T3 primer and the T7 primer (5'-CCCTATAGTGAGTCGTATTA-3'). Vector sequence was removed and contigs (~1500 bp) were constructed (90% minimum match, 10 base minimum overlap) using forward and reverse sequences from the same clone; when one direction of sequence passed quality control inspection but the other did not, the low quality sequence was not used. Chimeric sequences were identified with the Slayer, Uchime, and Bellerophon programs; non-chimeric sequences were manually aligned in ARB (Ludwig et al., 2004) in

reference to the Silva 111 NR98040812 database and used for subsequent phylogenetic analysis. The sequences were submitted to Genbank with the following accession numbers: KF616551-KF616600; KF616676-KF616751; KM356307-KM357226. See Table S3.1 for the number of sequences involved at each stage of analysis.

Non-metric multidimensional scaling (MDS) treatments and analysis of similarity (ANOSIM) were performed on these sequences in Primer 6.1.13 (Clarke and PRIMER, 2006) using Bray-Curtis similarity matrices that had been square-root transformed to prevent artificial over-emphasis of abundant taxa on community structure (Legendre and Legendre, 1998). Chao, Inverse Simpson, Bray-Curtis, and Weighted Unifrac indices were calculated from 97% sequence similarity OTUs in reference to the Silva 104 NR99100211 database using the Mothur platform (Schloss et al., 2009).

**Results & Discussion**

In this study, the microbial abundance and diversity of twelve samples representing six classes of methane seep habitats (Table 3.1) are assessed with the aim of establishing the influence of seepage activity and physical substrate type on the microbial community. Mineralogical examination, cell abundance calculations, and 16S rRNA gene archaeal and bacterial sequences, as well as statistical analyses of sequence diversity, reveal distinct patterns in, and raise intriguing questions about, the forcing of microbial community structure at methane seep-associated habitats.

*Mineralogy of Authigenic Carbonates in the Seep Environment*

XRD analysis of the 12 samples considered in this study supports four broad categories of mineralogical identification (Fig. S3.1): sediments containing a dominant siliciclastic component identified as quartz (AS-3730, AS-5119, LS-3433, LS-5164, OS-

3487, OS-3582); quartz, aragonite, and calcite mixtures (AN-3730N, AN-5119N, LC-5189); aragonitic carbonate rocks (AC-3439, LC-3662); and a dolomitic carbonate (AC-5120). Sediment with a low carbonate component was also reported by Orphan et al., (2004); the high proportion of quartz suggests a significant contribution from continental silicate weathering products, while other components including iron sulfide minerals are also likely present (Jørgensen et al., 2004; van Dongen et al., 2007).

Changes in porewater chemistry with depth in the sediment column, particularly sulfate concentration, are hypothesized to influence mineralogy during precipitation (Burton et al., 1993; Savard et al., 1996; Naehr et al, 2007). Among carbonate precipitates, aragonite is the most thermodynamically favored pseudomorph in high-sulfate, high-alkalinity conditions above the SMTZ (Burton, 1993; Savard et al., 1996), and, in particular, at Hydrate Ridge seafloor environmental conditions (Greinert et al., 2001). Calcite is believed to form lower in the sediment column where sulfate is depleted (Naehr et al., 2007), and seep-associated dolomites have $\delta^{13}C$ and $\delta^{18}O$ values that have been interpreted as consistent with formation in deeper methanogenic sediment horizons (Naehr et al., 2007; Meister et al., 2011). Mineralogical differences may thereby record information about the depth and local porewater composition during precipitation.

*Relative Microbial Abundance*

Relative cell abundance calculations (Table 3.2) demonstrate that active carbonates, which contained more abundant and larger, but less densely packed cell aggregates, exhibited the highest cell counts of all sample types, with AC-3439 containing the highest cell abundance of the sample set. Active seep sediment samples contained 77% (AS-3730)

and 56% (AS-5119) as many visible cells as the active carbonate AC-3439. Active carbonate nodule microbial abundance was roughly half that of active carbonates (49% and 44%, compared with 100% and 92% for active carbonate samples). Both nodule samples (AN-3730 and AN-5119) contained more (though less densely-packed) aggregates than the corresponding sediment horizons (AS-3730 and AS-5119) from which they were collected. Samples collected from areas of lower seepage activity had fewer microbial aggregates and larger numbers of single cells, resulting in relative cell abundance values of 35% and 37% for low-activity sediments (LS-3433 and LS-5164, respectively) and 16% and 17% for low-activity carbonates (LC-3662 and LC-5189, respectively). The microbial abundance of off-seep background sediments was approximately two orders of magnitude lower than active seep and low-activity samples and was composed almost exclusively of single cells.

| Sample | # Aggregates / $cm^3$ | Aggregate Diameter, um (std dev) | Aggregate Biovolume Factor (std dev) | Proportion of Single Cells | Cell Abundance (per $cm^3$) | Relative Cell Abundance |
|---|---|---|---|---|---|---|
| AS-3730 | 9.59E+07 | 6.2 (1.3) | 1* (0.19) | 0.15 | 1.99E+10 | 0.77 |
| AS-5119 | 8.67E+07 | 5.7 (1.1) | 1* (0.19) | 0.18 | 1.45E+10 | 0.56 |
| AN-3730N | 1.04E+08 | 6.8 (1.7) | 0.46* (0.03) | 0.12 | 1.26E+10 | 0.49 |
| AN-5119N | 1.07E+08 | 6.4 (1.9) | 0.46* (0.03) | 0.16 | 1.14E+10 | 0.44 |
| AC-3439 | 1.35E+08 | 10.2* (2.2) | 0.215* (0.07) | 0.11 | 2.57E+10 | 1.00 |
| AC-5120 | 1.37E+08 | 9.7 (2.3) | 0.215* (0.07) | 0.16 | 2.36E+10 | 0.92 |
| LS-3433 | 4.08E+07 | 6.2 (0.9) | 0.88 (0.16) | 0.29 | 8.92E+09 | 0.35 |
| LS-5164 | 5.16E+07 | 5.8 (1.4) | 0.88 (0.16) | 0.31 | 9.50E+09 | 0.37 |
| LC-3662 | 6.49E+07 | 5.6 (1.7) | 0.35 (0.05) | 0.28 | 4.10E+09 | 0.16 |
| LC-5189 | 6.23E+07 | 5.9 (1.6) | 0.35 (0.05) | 0.23 | 4.30E+09 | 0.17 |
| OS-3487 | NA | NA | NA | >.99 | 1.93E+08 | 7.50E-03 |
| OS-3582 | NA | NA | NA | >.99 | 1.50E+08 | 5.85E-03 |

**Table 3.2**. Cell abundance parameters from all seep-associated samples. Values marked with * indicate data from Marlow et al., 2014.

Archaeal and bacterial diversity in seafloor methane seep sediments, carbonate nodules, and carbonate slabs were characterized by 16S rRNA gene clone libraries. Supplementary Data files 3.1 and 3.2 provide the genus-level phylogenetic assignments of each sequence. Combining the relative abundance of 16S rRNA genes from archaeal and bacterial clone libraries with bulk microbial abundance data of unknown domain-level distribution (Table 3.2), abundance-scaled charts of phylogenetic distributions were generated (Figs. 3.2, 3.3).

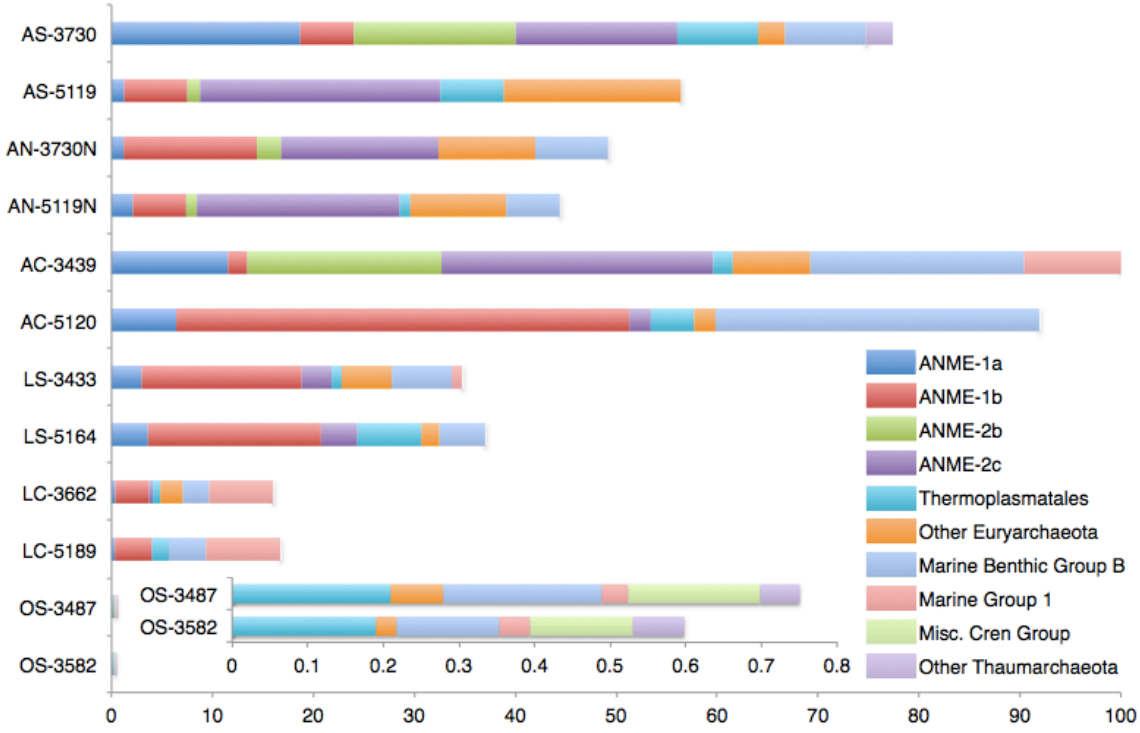


**Figure 3.2**. Distribution of archaeal 16S rRNA gene sequences recovered from carbonate, nodule and sediment samples. Phylogenetic groups that account for at least 20% of overall abundance in one or more samples are shown. In all cases, bar lengths are scaled by the microbial abundance observed in each sample, with AC-3439, which has the highest microbial abundance, as the longest bar (see Table 3.2). Each bar segment length represents the microbial abundance-weighted proportion of that sample's clones falling within the phylogenetic group in question. Inset: Off-seep samples OS-3487 and OS-3582 have biomass values orders of magnitude lower than those of seep-associated samples.

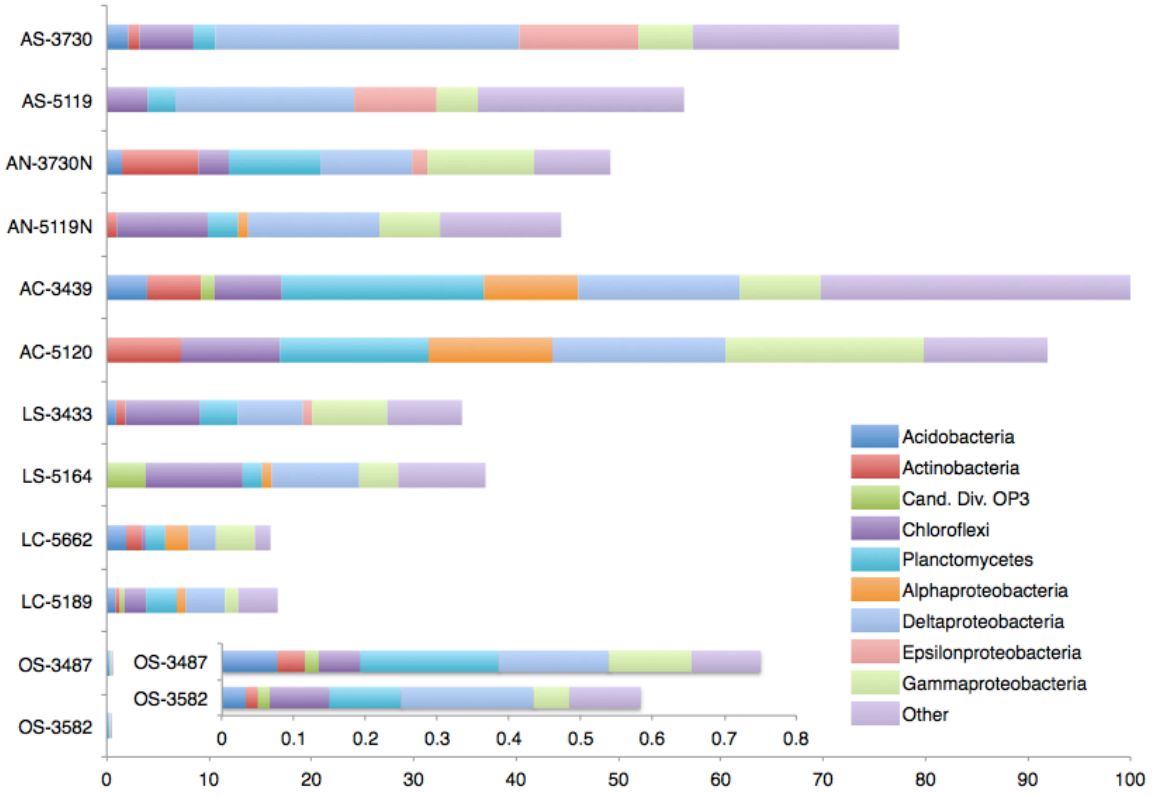


**Figure 3.3**. Distribution of bacterial 16S rRNA gene sequences recovered from carbonate, nodule and sediment samples. Phylogenetic categories representing phyla (or class, in the case of *Proteobacteria*) that account for at least 10% of overall abundance in one or more samples are shown. Bar lengths are scaled as in Fig. 3.2.

*Archaeal Community Characterization*

Euryarchaeota belonging to diverse ANME groups dominated the archaeal 16S rRNA gene sequences recovered from active seep sediments (82.4% of all archaeal clones; percentages compiled from pooled sequences of a given sample type, see Supplementary Data file 3.1c). Similarly, ANME sequences composed 84.3% of the total archaeal diversity from active nodules; this proportion was 59.6% for archaeal sequences recovered from active carbonates and 71.1% for archaeal sequences from low-activity sediments. Archaeal clone libraries constructed from low-activity carbonates showed a smaller proportion of ANME sequences, representing 24.7% of all archaeal sequences, while

ANME sequences were not recovered in off-seep background sediment clone libraries, which instead contained abundant representatives of the uncultured Thaumarchaeotal lineage Marine Benthic Group B (MBGB) (Vetriani et al., 1999).

Among ANME representatives, ANME-1 – predominantly the ANME-1b subgroup (Teske et al., 2002) – were more abundant in low-activity samples (83.1% of all ANME sequences from low-activity sediments and carbonates; Supplementary Data file 3.1e) than samples associated with actively venting seeps (34.2% of pooled ANME sequences from active sediments, nodules, and carbonates). ANME-2 – mostly the ANME-2c subgroup (Orphan et al., 2001) – exhibited the opposite pattern, accounting for 58.3% of ANME sequences recovered from active samples and 13% from low-activity samples. The exception to this trend is the phylogenetic distribution of sequences recovered from the active dolomitic sample AC-5120, whose archaeal clone library contained 48.8% ANME-1b and 2.3% ANME-2c representatives. Members of the ANME-3 group were observed in most active and low-activity seep sediment samples and carbonate nodules (6.8% of total archaeal diversity on average among these samples), but were not recovered from any of the seafloor exposed carbonate rock samples or off-seep sediments (Supplementary Data file 3.1).

Members of the ANME lineages are the dominant Archaea linked to sulfate-coupled methane oxidation at marine methane seeps (Knittel and Boetius, 2009), and their environmental abundances often correlate with methane flux in sulfate-perfused, anoxic sediment near the seabed. When compared with 16S rRNA gene sequences recovered from active seep sediments, our data demonstrate that the carbonate rock substrate variable accounted for an approximate 25% decrease in ANME sequence abundance relative to

active sediments. (To make this calculation, active carbonate archaeal sequences were pooled (n=94 sequences), relative abundance was determined, and this value was compared with the analogous value derived from combined active seep sediment samples (n=74 sequences); see Supplementary Data file 3.1c). Low seepage activity accounted for a 14% decrease (pooled low-activity sediment sequences compared with combined active seep sediment sequences). When low-activity carbonate samples' sequences were pooled, a 70% decrease in ANME relative abundance (compared with active sediment samples) was observed. This finding suggests that the combination of factors relating to methane seepage activity (low-activity) and physical substrate (carbonate) negatively impacts the relative ANME abundance more than the sum of each factor individually. For example, in low-activity carbonate habitats, anaerobic archaeal methanotrophs may become energy or carbon limited as a result of self-entombment (e.g., Luff et al., 2004). Additionally, unfavorable geochemical conditions associated with decreased methane flux and/or the intrusion of oxygenated seawater after exposure on the seafloor may limit the successful persistence of these obligate anaerobes. Other archaeal groups – most notably marine group 1 (MG 1) Thaumarchaeota – were more prevalent in low-activity carbonate communities, which may be attributable to their colonization of a habitat less suitable for anaerobic methanotrophs and/or a diminished ability of MG 1 to inhabit the reducing active seep settings.

ANME-1 are believed to be better adapted to lower sulfate and/or methane conditions than their ANME-2 counterparts based on observations of niche differentiation in Japan Sea sediments (Yanagawa et al., 2011), Black Sea mats (Blumenberg et al., 2004), diffusion driven continental margin sediments (Harrison et al., 2009), and other

environmental comparisons (Nauhaus et al., 2005; Rossel et al., 2011). Our findings corroborate this trend: ANME-1 representatives constituted 25.5% of archaeal sequences from active seep sites and 37.9% of combined archaeal sequences recovered from low-activity sediment and carbonate samples (Supplementary Data file 3.1d). It remains unclear whether all members of the ANME-1 are methanotrophs physiologically adapted for low-methane conditions, or facultative methanogens (Lloyd et al., 2011; House et al., 2009; Reitner et al., 2005), a metabolic plasticity that would confer a competitive advantage in zones of limited methane. The relative abundance of ANME-1 sequences recovered from AC-5120 is markedly higher than that of other active-site samples, an observation that may suggest a contributing role of mineralogy in community structure (Fig. 3.2, see discussion below). ANME-3 representatives were not recovered in our carbonate rock diversity surveys. Whether this is due to their relative low abundance in the Hydrate Ridge ecosystem overall (~9% of archaeal sequences in active seep sediments) or if the apparent absence of ANME-3 in carbonates is indicative of habitat preference requires further investigation (Supplementary Data file 3.1). Members of the ANME-3 are typically reported as minor constituents from diverse seep sediment habitats and have only been reported as a dominant member from one site (Haakon Mosby mud volcano) to date (Lösekann et al., 2007).

Archaeal lineages not traditionally linked to methane oxidation also demonstrate activity-based trends. Euryarchaeotal Thermoplasmata were detected in 11 of the 12 samples, comprising a low percentage of the total archaeal sequences in active seep (5.2%) and low-activity samples (9.5%), and were observed at substantially higher proportions in off-seep background samples (31%; Supplementary Data file 3.1d). Sequences from the

Halobacteria class, related to sequences from methane seep sediments (Harrison et al., 2009) or hydrothermal vents (Schauer et al., 2009), were recovered in low abundance (2.5% average of archaeal sequences, across all samples) from nearly all sample types with the exception of active carbonates.

The most prevalent thaumarchaeotal classes included Marine Benthic Group B (MBGB) and Marine Group 1 (MG1). Sequences most closely related to the MBGB family, whose representatives are common in anoxic sediments (Vetriani et al., 1999), including those influenced by methane (Biddle et al., 2006), were abundant in clone libraries from all carbonates and low-activity and off-seep sediments (20.9% of pooled archaeal sequences recovered from these samples). The relative proportion of recovered MBGB sequences was lower in sediment and nodules from active seeps (8.9%). MG1 accounted for 39.5% (LC-3662) and 44% (LC-5189) of the total archaeal sequences of the two low-activity carbonate samples recovered from the seabed outside of active seepage areas; this proportion never exceeded 13.7% (AC-3439) in any of the other ten samples.

The thaumarchaeotal class MG1 is pervasive in the deep-water column (Karner et al., 2001; Massana et al., 1997), and its high relative abundance in archaeal diversity surveys of the low-activity carbonates is likely reflective of seawater infiltration of these exposed carbonates at the seabed. Neither surface-exposed carbonates from active seep sites nor low-activity / off-seep sediments display the same MG1 abundance. This observation indicates that both low seepage activity (with low corresponding levels of methane and sulfide) and carbonate rock substrate appear to be necessary factors for MG1 prevalence, a finding that is consistent with MG1 acting as a passive colonizer of seawater-infused carbonates. In hydrothermal vent-associated basalt, MG1 representatives appear to

be more abundant in weathered, off-vent samples (Lysnes et al., 2004) compared with initial communities in subseafloor hydrothermal environments (Huber et al., 2002). Channels of concentrated fluid flow developed by faulting and exploited by upward advection of methane-rich fluids during periods of seep activity may serve as conduits for downward, tidally-enhanced fluid delivery (Tryon et al., 2002) during subsequent periods of quiescence. Convection (Aloisi et al., 2004) and hydrologic recharge mechanisms at mound bases (Paull et al., 1991; Teichert et al., 2005) may also remain active. These processes may have preferentially seeded carbonate rocks from low-activity settings, where upward advection is less prominent, with MG1 representatives from bottom water. Alternatively, the presence of MG1 organisms may represent a secondary colonization resulting from carbonate exposure to bottom water following exhumation. The low-activity and off-seep sediment samples encompassing the 0-6 cmbsf horizon (LS-3433 and OS-3487) displayed minimal MG1 representation, suggesting that they may be outcompeted in the sediment habitat. MG1 representatives have been implicated in ammonium oxidation (Konneke et al., 2005; Nicol and Schleper, 2006), but the metabolic proclivities of carbonate-associated MG1 is not currently known.

*Bacterial Community Characterization*

Among bacterial sequences, Deltaproteobacteria was the most abundant class recovered from 8 of the 12 samples (AS-3730, AS-5119, AN-5119N, AC-3439, LS-5164, LC-5189, OS-3487, and OS-3582), and the second most abundant class detected in the remaining samples, with the exception of LS-3433 (Supplementary Data file 3.2c). Desulfobacteraceae and Desulfobulbaceae representatives were the most abundant deltaproteobacterial families recovered in active-seep samples (sediments, nodules, and

carbonates), which likely reflects these taxa's role in AOM (e.g., Orphan et al., 2001; Green-Saxena et al., 2014; Schreiber et al., 2010; Kleindienst et al., 2012). These families were abundant in bacterial diversity surveys from low-activity sediments as well (accounting for 75% of Deltaproteobacteria; Supplementary Data file 3.2d) but significantly less so in low-activity carbonates and off-seep sediments (15%), where members of the uncultured deltaproteobacterial groups SAR324 and SH765B-TzT-29 were more prevalent. Relatives from the SAR324 and SH765B-TzT-29 groups have been described from seafloor lavas (Santelli et al., 2008), South Atlantic Ocean sediment (Schauer et al., 2009), and river estuaries (Jiang et al., 2009). This geographic range suggests that these groups are widely distributed and have no particular dependence on methane geochemistry, though SAR324 methanotrophy has been proposed (Swan et al., 2011). Cultured representatives of these clades are lacking, but recent meta-omics approaches have begun to shed light on their physiological capabilities; members of the SAR324 clade associated with hydrothermal vent plumes, for example, have been implicated in several facultative metabolic modes, including sulfur and hydrocarbon oxidation (Sheik et al., 2014).

Epsilonproteobacteria most closely related to *Sulfurovum sp.* recovered from other methane seeps (Pernthaler et al., 2008; Beal et al., 2009; Mills et al., 2005) were prevalent in sediment samples from active seeps, but were detected at very low relative abundances in other active seep habitats including nodules and carbonate rocks. This observation potentially reflects a substrate-based control on diversity (Supplementary Data file 3.2b,c). Similar trends between seep sediments and their associated carbonate nodules were observed in an additional set of cores from Hydrate Ridge and Eel River Basin seeps

(Mason and Orphan, personal observation). *Sulfurovum* from deep-sea hydrothermal vents are capable of multiple sulfur oxidation pathways (Yamamoto et al., 2010), and representatives of this genus have been described from methane seep sediments (Arakawa et al., 2006; Roalkvam et al., 2011) and methane-impacted terrestrial mud volcanoes (Green-Saxena et al., 2012). In this study, the near-exclusive presence of *Sulfurovum* in active sediments – even in horizons 6+ cm beneath the seafloor (AS-5119) – suggests that these environments contain dynamic sulfur cycles, with sulfide produced through sulfate-coupled AOM potentially being re-oxidized to sulfate by members of the Epsilonproteobacteria and Gammaproteobacteria.

Aerobic methanotrophic activity has been documented using radiotracer methods in sediments and carbonates from both actively seeping and low-activity locations at Hydrate Ridge (Marlow et al., 2014). Surprisingly, the majority of samples lacked 16S rRNA evidence of known aerobic methanotrophs with the exception of AC-5120, a dolomite sample collected from an active seep site, where sequences affiliated with gammaproteobacterial Methylococcales comprised 8% of recovered sequences (Supplementary Data file 3.2a). In contrast to the 16S rRNA findings, previous studies have reported the common occurrence of diverse particulate methane monooxygenase (*pmo*) genes related to gammaproteobacterial aerobic methanotrophs in surface sediments within seeps (Tavormina et al., 2008) as well as from the water column overlying seeps, at more than 50 times the abundance of sites over non-seep locations (Tavormina et al., 2010). Whether this general discrepancy between 16S rRNA and *pmo* findings is due to primer bias, low gammaproteobacterial methanotroph abundance, or the occurrence of as yet unidentified methane-oxidizing bacteria requires further investigation.

Verrucomicrobia – some of whose members have been implicated in aerobic methanotophic metabolism (Op den Camp et al., 2009) – were recovered only from active seep carbonates, comprising 7% of pooled active carbonate bacterial sequences (Supplementary Data file 3.2c). This sample-based specificity may suggest a dependence on methane or other geochemical components associated with active seeps. In addition, an indirect stimulation of heterotrophy (Freitas et al., 2012) associated with the high microbial abundances linked to active carbonates could sustain members of this phylum. The most closely related Verrucomicrobia sequences were reported from deep-sea sediment unaffiliated with methane seepage (Schauer et al., 2009), though some members of the phylum have been recovered from authigenic carbonate crusts linked to mud volcano AOM (Heijs et al., 2006).

*Diversity Analysis: Environmental Controls on Community Structure*

Alpha (within sample) and beta (between sample) diversity statistics demonstrate how communities are structured and how they relate to each other (Table 3.3). Examining how environmental variables such as seep activity and substrate type map onto these relationships can help reveal factors that may play a role in determining microbial community structure. Such analysis may also help us understand the ecology of animal consumers, which exhibit trophic partitioning of microbial resources at Hydrate Ridge (Thurber et al., 2012; Levin et al., 2013).

Alpha diversity analyses, as computed by Chao-1 and Inverse Simpson values, provide comparative information capturing the two main components of community diversity: richness and evenness. Inverse Simpson values, which incorporate both parameters, reveal higher diversity in recovered bacterial sequences compared with

archaeal sequences, a finding in agreement with Heijs et al.'s (2006) analysis of carbonate crust-associated microbial communities from Mediterranean mud volcanoes. A high degree of localized heterogeneity among Bacteria at the 97% sequence similarity OTU level was also observed, and archaeal diversity was substantially higher at off-seep locations compared with seep-associated sites, suggesting a larger range of niches available to Archaea in such environments (Table 3.3).

| | Archaea | | | | Bacteria | | | |
|---|---|---|---|---|---|---|---|---|
| **Sample** | **Chao-1** | **Chao-1 LCI, HCI** | **Inv Simpson** | **Inv Simpson LCI, HCI** | **Chao-1** | **Chao-1 LCI, HCI** | **Inv Simpson** | **Inv Simpson LCI, HCI** |
| AS-3730 | 10 | 9.1, 19.7 | 7.3 | 5.2, 11.9 | 109 | 56.0, 279.4 | 14.5 | 10, 25.9 |
| AS-5119 | 8.5 | 8, 16.3 | 4.4 | 3.1, 7.2 | 41.1 | 29.2, 80.5 | 16.6 | 9.5, 64.1 |
| AN-3730N | 8.5 | 8, 16.3 | 5.2 | 3.9, 7.7 | 28.3 | 19.7, 64.7 | 13.8 | 8.7, 33.1 |
| AN-5119N | 8.5 | 8, 16.3 | 4.1 | 2.9, 7.4 | 58 | 34.1, 138.4 | 15 | 9.2, 40.2 |
| AC-3439 | 11 | 10.1, 20.7 | 6.2 | 4.9, 8.5 | 103.1 | 71.6, 178.4 | 49.1 | 30.9, 120.5 |
| AC-5120 | 6.5 | 6, 14.3 | 2.8 | 2.2, 3.8 | 52.2 | 33.3, 114.5 | 28.3 | 17.4, 74.8 |
| LS-3433 | 10 | 9.1, 19.7 | 4.5 | 3, 9 | 61.2 | 37.8, 135.1 | 41.1 | 24.7, 121.8 |
| LS-5164 | 9 | 8.1, 21.9 | 4.1 | 2.8, 7.5 | 32.4 | 25.5, 58.9 | 29.3 | 19, 63.9 |
| LC-3662 | 15 | 10.8, 42.1 | 4.6 | 3.3, 7.5 | 86.8 | 47.6, 208 | 41 | 24.1, 137.6 |
| LC-5189 | 7 | 6.1, 19.7 | 3.5 | 2.8, 4.8 | 97 | 54.7, 218.5 | 78 | 41.2, 720.7 |
| OS-3487 | 20.5 | 14.3, 55.5 | 7.9 | 5.5, 13.9 | 45.4 | 32.1, 88.3 | 32.8 | 19.6, 101.4 |
| OS-3582 | 14.5 | 13.2, 25.5 | 8.9 | 6.4, 14.7 | 60.2 | 36.8, 134.1 | 32.2 | 18.4, 127.3 |

**Table 3.3**. Chao-1 and Inverse Simpson values for Archaeal and Bacterial clone libraries made from each of the 12 samples examined in this study. Larger values indicate higher alpha diversity. LCI and HCI indicate the 95% low-end and high-end confidence intervals, respectively.

There is no clear distinction in Chao-1 values between active and low-activity samples for archaeal and bacterial communities in sediment and carbonates, but bacterial communities in low-activity sediments and carbonates do exhibit higher Inverse Simpson values than

their active-site counterparts. This finding suggests that bacterial communities in active seep habitats are dominated by lineages dependent upon seep-based physico-chemical conditions and/or groups associated with methanotrophic archaea. However, with longer residence time on the seafloor – during which alteration products or additional mineral phases can develop and the reducing, anoxic conditions related to active seep environments can dissipate – a broader range of methane-independent metabolic (or physical) niches may become available. A similar link between bacterial diversity and the degree of substrate alteration in weathered seafloor basalts was observed by Santelli et al. (2009). We observed no correspondence between sample-specific archaeal and bacterial alpha diversity metrics (linear best fit $R^2$ values were $2.8x10^{-5}$ and 0.029 for Chao-1 and Inverse Simpson inter-domain comparisons, respectively), suggesting that the two Domains respond differently to physico-chemical and ecological drivers of diversity (Fig. S3.2).

Beta diversity analyses were used to characterize community differences among different habitat types. After sequences were combined by either activity level or substrate type, the dependence of community structure on these environmental variables was evaluated. Through our assessment of seep activity, we established a scale from most methane seep activity ("active") to least ("off-seep"), with "low-activity" occupying an intermediate position. If seep activity is an important control on diversity, active and low-activity communities would be more similar than active and off-seep communities as judged by beta diversity metrics. Similarly, off-seep and low-activity communities would be less divergent than off-seep and active communities. Equivalent expectations can be stated regarding substrate type, along the sliding scale of lithification, from least ("sediment") to most consolidated ("carbonate"), with "nodules" as the intermediate group.

Beta diversity statistics were used in order to evaluate not only significant differences between communities, but also the relative magnitude of such differences (Fig. 3.4). Bray-Curtis analysis (Bray and Curtis, 1957) quantifies the similarity between samples based on the relative abundances of constituent OTUs, while weighted UniFrac (Lozupone et al., 2007) statistics incorporate phylogenetic distances between constituent 16S rRNA gene sequences; both approaches can be used as distance measures (Faith et al., 1987; Lozupone et al., 2011). Our results indicate that off-seep and low-activity archaeal and bacterial communities are more similar than off-seep and active communities. Similarly, active and low-activity archaeal and bacterial communities are more similar than active and off-seep communities (Fig. 3.4a, 3.4c). The wide range in archaeal beta diversity comparison values, particularly noticeable in Fig. 3.4a, suggests that archaeal communities are more strongly shaped by seepage, and that even low apparent methane flux moves the community away from background off-seep composition. High lateral heterogeneity in geochemistry, microbial assemblages, as well as in rates of sulfate reduction and methane oxidation, have been reported on sub-meter scales within and adjacent to seep-associated sulfide-oxidizing microbial mats and chemosynthetic invertebrate communities, illustrating the importance of seepage activity as a dominant control on the sediment-hosted microbial community (e.g., Lloyd et al., 2010; Barry et al., 1996). When substrate type is examined, both beta diversity measurements demonstrate that sediment and nodule communities are more similar than sediment and carbonate communities (Fig. 3.4b, 3.4d). This finding may be partially attributable to spatial proximity, as the sediment-hosted nodules were recovered directly from the active seep sediment cores analyzed in this study. Weighted UniFrac analysis indicates that bacterial communities in carbonates and nodules are more similar

than those in carbonates and sediment. However, the reverse was observed for archaeal communities, suggesting that bacterial diversity may be more dependent on substrate type than seepage level.

a) **Seep Activity**

**Bray-Curtis distance**

| | Active | Low-Activity | Off-Seep |
|---|---|---|---|
| Active | | 38.3 | 22.1 |
| Low-Activity | 44.7 | | 36.3 |
| Off-Seep | 4.9 | 8.1 | |

b) **Physical Substrate**

| | Sediment | Nodule | Carbonate |
|---|---|---|---|
| Sediment | | 38.9 | 20.1 |
| Nodule | 50.2 | | 25.5 |
| Carbonate | 35.8 | 46.1 | |

c)

**Weighted Unifrac**

| | Active | Low-Activity | Off-Seep |
|---|---|---|---|
| Active | | 32 | 27 |
| Low-Activity | 64 | | 30 |
| Off-Seep | 50 | 58 | |

d)

| | Sediment | Nodule | Carbonate |
|---|---|---|---|
| Sediment | | 33 | 24 |
| Nodule | 72 | | 25 |
| Carbonate | 71 | 65 | |

**Figure 3.4**. Results from beta diversity analyses of sequences binned by seep activity (a and c) or physical substrate (b and d). a) and b) provide Bray-Curtis similarities derived from comparison of proportional abundances of 97% sequence similarity OTUs. c) and d) show weighted UniFrac-derived data for which all pairwise P-values are <0.001. Green-shaded fields contain data from archaeal sequences; blue-shaded fields contain Bacteria-specific data. Weighted UniFrac values were subtracted from 1 and multiplied by 100 to provide a more intuitive statistic; in all cases, higher numbers indicate more similar communities.

Non-metric MDS assessments (Fig. 3.5) visualize Bray-Curtis community similarities between the 12 samples. In the two-dimensional plot of archaeal data, communities cluster primarily by seepage activity (Fig. 3.5a). (The dolomitic sample AC-5120 is the single exception to this framework, which may be related to its unique mineralogy, discussed below.) This observation corroborates the Bray-Curtis and weighted UniFrac data that point to seepage activity as the primary determinant of archaeal community structure in and around methane seeps; similar qualitative observations have been reported at a number of seep habitats (e.g., Lloyd et al., 2010). ANOSIM supports the finding that seepage activity is a significant determinant of archaeal community structure

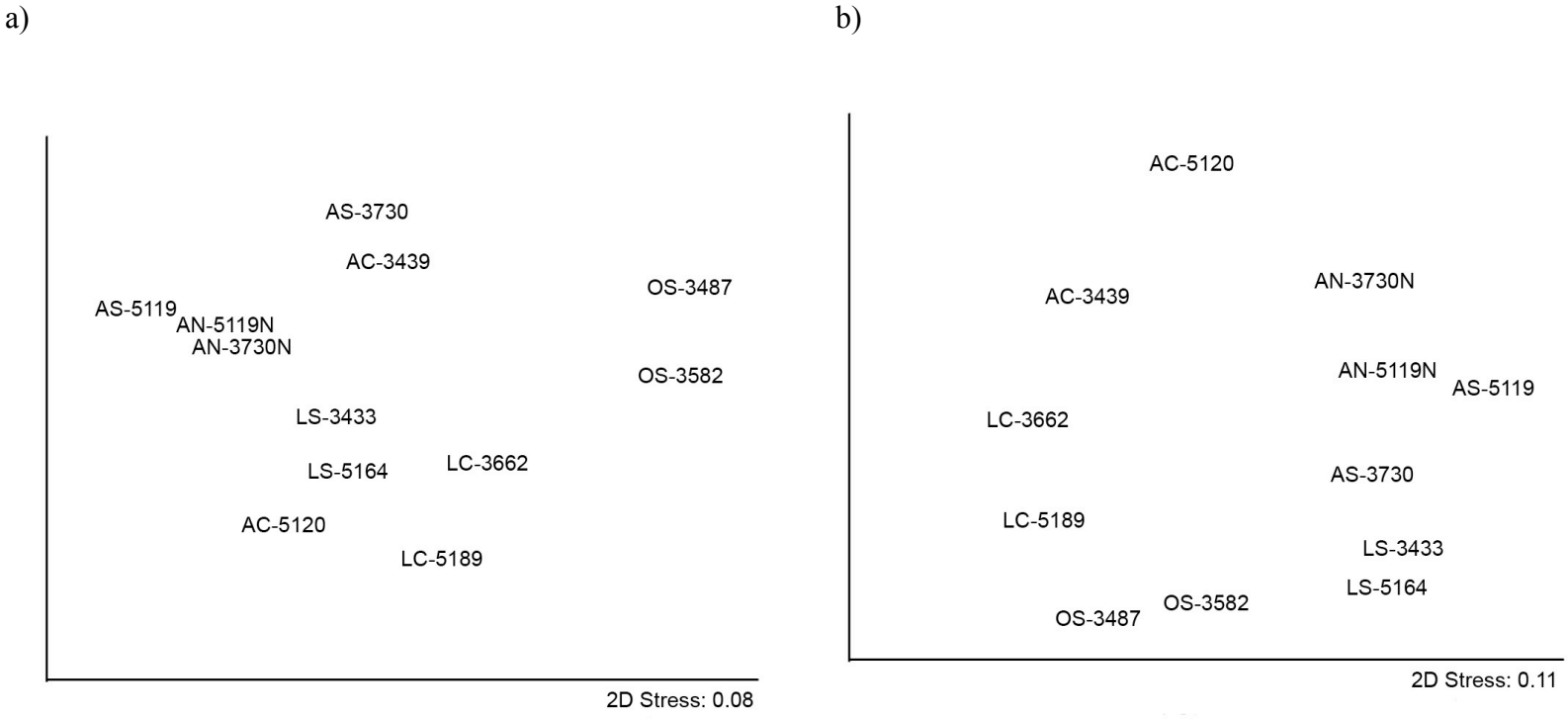


**Figure 3.5**. Non-metric MDS showing a) archaeal, and b) bacterial communities derived from genus-level relative abundances.

(global R = 0.65, p-value = 0.002) rather than physical substrate (e.g., sediment, nodule, carbonate; R = -0.04, p = 0.509; see Table S3.2a for all pairwise values).

The bacterial non-metric MDS plot (Fig. 3.5b) suggests a primary dependence on substrate type: sediments are distributed in the lower / lower right portion of the coordinate system, sediment-hosted nodules are positioned to the upper right, and seafloor carbonates to the left. ANOSIM reveals that physical substrate is a significant driver of bacterial community structure (global R = 0.41, p = 0.021), while seep activity level is not (global R = 0.215, p = 0.094; Table S3.2b). The fact that substrate appears to discriminate among bacterial inhabitants is counter to an analogous study of seafloor basalts showing that the majority of clades are represented in both seafloor basalts and sediments (Mason et al., 2007). This discrepancy may be attributable to other environmental aspects distinctive of methane seep carbonates, such as fluid chemistry, mineralogy, predation pressure, permeability, or authigenic mineral formation (Heijs et al., 2006; Thurber et al., 2012). Indeed, activity appears to play a secondary role in separating bacterial communities, with active samples at the upper segment of the plot, off-seep samples to the bottom, and low-activity samples in between.

Mineralogy is another potential determinant of diversity. The geochemical association of sulfate-coupled AOM with carbonate minerals provides a direct link between microbial metabolism and authigenic mineral precipitation, a feedback that may, in turn, influence microbial community structure through physical constraints (Luff et al., 2004) and/or thermodynamic forcing (Knab et al., 2008). Specific links between diversity and carbonate mineralogy were difficult to discern with the relatively limited sample set included in this study. Aragonitic carbonates (AC-3439 and LC-3662) both contained

abundant ANME sequences, an observation that is consistent with initial precipitation in zones of both high sulfate concentrations and high rates of AOM near the seabed (Greinert et al., 2001; Teichert et al., 2005; Burton, 1993; Savard et al., 1996). The lack of sulfate-reducing deltaproteobacteria in the calcitic LC-5189 is consistent with both a low-sulfate calcite formation environment (Naehr et al., 2007) as well as its current low methane seepage habitat, but it is difficult to parse the relative magnitudes of these influences. Sample AC-5120, a dolomite, may have formed in a deeper sediment horizon exhibiting low relative rates of AOM, as has been hypothesized on the basis of dolomite $\delta^{13}C$ and $\delta^{18}O$ isotopic signatures (Naehr et al., 2007; Meister et al., 2011). The divergence of this sample's archaeal community from those of other active site samples, characterized by the relative abundance of ANME-1 and lack of ANME-2 phylotypes, is consistent with formation in deeper sediment horizons (Knittel et al., 2005; Harrison et al., 2009), or may be uniquely influenced by the dolomitic mineralogy. In general, however, microbial community composition appears to be more dependent upon current environmental context rather than the original precipitation environment, as interpreted from mineralogical signatures. Indeed, when sample mineralogy is specifically plotted within the archaeal and bacterial MDS plots (Fig. S3.3), the partitioning of communities is less clear than when only seepage activity or the degree of lithification (sediment, nodule, or carbonate, irrespective of mineralogy) is considered (Fig. 3.5). The subsidiary importance of mineralogy in conveying microbial community relationships in our dataset suggests that this parameter is less significant than both methane seepage activity and lithification, which likely exert stronger influences over nutrient supply and metabolic intermediate exchange.

The importance of mineralogy as a determinant of community composition has been documented at inactive hydrothermal vent deposits (Toner et al., 2012); with a more extensive dataset focused on mineralogy, it remains possible that this variable may help to explain additional microbial community differences unaccounted for by methane seepage activity or substrate type.

**Conclusion**

The analysis of mineralogy, microbial abundance, and archaeal and bacterial community structure across a range of habitats within and surrounding marine methane seeps reveals several key findings with implications for microbial ecology and seep development beyond what has been previously reported for marine sediment habitats.

Microbial community composition, as determined by 97% sequence similarity OTU-level 16S rRNA gene clone libraries, was remarkably similar among samples with similar seep activity levels and substrates – even if separated by several kilometers and acquired from different sediment depth horizons. This finding suggests that divergence owing to spatial heterogeneity, which has been reported in isotopic, geochemical, and community composition at the cm-scale in seep sediment (Orphan et al., 2004; Lloyd et al., 2010; House et al., 2009), is a less significant driver of bulk microbial diversity on its own than methane flux and/or substrate type.

The persistence of ANME Archaea and microbial aggregates typically associated with AOM in low-activity samples suggests that even at fluxes that do not support established sulfide-based chemosynthetic communities at the seabed (microbial mats or chemosynthetic clam beds), potential for anaerobic methanotrophy remains (Marlow et al., 2014). These findings imply that methanotrophic potential is pervasive on and below the

seafloor across substrate types, and the degree to which ancient seep deposits preserve signals of microbial community succession is unknown. Studies of carbonate crusts from active mud volcanoes (Stadnitskaia et al., 2005) and of Black Sea AOM mats (Blumenberg et al., 2004) demonstrated an imperfect link between recovered lipids and 16S rRNA gene sequences, in which higher complexity lipid profiles suggested a more diverse microbial assemblage. In this context, lipid biomarkers, which are commonly used in geobiological studies to constrain communities or environmental conditions (e.g., Vestal and White, 1989; Turich and Freeman, 2011), may represent a time-integrated signal of microbial constituents and/or an accumulation of exogenous material rather than a faithful snapshot of a single community.

Statistical analyses of recovered 16S rRNA phylotypes reveal differences between sample types and point to distinct physico-chemical determinants of microbial diversity. Archaeal communities, dominated by anaerobic methanotrophs, sort strongly by seep activity; whereas bacterial communities show a preferential association with physical substrate type. This discrepancy suggests that methane influx, while influencing the distribution of anaerobic archaeal methanotrophs, has less of an effect on bacterial diversity and serves as an overlaid imprint on, not a sole arbiter of, community structure. Rather, the physical nature of the habitat – a combination of factors likely including permeability, mineralogy, and hydrology – plays a more significant role in determining bacterial assemblages around methane seeps. Several archaeal and bacterial lineages also appear to demonstrate specific activity-substrate pairing preferences, reflecting the interplay between seepage activity, environmental variation and succession, and microbial community structure. Our analysis exposes and begins to parse the intricate coupling of physical

substrate and methane seepage as factors in environmental pressure and ecological determination; understanding the precise nature of these influences represents a fruitful area for continued research in microbial ecology.

**References:**


Aloisi, G. et al. (2004) Chemical, biological and hydrological controls on the 14C content of cold seep carbonate crusts: numerical modeling and implications for convection at cold seeps. *Chemical Geology* **213**: 359–383.

Aloisi, G. et al. (2002) CH4-consuming microorganisms and the formation of carbonate crusts at cold seeps. *Earth and Planetary Science Letters* **203**: 195–203.

Arakawa, S. et al. (2006) Molecular phylogenetic and chemical analyses of the microbial mats in deep-sea cold seep sediments at the northeastern Japan Sea. *Extremophiles* **10**: 311–319.

Bahr, A. et al. (2009) Authigenic carbonate precipitates from the NE Black Sea: a mineralogical, geochemical, and lipid biomarker study. *International Journal of Earth Sciences* **98**: 677–695.

Barry, J.P. et al. (1996) Biologic and geologic characteristics of cold seeps in Monterey Bay, California. *Deep Sea Research Part I: Oceanographic Research Papers* **43**: 1739–1762.

Beal, E.J. et al. (2009) Manganese- and Iron-Dependent Marine Methane Oxidation. *Science* **325**: 184–187.

Bergmann, K.D. (2013) Constraints on the carbon cycle and climate during the early evolution of animals.

Bian, Y. et al. (2013) Tracing the evolution of seep fluids from authigenic carbonates: Green Canyon, northern Gulf of Mexico. *Marine and Petroleum Geology* **44**: 71–81.

Biddle, J.F. et al. (2006) Heterotrophic Archaea dominate sedimentary subsurface ecosystems off Peru. *Proceedings of the National Academy of Sciences of the United States of America* **103**: 3846–3851.

Blumenberg, M. et al. (2004) Membrane lipid patterns typify distinct anaerobic methanotrophic consortia. *Proceedings of the National Academy of Sciences of the United States of America* **101**: 11111–11116.

Boetius, A. et al. (2000) A marine microbial consortium apparently mediating anaerobic oxidation of methane. *Nature* **407**:

Boetius, A. and Suess, E. (2004) Hydrate Ridge: a natural laboratory for the study of microbial life fueled by methane from near-surface gas hydrates. *Chemical Geology* **205**: 291–310.

Bray, J.R. and Curtis, J.T. (1957) An ordination of the upland forest communities of southern Wisconsin. *Ecological monographs* **27**: 325–349.

Burton, E.A. (1993) Controls on marine carbonate cement mineralogy: review and reassessment. *Chemical Geology* **105**: 163–179.

Clarke, K. and PRIMER, G.R. (2006) V6: user manual/tutorial. *Primer-E Ltd. Plymouth.–2006*.

Claypool, G.E. and Kvenvolden, K.A. (1983) Methane and other hydrocarbon gases in marine sediment. *Annual Review of Earth and Planetary Sciences* **11**: 299.

Daims, H. et al. (2006) Daime, a novel image analysis program for microbial ecology and biofilm research. *Environmental microbiology* **8**: 200–213.

Van Dongen, B.E. et al. (2007) Formation of iron sulfide nodules during anaerobic oxidation of methane. *Geochimica et Cosmochimica Acta* **71**: 5155–5167.

Van Dover, C.L. et al. (2003) Blake Ridge methane seeps: characterization of a soft-sediment, chemosynthetically based ecosystem. *Deep Sea Research Part I: Oceanographic Research Papers* **50**: 281–300.

Faith, D. et al. (1987) Compositional dissimilarity as a robust measure of ecological distance. *Vegetatio* **69**: 57–68.

Freitas, S. et al. (2012) Global distribution and diversity of marine Verrucomicrobia. *ISME J* **6**: 1499–1505.

Gontharet, S. et al. (2009) Palaeo methane-seepage history traced by biomarker patterns in a carbonate crust, Nile deep-sea fan (Eastern Mediterranean Sea). *Marine Geology* **261**: 105–113.

Green-Saxena, A. et al. (2012) Active sulfur cycling by diverse mesophilic and thermophilic microorganisms in terrestrial mud volcanoes of Azerbaijan. *Environ Microbiol* **14**: 3271–3286.

Green-Saxena, A. et al. (2014) Nitrate-based niche differentiation by distinct sulfate-reducing bacteria involved in the anaerobic oxidation of methane. *ISME J* **8**: 150–163.

Greinert, J. et al. (2001) Gas hydrate-associated carbonates and methane-venting at Hydrate Ridge: Classification, distribution, and origin of authigenic lithologies. In, *Natural Gas Hydrates: Occurrence, Distribution, and Detection*, Geophys. Monogr. Ser. AGU, Washington, DC, pp. 99–113.

Hallam, S.J. et al. (2004) Reverse methanogenesis: testing the hypothesis with environmental genomics. *Science* **305**: 1457–1462.

Harrison, B.K. et al. (2009) Variations in archaeal and bacterial diversity associated with the sulfate-methane transition zone in continental margin sediments (Santa Barbara Basin, California). *Applied and environmental microbiology* **75**: 1487–1499.

Heijs, S.K. et al. (2006) Microbial Community Structure in Three Deep-Sea Carbonate Crusts. *Microb Ecol* **52**: 451–462.

Hinrichs, K. et al. (1999) Methane-consuming archaebacteria in marine sediments. *Nature* **398**: 802–805.

Hoehler, T.M. et al. (1994) Field and laboratory studies of methane oxidation in an anoxic marine sediment: Evidence for a methanogen-sulfate reducer consortium. *Global Biogeochemical Cycles* **8**: 451–463.

Holler, T. et al. (2011) Thermophilic anaerobic oxidation of methane by marine microbial consortia. *ISME J* **5**: 1946–1956.

House, C. H. et al. (2009) Extensive carbon isotopic heterogeneity among methane seep microbiota. *Environmental Microbiology* **11**: 2207–2215.

Huber, J.A. et al. (2002) Temporal Changes in Archaeal Diversity and Chemistry in a Mid-Ocean Ridge Subseafloor Habitat. *Applied and Environmental Microbiology* **68**: 1585–1594.

Jiang, L. et al. (2009) Vertical distribution and diversity of sulfate reducing prokaryotes in the Pearl River estuarine sediments, Southern China. *FEMS microbiology ecology* **70**: 249–262.

Jørgensen, B.B. et al. (2004) Anaerobic methane oxidation and a deep H2S sink generate isotopically heavy sulfides in Black Sea sediments. *Geochimica et Cosmochimica Acta* **68**: 2095–2118.

Karner, M.B. et al. (2001) Archaeal dominance in the mesopelagic zone of the Pacific Ocean. *Nature* **409**: 507–510.

Kleindienst, S. et al. (2012) Distribution and *in situ* abundance of sulfate-reducing bacteria in diverse marine hydrocarbon seep sediments. *Environmental Microbiology* **14**: 2689–2710.

Knab, N.J. et al. (2008) Thermodynamic and kinetic control on anaerobic oxidation of methane in marine sediments. *Geochimica et Cosmochimica Acta* **72**: 3746–3757.

Knittel, K. et al. (2005) Diversity and Distribution of Methanotrophic Archaea at Cold Seeps. *Applied and Environmental Microbiology* **71**: 467–479.

Knittel, K. and Boetius, A. (2009) Anaerobic Oxidation of Methane: Progress with an Unknown Process. *Annu. Rev. Microbiol.* **63**: 311–334.

Konneke, M. et al. (2005) Isolation of an autotrophic ammonia-oxidizing marine archaeon. *Nature* **437**: 543–546.

Kontoyannis, C.G. and Vagenas, N.V. (2000) Calcium carbonate phase analysis using XRD and FT-Raman spectroscopy. *Analyst* **125**: 251–255.

Legendre, P. and Legendre, L. (1998) Numerical ecology: second English edition. *Developments in environmental modelling* **20**:

Levin, L. et al. (2013) Ecological release and niche partitioning under stress: Lessons from dorvilleid polychaetes in sulfidic sediments at methane seeps. *Deep-Sea Research II* **92**: 214–233.

Levin, L.A. (2005) Ecology of cold seep sediments: Interactions of fauna with flow, chemistry, and microbes. *Oceanography and Marine Biology: An Annual Review* **43**: 1–46.

Lloyd, K.G. et al. (2011) Environmental evidence for net methane production and oxidation in putative ANaerobic MEthanotrophic (ANME) archaea. *Environmental Microbiology* **13**: 2548–2564.

Lloyd, K.G. et al. (2010) Spatial structure and activity of sedimentary microbial communities underlying a Beggiatoa spp. mat in a Gulf of Mexico hydrocarbon seep. *PLoS One* **5**: e8738.

Lösekann, T. et al. (2007) Diversity and Abundance of Aerobic and Anaerobic Methane Oxidizers at the Haakon Mosby Mud Volcano, Barents Sea. *Applied and Environmental Microbiology* **73**: 3348–3362.

Lozupone, C. et al. (2011) UniFrac: an effective distance metric for microbial community comparison. *The ISME journal* **5**: 169.

Lozupone, C.A. et al. (2007) Quantitative and qualitative β diversity measures lead to different insights into factors that structure microbial communities. *Applied and environmental microbiology* **73**: 1576–1585.

Ludwig, W. et al. (2004) ARB: a software environment for sequence data. *Nucleic acids research* **32**: 1363–1371.

Luff, R. et al. (2004) Numerical modeling of carbonate crust formation at cold vent sites: significance for fluid and methane budgets and chemosynthetic biological communities. *Earth and Planetary Science Letters* **221**: 337–353.

Lysnes, K. et al. (2004) Microbial community diversity in seafloor basalt from the Arctic spreading ridges. *FEMS Microbiology Ecology* **50**: 213–230.

Marlow, J.J. et al. (2014) Carbonate-hosted methanotrophy represents an unrecognized methane sink in the deep sea. Nature Communications **5**.

Mason, O.U. et al. (2007) The phylogeny of endolithic microbes associated with marine basalts. *Environmental Microbiology* **9**: 2539–2550.

Massana, R. et al. (1997) Vertical distribution and phylogenetic characterization of marine planktonic Archaea in the Santa Barbara Channel. *Applied and Environmental Microbiology* **63**: 50–56.

Meister, P. et al. (2011) Dolomite formation within the methanogenic zone induced by tectonically driven fluids in the Peru accretionary prism. *Geology* **39**: 563–566.

Meyerdierks, A. et al. (2005) Insights into the genomes of archaea mediating the anaerobic oxidation of methane. *Environmental Microbiology* **7**: 1937–1951.

Mills, H.J. et al. (2005) Characterization of microbial community structure in Gulf of Mexico gas hydrates: comparative analysis of DNA-and RNA-derived clone libraries. *Applied and Environmental Microbiology* **71**: 3235–3247.

Milucka, J. et al. (2012) Zero-valent sulphur is a key intermediate in marine methane oxidation. *Nature* **491**: 541–546.

Naehr, T.H. et al. (2007) Authigenic carbonate formation at hydrocarbon seeps in continental margin sediments: A comparative study. *Deep Sea Research Part II: Topical Studies in Oceanography* **54**: 1268–1291.

Nauhaus, K. et al. (2005) Environmental regulation of the anaerobic oxidation of methane: a comparison of ANME-I and ANME-II communities. *Environmental Microbiology* **7**: 98–106.

Nauhaus, K. et al. (2002) In vitro demonstration of anaerobic oxidation of methane coupled to sulphate reduction in sediment from a marine gas hydrate area. *Environmental Microbiology* **4**: 296–305.

Nicol, G.W. and Schleper, C. (2006) Ammonia-oxidising Crenarchaeota: important players in the nitrogen cycle? *Trends in Microbiology* **14**: 207–212.

Niemann, H. et al. (2013) Methane-carbon flow into the benthic food web at cold seeps–a case study from the Costa Rica subduction zone. *PloS one* **8**: e74894.

Op den Camp, H.J.M. et al. (2009) Environmental, genomic and taxonomic perspectives on methanotrophic Verrucomicrobia. *Environmental Microbiology Reports* **1**: 293–306.

Orcutt, B.N. et al. (2011) Microbial Ecology of the Dark Ocean above, at, and below the Seafloor. *Microbiology and Molecular Biology Reviews* **75**: 361–422.

Orphan, V.J. et al. (2001) Comparative Analysis of Methane-Oxidizing Archaea and Sulfate-Reducing Bacteria in Anoxic Marine Sediments. *Applied and Environmental Microbiology* **67**: 1922–1934.

Orphan, V.J. et al. (2004) Geological, geochemical, and microbiological heterogeneity of the seafloor around methane vents in the Eel River Basin, offshore California. *Chemical Geology* **205**: 265–289.

Orphan, V.J. et al. (2001) Methane-Consuming Archaea Revealed by Directly Coupled Isotopic and Phylogenetic Analysis. *Science* **293**: 484–487.

Orphan, V.J. et al. (2002) Multiple archaeal groups mediate methane oxidation in anoxic cold seep sediments. *Proceedings of the National Academy of Sciences* **99**: 7663–7668.

Paull, C. et al. (1991) Seawater circulation through the flank of the Florida Platform: evidence and implications. *Marine geology* **102**: 265–279.

Pernthaler, A. et al. (2008) Diverse syntrophic partnerships from deep-sea methane vents revealed by direct cell capture and metagenomics. *Proceedings of the National Academy of Sciences* **105**: 7052–7057.

Reeburgh, W.S. (2007) Oceanic Methane Biogeochemistry. *Chem. Rev.* **107**: 486–513.

Reeburgh, W.S. (1983) Rates of biogeochemical processes in anoxic sediments. *Annual Review of Earth and Planetary Sciences* **11**: 269–298.

Reitner, J et al. (2005) Concretionary methane-seep carbonates and associated microbial communities in Black Sea sediments. *Palaeogeography, Palaeoclimatology, Palaeoecology* **227**: 18–30.

Roalkvam, I. et al. (2011) New insight into stratification of anaerobic methanotrophs in cold seep sediments. *FEMS Microbiology Ecology* **78**: 233–243.

Rossel, P.E. et al. (2011) Factors controlling the distribution of anaerobic methanotrophic communities in marine environments: Evidence from intact polar membrane lipids. *Geochimica et Cosmochimica Acta* **75**: 164–184.

Santelli, C.M. et al. (2008) Abundance and diversity of microbial life in ocean crust. *Nature* **453**: 653–656.

Santelli, C.M. et al. (2009) The diversity and abundance of bacteria inhabiting seafloor lavas positively correlate with rock alteration. *Environmental Microbiology* **11**: 86–98.

Savard, M.M. et al. (1996) Significance of aragonite cements around Cretaceous marine methane seeps. *Journal of Sedimentary Research* **66**:

Schauer, R. et al. (2009) Bacterial diversity and biogeography in deep-sea surface sediments of the South Atlantic Ocean. *ISME J* **4**: 159–170.

Schloss, P.D. et al. (2009) Introducing mothur: open-source, platform-independent, community-supported software for describing and comparing microbial communities. *Applied and environmental microbiology* **75**: 7537–7541.

Schreiber, L. et al. (2010) Identification of the dominant sulfate reducing bacterial partner of anaerobic methanotrophs of the ANME 2 clade. *Environmental microbiology* **12**: 2327–2340.

Sheik, C.S. et al. (2014) Metabolic flexibility of enigmatic SAR324 revealed through metagenomics and metatranscriptomics. *Environmental Microbiology* **16**: 304–317.

Stadnitskaia, A. et al. (2005) Biomarker and 16S rDNA evidence for anaerobic oxidation of methane and related carbonate precipitation in deep-sea mud volcanoes of the Sorokin Trough, Black Sea. *Marine Geology* **217**: 67–96.

Stadnitskaia, A. et al. (2008) Extended hydroxyarchaeol, a novel lipid biomarker for anaerobic methanotrophy in cold seepage habitats. *Organic Geochemistry* **39**: 1007–1014.

Steinhaus, H. (1999) Mathematical snapshots Courier Dover Publications.

Suess, E. et al. (1999) Gas hydrate destabilization: enhanced dewatering, benthic material turnover and large methane plumes at the Cascadia convergent margin. *Earth and Planetary Science Letters* **170**: 1–15.

Swan, B.K. et al. (2011) Potential for Chemolithoautotrophy Among Ubiquitous Bacteria Lineages in the Dark Ocean. *Science* **333**: 1296–1300.

Tavormina, P.L. et al. (2010) Distributions of putative aerobic methanotrophs in diverse pelagic marine environments. *The ISME journal* **4**: 700–710.

Tavormina, P.L. et al. (2008) Planktonic and sediment-associated aerobic methanotrophs in two seep systems along the North American margin. *Applied and environmental microbiology* **74**: 3985–3995.

Teichert, B. et al. (2005) Chemoherms on Hydrate Ridge—Unique microbially-mediated carbonate build-ups growing into the water column. *Palaeogeography, Palaeoclimatology, Palaeoecology* **227**: 67–85.

Tennant, C. and Berger, R. (1957) X-ray determination of dolomite-calcite ratio of a carbonate rock. *American Mineralogist* **42**: 23–29.

Teske, A. et al. (2002) Microbial Diversity of Hydrothermal Sediments in the Guaymas Basin: Evidence for Anaerobic Methanotrophic Communities. *Applied and Environmental Microbiology* **68**: 1994–2007.

Thamdrup, B. and Dalsgaard, T. (2002) Production of N2 through Anaerobic Ammonium Oxidation Coupled to Nitrate Reduction in Marine Sediments. *Applied and Environmental Microbiology* **68**: 1312–1318.

Thurber, A.R. et al. (2012) Archaea in metazoan diets: implications for food webs and biogeochemical cycling. *ISME J* **6**: 1602–1612.

Toner, B.M. et al. (2012) Mineralogy Drives Bacterial Biogeography of Hydrothermally Inactive Seafloor Sulfide Deposits. *Geomicrobiology Journal* **30**: 313–326.

Treude, T. et al. (2003) Anaerobic oxidation of methane above gas hydrates at Hydrate Ridge, NE Pacific Ocean. *Mar Ecol Prog Ser* **264**: 1–14.

Treude, T. et al. (2007) Consumption of Methane and CO2 by Methanotrophic Microbial Mats from Gas Seeps of the Anoxic Black Sea. *Applied and Environmental Microbiology* **73**: 2271–2283.

Tryon, M.. et al. (2002) Fluid and chemical flux in and out of sediments hosting methane hydrate deposits on Hydrate Ridge, OR, II: Hydrological processes. *Earth and Planetary Science Letters* **201**: 541–557.

Turich, C. and Freeman, K.H. (2011) Archaeal lipids record paleosalinity in hypersaline systems. *Organic Geochemistry* **42**: 1147–1157.

Ussler III, W. and Paull, C.K. (2008) Rates of anaerobic oxidation of methane and authigenic carbonate mineralization in methane-rich deep-sea sediments inferred from models and geochemical profiles. *Earth and Planetary Science Letters* **266**: 271–287.

Vestal, J.R. and White, D.C. (1989) Lipid Analysis in Microbial Ecology. *BioScience* **39**: 535–541.

Vetriani, C. et al. (1999) Population Structure and Phylogenetic Characterization of Marine Benthic Archaea in Deep-Sea Sediments. *Applied and Environmental Microbiology* **65**: 4375–4384.

Watanabe, Y. et al. (2008) U–Th dating of carbonate nodules from methane seeps off Joetsu, Eastern Margin of Japan Sea. *Earth and Planetary Science Letters* **272**: 89–96.

Yamamoto, M. et al. (2010) Molecular characterization of inorganic sulfur-compound metabolism in the deep-sea epsilonproteobacterium Sulfurovum sp. NBC37-1. *Environmental Microbiology* **12**: 1144–1153.

Yanagawa, K. et al. (2011) Niche Separation of Methanotrophic Archaea (ANME-1 and -2) in Methane-Seep Sediments of the Eastern Japan Sea Offshore Joetsu. *Geomicrobiology Journal* **28**: 118–129.

Zhang, F. et al. (2010) A relationship between d104 value and composition in the calcite-disordered dolomite solid-solution series. *American Mineralogist* **95**: 1650–1656.

*C h a p t e r  4*

# STABLE ISOTOPE PROBING METAPROTEOMICS REVEALS DYNAMIC METABOLISM AT MARINE METHANE SEEPS

Jeffrey J. Marlow[1], Connor T. Skennerton[1], Zhou Li[2], Chongle Pan[2], Karuna Chourey[2], Robert Hettich[2], Victoria J. Orphan[1]

[1]Division of Geological and Planetary Sciences, California Institute of Technology
[2]Organic and Biological Mass Spectrometry Group, Oak Ridge National Laboratory

## Introduction

Marine methane seep sediments harbor complex microbial communities that play significant roles in the global carbon and sulfur biogeochemical cycles (1, 2). Studies of these features have predominately focused on biodiversity (e.g., 3–5), the energetic and biochemical basis of syntrophic partnerships (6, 7), and ecosystem-wide contributions to global methane processing (1). Such studies revealed that one of the dominant metabolisms at seep sites – the anaerobic oxidation of methane (AOM) – is enacted by consortia of anaerobic methanotrophs (ANME) most closely related to methanogens and sulfate-reducing deltaproteobacteria. In pursuit of more detailed answers to questions of constituent identity, function, and activity, phylogenetically-linked measures of anabolic activity and growth using stable isotope probing have identified intricately coupled microbial metabolisms (8–10), while metagenomics and metatranscriptomics studies have pointed to metabolic potential and associated biochemical pathways (4, 11–14). Proteomic stable isotope probing (SIP) can couple these experimental objectives by offering both a functionally- and phylogenetically-constrained enzymatic profile of constituent organisms as well as a temporal reporter of protein synthesis and metabolic response to distinct conditions (15–17).

Microbial communities in energy-limited environments, including anoxic methane seep sediments and an array of subsurface habitats, are particularly recalcitrant to activity-based analyses due to slow growth rates. Radiotracers are sensitive to rates on the order of $10^{-19}$ to $10^{-16}$ mol cell$^{-1}$ day$^{-1}$ (18), but the range of discoverable metabolic reactions is severely constrained. Fluorescence *in situ* hybridization (FISH) coupled with nanoscale secondary ion mass spectrometry (nanoSIMS; e.g., 19) can detect assimilation rates as low

as $10^{-17}$ mol $cell^{-1}$ $day^{-1}$ (20) and visualize phylogenetically constrained spatial associations, though experimental throughput is low and only assimilatory processes can be queried. Whole-cell bioorthogonal non-canonical amino acid tagging (BONCAT) coupled with FISH can be used to fluorescently visualize microorganisms active in protein synthesis (21), but identification of specific proteins involves additional steps that require further development in environmental systems. Proteomic SIP represents an important entry in the analysis of metabolic activity in low-energy microbial systems, due to its spatially broad, yet functionally- and phylogenetically-specific search space. The procedure is able to identify particular metabolic pathways or enzyme-mediated responses (17, 22) that can be integrated across constituents of a particular lineage, accessing a segment of the low-activity biosphere that would go undetected by other methods due to low levels of anabolism by individual organisms. Although challenges remain – particularly surrounding protein extraction, peptide quantification, and the interpretation of non-detections – proteomic SIP offers the most direct assessment of *in vivo* activity and catalytic function of microbial communities.

Culture-independent studies of energy-limited methane seep settings have included meta-omics investigations focused largely on the pathway responsible for AOM. Metagenomic fosmid libraries identified all of the methanogenesis pathway genes, with the exception of the methylenetetrahydromethanopterin reductase (*mer*) gene and some subunits of other enzymes in ANME genomes, bolstering the case for the "reverse methanogenesis" metabolism (11, 12). Recent metagenomic sequencing efforts have expanded on the diversity of sequenced ANME lineages, with three draft genomes currently available from distinct clades (ANME-1, ANME-2a and ANME-2d). ANME-1

draft genomes and fosmids lack the *mer* gene (11, 13) and have prompted the proposition of a reverse-methanogenesis bypass, while the ANME-2a (14) and nitrate-reducing ANME-2d (23) genomes, as well as a magnetic enrichment of ANME-2c consortia (4), contained the *mer* gene. Corresponding gene expression profiles revealed ANME-1 methylenetetrahydromethanopterin dehydrogenase (*mtd*), heterodisulfide reductase subunits A and B (*hdrAB*), and methyl-coenzyme M reductase subunit A (*mcrA*) transcripts (11); ANME-2a and ANME-2d exhibited highly expressed methyl-tetrahydromethanopterin coenzyme M methyltransferase (*mtr*), *mcr*, and methenyltetrahydromethanopterin cyclohydrolase (*mch*) transcripts and substantially lower levels of *mtd* and several formylmethanofuran dehydrogenase (*fmd*) subunits (14, 23).

Proteomic SIP enables the identification of isotopically enriched proteins synthesized by a community after incubation with an isotopically labeled substrate (e.g. $^{15}$N-ammonium). The application of proteomic SIP to slow growing methane seep microbial communities offers an opportunity to examine production patterns of reverse methanogenesis enzymes central to ANME-facilitated methane-oxidation, as well as to identify the proteins expressed by syntrophic bacterial partners and other organisms within the seep ecosystem. This approach can highlight metabolic shifts resulting from incubation conditions, reveal the fraction of proteins that are newly synthesized, and facilitate the construction of a framework for interspecies metabolic relationships (24, 25). The greatest insights from environmental metaproteomic studies to date have been associated with time-resolved analyses of low-complexity microbial systems (i.e., acid mine drainage microbial mats; 26), while similar efforts with sponge symbionts (27), sinking marine particulates (28), and the human gut (29, 30) have clarified interspecies relationships and dominant

biogeochemical functionalities. There have been comparatively few studies applying proteomics to methane seep ecosystems; these have focused on individual enzymes (31), explored specific biochemical questions (32), or achieved relatively low coverage of the full ecosystem (13). This work moves beyond previous efforts by exploring multiple methane seep sediments containing diverse ANME and bacterial lineages and exhibiting a range of methanotrophic activity levels. Protein-based $^{15}$N-SIP analysis offers a novel dimension of functional and activity-based insight for these low-energy and biogeochemically important ecosystems.

**Methods**

*Sample Collection*

Seafloor sediment was collected from actively seeping sites at Hydrate Ridge, Oregon, an area that has served as a natural laboratory for the study of AOM (Suess et al. 1999; Tryon et al. 2002; Treude et al. 2003; Boetius & Suess 2004; Marlow et al. 2014). Field campaigns included R/V *Atlantis* leg AT-15-68 with the *DSV Alvin* (August 2010) and *Atlantis* leg AT-18-10 with the *ROV Jason* (September 2011). Samples are referenced according to unique four-digit serial numbers. Push core 16 from *Alvin* dive 4635 at Hydrate Ridge South recovered 12 cm of sediment and was divided into an upper half (sample #3730, used to generate metagenomic data) and a lower half (#3731, used for metaproteomic and SIMS-based analyses). #5133 and #5579 refer to elevator 3A push cores 47 and 41, respectively, collected at Hydrate Ridge North during *Jason* dive J2-593 from an area of active seepage marked by bubble ebullition and surface expression of white microbial mat. #5133 recovered 9 cm of sediment, with a dark sulfidic zone at ~4-5 cm

depth; #5579 contained 12 cm of sediment. Site details and shipboard processing information are provided in Appendix 4.

*Laboratory-based Incubations*

In advance of experimental set-up, sediment slurry was reconstituted under anoxic conditions using 0.22 μm filtered, anoxic $N_2$-sparged Hydrate Ridge bottom water (at a 1:2 sediment : bottom water ratio by volume) and maintained under a 30 psi $CH_4$ headspace for one month. $NH_4^+$ concentrations of filtered bottom water were 496 μM, as measured with a Dionex DX-500 Ion Chromatograph based on the protocol specified in Green-Saxena et al. (2014). Incubations destined for proteomics analysis were taken from this bulk bottle; four incubations were set up, corresponding to two sediment samples (#3731 and #5133), each receiving two experimental treatments. Compared with *in situ* seafloor sediment, these incubations allowed for rapid sample processing and a minimized risk of proteome perturbation during sampling procedures. 60 mL of #3731 slurry was placed in each of two 120 mL serum bottles and supplemented with 1 mM of either $^{14}NH_4Cl$ or $^{15}NH_4Cl$. The vials were sealed with butyl rubber stoppers, flushed for five minutes each with Ar and then $CH_4$, and overpressured with $CH_4$ to a final pressure of 30 psi. #5133 $^{14}NH_4^+$ and $^{15}NH_4^+$ experiments were set up in the same manner, with the exception that the serum bottles were 35 mL and initial slurry volumes were 20 mL. All samples were kept at 4 °C until sampling.

*16S rRNA Gene Tag Sequencing*

Microbial communities were profiled using the 515f (5'-GTGYCAGCMGCCGCGGTAA-3') and 806r (5'-GGACTACNVGGGTWTCTAAT-3') primer pair. Amplicons were sequenced on the Illumina MiSeq platform (Laragen Inc.,

Culver City, CA) generating paired 250bp reads which were analyzed using Qiime 1.8 (Caporaso et al. 2010). Taxonomy was assigned to each OTU representative using the SILVA 115 rRNA database using uclust. The full iTAG processing protocol is provided in Appendix 4.

*Metagenome Database Construction*

The metagenomic database against which mass spectra were referenced to identify proteins was constructed from several sources (Table S4.1). Metagenomes were sequenced from bulk sediment and from magneto-FISH experiments from Hydrate Ridge (Pernthaler et al. 2008; Dekas et al. 2009; Glass et al. 2014). Bulk sediment metagenomes from samples #3730, #5133 and #5579 were sequenced using the Illumina HiSeq platform; four magneto-FISH metagenomes (targeting ANME-2c) were sequenced using 454 GS-20 (BC02, Pernthaler et al. 2008), 454 GS-FLX (BC03), and 454 GS-Titanium (BC04 and BC05). Details of the processing and annotation protocols are specified in Appendix 4.

*Metaproteomic Sampling and Analysis*

Sample #3731 incubations were sampled after 17 days ($T_{17d}$) and 326 days ($T_{326d}$) of incubation with methane; #5133 was sampled only once, after 160 days ($T_{160d}$). At the designated sampling times, 20 mL (#3731) or 5 mL (#5133, small volume due to sample limitation) of sediment slurry was flash frozen with liquid nitrogen to stop biological reactions and preserve the proteomes representative of the incubation conditions. Proteins were extracted and digested using an SDS-TCA-based protocol, and peptides were separated by liquid chromatography as outlined in Chourey et al., (2010) and described in Appendix 4. A range of Orbitrap instruments was used for peptide selection, fragmentation,

and mass analysis, in accordance with the best available technology at the time of experimentation (see Appendix 4).

MS/MS data was searched using the Sipros / ProRata 3.0 program (Wang et al. 2013) and the customized metagenomic database specified in Table S4.1. A 1% false detection rate at the peptide level was used, and protein identification and analysis utilized 2 total peptide and 1 unique peptide search parameters (expressed with the notation 2TP, 1UP) as well as a 1% false positive detection rate (FDR), 1TP, 1UP requirement. PTMs associated with the McrA protein were evaluated as described in Li et al. (2014). Further details on data processing can be found in Appendix 4.

A smaller database constructed of all ORFs identified during the initial non-SIP 1TP, 1UP analyses (22,312 ORFs) was used for SIP searches due to computational limitations. Because protein identification is predicated on the detection of constituent peptides, and because 1TP, 1UP identifications were considered in the analysis, designations of "enriched" proteins (defined as proteins that contain $^{15}N$ with statistical confidence) must be made at the peptide level. This value was set at 5% $^{15}N$ – the same enrichment level has been used as a threshold in other SIP studies (Justice et al. 2012; Pan et al. 2011) – after consideration of multiple factors (see Appendix 4).

**Results & Discussion**

***Microcosm Activity and Community Composition***

Two aliquots of Hydrate Ridge sediment (hereafter referred to as #3731 and #5133) were each allocated into two methane-infused microcosm incubations, amended with either $^{14}NH_4^+$ (unlabeled treatment) or $^{15}NH_4^+$ (labeled treatment). Cell aggregate abundance and sulfide concentrations, both of which correlate positively with AOM activity (Iversen &

Jorgensen 1985; Nauhaus et al. 2002), were monitored throughout the incubation period (Table S4.2). Aggregate abundances in the #5133 incubations increased slightly during the 160-day experiment, while counts in #3731 samples started lower and decreased during the 326-day period. #5133 sulfide concentrations increased from a mean of 1.112 mM after 6 days to a mean of 16.093 mM at $T_{160d}$, while those of sample #3731 increased from 0.874 mM to a mean value of 3.61 mM at $T_{326d}$.

Microbial communities were analyzed using 16S rDNA sequencing to compare the changes between the two time points of #3731 and between sediment #3731 and #5133. Across all three samples, the most abundant representatives were deltaproteobacterial SEEP-SRB1 (accounting for 7.2% of sequences on average, +/- 0.75% SE) and SEEP-SRB2 (5.1% +/- 0.98% SE), epsilonproteobacterial *Sulfurovum* (6.7% +/- 1.6% SE), and methanomicrobial ANME-1a (6% +/- 1.5% SE) and ANME-1b (5% +/- 0.75% SE). The community in sediment #3731 was relatively stable between $T_{0d}$ and $T_{326d}$ (Supplementary Data File 4.1a). When the sequenced #5133 community was compared with that from #3731 $T_{326d}$, *Sulfurovum* (+5.6%), ANME-1a (-4.9%), SEEP-SRB2 (-3.1%), and *Flavobacteriaceae* (+3.0%) OTUs accounted for the most substantial differences in relative abundance. These distinctions suggest that the nature of the inoculum plays a role in subsequent community structure, as both *Sulfurovum* and *Flavobacteriaceae* were likely more prevalent in the shallow sediment horizons of #5133. In all three samples, large relative abundance ratios of ANME to methanogen lineages were observed (#3731 $T_{0d}$: 918; #3731 $T_{326d}$: 579; #5133 $T_{170d}$: 419, Supplementary Data File 4.1b), suggesting that the vast majority of archaeal proteins of unspecified lineage – and reverse methanogenesis enzymes in particular – likely derive from ANME representatives.

***Peptide and Protein Identifications***

The metaproteomic dataset produced in this study represents the largest known repository of proteins from methane seep sediments. The SIP analyses yielded thousands of peptide identifications at the 1% FDR level (ranging from 16974 to 36365), an average of 7795 (2312 SD) protein identifications under the 1 total peptide, 1 unique peptide (1TP, 1UP) condition, and an average of 2755 (1031 SD) protein identifications under the 2 total peptides, 1 unique peptide (2TP, 1UP) condition (see Table 4.1). Compared with most other environmental metaproteomic efforts, more proteins were identified in this effort (Table S4.3), indicating that increased microbial diversity, low overall activity levels, and challenging physicochemical conditions are not insurmountable challenges in SIP-resolved metaproteomic studies.

| Sample | Protein Identifications | |
|---|---|---|
| | 2TP 1UP | 1TP 1UP |
| Hydrate Ridge Seep Sediment #3731 $^{14}N$ $T_1$ | 3149 | 8663 |
| Hydrate Ridge Seep Sediment #3731 $^{15}N$ $T_1$ | 3266 | 8747 |
| Hydrate Ridge Seep Sediment #3731 $^{14}N$ $T_2$ | 1688 | 5214 |
| Hydrate Ridge Seep Sediment #3731 $^{15}N$ $T_2$ | 1720 | 5045 |
| Hydrate Ridge Seep Sediment #5133 $^{14}N$ | 4346 | 11080 |
| Hydrate Ridge Seep Sediment #5133 $^{15}N$ | 2360 | 8023 |

Table 4.1: The number of proteins identified in this study.

When all six samples' datasets were combined, 19331 and 7761 unique protein identifications were made, under 1TP, 1UP and 2TP, 1UP conditions, respectively. Of these, roughly half were found in only one sample (8631 1TP, 1UP and 3903 2TP, 1UP), and 994 (1TP, 1UP) and 403 (2TP, 1UP) proteins were detected in all six samples. Of the proteins observed in all samples, the five most common functional categories were were unannotated "hypothetical" proteins (comprising 47.3%, relative abundances averaged

between the search conditions), AprA (4.1%), McrB (3.2%), ATPaseB (2.5%), and McrA (2.4%). Phylogenetic assignments of the cumulative metaproteome demonstrated a higher relative abundance of Bacteria-classified proteins (63.6% 1TP, 1UP; 57.7% 2TP, 1UP) than those assigned to Archaea (34.1% 1TP, 1UP; 39.7% 2TP, 1UP).

***SIP Analysis***

The quantification of peptides' $^{15}N$ composition allows for the activity-based characterization of protein production on functionally constrained, and phylogenetically specific levels. The SIP principle has been incorporated into time-resolved functional studies of individual strains in co-cultures (e.g., Jehmlich et al. 2008) as well as model consortia (Taubert et al. 2012; Morris et al. 2012) and low-complexity environmental communities (Justice et al. 2014). For energy-limited organisms with long doubling times such as ANME-SRB aggregates (Nauhaus et al. 2007), SIP metaproteomics is particularly promising, providing a wide view of catabolic response (Taubert et al. 2011) that is not strongly dependent on cell-integrated anabolism. In parallel with proteomics-based $^{15}N$ enrichment analyses, nanoSIMS examinations of bulk protein extract and ANME-SRB consortia were used to provide an independent measure of amino acid and cell associated $^{15}N$ enrichment of each incubation.

Sample #3731 exhibited a small but detectable isotopic enrichment of its protein pool during the 326-day incubation period. The $^{15}N$ atom % enrichment of the entire #3731 $^{15}N$ peptide pool was 0.44% at $T_{17d}$, increasing to 0.78% at $T_{326d}$. The corresponding values of the control incubations that were provided $^{14}NH_4^+$ were 0.45% and 0.35%, respectively. Sediment bulk protein extracts were measured on the nanoSIMS, yielding 0.45 atom %

enrichment at $T_{17d}$ and 0.53 atom % at $T_{326d}$; both #3731 $^{14}N$ samples were measured at 0.38 atom % (Table 4.2).

Peptides recovered from sample #5133 $^{15}N$ after 160 days of incubation demonstrated an isotopic enrichment of 9.49 atom % $^{15}N$, while peptides from the corresponding $^{14}NH_4^+$ control were enriched to 0.49%. NanoSIMS analysis of ANME-SRB aggregates from the same sample showed substantially higher $^{15}N$ incorporation levels, reaching 23.76% after 64 days (Table 4.2).

| Peptide LC MS/MS Analysis | | | |
|---|---|---|---|
| Sample ID | Incubation Time (d) | $^{15}N$ Atom % Mean (SE) | % of Enriched Peptides (>5% $^{15}N$) |
| #3731 $^{14}N$ $T_1$ | 17 | 0.45 (0.03) | 0.44 (0.03) |
| #3731 $^{15}N$ $T_1$ | 17 | 0.44 (0.01) | 0.52 (0.07) |
| #3731 $^{14}N$ $T_2$ | 326 | 0.35 (0.09) | 0.62 (0.07) |
| #3731 $^{15}N$ $T_2$ | 326 | 0.78 (0.04) | 1.48 (0.04) |
| #5133 $^{14}N$ $T_1$ | 160 | 0.49 (<0.01) | 0.87 (0.03) |
| #5133 $^{15}N$ $T_2$ | 160 | 9.49 (0.38) | 18.06 (0.68) |

| SIMS Bulk Protein Extract Analysis | | |
|---|---|---|
| Sample ID | Incubation Time (d) | $^{15}N$ Atom % Mean (SE) |
| #3731 $^{14}N$ $T_1$ | 17 | 0.38 (0) |
| #3731 $^{15}N$ $T_1$ | 17 | 0.45 ($5x10^{-5}$) |
| #3731 $^{14}N$ $T_2$ | 326 | 0.38 (0) |
| #3731 $^{15}N$ $T_2$ | 326 | 0.53 ($5x10^{-5}$) |

| nanoSIMS Whole Aggregate Analysis | | |
|---|---|---|
| Sample ID | Incubation Time (d) | $^{15}N$ Atom % |
| #5133 $^{15}N$ | 6 | 0.366 |
| #5133 $^{15}N$ | 20 | 7.48 |
| #5133 $^{15}N$ | 64 | 23.76 |
| *Clostridia* spores | NA | 0.36 |

Table 4.2: $^{15}N$ enrichment values of proteome-derived peptides, bulk protein extract, and whole aggregates.

The peptide-based enrichment value likely provides a more representative constraint on community-wide anabolic rates, despite the under-representation of membrane-bound proteins (Chourey et al. 2010; Trötschel & Poetsch 2015), because ANME-SRB constituents constitute a particularly active subset of the community. When the peptide enrichments were parsed by phylogenetic affiliation, those that uniquely mapped to ANME had a mean $^{15}N$ value of 13.8%, while those attributed to the most significant contributor to sulfate reduction (*Desulfobacterales*) had a mean enrichment value of 10.1%. Proteins involved in the reverse methanogenesis pathway had a mean enrichment of 18.3%, whereas proteins of the dissimilatory sulfate reducing pathway exhibited a mean enrichment of 9.3%. These values suggest that ANME responded to incubation conditions with heightened biosynthetic activity compared to their putative SRB partners, and that a higher proportion of reverse methanogenesis enzymes were newly synthesized compared to all ANME proteins.

The observation of enhanced $^{15}N$ incorporation in nanoSIMS analysis implies that a non-protein or undetected proteinaceous source of cellular nitrogen is more enriched than the ANME- and SRB-specific proteins detected in our analysis. Approximately 68% of a microbial cell's nitrogen pool is incorporated into amino acids; nucleotides (28% of cellular N) or various amines and cell wall components (4%) may exhibit heightened $^{15}N$ enrichment levels, contributing to the observed discrepancy between proteome and nanoSIMS enrichment values (Reitzer 2003). Between 20-30% of prokaryotic proteomes are membrane proteins (Stevens & Arkin 2000), yet this fraction is likely under-represented by approximately half in our analysis (Chourey et al. 2010). Preferential incorporation of $^{15}N$ into membrane proteins, such as receptors, transporters, or oxidoreductases may be

partially responsible for the $^{15}N$ unaccounted for in our SIP metaproteomic analysis. The over-representation of bacterial F-Type ATPases in the #5133 $^{15}N$ enriched fraction (see below) may be representative of biosynthetic investments in membrane-bound energetic machinery by aggregate constituents resulting from incubation conditions.

The observed bimodality of peptide enrichment distributions from both #3731 $^{15}N$ and #5133 $^{15}N$ experiments (Fig. S4.1, Supplementary discussion, Appendix 4) offers insight into protein synthesis and nitrogen-cycling dynamics. A SIP-based study of acid mine drainage biofilms revealed a trimodal distribution of protein enrichments, likely attributable to distinct modes of protein synthesis linked to iron oxidation metabolism (Justice et al. 2014). The presence of two distinct peptide pools in the data presented here implies that most of the detected proteins (peptides with $^{15}N$ values below 5%) were likely synthesized before the addition of $^{15}NH_4^+$ and were not fully degraded, while the remainder was newly synthesized. The lack of peptides with intermediate enrichment values argues against substantial heterotrophic predation on the system's primary producers. Given the slow growth rates of seep-based microorganisms, any signal of mixed amino acid source pools (Kermer et al. 2012), if initiated, would likely remain resolvable, suggesting that the enriched fraction is not exclusively composed of mixed-pool proteins.

***Functional and Phylogenetic Distributions of Enriched Proteins***

Of the 2360 proteins identified from the #5133 $^{15}N$ sample (2TP, 1UP criterion), 704 (29.8%) were enriched. To determine which functional traits or phylogenetic affiliations were disproportionately represented in either the enriched or unenriched protein pools, proteins were partitioned by enzyme type or phylogenetic assignment of the corresponding ORF. The relative abundance of these categories was calculated for both the

enriched and unenriched proteins, and the variance contributed by each bin was determined (calculated by the square of the difference in relative abundances).

18 functional protein types accounted for 79.8% of the variance between enriched and unenriched proteins, with each contributing at least 1% of the variance (Fig. 4.1a). The largest contributor, whose distribution produced 24.8% of the observed variance, was RNA polymerase (RNAP), which was more prominent in the unenriched protein pool. By examining the phylogenetic assignments of RNAP orthologs, the enzyme serves as a representative signal of organism-wide regulation. The relative lack of observed newly produced RNAP proteins could indicate that all transcription needs were met by pre-existing, long-lived copies, or that incubation conditions were deleterious to active transcription and, perhaps, survival; the rare occurrence of enriched proteins from similar phylogenetic groupings suggests that the latter scenario is more probable. In this context, the lineages responding most negatively to incubation conditions include *Pseudomonas*, *Chromatiales*, *Alteromonadales*, *Methylococcales*, and *Sulfurovum* (Fig. 4.1a inset), indicating a shift away from metabolisms amenable to the oxidizing conditions of upper seep sediment layers afforded by overlying seawater and bioturbation.

Of the predominantly enriched protein types, chaperonin GroEL accounts for the most variance (10.9%) between the enriched and unenriched pools, followed by F-type ATPase subunits B (8.4%), and A (6.1%). Most of the enriched occurrences of these proteins were affiliated with *Deltaproteobacteria*. GroEL prevents the formation of low-energy amorphous aggregations (Hartl et al. 2011) and facilitates proper folding of a wide variety of proteins (Kerner et al. 2005). A higher prevalence of deltaproteobacterial GroEL under incubation conditions suggests a general trend toward energy conservation among

these organisms – perhaps investing in the refolding of previously synthesized proteins rather than the generation of new copies; indeed, the chaperonins are commonly implicated in stress response (Kim et al. 2013). One potential source of physiological and energetic stress among sulfate-reducing *Deltaproteobacteria* is the build-up of sulfide in incubation bottles. For the last hundred days of the incubation period, sulfide levels were above 13 mM (Table S4.2), far above the values in porewater collected shipboard from the same push core (1.81 – 5.89 mM). The likely increase in F-type ATPase enzymes during the incubation, as well as bacterial pyrophosphatase PpaC (accounting for 1.4% of variance), also indicates a response to a shifting energetic landscape (Alexandre et al. 2001).

Several high-variance proteins distinguishing the enriched and unenriched pools from sample #5133 $^{15}$N are involved in reverse methanogenesis and sulfate reduction pathways. AprA (5.1%), McrB (3.0%), McrG (2.8%), DsrB (2.4%), McrA (2.1%), MtrA (1.7%), AprB (1.4%), and Sat (1.3%) were all more prevalent in the $^{15}$N enriched fraction, highlighting the importance of sulfate-coupled AOM in seep sediments, particularly under incubation conditions that favored the metabolism. High-variance proteins that were detected at higher levels within the unenriched fraction may reveal metabolic capabilities that were less pressing under incubation conditions. Methyl-accepting chemotaxis proteins (accounting for 1.6% of the variance) may be used in biofilm-linked cell signaling or orientation towards favorable environmental conditions (Morgan et al. 2006); their near-absence in the $^{15}$N-enriched protein pool suggests decreased need for mobility-linked sensing and/or less communication among constituents. Glutamine synthetases (3.0%) were not produced at detectable levels during the experiment; unenriched orthologs were derived from a range of lineages. This protein catalyzes the formation of glutamine from

glutamate and ammonia; its minimal presence among enriched proteins could indicate the accessibility of free glutamine (and likely other amino acids) from biomass degraded during the incubation, or a heightened reaction rate – facilitated by increased $NH_4^+$ concentrations – that did not necessitate new glutamine synthetase production.

15 phylogenetic bins each contributed at least 1% of the variance between enriched and unenriched proteins recovered from #5133 $^{15}N$ when proteins' phylogenetic affiliations were considered (Fig. 4.1b), representing 92.5% of the total variance. Among the more notable differences was the prevalence of enriched proteins linked to methane-metabolizing lineages (accounting for 32.3% of the variance) and *Deltaproteobacteria* (27.7%), particularly orders with known sulfur reducers (18.3%) expressing carbon fixation, sulfate reduction, GroEL, and ribosomal proteins. Proteins attributed to *Epsilonproteobacteria* (20.8%) and especially *Sulfurovum* RNAP, Apr, and ATPase (15.3%) were markedly less prevalent in the enriched pool. The dearth of enriched epsilonproteobacterial protein products is consistent with these organisms' proposed susceptibility to changing conditions (Case et al., in prep), manifested in this case through protein synthesis shut-off. The high relative abundance of *Sulfurovum* from the #5133 tag sequencing data (Supplementary Data File 4.1a) highlights the utility of SIP proteomics: the persistence of 16S rRNA genes is not always reflective of biosynthetically active participants in an environment.

Finally, of the proteins that remained unannotated following secondary search processes (see Appendix 4) 46 (2TP, 1UP) were enriched in the #5133 $^{15}N$ sample and were present in all six sample proteomes. Based on InterPro analysis (Mitchell et al. 2014), five products may be involved in signaling and five others contain transmembrane motifs; the remainder yielded no notable conserved domains. Approximately half of the

unannotated ORFs were attributed to uncultured *Archaea* while most of the remainder were associated with sulfate-reducing *Deltaproteobacteria* (Table S4.4). These 46 uncharacterized proteins likely play important roles in seep sediments under anaerobic methanotrophic conditions and should be prioritized for functional biochemical study.

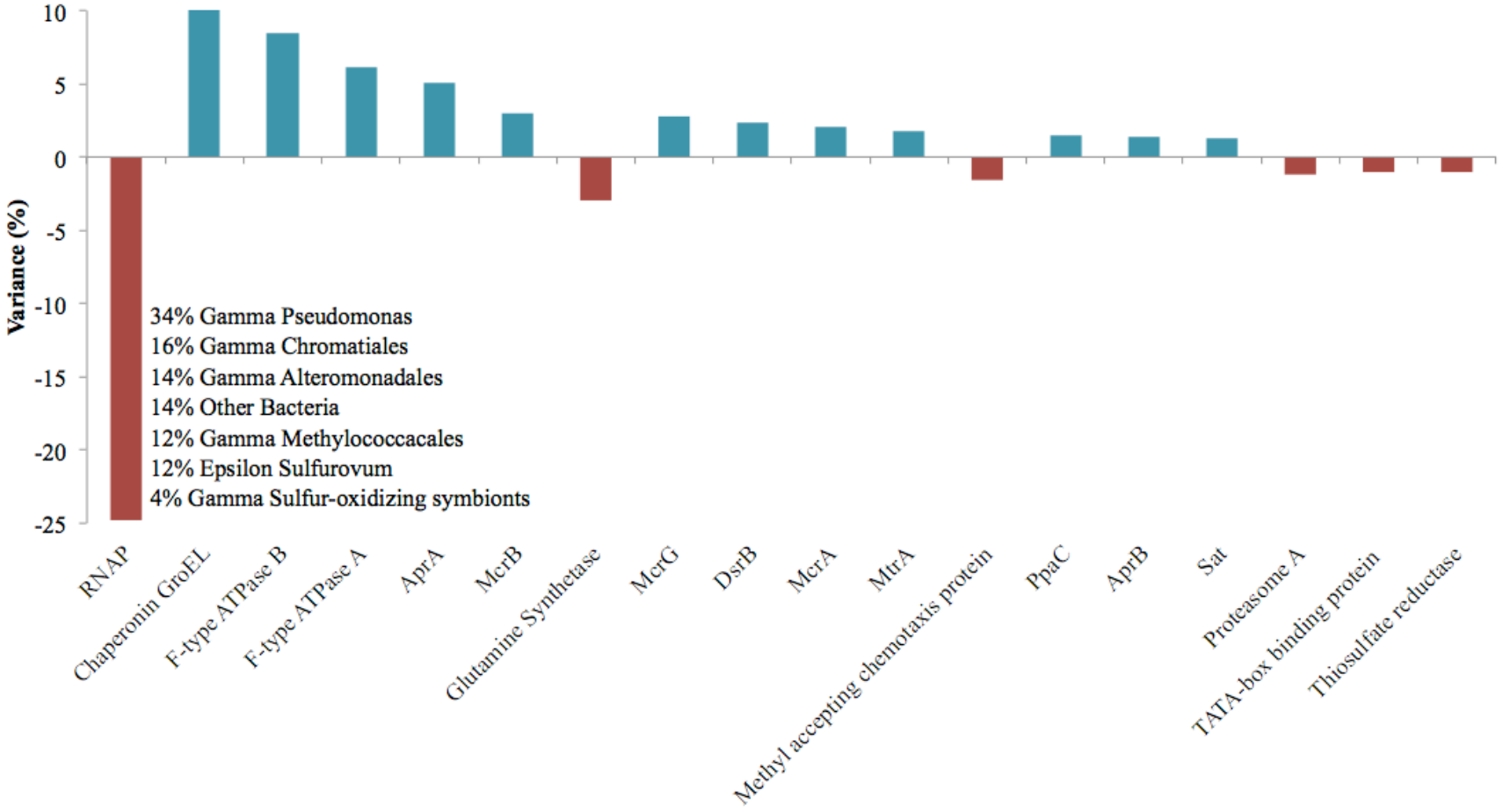


Fig. 4.1a: Protein functional groups accounting for at least 1% of variance between the enriched and unenriched #5133 15N protein pools. Positive values reveal protein types that are more abundant in the enriched fraction; negative values indicate those more prevalent in the unenriched fraction. Inset table shows the phylogenetic affiliations of RNAP proteins.

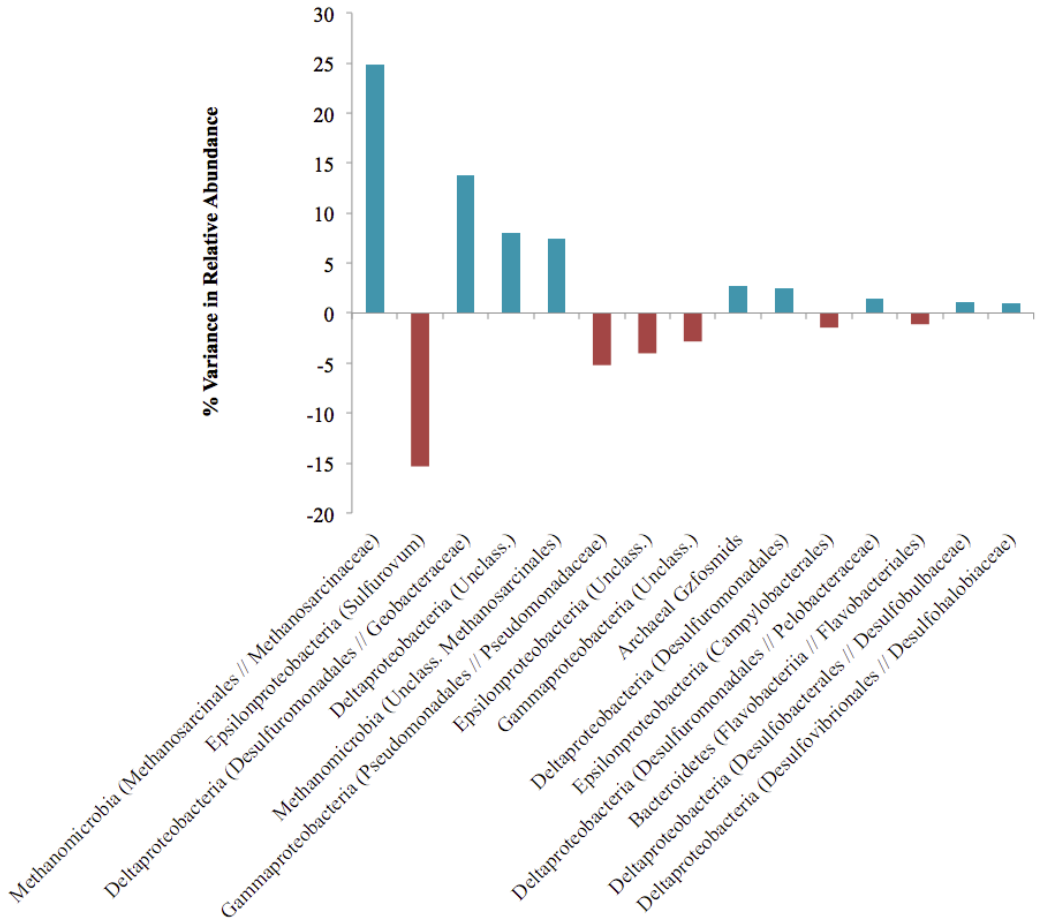


Fig 4.1b) Phylogenetic associations accounting for at least 1% of variance between the enriched and unenriched #5133 15N protein pools. Positive values reveal protein types that are more abundant in the enriched fraction; negative values indicate those more prevalent in the unenriched fraction. Phylogenetic assignments were made at the family level; higher level assignments are provided if no family-level specificity was available, and genus-level assignments are provided if no other genera were observed in the same family.

### *Metabolic Pathways*

#### *Methane Metabolism*

Anaerobic oxidation of methane (AOM) is a dominant metabolism at Hydrate Ridge methane seeps. Components of all enzymes involved in the reverse methanogenesis pathway were recovered from incubated seep sediment, frequently with many distinct orthologs (Fig. 4.2). Methyl-coenzyme M reductase (Mcr) is one of the most abundant enzymes in ANME, accounting for 7% of total extractable proteins from the ANME-1 rich Black Sea mats (Krüger et al. 2003). Across all six proteomic data sets, 10.4% of peptides were attributable to Mcr; within the enriched fraction of the #5133 $^{15}$N sample, 34.6% of unique peptides were assigned to Mcr subunits. Approximately 20 orthologs of each Mcr subunit were identified in the pan-metaproteome, with 48% of the Mcr orthologs present in the metagenomic database detected (20 of 40 McrA, 21 of 43 McrB, 19 of 41 McrG), most of which were present in all six samples. These three catalytic subunits demonstrated substantial ANME-1 representation (accounting for 48.3% of detected orthologs), with smaller contribution of ANME-2a- (20%), Methanosarcinaceae- (13.3%), ANME-2c- (11.7%), and ANME-2b-derived (6.7%) orthologs. The three non-catalytic Mcr components (McrA2, McrC, McrD) were also identified. The precise functions of these components are not well understood, but *in vitro* studies of enzyme extract from the methanogen *M. marburgenesis* suggested that McrC and McrD are electron-donating activating units, while McrA2 acts upstream by donating ATP to McrC (Prakash et al. 2014). These putative (methanogenic) activation domains were less prevalent in the metaproteome: of the nine detected orthologs, only two were associated with ANME genomes, and individual orthologs were detected in approximately half of the samples (on

average 3/6 samples) compared with broader representation of McrA (4.9), McrB (5.6), and McrG (5.0) orthologs. These decreased detection rates may reveal a lower copy number of the McrA2, McrC, and McrD subunits, potentially due to their re-use as activating components, lower turnover rates, or minimized relevance under methanotrophic conditions.

Several previous ANME-targeted meta-omics efforts have sought to reconstruct the reverse methanogenesis pathway (e.g., Hallam et al. 2004; Meyerdierks et al. 2010; Stokke et al. 2012; Haroon et al. 2013; Wang et al. 2014; Table S4.5). Recent ANME-2-focused gene- and transcript-based studies have found evidence of all reverse methanogenesis subunits (Haroon et al. 2013; Wang et al. 2014), but the *mer* gene in particular has proven challenging to identify in studies of ANME-1 rich methane seep environments (Hallam et al. 2004; Meyerdierks et al. 2010; Stokke et al. 2012). In our proteomic experiments, seven Mer orthologs were identified, exhibiting best homology to ANME-2a and unspecified Methanosarcinales lineages; given the large ANME to methanogens relative abundance ratios determined by tag sequencing (Supplementary Data File 4.1b), most of these orthologs of poor homology likely derive from ANME representatives. It remains possible that ANME-1 methane oxidation proceeds via the *mer* bypass (Meyerdierks et al. 2010), whereby activated methane is converted first to methyl-containing intermediates and then to formaldehyde, which is processed to methylene-$H_4$MPT by a formaldehyde-activating enzyme (Fae) and hexulose-6-phosphate (Hps). (The viability of the methanogenic version of this pathway has been demonstrated with an *M. barkeri mer* deletion mutant (Welander & Metcalf 2008)). An ANME-1 *mer* copy has not yet been identified, and 12 orthologs of the Fae/Hps fusion protein were detected across all samples (1TP, 1UP).

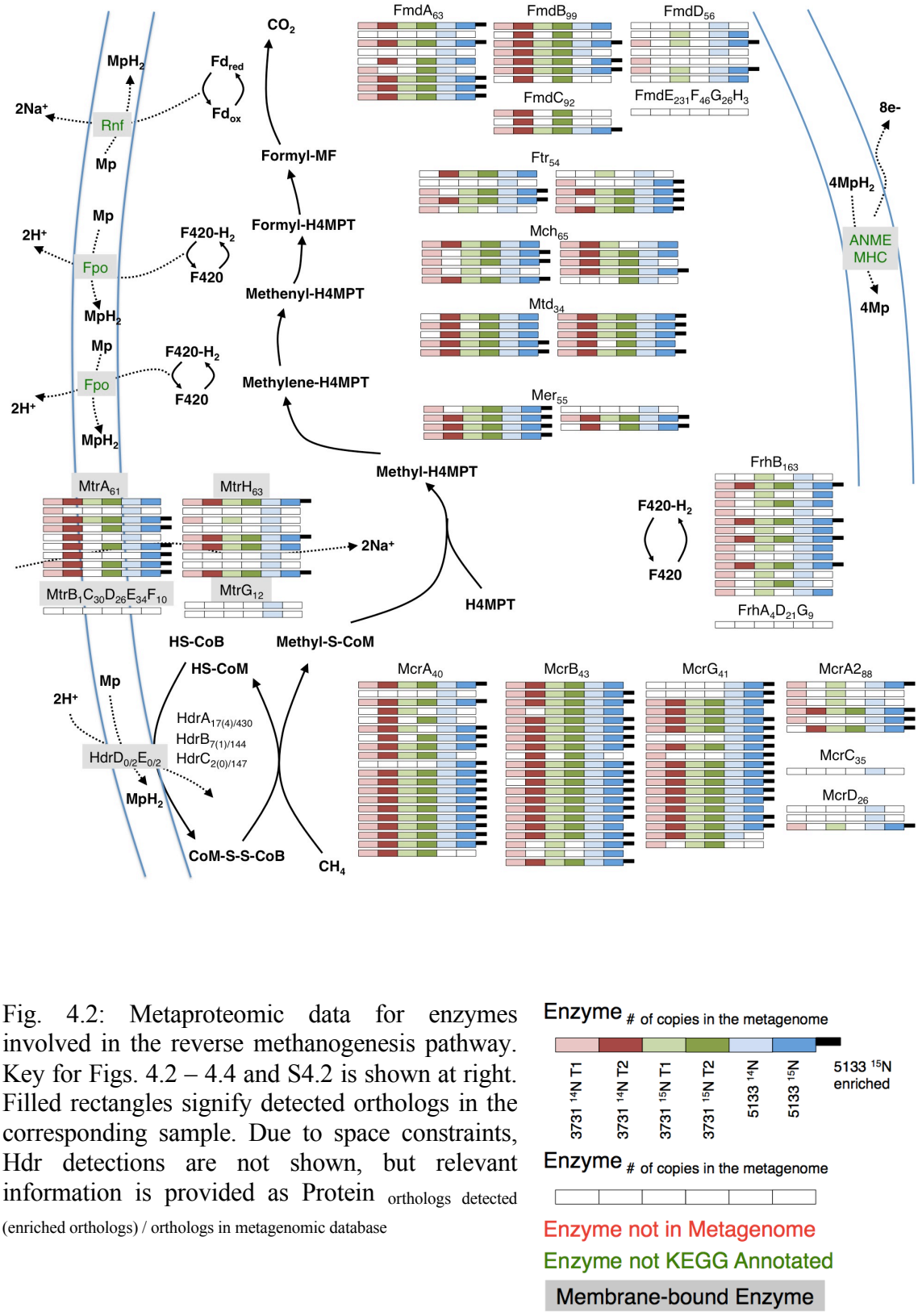


Fig. 4.2: Metaproteomic data for enzymes involved in the reverse methanogenesis pathway. Key for Figs. 4.2 – 4.4 and S4.2 is shown at right. Filled rectangles signify detected orthologs in the corresponding sample. Due to space constraints, Hdr detections are not shown, but relevant information is provided as Protein orthologs detected (enriched orthologs) / orthologs in metagenomic database

Building upon the proteomic dataset generated from the Nyegga seep (Stokke et al. 2012), several other subunits of enzymes putatively involved in reverse methanogenesis were newly detected, including HdrA, HdrC, McrG, McrA2, and McrD (Table S4.5). Of the components not found in the proteome, some of those present in the site-linked metagenomes (MtrBCDEF, HdrDE) are membrane-bound (Thauer et al. 2008) and thus more difficult to quantitatively recover (Trötschel & Poetsch 2015).

*McrA Post Translational Modifications*

To better understand the range of variability found between McrA orthologs and potentially distinguish functionally distinct forms of the enzyme, we conducted a computational search for selected post-translational modifications (PTMs; Li et al. 2014). MS-based PTM analysis has been used to corroborate crystal structure derived modifications (Selmer et al. 2000) and as a discovery tool supplemented by subsequent crystallographic confirmation (Moellering & Cravatt 2013). Spectra from sample #5133 $^{14}$N were used due to its enhanced metabolic activity relative to #3731 (Table S4.2) and unlabeled peptides, which ensured the accuracy of PTM mass windows. Roughly 40% (14/34) of the searchable PTMs were observed among 10 of the 19 McrA orthologs detected in sample #5133 $^{14}$N, 15 of 21 McrB orthologs, and 8 of 18 McrG orthologs. Five McrA2, one McrC, and three McrD orthologs were detected but were PTM-free. Observed modifications included mono-, di-, and tri-methylations, oxidation, beta-methylthiolation, and acetylation (Fig. 4.3), and are primarily found at externally exposed residues. None of these observed PTMs appear to be associated with active-site residues (Shima et al. 2012), potentially due to the apparent preference for unreactive amino acids in this portion of the enzyme to protect against reactive radical intermediates (Ermler et al. 1997).

Previous structural analyses of Mcr orthologs from methanogenic and ANME-1 organisms revealed a range of PTM differences detected by MS analysis of peptides (Kahnt et al. 2007) and a combined MS and crystal structure analysis (Shima et al. 2012; Fig. 4.3). Kahnt et al. (2007) rejected the hypothesis that Mcr PTMs modulate the enzyme's kinetics, and instead proposed protective effects against reaction intermediates and improved binding of reactants in the final step of methanogenesis. In our analysis, the two non-ANME McrA proteins, which show closest homology with cultured *Methanosarcinaceae*, exhibit neither novel PTMs nor previously proposed modifications at His 296 and Gln 448 (Fig. 4.3). Among Mcr subunits attributed to ANME, 51% exhibited at least one PTM; for observed McrA proteins, the average detection rate was 1.8 PTMs per ortholog, with an average of 1 PTM per 84 amino acids. This high rate of occurrence is consistent with previous MS-based analyses of environmental systems: 29% of a dominant constituent's proteins exhibited PTMs in an acid mine drainage biofilm, with distinct modification profiles among closely related organisms (Li et al. 2014). Our account is likely an under-representation of PTM pervasiveness, as many known but less common modifications were not included in the search space (Wang et al. 2013) and others – particularly phosphorylations – may have been under-detected due to incompatible procedural steps (Gilmore et al. 2012; Olsen & Mann 2013).

The low stoichiometry of detected PTMs between orthologs, in addition to their positioning away from active site residues, suggests a dominance of regulatory PTMs (Olsen & Mann 2013). These modifications may influence a wide range of functions, including environmental sensing and intracellular signaling (Ivan et al. 2001), formation and activity of protein complexes (Kovacs et al. 2005), stability and subcellular localization

(Chuikov et al. 2004), and protein folding or degradation (Deribe et al. 2010 and references therein). Methylation, the most common detected McrA modification (Fig. 4.3), has been implicated in stress response (Desrosiers & Tanguay 1988), protein repair (Najbauer et al. 1996), and signal transduction (Aletta et al. 1998). The substantial heterogeneity we observed may be reflective of non-enzymatically induced modifications (Weinert et al. 2013) that may be responsive to and indicative of environmental variation (Olsen et al. 2010).

None of the seven previously proposed PTMs (Kahnt et al. 2007; Shima et al. 2012) were detected in our experiments, though only three of the nine phylogenetically-specified modifications were potentially discoverable based on detected peptides. The lack of correspondence between our PTM observations and earlier reports may be attributable to low coverage or differences between experimental conditions and analytical procedures. However, the detection of abundant and differentially expressed PTMs among McrA orthologs suggests that such modifications are not only common, but are phylogenetically and/or environmentally heterogeneous. Further investigation of the time or condition-specific manifestation of PTMs will be important in future work. Functional traits can be substantially influenced by the expression of such modifications (Moellering & Cravatt 2013) and they may prove informative in distinguishing methanogenic from methanotrophic Mcr *in vivo*.

*Sulfur Metabolism*

The dissimilatory sulfate reduction pathway was well represented in the metaproteomes from all six seep sediment incubation samples (Fig. 4.4). 20 Sat, 41 AprA, 19 AprB, 14 DsrA, and 20 DsrB orthologs were recovered, accounting for 33% of the

potential metagenomic search space among these enzyme subunits. Previous protein-based examinations of sulfate reduction in methane seep environments have demonstrated a full sulfate reduction pathway capability in bulk Black Sea mat extract (Basen et al. 2011) and have localized the enzymatic machinery to ANME-affiliated sulfate SRB via antibody detection (Wrede et al. 2012; Milucka et al. 2013). Proteins comprising the sulfate reduction pathway were recovered from the Nyegga seep, with the exception of AprB and DsrB (Stokke et al. 2012).

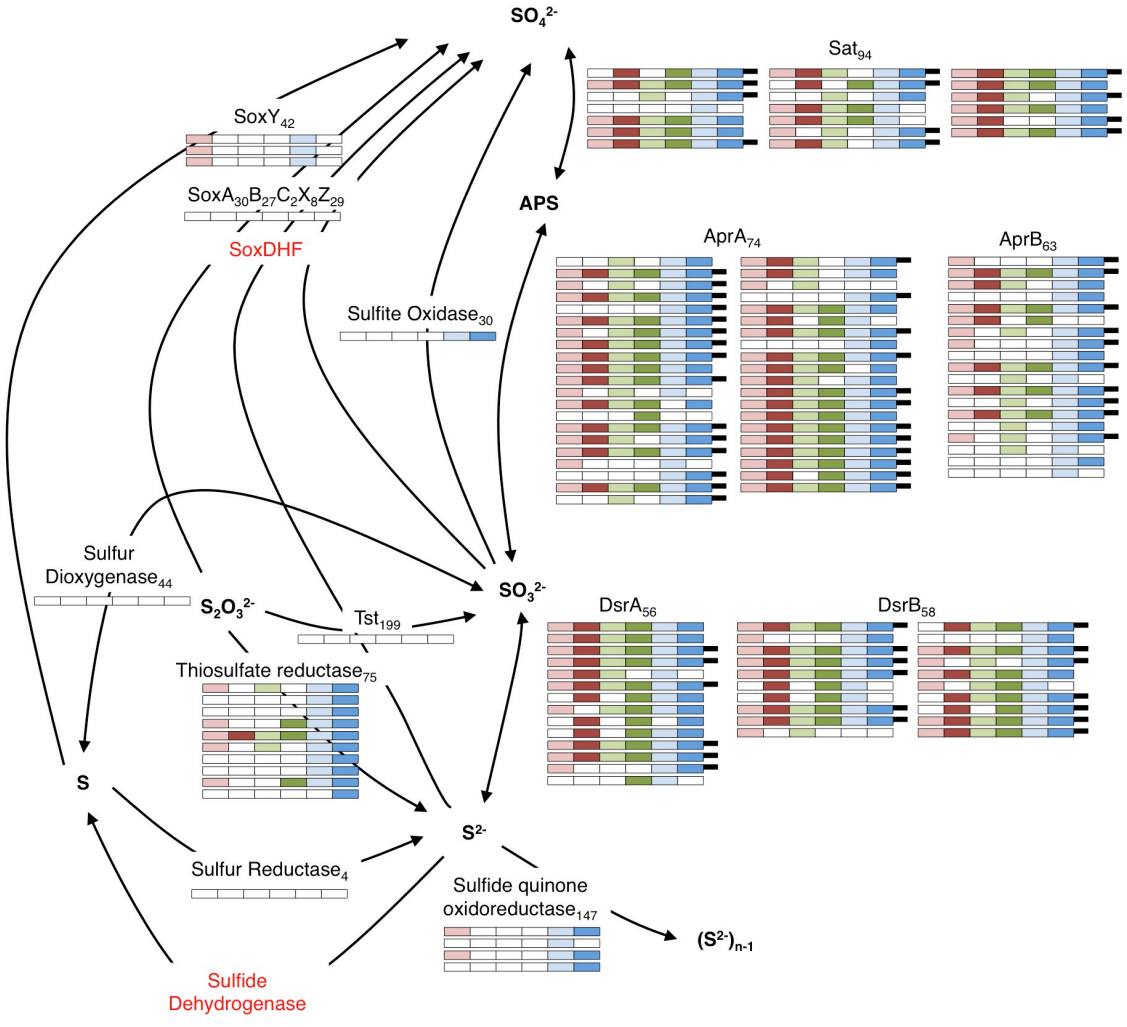


Fig. 4.4: Metaproteomic data for enzymes involved in sulfur metabolisms.

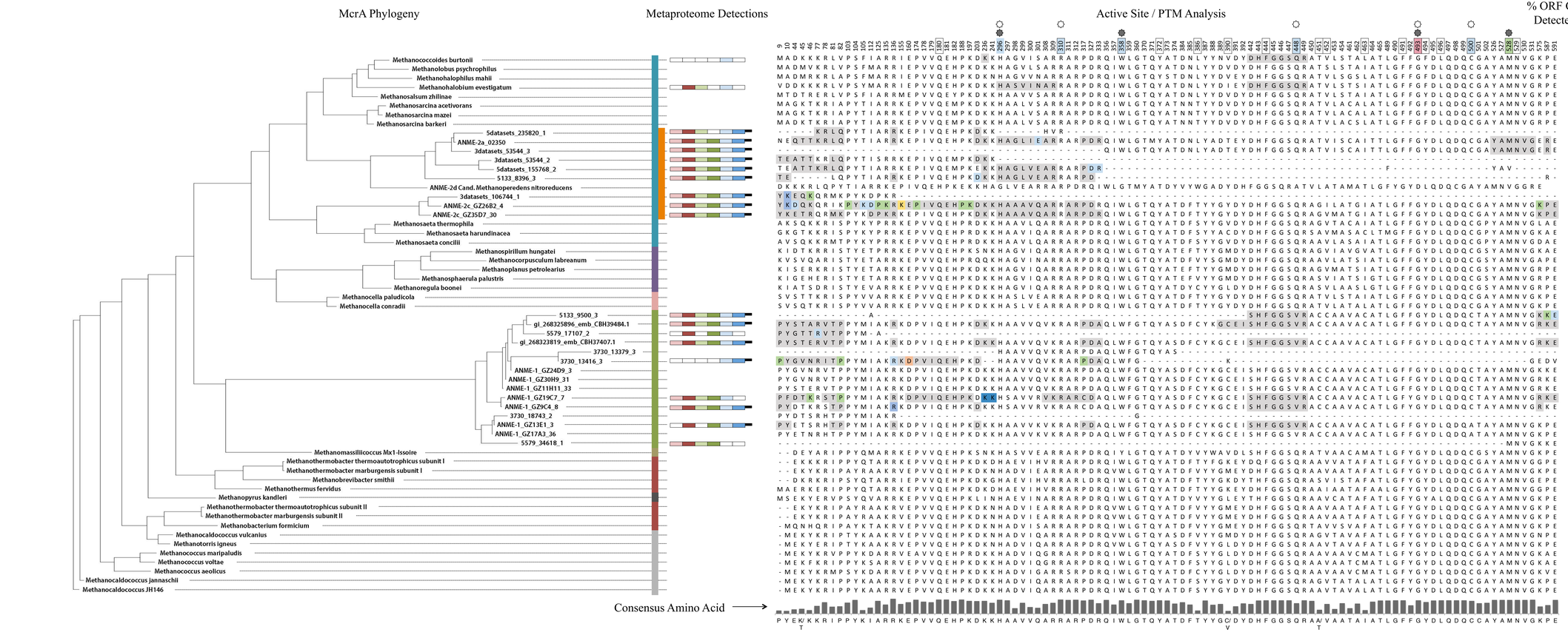


Fig.3: A phylogenetic and PTM-based analysis of the McrA subunit. The left panel shows a Muscle-aligned phylogenetic tree of all McrA sequences in the metagenomic database, as well as additional cultured organisms to account for all seven methanogenic orders and other ANME representatives. The metaproteomic detection panel shows the presence/absence bars from Fig.1, positioned next to their corresponding ORF label. The active site / PTM analysis panel provides alignments generated by Jalview for selected amino acid positions of note that together account for all PTMs observed in this and previous studies, as well as residues implicated in the enzyme's active site. Amino acids detected in proteomics analyses are highlighted in gray; colored residues exhibited PTMs specified in the figure key. PTMs observed in previous studies are portrayed by color-coding of amino acid position numbers at the top of the alignment; boxed numbers correspond with active site residues described in Shima et al., 2012. ORF coverage was calculated by dividing the number of amino acids in an ORF's detected peptides by that ORF's full length. All PTM analysis only includes data from #5133 $^{14}$N.

Phylogenetic affiliations of all sulfate reduction pathway orthologs identified in the pan-metaproteome (Sat, AprA, AprB, DsrA, and DsrB) are shown in Table S4.6. Of those classified to class level, deltaproteobacterial enzymes (77%) were more abundant than orthologs linked to *Gammaproteobacteria* (18%), *Betaproteobacteria* (3%), or *Nitrospira* (2%), with *Desulfobacterales* as the most common family (39% of all class-level partitioned orthologs). Based on the 16S rDNA community data, the majority of the deltaproteobacteria were members of the SEEP-SRB1 and SEEP-SRB2 clades within the *Desulfobacterales* (Supplementary Data File 4.1a). These findings are consistent with the frequent SEEP-SRB association with ANME (Knittel et al. 2005; Orphan et al. 2002), as well as the more rare observation of *Betaproteobacteria* with ANME-2c (Knittel & Boetius 2009). It is also noteworthy that none of the dissimilatory sulfate-reducing proteins are derived from an identifiable archaeal sequence. This finding suggests that archaeal-based sulfate reduction through canonical mechanisms (Dahl et al. 1994) is not a significant feature of our experimental incubations, though it is difficult to rule out novel sulfate reduction components given the prevalence of unannotated hypothetical proteins.

Other sulfur metabolism genes and proteins offer insight into the metabolic potential of Hydrate Ridge seep sediments and the community response to anaerobic experimental conditions generated in lab-based incubations. Enzymes facilitating oxidative pathways were present in the co-localized metagenomes, with the exception of SoxX and sulfide dehydrogenase; this observation indicates that the sediments possess a widespread potential for the oxidation of sulfur compounds. Tag sequencing data revealed a substantial proportion of the *Sulfurovum* genus, accounting for between 4%-9.6% of total 16S rRNA gene sequences (Supplementary Data File 4.1a). *Sulfurovum* species are frequently invoked

as sulfur-oxidizing constituents in anoxic zones (e.g., Urich et al. 2014; Sylvan et al. 2012; Schunck et al. 2013); reconciling their high relative abundance in our incubations with the low recovery of sulfur-oxidizing proteins suggests that this lineage may be more active in other catabolic pathways – including elemental sulfur reduction (Yamamoto et al. 2010) or hydrogen oxidation (Yamamoto & Takai 2011) – or is well-preserved despite unfavorable geochemical conditions. Indeed, 222 enriched proteins exhibiting closest phylogenetic association with *Sulfurovum* (1TP, 1UP) were identified, the majority of which were unannotated hypothetical proteins.

Ten thiosulfate reductase orthologs attributed to *Delta-* and *Epsilonproteobacteria* were detected in the pan-metaproteome (2TP, 1UP), suggesting that thiosulfate reduction is a relatively common metabolic capability within seep sediments, and particularly the 0-9 cm horizon encompassed by #5133. This observation is consistent with previous evidence of thiosulfate reduction from ANME-1-rich seep sediment incubations from Eckernförde Bay (Jagersma et al. 2012) and thiosulfate disproportionation in ANME-1- and ANME-2-dominant samples (Nauhaus et al. 2005). In both cases, the process was seemingly disconnected from AOM, and we observe no evidence of thiosulfate reductase synthesized after 170 days of incubation. The connection between AOM-linked sulfate reduction and thiosulfate production and reduction remains uncertain, and may represent an important interaction between ANME and other members of the community.

***Conclusion***

In this multi-site metaproteomics study, we report the most complete detection of proteins associated with methane seeps to date, providing a broad sense of *in situ* functionally active metabolic pathways and those actively produced under laboratory-based

methanotrophic conditions. Components of all of the proteins involved in the reverse methanogenesis pathway were identified, and Mcr was shown to account for 10.4% of all detected peptides. The prevalence of $^{15}N$ enriched orthologs involved in reverse methanogenesis and sulfate reducing pathways bolsters our understanding that AOM is the dominant biogeochemical process in seep-simulating incubation conditions, indicating that metabolic activity need not scale with community composition as determined by 16S rRNA gene relative abundances.

This work demonstrates the utility of SIP metaproteomics as a discovery platform for enriched, pervasive uncharacterized proteins that are likely ecologically important and should be prioritized for subsequent biochemical characterization. The approach, when attuned to PTM detection windows, is well suited to reveal a wider functional diversity than that encoded by nucleic acid sequences alone, a potentially common reality with significant metabolic repercussions. Finally, SIP shotgun metaproteomics can inform more focused proteomic investigations to quantify enzymes of pathways of interest; such values could then be integrated into flux balance models of carbon, sulfur, and nitrogen cycles to better constrain the dynamics and rates of reactions at both the consortium and ecosystem scales.

Tracking the metabolic activity of energy-limited microbial communities has long challenged analytical techniques that address specific microscale anabolic reactions, system-wide metabolic potential, or broad biogeochemical transformations. SIP metaproteomics enables the functionally-, phylogenetically-, and temporally-constrained understanding of protein synthesis, opening access to a previously untapped array of distributed low-growth microorganisms active in selected catabolic pathways. Developing

a more nuanced appreciation of metabolite flow and interspecies interaction in this way is crucial for the improved understanding and management of microbial ecosystems and their global impacts.

## References


Aletta JM, Cimato TR, Ettinger MJ. (1998). Protein methylation: a signal event in post-translational modification. Trends in Biochemical Sciences 23:89–91.

Alexandre H, Ansanay-Galeote V, Dequin S, Blondin B. (2001). Global gene expression during short-term ethanol stress in Saccharomyces cerevisiae. FEBS Letters 498:98–103.

Alperin MJ, Hoehler TM. (2009). Anaerobic methane oxidation by archaea/sulfate-reducing bacteria aggregates: 1. Thermodynamic and physical constraints. American Journal of Science 309:869–957.

Basen M, Krüger M, Milucka J, Kuever J, Kahnt J, Grundmann O, et al. (2011). Bacterial enzymes for dissimilatory sulfate reduction in a marine microbial mat (Black Sea) mediating anaerobic oxidation of methane. Environmental Microbiology 13:1370–1379.

Bidle KA, Kastner M, Bartlett DH. (1999). A phylogenetic analysis of microbial communities associated with methane hydrate containing marine fluids and sediments in the Cascadia margin (ODP site 892B). FEMS microbiology letters 177:101–108.

Boetius Antje, Suess E. (2004). Hydrate Ridge: a natural laboratory for the study of microbial life fueled by methane from near-surface gas hydrates. Chemical Geology 205:291–310.

Bozinovski D, Herrmann S, Richnow H-H, Von Bergen M, Seifert J, Vogt C. (2012). Functional analysis of an anaerobic m-xylene-degrading enrichment culture using protein-based stable isotope probing. FEMS Microbiology Ecology 81:134–144.

Caporaso JG, Kuczynski J, Stombaugh J, Bittinger K, Bushman FD, Costello EK, et al. (2010). QIIME allows analysis of high-throughput community sequencing data. Nature methods 7:335–336.

Chourey K, Jansson J, VerBerkmoes N, Shah M, Chavarria KL, Tom LM, et al. (2010). Direct Cellular Lysis/Protein Extraction Protocol for Soil Metaproteomics. J. Proteome Res. 9:6615–6622.

Chuikov S, Kurash JK, Wilson JR, Xiao B, Justin N, Ivanov GS, et al. (2004). Regulation of p53 activity through lysine methylation. Nature 432:353–360.

Dahl C, Speich N, Trüper HG. (1994). [23] Enzymology and molecular biology of sulfate reduction in extremely thermophilic archaeon Archaeoglobus fulgidus. In:Methods in Enzymology, Harry D. Peck, J, Jean LeGall, ed (ed). Vol. Volume 243, Academic Press, pp. 331–349. http://www.sciencedirect.com/science/article/pii/007668799443025X.

Dekas A, Poretsky RS, Orphan Victoria J. (2009). Deep-Sea Archaea Fix and Share Nitrogen in Methane-Consuming Microbial Consortia. Science 326:422–426.

Denef VJ, Mueller RS, Banfield JF. (2010). AMD biofilms: using model communities to study microbial evolution and ecological complexity in nature. ISME J 4:599–610.

Deribe YL, Pawson T, Dikic I. (2010). Post-translational modifications in signal integration. Nat Struct Mol Biol 17:666–672.

Desrosiers R, Tanguay R. (1988). Methylation of Drosophila histones at proline, lysine, and arginine residues during heat shock. Journal of Biological Chemistry 263:4686–4692.

Ermler U, Grabarse W, Shima S, Goubeaud M, Thauer RK. (1997). Crystal Structure of Methyl-Coenzyme M Reductase: The Key Enzyme of Biological Methane Formation. Science 278:1457–1462.

Gilmore JM, Kettenbach AN, Gerber SA. (2012). Increasing phosphoproteomic coverage through sequential digestion by complementary proteases. Analytical and bioanalytical chemistry 402:711–720.

Glass JB, Yu H, Steele JA, Dawson KS, Sun S, Chourey K, et al. (2014). Geochemical, metagenomic and metaproteomic insights into trace metal utilization by methane oxidizing microbial consortia in sulphidic marine sediments. Environmental microbiology 16:1592–1611.

Green-Saxena A, Dekas A E, Dalleska NF, Orphan V J. (2014). Nitrate-based niche differentiation by distinct sulfate-reducing bacteria involved in the anaerobic oxidation of methane. ISME J 8:150–163.

Hallam SJ, Girguis PR, Preston CM, Richardson PM, DeLong EF. (2003). Identification of Methyl Coenzyme M Reductase A (mcrA) Genes Associated with Methane-Oxidizing Archaea. Applied and Environmental Microbiology 69:5483–5491.

Hallam SJ, Putnam N, Preston CM, Detter JC, Rokhsar D, Richardson PM, et al. (2004). Reverse methanogenesis: testing the hypothesis with environmental genomics. Science 305:1457–1462.

Haroon MF, Hu S, Shi Y, Imelfort M, Keller J, Hugenholtz P, et al. (2013). Anaerobic oxidation of methane coupled to nitrate reduction in a novel archaeal lineage. Nature 500:567–570.

Hartl FU, Bracher A, Hayer-Hartl M. (2011). Molecular chaperones in protein folding and proteostasis. Nature 475:324–332.

Hatzenpichler R, Scheller S, Tavormina PL, Babin BM, Tirrell DA, Orphan Victoria J. (2014). *In situ* visualization of newly synthesized proteins in environmental microbes using amino acid tagging and click chemistry. Environ Microbiol 16:2568–2590.

Hawley AK, Brewer HM, Norbeck AD, Paša-Tolić L, Hallam SJ. (2014). Metaproteomics reveals differential modes of metabolic coupling among ubiquitous oxygen minimum zone microbes. Proceedings of the National Academy of Sciences 111:11395–11400.

Ivan M, Kondo K, Yang H, Kim W, Valiando J, Ohh M, et al. (2001). HIFα Targeted for VHL-Mediated Destruction by Proline Hydroxylation: Implications for O2 Sensing. Science 292:464–468.

Iversen N, Jorgensen Bo Barker. (1985). Anaerobic methane oxidation rates at the sulfate-methane transition in marine sediments from Kattegat and Skagerrak (Denmark)1. Limnol. Oceanogr. 30:944–955.

Jagersma CG, Meulepas RJW, Timmers PHA, Szperl A, Lens PNL, Stams AJM. (2012). Enrichment of ANME-1 from Eckernförde Bay sediment on thiosulfate, methane and short-chain fatty acids. Journal of Biotechnology 157:482–489.

Jehmlich N, Schmidt F, Von Bergen M, Richnow H-H, Vogt C. (2008). Protein-based stable isotope probing (Protein-SIP) reveals active species within anoxic mixed cultures. ISME J 2:1122–1133.

Jørgensen B, Kasten S. (2006). Sulfur Cycling and Methane Oxidation. In:Marine Geochemistry, Schulz, H & Zabel, M, eds (ed)., Springer Berlin Heidelberg, pp. 271–309. http://dx.doi.org/10.1007/3-540-32144-6_8.

Justice NB, Li Z, Wang Y, Spaudling SE, Mosier AC, Hettich RL, et al. (2014). 15N- and 2H proteomic stable isotope probing links nitrogen flow to archaeal heterotrophic activity. Environ Microbiol 16:3224–3237.

Justice NB, Pan C, Mueller R, Spaulding SE, Shah V, Sun CL, et al. (2012). Heterotrophic Archaea Contribute to Carbon Cycling in Low-pH, Suboxic Biofilm Communities. Applied and Environmental Microbiology 78:8321–8330.

Kahnt J, Buchenau B, Mahlert F, Krüger M, Shima S, Thauer RK. (2007). Post-translational modifications in the active site region of methyl-coenzyme M reductase from methanogenic and methanotrophic archaea. FEBS Journal 274:4913–4921.

Kermer R, Hedrich S, Taubert M, Baumann S, Schlömann M, Johnson DB, et al. (2012). Elucidation of carbon transfer in a mixed culture of Acidiphilium cryptum and Acidithiobacillus ferrooxidans using protein-based stable isotope probing. Journal of Integrated OMICS 2:37–45.

Kerner MJ, Naylor DJ, Ishihama Y, Maier T, Chang H-C, Stines AP, et al. (2005). Proteome-wide Analysis of Chaperonin-Dependent Protein Folding in Escherichia coli. Cell 122:209–220.

Kim YE, Hipp MS, Bracher A, Hayer-Hartl M, Ulrich Hartl F. (2013). Molecular Chaperone Functions in Protein Folding and Proteostasis. Annu. Rev. Biochem. 82:323–355.

Knittel Katrin, Boetius Antje. (2009). Anaerobic Oxidation of Methane: Progress with an Unknown Process. Annu. Rev. Microbiol. 63:311–334.

Knittel Katrin, Lösekann T, Boetius Antje, Kort R, Amann R. (2005). Diversity and Distribution of Methanotrophic Archaea at Cold Seeps. Applied and Environmental Microbiology 71:467–479.

Kovacs JJ, Murphy PJM, Gaillard S, Zhao X, Wu J-T, Nicchitta CV, et al. (2005). HDAC6 Regulates Hsp90 Acetylation and Chaperone-Dependent Activation of Glucocorticoid Receptor. Molecular Cell 18:601–607.

Krüger M, Meyerdierks A, Glöckner FO, Amann R, Widdel F, Kube M, et al. (2003). A conspicuous nickel protein in microbial mats that oxidize methane anaerobically. Nature 426:878–881.

Li Z, Wang Y, Yao Q, Justice NB, Ahn T-H, Xu D, et al. (2014). Diverse and divergent protein post-translational modifications in two growth stages of a natural microbial community. Nat Commun 5. http://dx.doi.org/10.1038/ncomms5405.

Liu M, Fan L, Zhong L, Kjelleberg S, Thomas T. (2012). Metaproteogenomic analysis of a community of sponge symbionts. ISME J 6:1515–1525.

Marlow JJ, Steele JA, Ziebis W, Thurber AR, Levin LA, Orphan Victoria J. (2014). Carbonate-hosted methanotrophy represents an unrecognized methane sink in the deep sea. Nature Communications.

Meyerdierks A, Kube M, Kostadinov I, Teeling H, Glöckner FO, Reinhardt R, et al. (2010). Metagenome and mRNA expression analyses of anaerobic methanotrophic archaea of the ANME-1 group. Environmental Microbiology 12:422–439.

Milucka J, Widdel F, Shima S. (2013). Immunological detection of enzymes for sulfate reduction in anaerobic methane-oxidizing consortia. Environ Microbiol 15:1561–1571.

Mitchell A, Chang H-Y, Daugherty L, Fraser M, Hunter S, Lopez R, et al. (2014). The InterPro protein families database: the classification resource after 15 years. Nucleic acids research gku1243.

Moellering RE, Cravatt BF. (2013). Functional lysine modification by an intrinsically reactive primary glycolytic metabolite. Science 341:549–553.

Moore EK, Nunn BL, Goodlett DR, Harvey HR. (2012). Identifying and tracking proteins through the marine water column: Insights into the inputs and preservation mechanisms of protein in sediments. Geochimica et Cosmochimica Acta 83:324–359.

Morgan R, Kohn S, Hwang S-H, Hassett DJ, Sauer K. (2006). BdlA, a Chemotaxis Regulator Essential for Biofilm Dispersion in Pseudomonas aeruginosa. Journal of Bacteriology 188:7335–7343.

Morono Y, Ito M, Inagaki F. (2014). Detecting slow metabolism in the subseafloor: analysis of single cells using NanoSIMS. In:Microbial Life of the Deep Biosphere, De Gruyter: Berlin, pp. 101–120.

Morris BEL, Herbst F-A, Bastida F, Seifert J, Von Bergen M, Richnow H-H, et al. (2012). Microbial interactions during residual oil and n-fatty acid metabolism by a methanogenic consortium. Environmental Microbiology Reports 4:297–306.

Najbauer J, Orpiszewski J, Aswad DW. (1996). Molecular Aging of Tubulin: Accumulation of Isoaspartyl Sites in Vitro and in Vivo. Biochemistry 35:5183–5190.

Nauhaus K, Albrecht M, Elvert M, Boetius Antje, Widdel F. (2007). In vitro cell growth of marine archaeal-bacterial consortia during anaerobic oxidation of methane with sulfate. Environmental Microbiology 9:187–196.

Nauhaus K, Boetius Antje, Krüger M, Widdel F. (2002). In vitro demonstration of anaerobic oxidation of methane coupled to sulphate reduction in sediment from a marine gas hydrate area. Environmental Microbiology 4:296–305.

Nauhaus K, Treude Tina, Boetius Antje, Krüger M. (2005). Environmental regulation of the anaerobic oxidation of methane: a comparison of ANME-I and ANME-II communities. Environmental Microbiology 7:98–106.

Olsen JV, Mann M. (2013). Status of large-scale analysis of post-translational modifications by mass spectrometry. Molecular & Cellular Proteomics 12:3444–3452.

Olsen JV, Vermeulen M, Santamaria A, Kumar C, Miller ML, Jensen LJ, et al. (2010). Quantitative phosphoproteomics reveals widespread full phosphorylation site occupancy during mitosis. Science signaling 3:ra3–ra3.

Orphan Victoria J., House CH, Hinrichs K-U, McKeegan KD, DeLong EF. (2002). Multiple archaeal groups mediate methane oxidation in anoxic cold seep sediments. Proceedings of the National Academy of Sciences 99:7663–7668.

Orphan Victoria J., Turk KA, Green AM, House CH. (2009). Patterns of 15N assimilation and growth of methanotrophic ANME-2 archaea and sulfate-reducing bacteria within structured syntrophic consortia revealed by FISH-SIMS. Environmental Microbiology 11:1777–1791.

Pan C, Fischer CR, Hyatt D, Bowen BP, Hettich RL, Banfield JF. (2011). Quantitative Tracking of Isotope Flows in Proteomes of Microbial Communities. Molecular & Cellular Proteomics 10. http://www.mcponline.org/content/10/4/M110.006049.abstract.

Parkes R, Cragg B, Fry J, Herbert R, Wimpenny J, Allen J, et al. (1990). Bacterial Biomass and Activity in Deep Sediment Layers from the Peru Margin [and Discussion]. Philosophical Transactions of the Royal Society of London. Series A, Mathematical and Physical Sciences 331:139–153.

Pernthaler A, Dekas Anne E, Brown CT, Goffredi SK, Embaye T, Orphan Victoria J. (2008). Diverse syntrophic partnerships from deep-sea methane vents revealed by direct cell capture and metagenomics. Proceedings of the National Academy of Sciences 105:7052–7057.

Prakash D, Wu Y, Suh S-J, Duin EC. (2014). Elucidating the Process of Activation of Methyl-Coenzyme M Reductase. Journal of Bacteriology 196:2491–2498.

Reeburgh WS. (2007). Oceanic Methane Biogeochemistry. Chem. Rev. 107:486–513.

Reitzer L. (2003). Nitrogen assimilation and global regulation in Escherichia coli. Annual Reviews in Microbiology 57:155–176.

Schunck H, Lavik G, Desai DK, Großkopf T, Kalvelage T, Löscher CR, et al. (2013). Giant hydrogen sulfide plume in the oxygen minimum zone off Peru supports chemolithoautotrophy. PLoS One 8:e68661.

Seifert J, Taubert M, Jehmlich N, Schmidt F, Völker U, Vogt C, et al. (2012). Protein based stable isotope probing (protein SIP) in functional metaproteomics. Mass spectrometry reviews 31:683–697.

Selmer T, Kahnt J, Goubeaud M, Shima S, Grabarse W, Ermler U, et al. (2000). The Biosynthesis of Methylated Amino Acids in the Active Site Region of Methyl-coenzyme M Reductase. Journal of Biological Chemistry 275:3755–3760.

Shima S, Krueger M, Weinert T, Demmer U, Kahnt J, Thauer RK, et al. (2012). Structure of a methyl-coenzyme M reductase from Black Sea mats that oxidize methane anaerobically. Nature 481:98–101.

Stams AJM, Plugge CM. (2009). Electron transfer in syntrophic communities of anaerobic bacteria and archaea. Nat Rev Micro 7:568–577.

Stevens TJ, Arkin IT. (2000). Do more complex organisms have a greater proportion of membrane proteins in their genomes? Proteins: Structure, Function, and Bioinformatics 39:417–420.

Stokke R, Roalkvam I, Lanzen A, Haflidason H, Steen IH. (2012). Integrated metagenomic and metaproteomic analyses of an ANME 1 dominated community in marine cold seep sediments. Environmental microbiology 14:1333–1346.

Suess E, Torres M, Bohrmann G, Collier R, Greinert J, Linke P, et al. (1999). Gas hydrate destabilization: enhanced dewatering, benthic material turnover and large methane plumes at the Cascadia convergent margin. Earth and Planetary Science Letters 170:1–15.

Sylvan JB, Toner BM, Edwards KJ. (2012). Life and Death of Deep-Sea Vents: Bacterial Diversity and Ecosystem Succession on Inactive Hydrothermal Sulfides. mBio 3. http://mbio.asm.org/content/3/1/e00279-11.abstract.

Taubert M, Jehmlich N, Vogt C, Richnow HH, Schmidt F, Von Bergen M, et al. (2011). Time resolved protein-based stable isotope probing (Protein-SIP) analysis allows quantification of induced proteins in substrate shift experiments. Proteomics 11:2265–2274.

Taubert M, Vogt C, Wubet T, Kleinsteuber S, Tarkka MT, Harms H, et al. (2012). Protein-SIP enables time-resolved analysis of the carbon flux in a sulfate-reducing, benzene-degrading microbial consortium. ISME J 6:2291–2301.

Thauer RK, Kaster A-K, Seedorf H, Buckel W, Hedderich R. (2008). Methanogenic archaea: ecologically relevant differences in energy conservation. Nat Rev Micro 6:579–591.

Treude T., Boetius A., Knittel K., Wallmann K., Jorgensen B.B. (2003). Anaerobic oxidation of methane above gas hydrates at Hydrate Ridge, NE Pacific Ocean. Mar Ecol Prog Ser 264:1–14.

Trötschel C, Poetsch A. (2015). Current approaches and challenges in targeted absolute quantification of membrane proteins. Proteomics.

Tryon M., Brown K., Torres M. (2002). Fluid and chemical flux in and out of sediments hosting methane hydrate deposits on Hydrate Ridge, OR, II: Hydrological processes. Earth and Planetary Science Letters 201:541–557.

Urich T, Lanzén A, Stokke R, Pedersen RB, Bayer C, Thorseth IH, et al. (2014). Microbial community structure and functioning in marine sediments associated with diffuse hydrothermal venting assessed by integrated meta-omics. Environ Microbiol 16:2699–2710.

Verberkmoes NC, Russell AL, Shah M, Godzik A, Rosenquist M, Halfvarson J, et al. (2009). Shotgun metaproteomics of the human distal gut microbiota. The ISME journal 3:179–189.

Wang F-P, Zhang Y, Chen Y, He Y, Qi J, Hinrichs K-U, et al. (2014). Methanotrophic archaea possessing diverging methane-oxidizing and electron-transporting pathways. ISME J 8:1069–1078.

Wang Y, Ahn T-H, Li Z, Pan C. (2013). Sipros/ProRata: a versatile informatics system for quantitative community proteomics. Bioinformatics 29:2064–2065.

Weinert BT, Iesmantavicius V, Wagner SA, Schölz C, Gummesson B, Beli P, et al. (2013). Acetyl-phosphate is a critical determinant of lysine acetylation in E. coli. Molecular cell 51:265–272.

Welander PV, Metcalf WW. (2008). Mutagenesis of the C1 Oxidation Pathway in Methanosarcina barkeri: New Insights into the Mtr/Mer Bypass Pathway. Journal of Bacteriology 190:1928–1936.

Wrede C, Krukenberg V, Dreier A, Reitner J, Heller C, Hoppert M. (2012). Detection of Metabolic Key Enzymes of Methane Turnover Processes in Cold Seep Microbial Biofilms. Geomicrobiology Journal 30:214–227.

Xiong W, Giannone RJ, Morowitz MJ, Banfield JF, Hettich RL. (2015). Development of an Enhanced Metaproteomic Approach for Deepening the Microbiome Characterization of the Human Infant Gut. J. Proteome Res. 14:133–141.

Yamamoto M, Nakagawa S, Shimamura S, Takai K, Horikoshi K. (2010). Molecular characterization of inorganic sulfur-compound metabolism in the deep-sea epsilonproteobacterium Sulfurovum sp. NBC37-1. Environmental Microbiology 12:1144–1153.

Yamamoto M, Takai K. (2011). Sulfur Metabolisms in Epsilon- and Gamma-Proteobacteria in Deep-Sea Hydrothermal Fields. Frontiers in Microbiology 2:192.

*C h a p t e r  5*

# THE POTENTIAL FOR BIOLOGICALLY CATALYZED ANAEROBIC METHANE OXIDATION ON ANCIENT MARS

Jeffrey J. Marlow[1*], Douglas E. LaRowe[2], Bethany L. Ehlmann[1,4], Jan P. Amend[2,3], Victoria J. Orphan[1]

[1]Division of Geological and Planetary Sciences, California Institute of Technology; [2]Department of Earth Sciences, University of Southern California; [3]Department of Biological Sciences, University of Southern California; [4]Jet Propulsion Laboratory, California Institute of Technology

*Adapted from Marlow, Jeffrey J., et al. "The potential for biologically catalyzed anaerobic methane oxidation on ancient Mars." Astrobiology 14.4 (2014): 292-307. DOI: http://doi.org/10.1089/ast.2013.1078

**Abstract**

This study examines the potential for the biologically mediated anaerobic oxidation of methane (AOM) coupled to sulfate reduction on ancient Mars. Seven distinct fluids representative of putative martian groundwater are used to calculate Gibbs energy values in the presence of dissolved methane under a range of atmospheric $CO_2$ partial pressures. In all scenarios, AOM is exergonic, ranging from -31 to -135 kJ/mol $CH_4$. A reaction transport model was constructed to examine how environmentally relevant parameters such as advection velocity, reactant concentrations, and biomass production rate affect the spatial and temporal dependences of AOM reaction rates. Two geologically supported models for ancient martian AOM are presented: a sulfate-rich groundwater with methane produced from serpentinization byproducts, and acid-sulfate fluids with methane from basalt alteration. The simulations presented in this study indicate that AOM could have been a feasible metabolism on ancient Mars, and fossil or isotopic evidence of this metabolic pathway may persist beneath the surface and in surface exposures of eroded ancient terrains.

**Introduction**

During its Noachian (4.1–3.7 Ga) and Hesperian (3.7–3.0 Ga) periods, Mars was a geologically active body, with frequent impacts (Hartmann & Neukum, 2001), extensive volcanism (McEwen et al., 1999), and subsurface and surficial liquid water (Carr & Head, 2010). As a result of these processes, water-rock interactions provided a potentially exploitable energy source for biological processes. Based on assumed martian geochemical conditions, several microbial metabolisms have been proposed, including iron

or manganese reduction or oxidation, methanogenesis, acetogenesis, and sulfur-processing pathways (Boston et al., 1992; Varnes et al., 2004).

The discovery of syntrophic methane-oxidizing Archaea and sulfate-reducing Bacteria on Earth, along with evidence of methane production and sulfate-bearing minerals on Mars, suggest that the anaerobic oxidation of methane (AOM) may have been a viable metabolism for subsurface microbial communities on ancient Mars. Martian AOM has been proposed (Miller et al., 2011; House et al., 2011), but a rigorous assessment of its energetic viability under environmentally relevant parameters is lacking. Here, we calculate Gibbs energies of the metabolism and incorporate reaction transport modeling to demonstrate the feasibility of AOM on ancient Mars.

In the terrestrial context, AOM is an important component of the Earth's carbon cycle, consuming an estimated 80-90% of the methane produced beneath the world's oceans (Reeburgh, 2007). Microbial consortia comprised of Archaea and Bacteria mediate the metabolic consumption of methane in methane-rich anoxic systems (Boetius et al., 2000; Orphan et al., 2001). Although the identities of all possible electron acceptors and metabolic intermediates of the microbial partners are topics of active debate (LaRowe et al., 2008; Strous & Jetten, 2004; Beal et al., 2009; Milucka et al., 2012; Stams & Plugge, 2009), the overall process can be summarized with the following reaction:

$$CH_{4(aq)} + SO_4^{2-} + H^+ \rightarrow HCO_3^- + H_2S_{(aq)} + H_2 \quad (1)$$

The electron donor and acceptor – methane and sulfate, respectively – were both likely present on early Mars as a result of abiotic chemical reactions. Sulfate minerals are

widespread, having been detected or inferred from elemental chemistry at every Mars landing site to date (Kounaves et al., 2010; Squyres et al., 2004; Toulmin et al., 1977; Wang et al., 2006; Wänke et al., 2001). Ca-, Mg-, and Fe- hydrated sulfates have also been identified from Mars orbit (e.g., Gendrin et al., 2005) in numerous locations correlated with expected locations of groundwater upwelling (Murchie et al., 2009). The geologic characteristics of these deposits are diverse, including lacustrine (Gendrin et al., 2005; Wray et al., 2011), evaporitic (Tosca et al., 2005), diagenetic (McLennan et al., 2005), near-surface weathering (Hurowitz et al., 2006), and hydrothermal (Thollot et al., 2012) settings. This range of environments indicates a sulfate component in waters across many locations on ancient Mars.

Surface exposures of serpentine in Noachian terrains (Ehlmann et al., 2010) suggest that methane was once formed in substantial quantities by hydrogen-forming serpentinization and subsequent abiotic methanogenesis as proposed by Oze & Sharma (2005), e.g.,

$$(Fe,Mg)_2SiO_4 + H_2O(l) \rightarrow (Fe,Mg)_3Si_2O_5(OH)_4 + (Mg,Fe)(OH)_2 + Fe_3O_4 + H_2(g) \qquad (2)$$

Olivine Serpentine Brucite Magnetite

$$4H_2(g) + CO_2(g) \rightarrow CH_4(g) + 2H_2O(l) \qquad (3)$$

Serpentine has been identified in nearly a dozen locations in Noachian-age crust in three distinctive geologic settings: in stratigraphic section; in mélange terrains with other alteration minerals in discrete deposits; and in the ejecta, walls, and central peaks of impact craters (Ehlmann et al., 2010). Modern-day serpentinization has been proposed to explain

recent reports of methane in the atmosphere of Mars either from localized centers or microseeps (Atreya et al., 2007; Etiope et al., 2012; Mumma et al., 2009).

Lyons et al. (2005) offer a model of martian methane production that would generate a more widespread, pervasive source of the gas. They posit that when carbon-bearing hydrothermal fluid reacts with basaltic crust in metamorphic reactions, dissolved methane becomes the dominant carbon species. This process accounts for abiogenic methane at mid-ocean ridges on Earth (Welhan & Craig, 1979), and under predicted crustal permeability and oxygen fugacity conditions on Mars, methane could be pervasive in martian groundwaters between the near-surface and 9.5 km depth.

It is thus probable that sulfate-bearing waters interacted with methane-bearing fluids on Noachian Mars. Many exposures of clay minerals thought to form under hydrothermal conditions are found across Mars, occasionally co-located with sulfates (Ehlmann et al., 2011; Wray et al., 2009). Indeed, in one location, sulfate-bearing rocks have been detected overlying a unit with serpentine and olivine at the northeastern boundary of the Syrtis Major lava flows, west of the Isidis basin (Ehlmann & Mustard, 2012). In this context, AOM is a plausible metabolic pathway with habitability implications for both ancient and modern Mars. This study compiles a suite of fluid compositions representative of a range of martian geological provinces and calculates Gibbs energies of AOM within predicted chemical and physical constraints. In addition, a reaction-transport model is presented to demonstrate the biological potential of AOM as a function of several environmentally relevant variables. Finally, we offer proscriptive analysis of geological targets that may inform the search for evidence of AOM on Mars.

**Data Selection and Methods**

Martian Fluids

Several fluid compositions representing a range of potential past martian geochemical environments were compiled in order to calculate Gibbs energies of AOM and to seed reaction transport model simulations. Each scenario serves as a geochemical analog to particular past martian conditions – an important consideration in formulating theoretical and experimental hypotheses (Marlow et al., 2011). The specific relevance of each fluid to ancient Mars is discussed below and presented in Table 5.1, and chemical compositions are provided in Table 5.2.

Tosca et al. (2011) predict dilute fluids derived from the chemical weathering of synthetic basalts; these solutions are processed through evaporation simulations to give two stages of more concentrated brines. The aqueous chemistries cover a range of $HCO_3^-$:$SO_4^{2-}$ ratios (and thus a range of pH values), leading to various assemblages of saline minerals representative of Meridiani Planum, a region of Mars with sedimentary sulfate, silica, and hematite-bearing deposits formed by repeated episodes of groundwater upwelling and diagenesis (Squyres et al., 2004; Tosca & McLennan, 2006). The Tosca et al. (2011) brine composition most consistent with Meridiani mineralogy is used here as Fluid 1. In recognition of the challenges to life posed by highly acidic conditions, we also use one of Tosca et al.'s relatively neutral pH brines of intermediate composition (containing both $HCO_3^-$ and $SO_4^{2-}$), hereafter referred to as Fluid 4. Lewis et al. (1997) determine major ion concentrations of acid-sulfate waters in Yellowstone National Park (Fluid 2), while Marion et al. (2008) derive their fluid composition from the acid weathering of basaltic minerals (Fluid 3). Both solutions are reflective of a low-pH (2-3), sulfate-rich, oxidizing

Table 5.1: Characteristics and martian relevance of the fluids used for energetics calculations and reaction transport modeling in this study.

| Fluid # | Characteristics | Martian Relevance | Reference |
|---|---|---|---|
| 1 | Chemical weathering of synthetic basalt, highly acidic | Acid-sulfate alteration | Tosca et al., 2011 |
| 2 | Acid-sulfate waters from Yellowstone rhyolite weathering | Acid-sulfate alteration | Lewis et al., 1997 |
| 3 | Acid weathering of basaltic minerals | Acid-sulfate alteration | Marion et al., 2008 |
| 4 | Chemical weathering of synthetic basalt, moderately acidic | Acid-sulfate alteration | Tosca et al., 2011 |
| 5 | Dissolution of primary Icelandic basalt | Alkaline basalt alteration | Gislason & Arnorsson, 1993 |
| 6 | Deccan flood basalt hydrothermal spring | Alkaline basalt alteration | Minissale et al., 2000 |
| 7 | Serpentinization model fluid | Serpentinization site analog | Cardace & Hoehler, 2009 |

Table 5.2: Concentrations of dissolved species (mol / kg fluid) in the seven fluids used in this study.

| Fluid Label | **1** | **2** | **3** | **4** | **5** | **6** | **7** |
|---|---|---|---|---|---|---|---|
| Source | Tosca | Lewis | Marion | Tosca | Gislason | Minissale | Cardace |
| | | | | | | | |
| pH | 0.67 | 2 | 3 | 5.03 | 7.75 | 8.38 | 11.86 |
| Temp. (K) | 298 | 357 | 288 | 298 | 281 | 322 | 289 |
| | | | | | | | |
| $Na^+$ | 1.12 | 6.50E-04 | 3.15E-04 | 1.74 | 2.53E-04 | 1.97E-02 | 1.74E-03 |
| $K^+$ | 0.45 | 6.00E-04 | 1.05E-04 | 0.79 | 7.59E-06 | 1.86E-04 | 2.82E-05 |
| $NH_4^+$ | 0 | 0 | 0 | 0 | 0 | 2.92E-05 | 0 |
| $Li^+$ | 0 | 0 | 0 | 0 | 0 | 5.76E-06 | 0 |
| $Ca^{2+}$ | 0 | 8.00E-05 | 2.84E-03 | 0 | 9.61E-05 | 6.86E-03 | 1.20E-03 |
| $Mg^{2+}$ | 1.76 | 1.00E-05 | 5.56E-03 | 2.84 | 4.44E-05 | 8.23E-06 | 1.65E-05 |
| $Fe^{2+}$ | 1.52 | 1.35E-04 | 2.78E-03 | 0 | 8.06E-08 | 0 | 0 |
| $Fe^{3+}$ | 0 | 0 | 2.78E-03 | 0 | 0 | 0 | 0 |
| $Al^{3+}$ | 0 | 1.22E-03 | 1.99E-04 | 0 | 6.23E-07 | 0 | 1.48E-05 |
| $B^{3+}$ | 0 | 0 | 0 | 0 | 0 | 1.82E-05 | 0 |
| $Si^{4+}$ | 0 | 3.12E-03 | 0 | 0 | 0 | 0 | 0 |
| $Cl^-$ | 4.47 | 1.90E-04 | 4.18E-03 | 4.27 | 7.08E-05 | 2.99E-02 | 9.03E-04 |
| $F^-$ | 0 | 5.30E-05 | 0 | 0 | 4.68E-06 | 1.12E-04 | 0 |
| $Br^-$ | 0 | 0 | 0 | 0 | 0 | 4.21E-05 | 0 |
| $HCO_3^-$ | 0 | 0 | 0 | 2.94E-02 | 0 | 2.79E-04 | 0 |
| $NO_3^-$ | 0 | 0 | 0 | 0 | 0 | 5.81E-06 | 3.23E-06 |
| $HSO_4^-$ | 0.26 | 0 | 0 | 0 | 0 | 0 | 0 |
| $SO_4^{2-}$ | 2.23 | 1.38E-02 | 1.43E-02 | 1.96 | 3.66E-05 | 1.65E-03 | 1.46E-05 |
| $CO_3^{2-}$ | 0 | 0 | 0 | 0 | 0 | 4.17E-06 | 1.67E-12 |
| $CO_2$ | 0 | 0 | 0 | 0 | 4.50E-04 | 2.27E-07 | 0 |
| $H_2S$ | 1.01 | 2.50E-05 | 2.50E-05 | 1.55 | 6.60E-04 | 1.47E-07 | 9.12E-02 |
| $SiO_2$ | 0 | 0 | 2.29E-02 | 0 | 1.70E-04 | 1.02E-03 | 8.66E-05 |

$H_2S$ concentrations in Fluids 1 and 4 were determined by calculating the ratios of the five most abundant ions to sulfide in Fluid 2, which has a similar acid-sulfate geochemistry. The mean of the analogous ratios for Fluids 1 and 4 was used to set the sulfide concentration. The sulfide concentration in Fluid 2 was also used for Fluid 3, due to the

solutions' chemical similarities. The sulfide value for Fluid 5 was obtained from Seyfriend and Bischoff (1981), whose data come from similarly sourced Icelandic groundwater. An upper limit for sulfide in Fluid 7 is derived from Alt and Shanks, (2006), who characterize a serpentinization system in the Mariana forearc. Dissolved inorganic carbon is introduced to all fluids from atmospheric $CO_2$ as specified in the text.

geochemical regime implied by Meridiani minerals such as jarosite, differing in metal cation and chlorine composition because of differences in lithology (Klingelhöfer et al., 2004). The principal differences among the sulfate-rich fluids are the high ionic strengths of Fluids 1 and 4 and the bicarbonate present in Fluid 4.

The next three model fluids represent different, higher pH water-rock interactions. The mean composition of Icelandic rivers that result from the dissolution of primary basalts (Gislason & Arnórsson, 1993) are used for Fluid 5. Icelandic lava flows, which exhibit a relatively unaltered basaltic composition, have served as geological, geomorphological, and geochemical Mars analogs for decades (Allen et al., 1981; Nelson et al., 2005; Cousins et al., 2010; Ehlmann et al., 2012). Minissale et al. (2000) measure the fluid composition of the moderately hydrothermal (48°C) Deccan flood basalt springs, sourced from up to 3 km depth. This system has been used as a baseline for geochemical models of Gale Crater, the landing site for the Mars Science Laboratory mission (Schwenzer et al., 2012), and is the basis for Fluid 6 used in this study. Cardace and Hoehler (2009) describe the geochemical consequences of serpentinization, the water-mediated, heat-generating destabilization of ultramafic minerals such as olivine and pyroxene that results from the exposure of upper mantle material to surface temperatures and pressures. The aqueous chemistry they describe is used as our Fluid 7. Hydrogen forms as an abiotic by-product of serpentinization, which can reduce carbon dioxide to form methane; this mechanism has

been proposed as the source of putative methane signals on modern Mars (Oze & Sharma, 2005). The temperatures used in our calculations are those that produce the geochemical concentrations specified in Table 5.2; these values fall within the range of potential early Mars temperatures estimated from carbonate inclusions in martian meteorites (Brack & Pillinger, 1998) and mineral assemblages identified from Mars orbit (Ehlmann et al., 2011).

The precise formulation of the AOM reaction is dependent upon the host solution's pH, because carbonate, sulfate, and sulfide speciation vary ($H_2CO_3$:$HCO_3^-$ pKa=6.35, $HCO_3^-$:$CO_3^{2-}$ pKa=10.33; $H_2SO_4$:$HSO_4^-$ pKa=-3, $HSO_4^-$:$SO_4^{2-}$ pKa=1.92; $H_2S$:$HS^-$ pKa=7, $HS^-$:$S^{2-}$ pKa=13 at 25 °C). Thus, five different aqueous reactions can be expected at 25 °C:

| pH range | AOM reaction |
|---|---|
| < 1.92 | $CH_4 + HSO_4^- + H^+ \rightarrow CO_2 + H_2S + 2H_2O$ |
| 1.92 - 6.3 | $CH_4 + SO_4^{2-} + 2H^+ \rightarrow CO_2 + H_2S + 2H_2O$ |
| 6.35 – 7 | $CH_4 + SO_4^{2-} + H^+ \rightarrow HCO_3^- + H_2S + H_2O$ |
| 7 - 10.33 | $CH_4 + SO_4^{2-} \rightarrow HCO_3^- + HS^- + H_2O$ |
| 10.33 - 13 | $CH_4 + SO_4^{2-} \rightarrow CO_3^{2-} + HS^- + H^+ + H_2O$ |

The reaction chosen to best represent AOM in each environment is determined by the prevailing pH and temperature, which dictate the most abundant carbonate and sulfide species.

During Mars' ancient past, when liquid water would have been thermodynamically stable on and below the planet's surface, Mars' atmosphere was likely more dense than it is today. Such compositional differences are particularly relevant with regard to $CO_2$ levels, since dissolved oxidized carbon species are products of the AOM reaction and thereby

modulate the equilibrium state. We propose four different $CO_2$-dominated atmospheres, reflecting the likely oxidized nature of Mars' early atmosphere (Haberle, 1998) and encompassing a wide range of proposed compositions. The "atmosphere-independent" case models a potential habitat in which groundwater is not in contact with the atmosphere and negligible dissolved $CO_2$ (1 μM) is present. The "modern atmosphere" allows for a $CO_2$ partial pressure of 6 mbar, the "thick ancient atmosphere" accommodates the upper end of modeled $CO_2$ concentrations (2 bar, Yung et al., 1997), and the "ancient atmosphere" falls between the two extremes (200 mbar). The atmosphere scenarios indicate the quantity of $CO_2$ available to go into solution but are not indicative of the pressures at which Gibbs energies were calculated or the reaction transport model was run. For each environment (i.e., combination of fluid and atmospheric composition), the ratios of carbonate species were determined under the aforementioned concentrations of $CO_2$ by minimizing the Gibbs function for the constituent species using the SpecE8 program in Geochemist's Workbench.

Gibbs Energy Calculations

Calculating the Gibbs energy of potential catabolic reactions constrains the thermodynamic feasibility of these reactions under specific environmental conditions and indicates which metabolisms might be the most prevalent in a given system. These kinds of calculations have been carried out to describe a number of extreme environments on Earth, including submarine hydrothermal settings (Amend & Shock, 2001; LaRowe et al., 2008; McCollom, 2000, 2007; McCollom & Shock, 1997; Shock & Holland, 2004; Shock et al., 1995; Amend et al., 2011) shallow marine and terrestrial hydrothermal systems (Amend et al., 2003; Costa et al., 2009; Inskeep & McDermott, 2005; Inskeep et al., 2005;

Price et al., submitted; Rogers & Amend, 2005; Rogers & Amend, 2006; Rogers et al., 2007; Shock et al., 2010; Skoog et al., 2007; Spear et al., 2005; Vick et al., 2010; Windman et al., 2007) and, to a lesser extent, ocean sediments (Schrum et al., 2009; Wang et al., 2010) and basement rock (Bach & Edwards, 2003; Boettger et al., 2012; Cowen, 2004; Edwards et al., 2005). Furthermore, this type of analysis has been used to explore the biological potential beyond Earth (Hoehler, 2007), such as in Europa's oceans (Zolotov & Shock, 2003, 2004; McCollom, 1999).

The total amount of energy available to a microorganism can be readily quantified by calculating the Gibbs energy of reaction, $\Delta G_r$, at the particular temperature, pressure and composition of interest. Negative values of $\Delta G_r$ indicate that the electron donor-acceptor pair under consideration is not in equilibrium and could provide energy for organisms capable of catalyzing the transfer of electrons between the two molecules. Organisms must be able to catalyze these reactions faster than they occur abiotically if they are to gain energy from them. Values of Gibbs energies are calculated as follows:

$$\Delta G_r = RT \ln\left(\frac{Q}{K}\right) \qquad (4)$$

where $R$ stands for the gas constant (8.314 J / mol K), $T$ denotes the temperature in Kelvin, $Q$ designates the reaction quotient, and $K$ represents the equilibrium constant. Values of $Q$, which take into account the effects of aqueous chemistry on reaction energetics, can be calculated using

$$Q = \prod_i a_i^{v_i} \qquad (5)$$

where $a_i$ indicates the activity of the $i$th species and $v_i$ corresponds to the stoichiometric coefficient of the $i$th species. Values of $K$ were calculated using the revised-HKF equations of state (Helgeson et al., 1981; Shock et al., 1992; Tanger & Helgeson, 1988), the SUPCRT92 software package (Johnson et al. 1992), and thermodynamic data taken from several studies (Schulte et al., 2001; Shock & Helgeson, 1988, 1990; Shock et al., 1989; Sverjensky et al., 1997). Molalities of the $i$th species, $m_i$, listed in Table 5.2 were converted into activities using individual activity coefficients of the $i$th species ($\gamma_i$),

$$a_i = m_i \gamma_i \qquad (6)$$

Values of $\gamma_i$ were in turn computed as a function of temperature and ionic strength using an extended version of the Debye-Hückel equation (Helgeson, 1969) and Geochemist's Workbench. Non-redox species (e.g., $Na^+$, $Cl^-$) were used to charge balance the fluids described in Table 5.2 prior to thermodynamic calculations. All calculations of $\gamma_i$, $Q$, and $K$ were conducted at 1 bar but apply to the top several tens of kilometers of martian crust. The effect of changing lithostatic pressure on energetic parameters is negligible (<0.2%) within the top five kilometers of martian crust – the zone with which this study is concerned.

Reaction Transport Model

Gibbs energy calculations quantify the favorability of AOM reactions for a particular set of conditions. However, because these conditions are influenced by the rates of chemical reactions and the transport of reactant and product species, reaction transport models (RTMs) are required to assess the plausibility of biogeochemical processes in dynamic environments. In order to assess the likelihood that AOM could sustain life on

Mars, an RTM was developed that considers advection and diffusion of nutrients, AOM reaction rates, and the feedback between growing organisms' methane consumption and downstream concentrations.

Several other investigators have developed RTMs with specific AOM-centered questions in mind (for a recent review, see Regnier et al., 2011). Treude et al. (2003) model changing methane concentrations with time, considering diffusion and advection of dissolved sulfate and methane, depth-dependent sediment porosity, and a kinetically dictated rate of AOM. Dale et al. (2006) place AOM within a larger ecological context, ultimately applying the model to Skagerrak sediment cores to show that low levels of methane persist at the surface due to bioenergetic limitations (Dale et al., 2008). Orcutt and Meile (2008) examine AOM energetics at the consortium scale to show that the accumulation of proposed interspecies intermediates such as hydrogen or formate result in low Gibbs energy availability.

The RTM presented here builds upon many features of the models highlighted above, and is tailored to our specific investigation. We constructed a one-dimensional model that simulates a vertical column of groundwater-infused rocky martian crust receiving a methane flux from below. The source of $CH_4$ is attributed to serpentinization and downstream reactions that are hypothesized to have occurred on early Mars (Cardace & Hoehler, 2009; Oze & Sharma, 2007) and/or hydrothermal alteration of basalt with C-rich fluids (Lyons et al., 2005). An initial $CH_4$ concentration of 2 mM is used (Alperin et al., 1988; see Supplementary Information), and methane formation reactions (e.g., reactions 2 and 3) are not incorporated into the model.

The model tracks the changing concentrations of methane, sulfate, oxidized carbon species ($CO_2$, $HCO_3^-$, or $CO_3^{2-}$), and reduced sulfur species ($H_2S$ or $HS^-$), due to advection, diffusion, and AOM. Furthermore, the Gibbs energy of AOM, the reaction quotient ($Q$), and the amount of biomass are computed at each reaction step. The RTM was run in Matlab, simulating a 100 m-long layer of martian crust over 1000 Earth days. This mixing zone is often framed as a vertical column, with methane rich fluid coming from below, but it could be oriented in any manner such that advective flow facilitates movement of the fluid front. These parameters were selected to portray the initial perturbations and steady-state results of an AOM-based microbial system while minimizing computation intensity.

The upper boundary of the crustal layer under consideration could range from 12.5 m below the martian surface (to ensure sufficient pressure to maintain 2 mM dissolved methane) to several kilometers (beyond which chemical activities and equilibrium constants change significantly). Within the experimental zone, pressure was not considered, as effects on all reported parameters were insignificant.

Concentration of the *i*th species, $C_i$, was determined using a standard 1-D advection-diffusion-reaction equation (e.g., Berner, 1980),

$$\phi \frac{\partial C_i}{\partial t} = \frac{\partial}{\partial z}\left(\phi D_{i,T} \frac{\partial C_i}{\partial z}\right) - \frac{\partial}{\partial z}\left(\phi u C_i\right) - \phi R_{AOM} \qquad (7)$$

where $\phi$ represents porosity, $D_{i,T}$ stands for the temperature-dependent diffusion coefficient for species *i* ($m^2$/d), *u* indicates the advection velocity (m/d), $R_{AOM}$ represents the rate of consumption or production of species *i* due to AOM (mol/$m^3$ d), and *t* and *z* are time (d) and vertical distance (m), respectively. The partial differential equations were discretized, with components allowing for diffusive, advective, and reactive losses and gains, depending on whether the species was consumed or produced by AOM.

The rate of AOM, $R_{AOM}$, was described by a second order bimolecular rate law exhibiting Monod-type dependence on methane and sulfate concentrations, tempered by a thermodynamic term:

$$R_{AOM} = V_{\max}\left(\frac{C_{CH_4}}{C_{CH_4} + K_{CH_4}}\right)\left(\frac{C_{SO_4^{2-}}}{C_{SO_4^{2-}} + K_{SO_4^{2-}}}\right)F_T \qquad (8)$$

In equation (8), $V_{\max}$ indicates the maximum rate of AOM that has been observed in a terrestrial context (mol/$m^3$ d), *K* values represent half saturation constants for the indicated reactants (M), and $HSO_4^-$ concentration is used in place of $SO_4^{2-}$ concentration at pH < 1.92. $F_T$ stands for the thermodynamic rate-limiting term, which is calculated according to (LaRowe et al., 2012):

$$F_T = \frac{1}{\exp\left(\frac{\Delta G_r^0 + F\Delta\Psi}{RT}\right)+1} \quad \text{for } \Delta G_r^0 \leq 0 \qquad (9a)$$

$$F_T = 0 \qquad \text{for } \Delta G_r^0 > 0 \qquad (9b)$$

where $F$ signifies the Faraday constant and $\Delta\Psi$ represents the electric potential spanning an organism's membrane (V). A thermodynamic limiting term is included in Eq. (8) to accommodate limitation of catabolic reaction rates by their energy yield (Jin & Bethke, 2003) and as a check to ensure that the reaction under consideration is thermodynamically possible under the specified conditions. $F_T$ takes on values between 0 and 1.

Changes in microbial biomass ($X$) are computed using:

$$\frac{dX}{dt} = YR_{AOM} - DX \qquad (10)$$

where Y indicates the growth yield (mg biomass per mol of reaction turnover), and D represents the biomass decay constant ($d^{-1}$). Any calculation of biomass and its changing abundance assumes the non-limiting presence of nutrients and micronutrients other than methane and sulfate, which is not explicitly considered here. A maximum microbial load of $3\times10^6$ mg/m$^3$, beyond which no further growth was permitted, was used as an upper limit based on abundances measured at terrestrial cold seeps (Orcutt et al., 2005).

The Gibbs energy ($\Delta G_r$) and reaction quotient ($Q$) were calculated as described in equations (4) and (5), respectively. The parameter values used in the RTM are provided in the Supplementary Information. The RTM was run in two different modes in order to account for contingencies in the geochemical behavior of martian sulfate deposits. The "finite-sulfate" variation assumes that the sulfate present in the fluid at $t$ = 0 is the only

biologically available sulfate for the duration of the simulation. The "sulfate-replacement" mode allows for the replenishment of sulfate, a scenario that would reflect an aquifer hosted in readily soluble sulfate-bearing minerals.

**Results**

Gibbs energy calculations indicate that the AOM reactions (Table 5.3) in all seven fluids under all four atmospheric composition scenarios are exergonic, suggesting that this metabolism would have been possible on Mars given the assumptions described above.

Table 5.3: Initial $\Delta G_r$ values for the AOM reaction at various estimated $CO_2$ partial pressures in modeled martian atmospheres for the seven fluids considered in this study. All values in kJ per mol of methane.

| Fluid | Atm. Independent 1 μM $CO_2$ (aq) | Modern Atm. 6 mbar $CO_2$ | Ancient Atm. 200 mbar $CO_2$ | Thick Ancient Atm. 2 bar $CO_2$ |
|---|---|---|---|---|
| **1** | -126.90 | -113.72 | -105.03 | -99.33 |
| **2** | -134.86 | -122.20 | -111.74 | -104.90 |
| **3** | -104.10 | -90.69 | -82.22 | -76.69 |
| **4** | -48.41 | -60.75 | -52.07 | -46.36 |
| **5** | -66.00 | -67.16 | -58.43 | -52.00 |
| **6** | -106.40 | -108.72 | -99.40 | -93.11 |
| **7** | -52.53 | -39.38 | -36.64 | -31.04 |

Table 5.3 presents the Gibbs energies available immediately upon the introduction of 2 mM methane to the seven fluids. The RTM allows for microbial metabolism to consume methane and sulfate while increasing dissolved inorganic carbon (DIC) and reduced sulfur concentrations, effectively lowering the amount of available energy. Ultimately, either methane or sulfate becomes limiting, and the Gibbs energy of AOM becomes endergonic and thus thermodynamically unfeasible. To visualize the spatial dependence of usable energy, heat maps of Gibbs energy values at $t$ = 1000 days (steady

state) were generated (Figure 5.1). Each of the eight panels in this figure depicts data for a specific atmospheric composition-sulfate replacement condition; panels are subdivided by fluid composition, and each bar signifies an advection velocity. The y-axis indicates the distance from the introduction of methane-rich fluid into the modeled martian aquifer (where 0 represents the interface). All heat map coloration is on the same scale, from -135 kJ / mol (red) to 0 kJ / mol (green); positive Gibbs values (endergonic conditions) are plotted uniformly in gray. Overall, Gibbs energy maps of 224 distinct combinations of atmospheric composition, degree of sulfate replenishment, fluid composition, and advection velocity were generated and are provided in Figure 5.1.

The rate of biomass production was determined for each set of conditions. Two separate phases of productivity are apparent when biomass is plotted as a function of time (Figure 5.2). During the first phase, the quantity of biological material increases exponentially; thereafter, the rate of biomass increase is linear as the system reaches a steady state. The slopes of the associated best-fit lines represent the amount of biomass generated per day (until the carrying capacity is attained). These values are provided in Table 5.4 and demonstrate the biological production capacity of each simulated condition, which ranges from 4 mg/d in Fluids 5 and 7 ($u$ = 0 m/d and sulfate is not replenished) to 77269 mg/d in Fluid 5 (ancient atmosphere, $u$ =3 m/d, and sulfate is replaced). Ultimately, biomass saturation ($3x10^6$ mg/m$^3$) is reached in all zones of exergonic AOM.

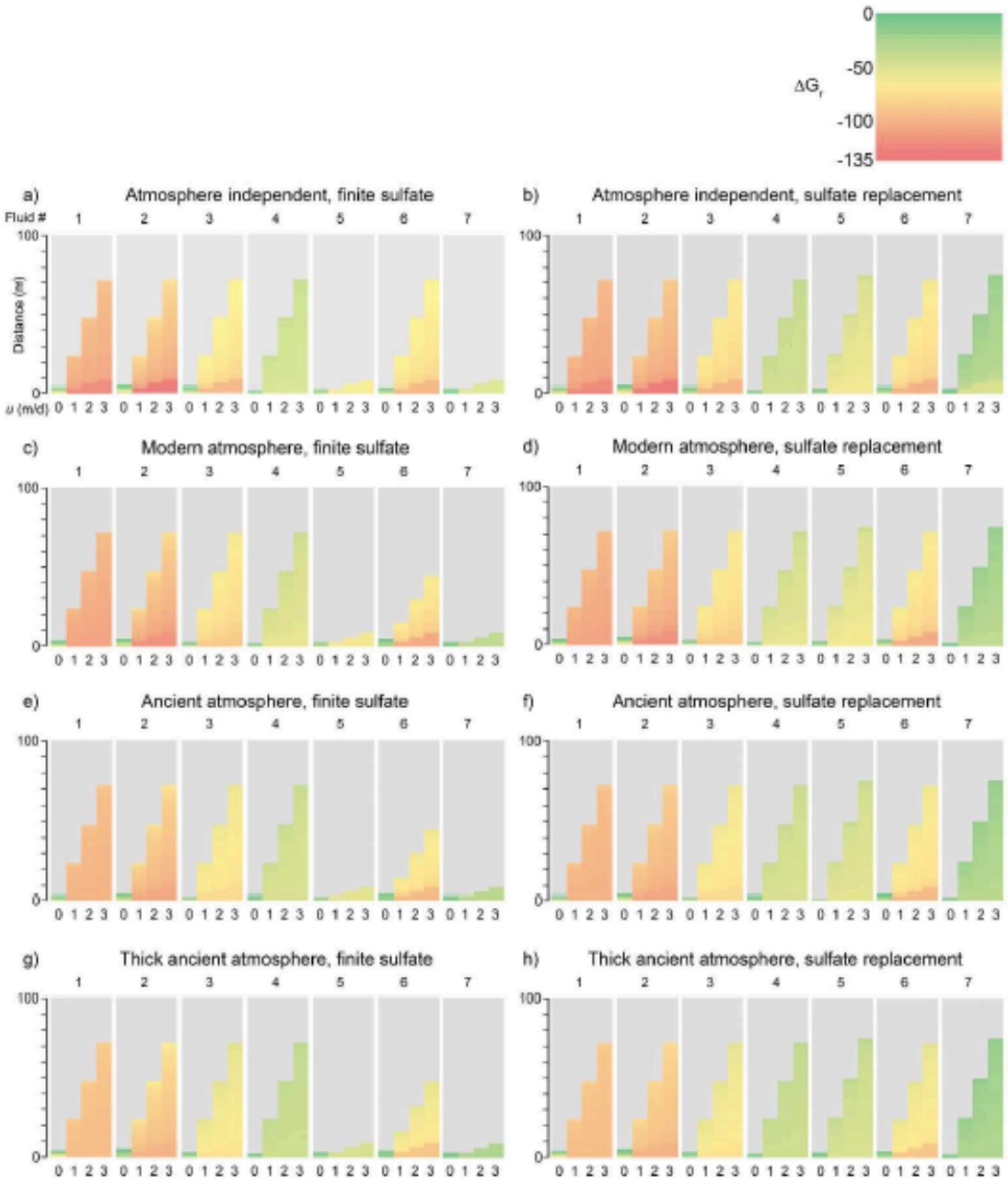


Figure 5.1: Heat maps representing Gibbs energies for AOM in seven fluids at $t$ = 1000 days and advection velocities $u$ of 0-3 m/d for both finite-sulfate and sulfate-replacement scenarios. Only negative Gibbs values are plotted on the heat map; positive values are undifferentiated and shown in gray. The vertical axis represents the distance away from the introduction of methane-rich fluid into the martian aquifer. All values are in kJ / mol $CH_4$ .

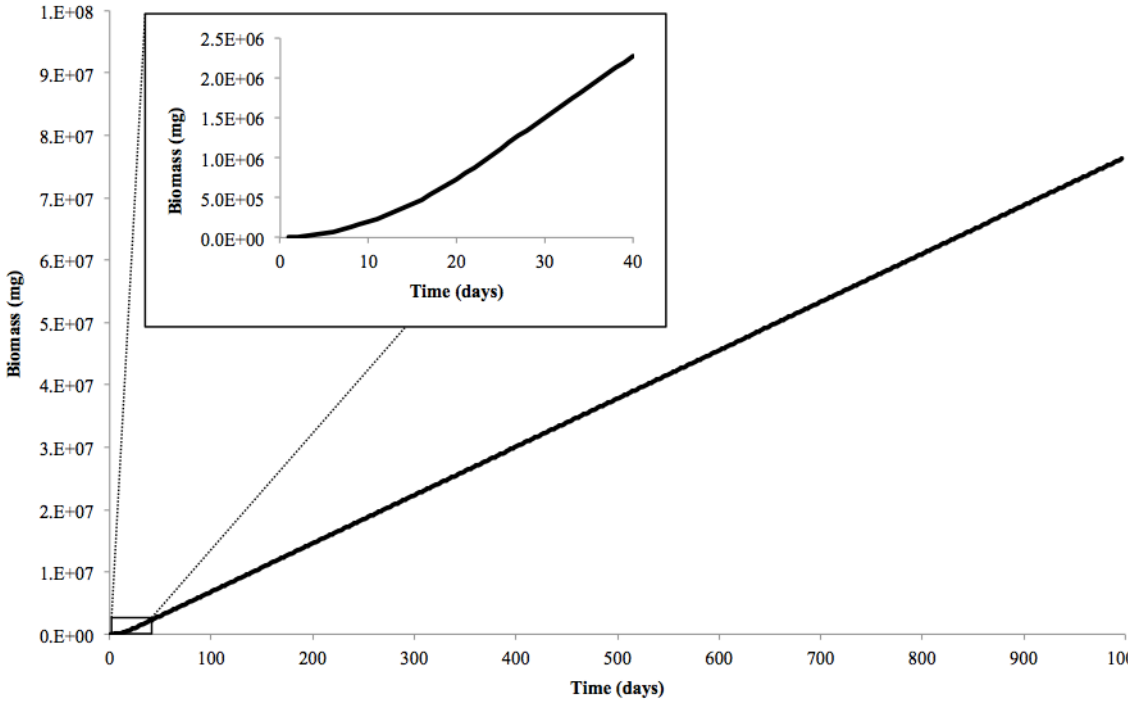


Figure 5.2: Biomass production rate of the entire mixing zone for a representative 1000-day model run (fluid 2, atmosphere-independent, u = 3, finite-sulfate). After an initial exponential increase in biomass with time (inset), the production rate reaches a constant value.

## Discussion

Controls on Energetic Feasibility of Martian AOM

Gibbs energy values for all considered fluid compositions and $CO_2$-dominated atmospheres are exergonic upon the introduction of 2 mM $CH_4$ ($t$ = 0). Values of available energy range from -31 kJ/mol (Fluid 7 under a thick ancient atmosphere) to -135 kJ/mol (Fluid 2 in the atmosphere-independent condition). All conditions are more exergonic than the estimated energetic limit for microbial life on Earth, which has been reported to be approximately -20 kJ/mol (Schink, 1997), though a wide range of values for this limit has been proposed (e.g., Hoehler, 2004 and references therein). It is also important to note that

our calculated Gibbs energy values are reflective of initial geochemical concentrations; localized intracellular energies could differ depending on transport mechanisms, and would dissipate as reactants are used and products are generated.

The Gibbs energy variations are tightly coupled to the initial activities of a fluid's reactants ($CH_4$, $HSO_4^-$, $SO_4^{2-}$) and products ($CO_2$, $HCO_3^-$, $CO_3^{2-}$, $H_2S$, $HS^-$). With atmospheres of higher $CO_2$ concentrations, the AOM reaction becomes less exergonic, as the putative organism must "push" against higher levels of DIC, which is a product of the reaction. Temperature is also an important factor (see Eq. 1): Fluid 2, which exhibits the largest energy yield across all atmospheric possibilities, does not have the largest difference between the equilibrium constant and the reaction quotient (see Eq. 4), but its high temperature (357 K) produces a more negative Gibbs energy result. Although 357 K is warmer than the optimal growth temperature of many terrestrial microorganisms, it is well within the survival range of thermophiles (Madigan & Orent, 1999), including thermophilic AOM-mediating organisms (Kallmeyer & Boetius, 2004; Holler et al., 2011).

Gibbs energy profiles produced by the RTM show that the spatial extent of AOM exergonicity is strongly dependent upon the advection velocity ($u$). For example, under atmosphere-independent, finite-sulfate conditions, Fluid 1 yields exergonic conditions for 4 m with an advection velocity of 0 m/d, 24 m for 1 m/d, 48 m for 2 m/d, and 72 m for 3 m/d (Figure 5.1a). For each meter per day that advection increases, approximately 24 additional meters of martian crust are perfused with an exergonic AOM aqueous chemistry, a relationship that is consistent across all non sulfate-limiting conditions.

The other major control on AOM-amenable crustal volume is the starting methane concentration. Under sulfate-replacement conditions, each 1 mM increase in the dissolved

Table 5.4: Rates of biomass production for each of the fluid – atmospheric composition – sulfate replacement combinations addressed in this study (mg biomass / day). All values are obtained from best linear fits to plots of overall biomass as a function of time between $t$ = 100 and $t$ = 1000 and represent steady state conditions.

| | | Atmosphere-independent | | | | Modern atmosphere | | | | Ancient atmosphere | | | | Thick ancient atmosphere | | | |
|---|---|---|---|---|---|---|---|---|---|---|---|---|---|---|---|---|---|
| Finite-sulfate | Fluid | $u=0$ | $u=1$ | $u=2$ | $u=3$ | $u=0$ | $u=1$ | $u=2$ | $u=3$ | $u=0$ | $u=1$ | $u=2$ | $u=3$ | $u=0$ | $u=1$ | $u=2$ | $u=3$ |
| | **1** | 42 | 25442 | 50845 | 76249 | 42 | 25442 | 50845 | 76249 | 42 | 25442 | 50845 | 76249 | 42 | 25442 | 50845 | 76247 |
| | **2** | 42 | 25419 | 50799 | 76179 | 42 | 25419 | 50838 | 76180 | 42 | 25419 | 50799 | 76179 | 10 | 25400 | 50764 | 76146 |
| | **3** | 39 | 25440 | 50842 | 76244 | 39 | 25440 | 50842 | 76244 | 39 | 25440 | 50842 | 76244 | 39 | 25440 | 50842 | 76244 |
| | **4** | 42 | 25442 | 50845 | 76249 | 39 | 25403 | 50807 | 76249 | 42 | 25442 | 50845 | 76247 | 42 | 25442 | 50845 | 76247 |
| | **5** | 4 | 2225 | 4447 | 6669 | 4 | 2225 | 4447 | 6669 | 4 | 2225 | 4446 | 6667 | 4 | 2225 | 4446 | 6667 |
| | **6** | 38 | 15665 | 31274 | 46932 | 38 | 15665 | 31298 | 46932 | 38 | 15670 | 31306 | 46945 | 38 | 16778 | 33521 | 50266 |
| | **7** | 4 | 2180 | 4356 | 6532 | 4 | 2177 | 4351 | 6524 | 4 | 2176 | 4348 | 6520 | 4 | 2176 | 4348 | 6520 |
| | | | | | | | | | | | | | | | | | |
| | | Atmosphere-independent | | | | Modern atmosphere | | | | Ancient atmosphere | | | | Thick ancient atmosphere | | | |
| Sulfate-replacement | Fluid | $u=0$ | $u=1$ | $u=2$ | $u=3$ | $u=0$ | $u=1$ | $u=2$ | $u=3$ | $u=0$ | $u=1$ | $u=2$ | $u=3$ | $u=0$ | $u=1$ | $u=2$ | $u=3$ |
| | **1** | 42 | 25442 | 50845 | 76249 | 42 | 25442 | 50845 | 76249 | 42 | 25442 | 50845 | 76249 | 42 | 25442 | 50845 | 76247 |
| | **2** | 48 | 25437 | 50834 | 76232 | 48 | 25437 | 50873 | 76232 | 48 | 25437 | 50831 | 76227 | 10 | 25400 | 50800 | 76199 |
| | **3** | 39 | 25441 | 50843 | 76245 | 39 | 25441 | 50843 | 76245 | 39 | 25441 | 50843 | 76245 | 39 | 25441 | 50843 | 76245 |
| | **4** | 42 | 25442 | 50845 | 76249 | 39 | 25403 | 50807 | 76249 | 42 | 25442 | 50845 | 76247 | 42 | 25442 | 50845 | 76247 |
| | **5** | 41 | 25778 | 51517 | 77256 | 41 | 25778 | 51516 | 77255 | 41 | 25783 | 51526 | 77269 | 41 | 25782 | 51525 | 77268 |
| | **6** | 44 | 25432 | 50787 | 76219 | 44 | 25432 | 50826 | 76219 | 44 | 25432 | 50826 | 76220 | 44 | 25433 | 50828 | 76222 |
| | **7** | 41 | 25510 | 50982 | 76454 | 41 | 25480 | 50922 | 76363 | 41 | 25471 | 50904 | 76336 | 39 | 25472 | 50905 | 76338 |

methane concentration puts an additional ~11*$u$ meters of crust under exergonic conditions (the exact coefficients of this relationship depend upon the precise fluid-atmospheric composition situation). The spatial extent of exergonic AOM reaches a steady state after the fluid front moves through the entire zone of negative Gibbs energy; in most cases, this occurs after 24 days. Even with significantly longer run times (e.g., $1\times10^6$ days), Gibbs energy values remain constant, as metabolic activity rates reach a steady state with reactant fluxes.

In zones of positive Gibbs energies, AOM is limited by insufficient sulfate or methane concentrations. Sulfate-replacement cases are spatially constrained by methane (Figure 5.1b, 5.1d, 5.1f, 5.1h); finite-sulfate scenarios can be limited by either reactant, depending on the initial fluid chemistry. Fluids 5, 6, and 7, which have the lowest starting sulfate concentrations, are sulfate-limited when sulfate is not replenished and methane-limited when sulfate is held constant at its initial concentration. The consequences are most visible in comparisons of spatial extent of exergonic conditions in panels 5, 6, and 7 between Figures 5.1a and 5.1b, 5.1c and 5.1d, 5.1e and 5.1f, and 5.1g and 5.1h.

Many transitions between Gibbs energy states are abrupt. The exergonic-endergonic shift is controlled by reactant concentration, while relative changes within the exergonic zone are driven by product accumulation (and, less significantly, by the RTM's 1-meter grid spacing). Endergonic sites are often neighbored by strongly exergonic locations, with little gradation between the two. In the panel for Fluid 1 in Figure 1a, for example, at 72 m past the mixing front when advection is 3 m/d, the steady state Gibbs energy is -97 kJ/mol. At 73 m, the Gibbs energy is highly endergonic. The transition is attributable to methane limitation (or sulfate limitation for the finite-sulfate cases of Fluids

5, 6, and 7). For the first 72 m of mixing space, incoming methane-rich fluid is able to supply more methane than AOM can process. This distance is advection velocity-dependent because higher flow rates deliver more methane per unit time to the system, overloading local AOM capabilities and allowing methane to advance further through the aquifer. However, even as the last methane is consumed from Fluid 1, the process is highly exergonic because sulfate concentrations remain high (2.21 mol/kg at 72 m, compared with 2.23 mol/kg at 0 m). In general, fluids that produce more exergonic conditions upon initial mixing (Table 5.3) generate more sudden spatial transitions from highly exergonic to endergonic conditions because the ancillary factors that made the reaction favorable in the first place (low sulfide concentration, or higher temperature, for example) remain even as the limiting reactant, whether sulfate or methane, is depleted.

The stark energetic transitions within the exergonic zone – most visibly at 4 m, 7 m, and 10 m for advection velocities of 1, 2, and 3 m/d, respectively – are caused by product accumulation and advection velocity. For example, in Figure 5.1a, Fluid 2, $u$=3 m/d, $Q$ increases by more than two orders of magnitude between 9 m and 10 m and $\Delta G_r$ changes from -135 kJ/mol to -116 kJ/mol. The location of this shift is dependent on $u$, as higher flow rates are able to push more exergonic conditions representative of the initial interface deeper into the mixing zone. The magnitude of the transition results from product build-up: when starting from low concentrations of AOM products, initial increases from biological activity represent a large proportional change and exert a significant effect on energetic parameters. The magnitude of these transitions lessens as initial DIC concentrations increase with thicker atmospheres, as seen with Fluid 2 in Figures 5.1a, 5.1c, 5.1e, and 5.1g. The transitions remain most abrupt for Fluid 6, which

has the lowest starting concentration of sulfide, meaning that its proportionally significant increase continues to drive Gibbs energy transitions despite higher initial DIC concentrations.

In the model scenarios presented in this study, Gibbs energy availability does not exhibit a strong deterministic effect on the rate of biomass production, as long as the reaction is exergonic. Gibbs energy values for a given fluid vary by an average of 29% across the range of atmospheric compositions; the variation in biomass production rates across atmospheric compositions averages 1% (for a given advection velocity). Rather, the spatial extent of negative Gibbs energies – determined largely by advection velocity and the distribution of reactants – exerts the strongest effect on biomass production rates. With sufficient time, all zones of exergonic AOM reach the model-specified biomass carrying capacity. Thus, higher advection velocities, which extend the zone of exergonic Gibbs energies, lead to higher overall biomass yields. The time required to attain this biomass varies from 7.3 years (Fluid 6, thick ancient atmosphere, $u$=1 m/s, finite-sulfate) to 6160 years (Fluids 5 and 7, all atmospheres, $u$=0, finite-sulfate). With no advection, rates of biomass production (Table 5.4) are approximately three orders of magnitude lower than under advective flow conditions, requiring longer timeframes to achieve biomass saturation.

Models for Martian AOM

The calculations described in this study demonstrate that AOM was likely an energetically viable metabolism on ancient Mars, yielding Gibbs energies in excess of those found in low-energy terrestrial environments (Hoehler et al., 2001; Jackson &

McInerney, 2002). The key question is thus whether it was possible or probable on ancient Mars for sulfate-bearing waters to interact with methane sources.

Sulfates need not be present at high environmental concentrations to sustain AOM (Beal et al., 2011); nonetheless, they are relatively common on Mars. Sulfur-bearing species have been identified at several surface sites (Kounaves et al., 2010; Squyres et al., 2004; Toulmin et al., 1977; Wang et al., 2006; Wänke et al., 2001). Various regionally extensive polyhydrated and monohydrated sulfate-bearing geologic units have been observed from orbit, distributed across the planet (Bibring & Langevin, 2008), and Murchie et al. (2009) describe five distinct classes of sulfates that express a range of co-occurring minerals and layer-forming tendencies. Oxidized sulfur is also present in the ubiquitous martian dust (6.8 wt% $SO_3$) and soil (6.2 wt% $SO_3$) (Taylor & McLennan, 2009). The multiple forms and widespread nature of sulfur species suggest that aqueously mobilized sulfate would have been prevalent, resulting from groundwater interaction with large sulfate deposits and/or sulfur-containing particulates.

Methane production can result abiotically either from the reaction of carbon dioxide with serpentinization-derived hydrogen in ultramafic rocks (Oze and Sharma, 2005) or hydrothermal alteration of basalt (Lyons et al., 2005) as noted above. Consequently, two endmember scenarios for geologic settings favorable to AOM on Mars can be envisaged – one rare (with a single location identified to date) and one common (with thousands of potential locations).

In the NE Syrtis model (Figure 5.3a), mineralogical expressions on the modern martian surface suggest an ancient groundwater regime that would have produced and then mixed both AOM reactants at the contact between two large, regionally extensive

geologic units. The eroded transition between the Syrtis Major lava flows and the Isidis Basin, a region known as NE Syrtis, exhibits multiple manifestations of extensive and prolonged aqueous activity, from fluvial morphology (Mangold et al., 2007) to mineral signatures indicative of varied geochemical conditions (Ehlmann et al., 2009; Ehlmann et al., 2010).

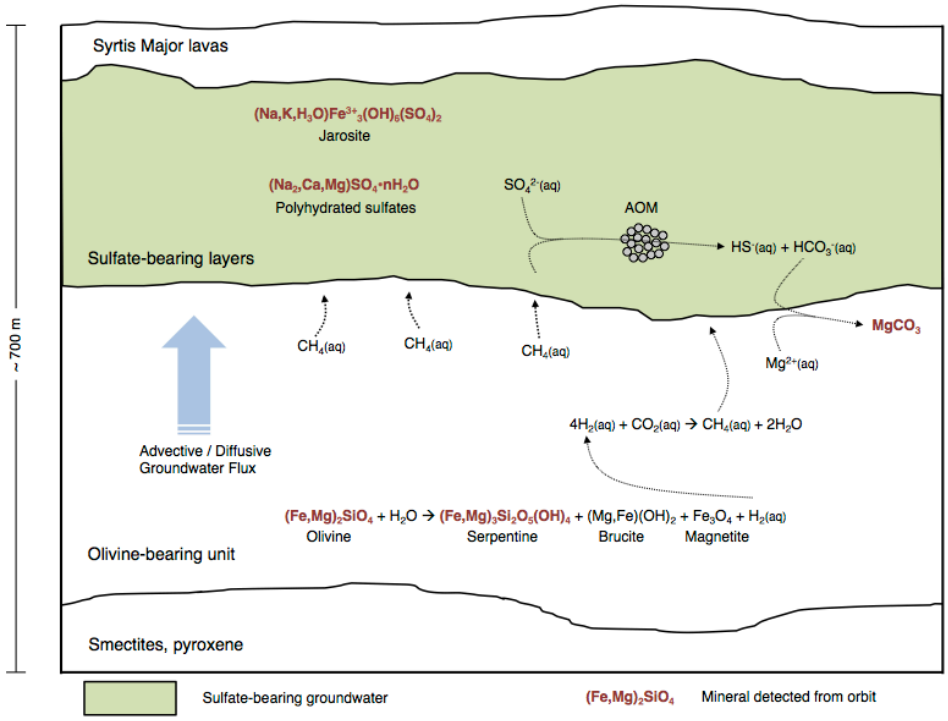


Figure 5.3a) A model for potential AOM on Mars, using the stratigraphy at NE Syrtis Major. Within a water-permeated section, serpentinization of the olivine-bearing unit produces hydrogen, which in turn generates methane in the abiotic reduction of $CO_2$. This methane diffuses upward and is entrained in buoyant, heat-driven advective flow. In the overlying jarosite-bearing layer, dissolved sulfate and incoming methane provide the reactants for AOM, which produces carbonate species that may form magnesium carbonate minerals. Many of the minerals involved in this model have been observed from orbit, and calculations suggest that the AOM metabolism is energetically favorable given modeled fluid chemistries.

Ehlmann and Mustard (2012) describe a particular ~700 m-thick stratigraphic section in which an olivine-rich unit underlies sulfate deposits. As observed elsewhere in

the region, the olivine-bearing unit appears to have been partially altered to serpentine and Mg-carbonate, both of which are consistent with AOM activity. Serpentinization provides potential fuel for AOM by generating hydrogen and facilitating abiotic methanogenesis, and carbonate ions are products of the AOM metabolism. Indeed, large carbonate mounds are frequently found in association with terrestrial cold seeps (Teichert et al., 2005). Overlying sulfate deposits, spectrally indicated by jarosite absorption features, point to a shift in geochemistry from neutral-alkaline to acidic waters (likely pH<4, Papike et al., 2006). The contact between olivine- and sulfate-bearing units may have allowed for methane- and sulfate-bearing groundwaters that could have formed the basis for biological AOM. Methane produced through serpentinization and subsequent reactions would have dissolved in the groundwater and moved upward, via diffusion and possibly advective flow, into sulfate-rich deposits (Figure 5.3a). In this case, the ridges within the sulfate units, inferred to be mineralized conduits of fluid flow, would be a prime target for astrobiological missions searching for organic carbon or AOM biomarkers.

NE Syrtis-type conditions appear to be rare. Evidence of hydrogen- (and thus methane)-generating serpentinization, in the form of the mineral serpentine, has been seen in about a dozen other orbital images across a range of geological provinces (Ehlmann et al. 2010), none of which is also in direct contact with sulfate-bearing units. On the other hand, the basalt alteration model (Figure 5.3b) allows for methane production from the reaction of hydrothermal, carbon-rich fluid with basaltic crust at several km depth (Lyons et al., 2005). Basalt is ubiquitous on Mars, making this scenario of methane production more promising on a large scale. Moreover, it has been proposed that groundwater

systems and hydrothermal subsurface aqueous alteration of basalt were globally widespread during the Noachian period, forming the hydrated silicate mineral assemblages found in thousands of exposures of Noachian crust on Mars (Mustard et al., 2008; Ehlmann et al., 2011).

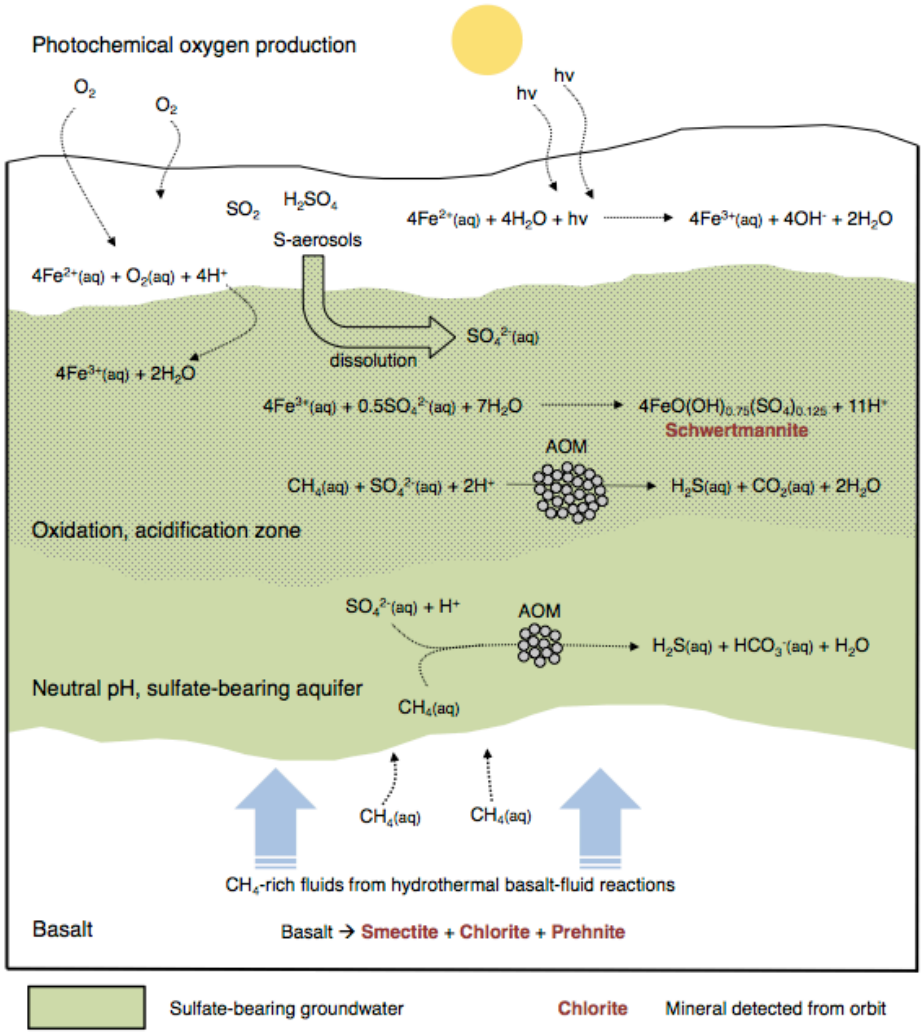


Figure 5.3b) An alternative scenario for martian AOM, in which methane is produced by subsurface hydrothermal alteration of basaltic crust (Lyons et al., 2005) and acid sulfate conditions (i.e., typical of fluids 1-3) are produced from fluids derived near the surface. Sulfate-bearing waters are formed by aerosol deposition and subsequent dissolution of oxidized sulfur species by water. Acidity is generated through iron oxidation and schwertmannite formation within sulfate-bearing groundwaters as is thought to have occurred at Meridiani Planum and other locations (Hurowitz et al., 2010). As methane is

produced through hydrothermal alteration of basalt in the subsurface, AOM could proceed at the zone of mixing of these waters. The reaction is particularly favorable in zones of acidic, sulfate-rich groundwater, potentially leading to larger biomass yields.

In the most potentially widespread scenario, sulfate-bearing groundwater is generated from the dissolution of oxidized sulfur aerosols, which may have precipitated from the atmosphere following volcanic expulsion (Settle, 1979). Iron oxidation, mediated by atmospheric molecular oxygen or solar radiation, and the precipitation of schwertmannite (an iron-oxyhydroxysulfate mineral) would have generated acidic geochemical conditions (Hurowitz et al., 2010). The low pH and high sulfate concentrations posited in this model are similar to Fluids 1, 2, and 3, all of which yielded highly exergonic AOM conditions. Because the hydrated silicate minerals formed by subsurface aqueous alteration of basalt are found in thousands of exposures of Noachian crust, many sites are available for astrobiological investigation. Locations with well-preserved evidence of fluid flow (e.g., ridges or hydrothermal zones) would be promising sites to search for evidence of past biological methane oxidation.

Several environmental and geological factors could preclude biological AOM on early Mars. In order for methanotrophic organisms to live off of methane- and sulfate-rich fluids, biochemical consumption of methane must be more kinetically or thermodynamically favorable than abiotic sinks. Given the high temperatures and exotic chemical catalysts required for abiotic methane oxidation (Li & Hoflund 2003), microbial metabolisms would have been favored over abiotic reactions in all environments considered in this study. Geochemical barriers to AOM include insufficient reactants or high concentrations of products that could substantially alter the reaction quotient.

Because of the importance of advection in extending the footprint of exergonic conditions, hydrologically inert sites would exhibit very low biomass levels. Subsurface AOM environments would be shielded against the direct effects of ionizing radiation, which are negligible below approximately 5 m depth (Dartnell et al. 2007).

**Conclusions / Implications**

This study demonstrates that AOM may have been an energy-yielding metabolism for putative organisms on ancient Mars, when liquid water was abundant on and below the planet's surface. Gibbs energy values indicate that exergonic conditions were present upon the addition of dissolved methane to model fluids representative of a range of martian geochemistries. Results from the RTM show that such energy yielding conditions would have persisted in steady state in a relatively narrow, advection velocity-determined envelope of the martian subsurface. Provided that additional physico-chemical requirements for life were met, including the availability of nitrogen, phosphorous, and other nutrients, AOM may have formed the basis for a sustainable ecosystem.

In order to establish a long-term biosphere, methane production would have needed to persist over hundreds of thousands or millions of years. Dissolved species transport, through diffusion or, more usefully, advection, would have been necessary to both supply nutrients and remove end products, maintaining favorable energetic conditions. Given these considerations, sites on Mars exhibiting significant deposits of sulfate minerals, particularly those co-located with serpentine and/or evidence of basalt alteration by groundwater, would be the most promising places to search for evidence of AOM. Advective transport of AOM reactants is the strongest determinant of overall biomass, making hydrologic investigations particularly important in an astrobiological

context. Future astrobiology oriented missions could scour mineralogically and geologically appropriate target areas for isotopically distinct carbonates or sulfur minerals indicative of biological fractionation or diagnostic organic molecular fossils (Pancost et al., 2001).

Conditions amenable to AOM may persist in the martian subsurface today. Crust alteration reactions could initiate the abiotic synthesis of methane, and oxidized sulfur species could be mobilized by groundwater flow. This study shows that methane is consumed quickly upon its production, suggesting that a methane signature at the surface need not be present for local conditions to support AOM activity. Thus, although the search for modern-day methane in the martian atmosphere is intriguing, its absence (Webster et al. 2013) would have no bearing on the possibility of subsurface AOM proposed here.

Warmer and wetter martian conditions may have supported a number of metabolisms on ancient Mars. Given the exergonic potential of several different Mars analog fluids and geological evidence of reactant-generating conditions, AOM should be considered among the most promising and observationally constrained possibilities to support past or present life on Mars.

**References**

Allen Carlton C., Gooding JL, Jercinovic M, Keil K. (1981). Altered basaltic glass: A terrestrial analog to the soil of Mars. Icarus 45:347–369.

Alperin M. J., Reeburgh W. S., Whiticar MJ. (1988). Carbon and hydrogen isotope fractionation resulting from anaerobic methane oxidation. Global Biogeochemical Cycles 2:279–288.

Alt JC, Shanks III WC. (2006). Stable isotope compositions of serpentinite seamounts in the Mariana forearc: Serpentinization processes, fluid sources and sulfur metasomatism. Earth and Planetary Science Letters 242:272–285.

Amend Jan P, Rogers KL, Shock Everett L, Gurrieri S, Inguaggiato S. (2003). Energetics of chemolithoautotrophy in the hydrothermal system of Vulcano Island, southern Italy. Geobiology 1:37–58.

Amend Jan P, Shock Everett L. (2001). Energetics of overall metabolic reactions of thermophilic and hyperthermophilic Archaea and Bacteria. FEMS microbiology reviews 25:175–243.

Amend Jan P., McCollom Thomas M., Hentscher M, Bach W. (2011). Catabolic and anabolic energy for chemolithoautotrophs in deep-sea hydrothermal systems hosted in different rock types. Geochimica et Cosmochimica Acta 75:5736–5748.

Atreya SK, Mahaffy PR, Wong A-S. (2007). Methane and related trace species on Mars: Origin, loss, implications for life, and habitability. Planetary and Space Science 55:358–369.

Bach W, Edwards KJ. (2003). Iron and sulfide oxidation within the basaltic ocean crust: implications for chemolithoautotrophic microbial biomass production. Geochimica et Cosmochimica Acta 67:3871–3887.

Beal E. J., Claire MW, House C. H. (2011). High rates of anaerobic methanotrophy at low sulfate concentrations with implications for past and present methane levels. Geobiology 9:131–139.

Beal Emily J., House Christopher H., Orphan VJ. (2009). Manganese- and Iron-Dependent Marine Methane Oxidation. Science 325:184–187.

Bethke C. (2008). Geochemical and Biogeochemical Reaction Modeling. Cambridge University Press.

Bibring JP, Langevin Y. (2008). Mineralogy of the Martian surface from Mars Express OMEGA observations. In:The Martian Surface - Composition, Mineralogy, and Physical Properties, Cambridge University Press, pp. 153–168.

Boetius A., Ravenschlag K, Schubert CJ, Rickert D, Widdel F., Gleseke A, et al. (2000). A marine microbial consortium apparently mediating anaerobic oxidation of methane. Nature 407.

Boettger J, Lin H-T, Cowen JP, Hentscher M, Amend Jan P. (2012). Energy yields from chemolithotrophic metabolisms in igneous basement of the Juan de Fuca ridge flank system. Chemical Geology.

Boston PJ, Ivanov MV, P. McKay C. (1992). On the possibility of chemosynthetic ecosystems in subsurface habitats on Mars. Icarus 95:300–308.

Brack A, Pillinger CT. (1998). Life on Mars: chemical arguments and clues from Martian meteorites. Extremophiles 2:313–319.

Bradley AS, Summons RE. (2010). Multiple origins of methane at the Lost City Hydrothermal Field. Earth and Planetary Science Letters 297:34–41.

Brazelton WJ, Schrenk MO, Kelley DS, Baross JA. (2006). Methane-and sulfur-metabolizing microbial communities dominate the Lost City hydrothermal field ecosystem. Applied and environmental microbiology 72:6257–6270.

Cardace D, Hoehler Tori M. (2009). Serpentinizing Fluids Craft Microbial Habitat. Northeastern Naturalist 16:272–284.

Carr MH, Head III JW. (2010). Geologic history of Mars. Earth and Planetary Science Letters 294:185–203.

Costa KC, Navarro JB, Shock Everett L, Zhang CL, Soukup D, Hedlund BP. (2009). Microbiology and geochemistry of great boiling and mud hot springs in the United States Great Basin. Extremophiles 13:447–459.

Coulson IM, Beech M, Nie W. (2007). Physical properties of Martian meteorites: Porosity and density measurements. Meteoritics & Planetary Science 42:2043–2054.

Cousins CR, Griffiths AD, Crawford IA, Prosser BJ, Storrie-Lombardi MC, Davis LE, et al. (2010). Astrobiological considerations for the selection of the geological filters on the ExoMars PanCam instrument. Astrobiology 10:933–951.

Cowen JP. (2004). The microbial biosphere of sediment-buried oceanic basement. Research in microbiology 155:497–506.

Dale A. W., Regnier P., Van Cappellen P. (2006). Bioenergetic Controls on Anaerobic Oxidation of Methane (AOM) in Coastal Marine Sediments: A Theoretical Analysis. American Journal of Science 306:246–294.

Dale A.W., Regnier P., Knab NJ, Jørgensen BB, Van Cappellen P. (2008). Anaerobic oxidation of methane (AOM) in marine sediments from the Skagerrak (Denmark): II. Reaction-transport modeling. Geochimica et Cosmochimica Acta 72:2880–2894.

Daniels L, Sparling R, Sprott GD. (1984). The bioenergetics of methanogenesis. Biochimica et Biophysica Acta (BBA) - Reviews on Bioenergetics 768:113–163.

Dartnell L, Desorgher L, Ward J, Coates A. (2007). Martian sub-surface ionising radiation: biosignatures and geology. Biogeosciences Discussions 4:455–492.

Dimroth P, Von Ballmoos C, Meier T, Kaim G. (2003). Electrical Power Fuels Rotary ATP Synthase. Structure 11:1469–1473.

Edwards KJ, Bach W, McCollom Thomas M. (2005). Geomicrobiology in oceanography: microbe–mineral interactions at and below the seafloor. TRENDS in Microbiology 13:449–456.

Ehlmann B, Bish D, Ruff S, Mustard J. (2012). Mineralogy and chemistry of altered Icelandic basalts: Application to clay mineral detection and understanding aqueous environments on Mars. Journal of Geophysical Research: Planets (1991–2012) 117.

Ehlmann B. L., Mustard J. F., Murchie S. L. (2010). Geologic setting of serpentine deposits on Mars. Geophysical Research Letters 37:L06201.

Ehlmann Bethany L, Mustard John F, Murchie Scott L, Bibring Jean-Pierre, Meunier A, Fraeman AA, et al. (2011). Subsurface water and clay mineral formation during the early history of Mars. Nature 479:53–60.

Ehlmann Bethany L., Mustard John F. (2012). An in-situ record of major environmental transitions on early Mars at Northeast Syrtis Major. Geophysical Research Letters 39:L11202.

Ehlmann Bethany L., Mustard John F., Fassett CI, Schon SC, Head III JW, Des Marais DJ, et al. (2008). Clay minerals in delta deposits and organic preservation potential on Mars. Nature Geosci 1:355–358.

Ehlmann Bethany L., Mustard John F., Murchie Scott L., Poulet Francois, Bishop JL, Brown AJ, et al. (2008). Orbital Identification of Carbonate-Bearing Rocks on Mars. Science 322:1828–1832.

Ehlmann Bethany L., Mustard John F., Swayze GA, Clark RN, Bishop JL, Poulet Francois, et al. (2009). Identification of hydrated silicate minerals on Mars using MRO-CRISM: Geologic context near Nili Fossae and implications for aqueous alteration. Journal of Geophysical Research: Planets 114:E00D08.

Etiope G, Ehlmann Bethany L., Schoell M. (2012). Low temperature production and exhalation of methane from serpentinized rocks on Earth: A potential analog for methane production on Mars. Icarus. http://www.sciencedirect.com/science/article/pii/S0019103512001832.

Freeze R, Cherry J. (1979). Groundwater.

Gibson R, Atkinson R, Gordon J. (2005). Ecology of cold seep sediments: interactions of fauna with flow, chemistry and microbes. Oceanography and Marine Biology: An Annual Review 43:1–46.

Gislason SR, Arnórsson S. (1993). Dissolution of primary basaltic minerals in natural waters: saturation state and kinetics. Chemical Geology 105:117–135.

Haberle RM. (1998). Early Mars Climate Models. Journal of Geophysical Research: Planets 103:28467–28479.

Hallam SJ, Putnam N, Preston CM, Detter JC, Rokhsar D, Richardson PM, et al. (2004). Reverse methanogenesis: testing the hypothesis with environmental genomics. Science 305:1457–1462.

Hartmann W, Neukum Gerhard. (2001). Cratering Chronology and the Evolution of Mars. Space Science Reviews 96:165–194.

Helgeson Harold C. (1969). Thermodynamics of hydrothermal systems at elevated temperatures and pressures. American Journal of Science 267:729–804.

Helgeson Harold C., Kirkham DH, Flowers GC. (1981). Theoretical prediction of the thermodynamic behavior of aqueous electrolytes by high pressures and temperatures; IV, Calculation of activity coefficients, osmotic coefficients, and apparent molal and standard and relative partial molal properties to 600 degrees C and 5kb. American Journal of Science 281:1249–1516.

Hoehler T. M. (2004). Biological energy requirements as quantitative boundary conditions for life in the subsurface. Geobiology 2:205–215.

Hoehler Tori M. (2007). An energy balance concept for habitability. Astrobiology 7:824–838.

Hoehler Tori M., Alperin Marc J., Albert DB, Martens CS. (2001). Apparent minimum free energy requirements for methanogenic Archaea and sulfate-reducing bacteria in an anoxic marine sediment. FEMS Microbiology Ecology 38:33–41.

Holler T, Widdel Friedrich, Knittel K, Amann Rudolf, Kellermann MY, Hinrichs K-U, et al. (2011). Thermophilic anaerobic oxidation of methane by marine microbial consortia. ISME J 5:1946–1956.

House Christopher H, Beal Emily J, Orphan VJ. (2011). The apparent involvement of ANMEs in mineral dependent methane oxidation, as an analog for possible Martian methanotrophy. Life 1:19–33.

Hurowitz JA, Fischer WW, Tosca Nicholas J, Milliken RE. (2010). Origin of acidic surface waters and the evolution of atmospheric chemistry on early Mars. Nature Geoscience 3:323–326.

Inskeep W, Ackerman G, Taylor W, Kozubal M, Korf S, Macur R. (2005). On the energetics of chemolithotrophy in nonequilibrium systems: case studies of geothermal springs in Yellowstone National Park. Geobiology 3:297–317.

Inskeep W, McDermott T. (2005). Geomicrobiology of acid-sulfate-chloride springs in Yellowstone National Park. Geothermal biology and geochemistry in Yellowstone National Park 143–162.

Jackson BE, McInerney MJ. (2002). Anaerobic microbial metabolism can proceed close to thermodynamic limits. Nature 415:454–456.

Jin Q, Bethke CM. (2003). A New Rate Law Describing Microbial Respiration. Applied and Environmental Microbiology 69:2340–2348.

Johnson JW, Oelkers EH, Helgeson Harold C. (1992). SUPCRT92: A software package for calculating the standard molal thermodynamic properties of minerals, gases, aqueous species, and reactions from 1 to 5000 bar and 0 to 1000°C. Computers & Geosciences 18:899–947.

Joye SB, Boetius Antje, Orcutt BN, Montoya JP, Schulz HN, Erickson MJ, et al. (2004). The anaerobic oxidation of methane and sulfate reduction in sediments from Gulf of Mexico cold seeps. Chemical Geology 205:219–238.

Kadenbach B. (2003). Intrinsic and extrinsic uncoupling of oxidative phosphorylation. Biochimica et Biophysica Acta (BBA) - Bioenergetics 1604:77–94.

Kallmeyer J, Boetius Antje. (2004). Effects of Temperature and Pressure on Sulfate Reduction and Anaerobic Oxidation of Methane in Hydrothermal Sediments of Guaymas Basin. Applied and Environmental Microbiology 70:1231–1233.

Klingelhöfer G, Morris RV, Bernhardt B, Schröder C, Rodionov DS, De Souza PA, et al. (2004). Jarosite and Hematite at Meridiani Planum from Opportunity's Mössbauer Spectrometer. Science 306:1740–1745.

Kounaves SP, Hecht MH, Kapit J, Quinn RC, Catling DC, Clark Benton C., et al. (2010). Soluble sulfate in the martian soil at the Phoenix landing site. Geophysical Research Letters 37:L09201.

Krüger M, Meyerdierks A, Glöckner FO, Amann Rudolf, Widdel Friedrich, Kube M, et al. (2003). A conspicuous nickel protein in microbial mats that oxidize methane anaerobically. Nature 426:878–881.

Kubitschek HE. (1986). Increase in cell mass during the division cycle of Escherichia coli B/rA. Journal of Bacteriology 168:613–618.

LaRowe D, Dale A, Regnier Pierre. (2008). A thermodynamic analysis of the anaerobic oxidation of methane in marine sediments. Geobiology 6:436–449.

LaRowe Douglas E., Dale Andrew W., Amend Jan P., Van Cappellen Philippe. (2012). Thermodynamic limitations on microbially catalyzed reaction rates. Geochimica et Cosmochimica Acta 90:96–109.

Lewis AJ, Palmer MR, Sturchio NC, Kemp AJ. (1997). The rare earth element geochemistry of acid-sulphate and acid-sulphate-chloride geothermal systems from Yellowstone National Park, Wyoming, USA. Geochimica et Cosmochimica Acta 61:695–706.

Li Z, Hoflund GB. (2003). A Review on Complete Oxidation of Methane at Low Temperatures. Journal of Natural Gas Chemistry 12:153–160.

Lyons JR, Manning C, Nimmo F. (2005). Formation of methane on Mars by fluid-rock interaction in the crust. Geophysical Research Letters 32:L13201.

Madigan MT, Orent A. (1999). Thermophilic and halophilic extremophiles. Current Opinion in Microbiology 2:265–269.

Mangold N, Poulet F., Mustard J. F., Bibring J.-P., Gondet B, Langevin Y., et al. (2007). Mineralogy of the Nili Fossae region with OMEGA/Mars Express data: 2. Aqueous alteration of the crust. Journal of Geophysical Research: Planets 112:E08S04.

Marion GM, Kargel JS, Catling DC. (2008). Modeling ferrous–ferric iron chemistry with application to martian surface geochemistry. Geochimica et Cosmochimica Acta 72:242–266.

Marlow JJ, Martins Z, Sephton MA. (2011). Organic host analogues and the search for life on Mars. International Journal of Astrobiology 10:31–44.

McCollom Thomas M. (2000). Geochemical constraints on primary productivity in submarine hydrothermal vent plumes. Deep Sea Research Part I: Oceanographic Research Papers 47:85–101.

McCollom Thomas M. (2007). Geochemical constraints on sources of metabolic energy for chemolithoautotrophy in ultramafic-hosted deep-sea hydrothermal systems. Astrobiology 7:933–950.

McCollom Thomas M. (1999). Methanogenesis as a potential source of chemical energy for primary biomass production by autotrophic organisms in hydrothermal systems on Europa. Journal of Geophysical Research 104:30729–30.

McCollom Thomas M, Shock Everett L. (1997). Geochemical constraints on chemolithoautotrophic metabolism by microorganisms in seafloor hydrothermal systems. Geochimica et cosmochimica acta 61:4375–4391.

McEwen AS, Malin MC, Carr MH, Hartmann WK. (1999). Voluminous volcanism on early Mars revealed in Valles Marineris. Nature 397:584–586.

Miller L, Carlstrom C, Baesman S, Coates J, Oremland R. (2011). Linking methane oxidation with perchlorate reduction: a microbial base for possible Martian life. In:Vol. 1, p. 0485.

Milucka J, Ferdelman TG, Polerecky L, Franzke D, Wegener Gunter, Schmid M, et al. (2012). Zero-valent sulphur is a key intermediate in marine methane oxidation. Nature 491:541–546.

Minissale A, Vaselli O, Chandrasekharam D, Magro G, Tassi F, Casiglia A. (2000). Origin and evolution of 'intracratonic' thermal fluids from central-western peninsular India. Earth and Planetary Science Letters 181:377–394.

Mumma MJ, Villanueva GL, Novak RE, Hewagama T, Bonev BP, DiSanti MA, et al. (2009). Strong Release of Methane on Mars in Northern Summer 2003. Science 323:1041–1045.

Murchie Scott L., Mustard John F., Ehlmann Bethany L., Milliken RE, Bishop JL, McKeown NK, et al. (2009). A synthesis of Martian aqueous mineralogy after 1 Mars year of observations from the Mars Reconnaissance Orbiter. Journal of Geophysical Research: Planets 114:E00D06.

Mustard John F, Murchie S, Pelkey S, Ehlmann B, Milliken R, Grant J, et al. (2008). Hydrated silicate minerals on Mars observed by the Mars Reconnaissance Orbiter CRISM instrument. Nature 454:305–309.

Nauhaus K, Albrecht M, Elvert M, Boetius Antje, Widdel Friedrich. (2007). In vitro cell growth of marine archaeal-bacterial consortia during anaerobic oxidation of methane with sulfate. Environmental Microbiology 9:187–196.

Nelson MJ, Newsom Horton E., Draper DS. (2005). Incipient hydrothermal alteration of basalts and the origin of martian soil. Geochimica et Cosmochimica Acta 69:2701–2711.

Oelkers EH. (1991). Calculation of diffusion coefficients for aqueous organic species at temperatures from 0 to 350 °C. Geochimica et Cosmochimica Acta 55:3515–3529.

Orcutt B., Meile C. (2008). Constraints on mechanisms and rates of anaerobic oxidation of methane by microbial consortia: process-based modeling of ANME-2 archaea and sulfate reducing bacteria interactions. Biogeosciences Discussions 5:1933–1967.

Orcutt Beth!, Boetius Antje, Elvert M, Samarkin V, Joye SB. (2005). Molecular biogeochemistry of sulfate reduction, methanogenesis and the anaerobic oxidation of methane at Gulf of Mexico cold seeps. Geochimica et Cosmochimica Acta 69:4267–4281.

Orphan VJ, House Christopher H., Hinrichs K-U, McKeegan KD, DeLong EF. (2001). Methane-Consuming Archaea Revealed by Directly Coupled Isotopic and Phylogenetic Analysis. Science 293:484–487.

Oze C, Sharma M. (2005). Have olivine, will gas: Serpentinization and the abiogenic production of methane on Mars. Geophysical Research Letters 32:L10203.

Oze C, Sharma M. (2007). Serpentinization and the inorganic synthesis of H2 in planetary surfaces. Icarus 186:557–561.

Pallud C, Van Cappellen Philippe. (2006). Kinetics of microbial sulfate reduction in estuarine sediments. Geochimica et Cosmochimica Acta 70:1148–1162.

Pancost R., Hopmans E., Sinninghe Damsté J. (2001). Archaeal lipids in Mediterranean cold seeps: molecular proxies for anaerobic methane oxidation. Geochimica et Cosmochimica Acta 65:1611–1627.

Papike JJ, Karner JM, Shearer CK. (2006). Comparative planetary mineralogy: Implications of martian and terrestrial jarosite. A crystal chemical perspective. Geochimica et Cosmochimica Acta 70:1309–1321.

Price RE, LaRowe D.E., Amend J.P. (submitted). Geochemistry and bioenergetic potential of a shallow sea hydrothermal vent system off Panarea Island, Aeolian Islands, Italy.

Reeburgh William S. (2007). Oceanic Methane Biogeochemistry. Chem. Rev. 107:486–513.

Regnier P., Dale A.W., Arndt S, LaRowe D.E., Mogollón J, Van Cappellen P. (2011). Quantitative analysis of anaerobic oxidation of methane (AOM) in marine sediments: A modeling perspective. Earth-Science Reviews 106:105–130.

Rogers K, Amend J. (2005). Archaeal diversity and geochemical energy yields in a geothermal well on Vulcano Island, Italy. Geobiology 3:319–332.

Rogers KL, Amend Jan P. (2006). Energetics of potential heterotrophic metabolisms in the marine hydrothermal system of Vulcano Island, Italy. Geochimica et cosmochimica acta 70:6180–6200.

Rogers KL, Amend Jan P, Gurrieri S. (2007). Temporal changes in fluid chemistry and energy profiles in the Vulcano Island hydrothermal system. Astrobiology 7:905–932.

Schink B. (1997). Energetics of syntrophic cooperation in methanogenic degradation. Microbiology and Molecular Biology Reviews 61:262–280.

Schrum HN, Spivack AJ, Kastner M, D'Hondt S. (2009). Sulfate-reducing ammonium oxidation: a thermodynamically feasible metabolic pathway in subseafloor sediment. Geology 37:939–942.

Schulte MD, Shock Everett L., Wood RH. (2001). The temperature dependence of the standard-state thermodynamic properties of aqueous nonelectrolytes. Geochimica et Cosmochimica Acta 65:3919–3930.

Schwenzer SP, Abramov O, Allen C.C., Bridges JC, Clifford SM, Filiberto J, et al. (2012). Gale Crater: Formation and post-impact hydrous environments. Planetary and Space Science 70:84–95.

Settle M. (1979). Formation and deposition of volcanic sulfate aerosols on Mars. Journal of Geophysical Research: Solid Earth 84:8343–8354.

Seyfried Jr W., Bischoff J. (1981). Experimental seawater-basalt interaction at 300°C, 500 bars, chemical exchange, secondary mineral formation and implications for the transport of heavy metals. Geochimica et Cosmochimica Acta 45:135–147.

Shima S, Thauer RK. (2005). Methyl-coenzyme M reductase and the anaerobic oxidation of methane in methanotrophic Archaea. Current opinion in microbiology 8:643–648.

Shock E.L., Oelkers E, Johnson J, Sverjensky D, Helgeson H.C. (1992). Calculation of the thermodynamic properties of aqueous species at high pressures and temperatures : effective electrostatic radii, dissociation constants and standards partial molal properties to 1000C and 5 kbar.

Shock Everett L, Helgeson Harold C, Sverjensky Dimitri A. (1989). Calculation of the thermodynamic and transport properties of aqueous species at high pressures and temperatures: Standard partial molal properties of inorganic neutral species. Geochimica et Cosmochimica Acta 53:2157–2183.

Shock Everett L, Holland M, Meyer-Dombard D, Amend Jan P, Osburn G, Fischer TP. (2010). Quantifying inorganic sources of geochemical energy in hydrothermal ecosystems, Yellowstone National Park, USA. Geochimica et Cosmochimica Acta 74:4005–4043.

Shock Everett L, Holland ME. (2004). Geochemical energy sources that support the subsurface biosphere. Geophysical Monograph Series 144:153–165.

Shock Everett L, McCollom T, Schulte MD. (1995). Geochemical constraints on chemolithoautotrophic reactions in hydrothermal systems. Origins of Life and Evolution of the Biosphere 25:141–159.

Shock Everett L., Helgeson Harold C. (1988). Calculation of the thermodynamic and transport properties of aqueous species at high pressures and temperatures: Correlation algorithms for ionic species and equation of state predictions to 5 kb and 1000°C. Geochimica et Cosmochimica Acta 52:2009–2036.

Shock Everett L., Helgeson Harold C. (1990). Calculation of the thermodynamic and transport properties of aqueous species at high pressures and temperatures: Standard partial molal properties of organic species. Geochimica et Cosmochimica Acta 54:915–945.

Skoog A, Vlahos P, Rogers KL, Amend Jan P. (2007). Concentrations, distributions, and energy yields of dissolved neutral aldoses in a shallow hydrothermal vent system of Vulcano, Italy. Organic geochemistry 38:1416–1430.

Spear JR, Walker JJ, McCollom Thomas M, Pace NR. (2005). Hydrogen and bioenergetics in the Yellowstone geothermal ecosystem. Proceedings of the National Academy of Sciences of the United States of America 102:2555–2560.

Squyres SW, Grotzinger JP, Arvidson R. E., Bell JF, Calvin W, Christensen PR, et al. (2004). *In Situ* Evidence for an Ancient Aqueous Environment at Meridiani Planum, Mars. Science 306:1709–1714.

Stams AJM, Plugge CM. (2009). Electron transfer in syntrophic communities of anaerobic bacteria and archaea. Nat Rev Micro 7:568–577.

Strous M, Jetten MS. (2004). Anaerobic oxidation of methane and ammonium. Annu. Rev. Microbiol. 58:99–117.

Sverjensky D.A., Shock E.L., Helgeson H.C. (1997). Prediction of the thermodynamic properties of aqueous metal complexes to 1000°C and 5 kb. Geochimica et Cosmochimica Acta 61:1359–1412.

Tanger JC, Helgeson Harold C. (1988). Calculation of the thermodynamic and transport properties of aqueous species at high pressures and temperatures; revised equations of state for the standard partial molal properties of ions and electrolytes. American Journal of Science 288:19–98.

Taylor SR, McLennan S.M. (2009). Planetary Crusts: Their Composition, Origin, and Evolution. Cambridge University Press.

Teichert BMA, Bohrmann G, Suess E. (2005). Chemoherms on Hydrate Ridge — Unique microbially-mediated carbonate build-ups growing into the water column. Palaeogeography, Palaeoclimatology, Palaeoecology 227:67–85.

Thurber AR, Levin LA, Orphan VJ, Marlow JJ. (2012). Archaea in metazoan diets: implications for food webs and biogeochemical cycling. ISME J 6:1602–1612.

Tivey MK, McDuff RE. (1990). Mineral precipitation in the walls of black smoker chimneys: A quantitative model of transport and chemical reaction. Journal of Geophysical Research: Solid Earth 95:12617–12637.

Toei M, Gerle C, Nakano M, Tani K, Gyobu N, Tamakoshi M, et al. (2007). Dodecamer rotor ring defines H+/ATP ratio for ATP synthesis of prokaryotic V-ATPase from Thermus thermophilus. Proceedings of the National Academy of Sciences 104:20256–20261.

Tosca Nicholas J., McLennan Scott M. (2006). Chemical divides and evaporite assemblages on Mars. Earth and Planetary Science Letters 241:21–31.

Toulmin P, Baird AK, Clark B. C., Keil K, Rose HJ, Christian RP, et al. (1977). Geochemical and mineralogical interpretation of the Viking inorganic chemical results. Journal of Geophysical Research 82:4625–4634.

Treude, Boetius, Knittel, Wallmann, Jorgensen. (2003). Anaerobic oxidation of methane above gas hydrates at Hydrate Ridge, NE Pacific Ocean. Mar Ecol Prog Ser 264:1–14.

Varnes ES, Jakosky BM, McCollom T. M. (2004). Biological Potential of Martian Hydrothermal Systems. Astrobiology 3:407–414.

Vick T, Dodsworth JA, Costa K, Shock E, Hedlund BP. (2010). Microbiology and geochemistry of Little Hot Creek, a hot spring environment in the Long Valley Caldera. Geobiology 8:140–154.

Wang A, Haskin LA, Squyres SW, Jolliff BL, Crumpler L, Gellert R, et al. (2006). Sulfate deposition in subsurface regolith in Gusev crater, Mars. Journal of Geophysical Research: Planets 111:E02S17.

Wang G, Spivack AJ, D'Hondt S. (2010). Gibbs energies of reaction and microbial mutualism in anaerobic deep subseafloor sediments of ODP Site 1226. Geochimica et Cosmochimica Acta 74:3938–3947.

Wänke H, Brückner J, Dreibus G, Rieder R, Ryabchikov I. (2001). Chemical Composition of Rocks and Soils at the Pathfinder Site. Space Science Reviews 96:317–330.

Webster CR, Mahaffy PR, Atreya SK, Flesch GJ, Farley KA, MSL Science Team. (2013). Low Upper Limit to Methane Abundance on Mars. Science 342:355–357.

Wegener G., Boetius A. (2009). An experimental study on short-term changes in the anaerobic oxidation of methane in response to varying methane and sulfate fluxes. Biogeosciences 6:867–876.

Welhan JA, Craig H. (1979). Methane and hydrogen in East Pacific Rise hydrothermal fluids. Geophysical Research Letters 6:829–831.

Windman T, Zolotova N, Schwandner F, Shock Everett L. (2007). Formate as an energy source for microbial metabolism in chemosynthetic zones of hydrothermal ecosystems. Astrobiology 7:873–890.

Wray J, Noe Dobrea E, Arvidson R, Wiseman S, Squyres S, McEwen A, et al. (2009). Phyllosilicates and sulfates at Endeavour Crater, Meridiani Planum, Mars. Geophysical Research Letters 36.

Yung YL, Nair H, Gerstell MF. (1997). CO2Greenhouse in the Early Martian Atmosphere: SO2Inhibits Condensation. Icarus 130:222–224.

Zatsepina OY, Buffett BA. (1997). Phase equilibrium of gas hydrate: Implications for the formation of hydrate in the deep sea floor. Geophysical Research Letters 24:1567–1570.

Zolotov MY, Shock Everett L. (2004). A model for low temperature biogeochemistry of sulfur, carbon, and iron on Europa. Journal of Geophysical Research: Planets (1991–2012) 109.

Zolotov MY, Shock Everett L. (2003). Energy for biologic sulfate reduction in a hydrothermally formed ocean on Europa. Journal of Geophysical Research: Planets (1991–2012) 108.

# *Conclusions & Future Directions*

The work presented herein offers an expansion of known methanotrophic habitats, an increased appreciation of protein-based functional diversity at methane seeps, and novel tools and theoretical models for characterizing methane-linked metabolisms. Nonetheless, as with any exploratory work, these results have only broadened the search space for future investigations, and follow-up and spin-off studies are anticipated and encouraged; a small subset of possible future directions is presented below.

The detection of active methanotrophy within methane seep authigenic carbonates inspires a more thorough charting of the range of methane-metabolizing communities. Conducing similar biomass, diversity, and consumption rate studies on a deeper vertical section of seep-hosted carbonate mounds – a putative goal of upcoming IODP work – would likely extend the range of AOM and further re-shape our understanding of carbon and sulfur cycling. Expanding outward from active seep sites would fill in the gradation of activity levels: as demonstrated by our re-christening of "inactive" sites to "low-activity" ones, AOM occurs beyond the range of visual cues found on the seafloor. Developing a more nuanced map of activity as a function of distance from seep, carbonate age, advection rate, and methane concentration would offer a more systematic view of this important metabolism. The potential dormancy range of methanotrophic communities is another fruitful line of inquiry: understanding the set of conditions from which quiescent seep microbiota can be resuscitated – as well as the time needed for colonization of previously methanotroph-free substrates – would provide a sense of the ecosystem's time-integrated methane consumption potential rather than its activity at a particular moment in

time. Seep-hosted carbonates represent one physical frontier for AOM activity, but an equally alluring potential substrate is methane hydrates. These solid "cages" of methane represent an enormous repository of the molecule, but the bioaccessability of that methane is poorly established. Finally, a more thorough investigation of the autoendolithic lifestyle – involving a coordinated set of laboratory-based experiments and proteomic or metabolomic surveys – would help answer key questions about the role of microorganisms in shaping geological structures, and how such feedback mechanisms influence microbial persistence, activity, and evolution. All of this work should be done in close collaboration with geochemists, geophysicists, and physical oceanographers, as the delineation of microbiological range is largely preceded by and dependent upon detailed characterization of energy sources.

Deuterated methane represents a useful tool not only in measuring rates of methane consumption, but for understanding the systematics of methane-linked metabolisms. Measuring D/H ratios at more regular intervals and earlier in an incubation's run would better constrain the technique's precision and detection limit. The development of a library of D/H : $^{14}CH_4$ rate ratios would also be an important resource for the scientific community. Chapter 2 provides such ratios for methanotrophic cultures and seep sediment and carbonates from active and low-activity settings under both oxic and anoxic conditions, but the universality of those ratios should be investigated. The extent to which these values differ by seep, substrate, or community composition would reveal potentially important distinctions in how methane is processed at different sites. Methane's hydrogen atoms represent potentially useful reporters of the molecule's partial or complete oxidation, as well as reversibility and catabolic / anabolic partitioning. A full suite of

analyses utilizing singly, doubly, triply, or fully deuterated methane along with isotopic analyses of biomass, water, intracellular solvent, and methane could help elucidate the flow of methane carbon and hydrogen through the community. Performing such experiments under a range of conditions with variable energetic or nutrient regimes, perhaps alongside metaproteomic analyses, would provide insight into adaptations under limiting conditions.

The novel habitats revealed through the detection of endolithic AOM prompted subsequent questions of diversity's determinants; the survey presented in Chapter 3 initiates this investigation, but many questions remain. Pending work from Case et al. advances the line of inquiry regarding colonization patterns and shifting communities of different methane seep regimes and substrate types, including wood and distinct carbonate mineralogies. Follow-up study of how mineralogy influences microbial activity on a cellular scale is an important geobiological question; although mineralogical proclivities are observed, the theoretical groundwork for these observations is lacking. Most physiological studies of seep-associated organisms have focused on ANME-SRB consortia, but semi-quantitative diversity analyses imply that other constituents may be equally relevant in elemental cycling at these settings. In particular, deeper investigation of commonly observed lineages such as *Sulfurovum* and uncultured SAR324 and SH765B-TzT-29 groups would likely reveal underappreciated roles that impinge upon broader community function. More generally, shifting microbiological surveys from a presence-based focus to an activity-based one is a critical step that would substantially advance our understanding of seep, seep-adjacent, and paleoseep observations.

Metaproteomics represents a very exciting tool to query a system's metabolic activity – not merely its potential – in a time-resolved and potentially quantitative manner. Our initial efforts with this tool demonstrate that the physical, chemical, biological, energetic, and mineralogical complexities of seep environments do not disqualify these settings from SIP metaproteomics investigations, and continually improving analytical capabilities will only expand the range of answerable questions. In particular, extending the search for and investigating the function of post-translational modifications across a broader set of proteins would constrain their rates and conditions of occurrence. PTMs enable a vastly larger functional diversity search space, with implications for phylogenetic relationships and physiological adaptations. More rigorously quantitative explorations of specific proteins (including the distribution of reverse methanogenesis orthologs and high-frequency hypothetical proteins) under distinct and well-characterized conditions through multiple reaction monitoring would begin to parse their metabolic roles. When paired with a thorough metagenomic database, metaproteomics also represents a promising discovery tool for unknown proteins: heterologous expression or antibody-based surveys of the high-frequency hypothetical proteins discussed in Chapter 4 would be an appealing next step. Finally, incorporating metaproteomic data into network analyses to reveal potential distributed metabolic pathways is a logical extension of the growing appreciation of interspecies interactions in environmental settings. Metaproteomic data represents a useful entrée into this line of inquiry, though energetic modeling and *in vivo* biochemical studies constitute a critical supporting scaffold.

The astrobiological implications of AOM are just beginning to be considered, and as missions throughout the solar system relay increasingly detailed data of alien worlds,

the list of potential habitats is expanding. Chapter 5 pinpoints Mars as a promising site for putative AOM during its warmer and wetter past, though a substantial gap between theoretical possibility and concrete geobiological evidence remains. The geological provinces and specific locations pinpointed in Chapter 5 – including NE Syrtis and sites of past fluid flow – warrant strong consideration as potential landing sties for future missions that could explore microscopic structures, examine mineralogical signatures, or cache samples for return to Earth-based laboratories. Expanding the characterization of AOM hotspots beyond Mars to other celestial bodies like Titan, Europa, and extrasolar planets is another attractive offshoot, particularly as fundamental geochemical and geophysical parameters are refined. Energetic evaluations represent an important pre-requisite for viability, but empirical data is essential for a more sober-minded consideration of extraterrestrial AOM. Molecular investigations of sulfate / olivine provinces on Mars, as well as time-resolved isotopic evaluations of martian methane or extrasolar planet atmospheres, represent useful next steps.

The use of culture-independent approaches in the service of understanding microbiological activities at methane seep settings is an important line of inquiry and presents lessons and tools that can be applied to a wide range of settings. After all, such low-energy microbial communities may well represent the most prevalent state of life on Earth, a common and biogeochemically relevant mode that governs environmental systems in unseen ways.

# Appendix 1: Supplementary Information for Chapter 1

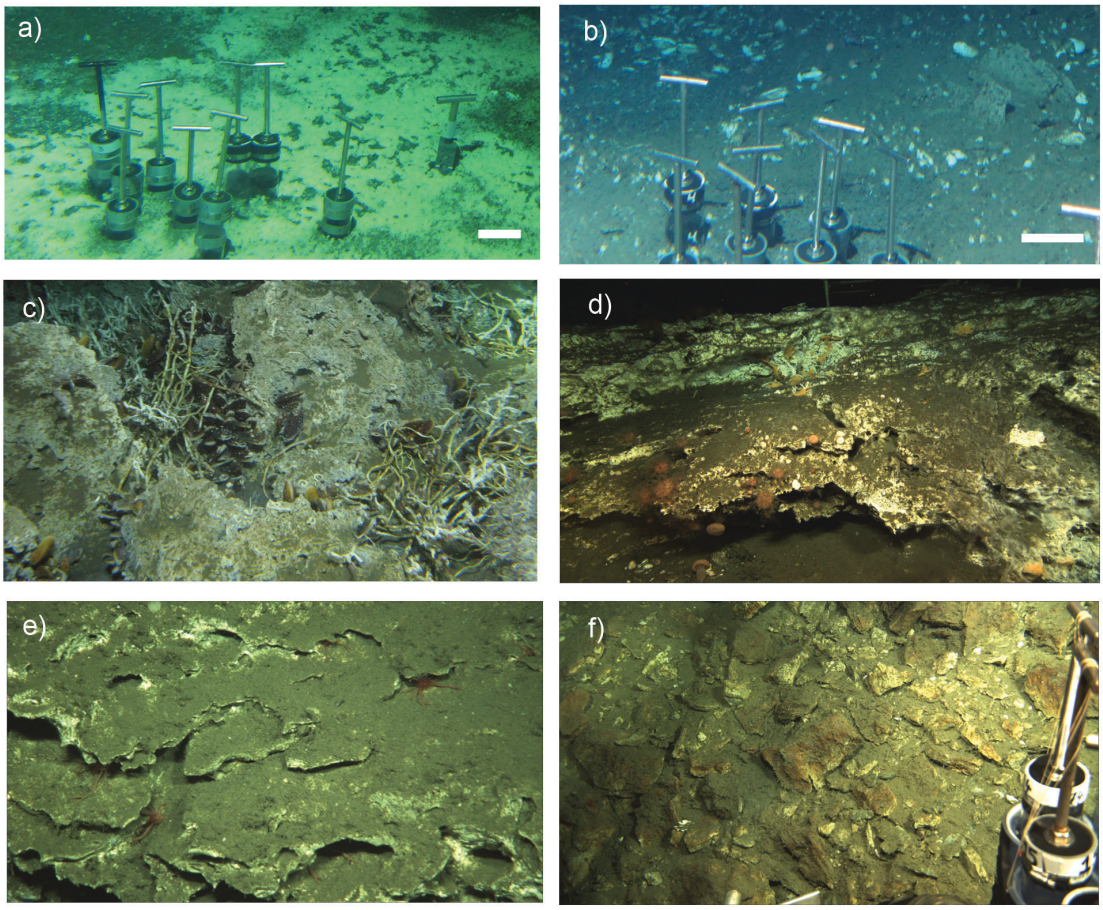


**Supplementary Figure 1.1**. Sampling sites representative of those discussed in this study. **(A)** A white bacterial mat indicative of an active methane seep at 802 m water depth at Hydrate Ridge South; sample A.Sed-3452 was collected from this site. **(B)** A vesicomyid clam bed at an active methane seep at Hydrate Ridge South seen during AD 4629 (800 m water depth). **(C)** Active carbonates at Mound 12, Costa Rica, at a water depth of 997 m. **(D)** Exhumed active carbonate at Hydrate Ridge South (804 m water depth). Low-activity carbonates at Hydrate Ridge are seen in both **(E)** cohesive sediment-draped pavements at 829 m water depth, and **(F)** deposits of fragmented carbonates at 842 m water depth. **(A)** and **(B)** scale bars are 10 cm; **(C)** and **(D)** foreground scenes are approximately 2.5 m and 4 m across, respectively; **(E)** and **(F)** are approximately 1 m across.

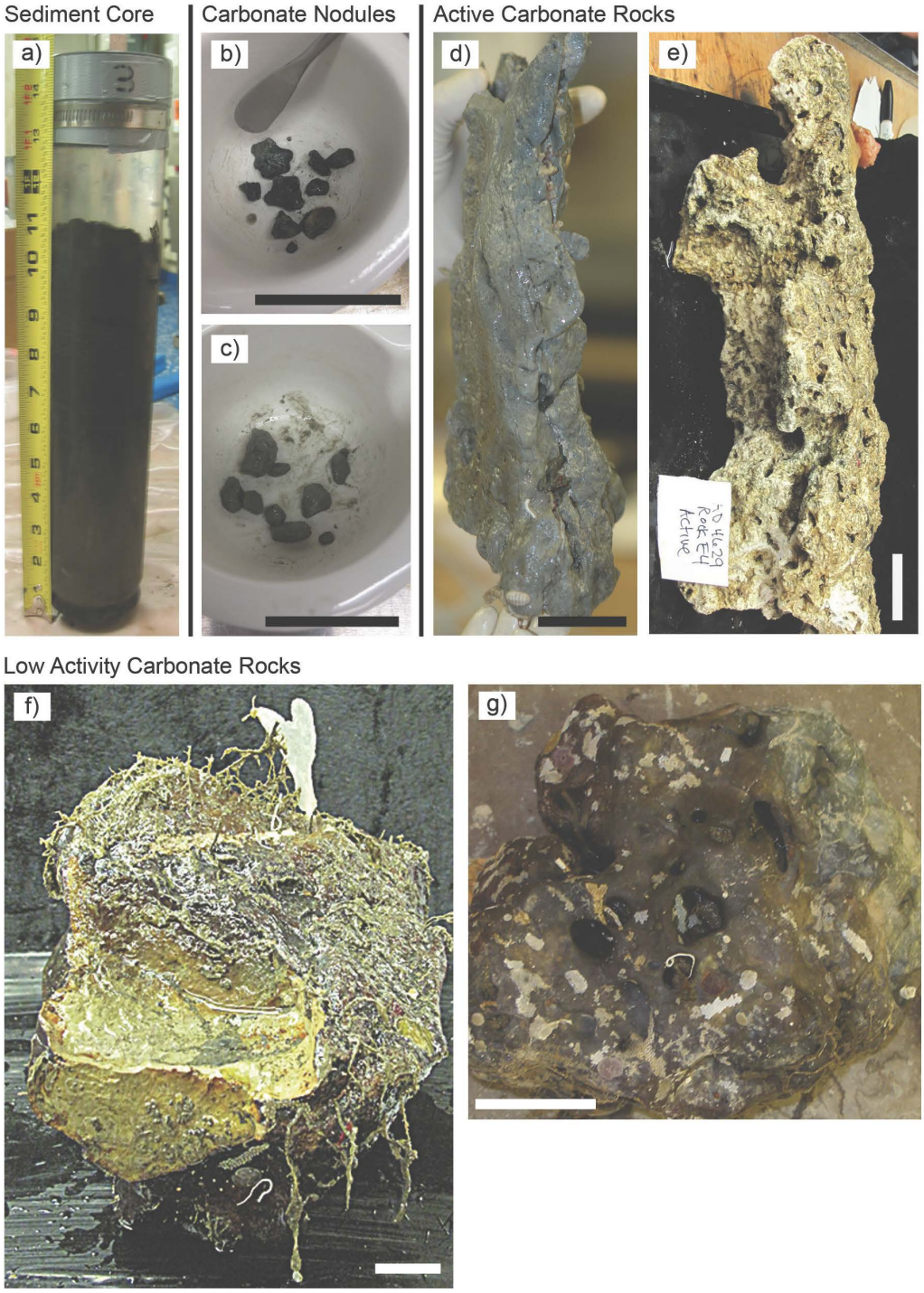


**Supplementary Figure 1.2**. Representative samples analyzed in this study. **(A)** Active 30-cm sediment core PC3 from AD 4511, 997 m water depth, Costa Rica Mound 12. **(B)** Nodules from AD 4511 PC3, Costa Rica, acquired from the core's 12-15 cm horizon. **(C)** Nodules from AD 4587 PC18 3-6 cm horizon, 996 m water depth, Mound 12, Costa Rica. **(D)** Active massive carbonate rock A.Carb-2840 collected from Mound 12, 997 m

water depth, Costa Rica during AD 4501. **(E)** Active porous carbonate rock A.Carb-3439 from AD 4629, 800 m water depth, Hydrate Ridge. **(F)** Low activity massive carbonate rock L.Carb-3604 from AD 4633, 623 m water depth, Hydrate Ridge. **(G)** Low activity massive carbonate rock L.Carb-2787 from Eel River Basin, water depth 540 m. Scale bars are 5 cm.

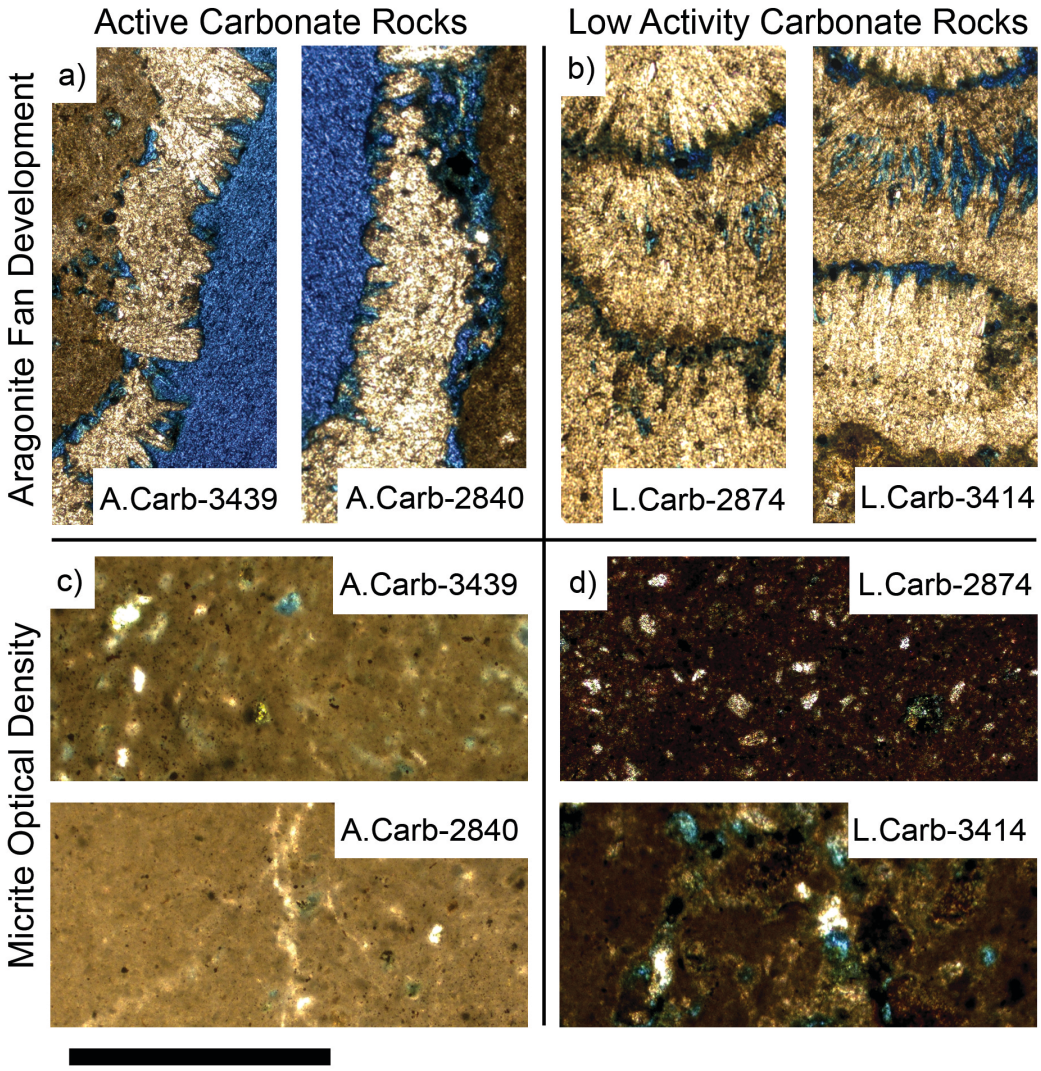


**Supplementary Figure 1.3**. Differences among active carbonate (**A** and **C**) and low-activity carbonate (**B** and **D**) thin sections. Images in the top panels (**A** and **B**) show the differences in aragonite fan development; those in the bottom panels (**C** and **D**) demonstrate the variation in micrite optical density. All images were taken at the same exposure and exhibit no post-processing; blue color represents the embedding matrix, which can be interpreted as pore space. Scale bar = 0.5 mm.

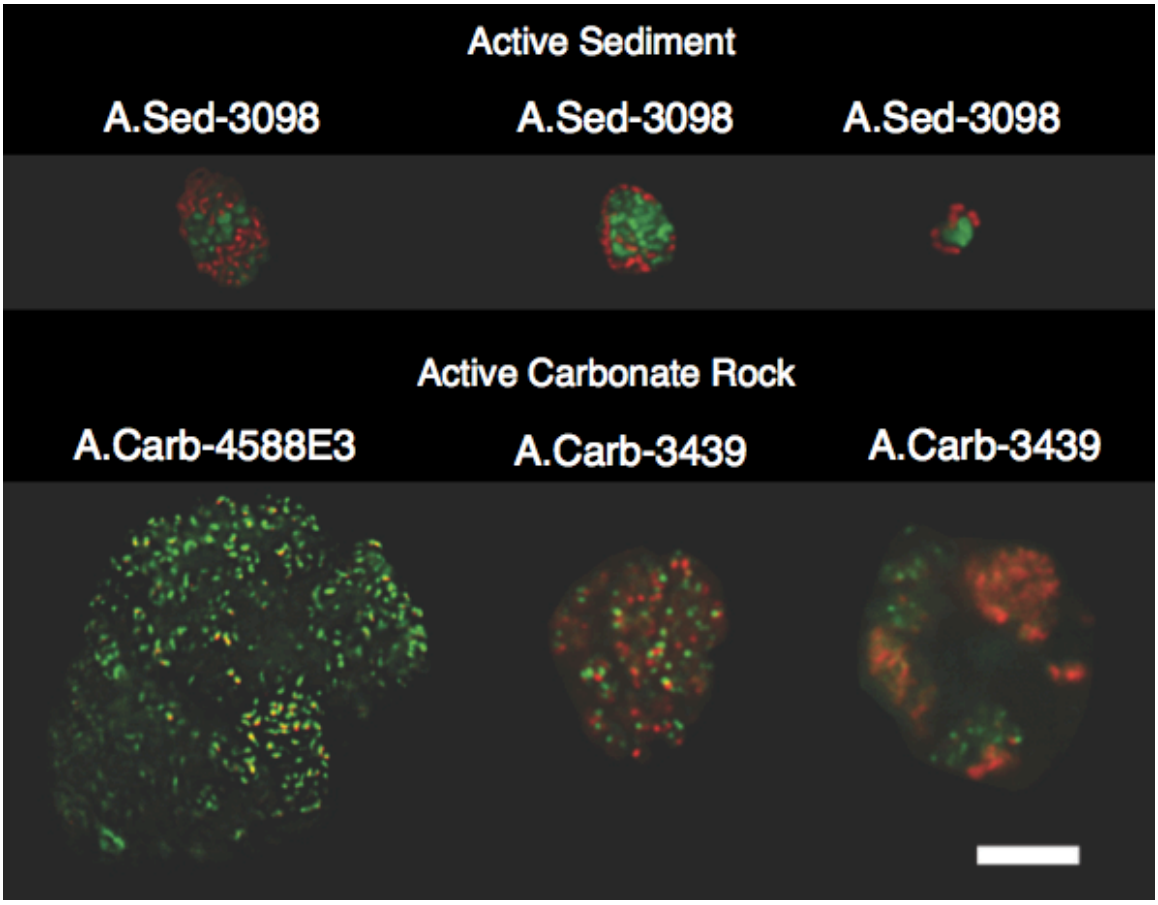


**Supplementary Figure 1.4**. Morphological comparisons between sediment- and carbonate-hosted microbial aggregates. CARD-FISH images of Archaea (Arch915 probe, green) and *Desulfosarcina / Desulfococcus* (DSS658 probe, red) aggregates from active sediment (A.Sed-3098) and active carbonate (A.Carb-4588E3, A.Carb-3439) samples. Scale bar = 5 μm.

**Supplementary Table 1.1**. Details of the 24 samples used in this study, including active sediment, active nodules, active porous carbonate, active massive carbonate, low activity sediment, and low activity massive carbonate. Serial numbers are unique identifier numerals preceded by an acronym of the sample's seep activity designation and degree of lithification. A.Sed = active sediment, A.Nod = active nodule, A.Carb = active carbonate, L.Sed = low activity sediment, and L.Carb = low activity carbonate. Definitions of seep activity and lithification designators are provided in the main and supplemental text. X = X-ray diffraction, CC = cell counts and aggregate characterization, PM = attempted *pmoA* gene amplification, PP = porosity and permeability tests, TS = petrographic thin section analysis, 16S = 16S rRNA gene clone library sequencing, 454 = pyrotag sequencing, SA = aggregate spatial arrangement study, $^{14}C = {}^{14}CH_4$ radiolabel rate measurement, NS = CARD-FISH / nanoSIMS analysis, BV = aggregate biovolume calculation.

| Serial # | Sample ID | Seep Activity | Lithification | Sampling Location | Analyses Performed |
|---|---|---|---|---|---|
| A.Sed-3098 | AD 4511 PC3 9-12 cm | Active | Sediment | Costa Rica | X, CC, BV |
| A.Sed-3452 | AD 4629 PC8 3-6 cm | Active | Sediment | Hydrate Ridge | X, CC, PM |
| A.Sed-3730 | AD 4635 PC16 0-6 cm | Active | Sediment | Hydrate Ridge | 16S |
| A.Sed-5128 | J2 593 E3 PC 40 0-12 cm | Active | Sediment | Hydrate Ridge | CC, $^{14}$C |
| A.Nod-2518 | AD 4249 PC8 3-6 cm | Active | Nodule | Hydrate Ridge | CC, 16S |
| A.Nod-2688 | AD 4256 PC29 6-9 cm | Active | Nodule | Eel River Basin | CC |
| A.Nod-3099 | AD 4511 PC3 12-15 cm | Active | Nodule | Costa Rica | X, CC, BV, PM |
| A.Nod-3294 | AD 4587 PC18 3-6 cm | Active | Nodule | Costa Rica | X, NS |
| A.Carb-3439 | AD 4629 Jefe | Active | Porous Carbonate | Hydrate Ridge | TS, CC, BV, 16S, NS, 454 |
| A.Carb-5305 | J2 593 E7A B8B | Active | Porous Carbonate | Hydrate Ridge | X, CC, $^{14}$C |
| A.Carb-2840 | AD 4501 L1 | Active | Massive Carbonate | Costa Rica | TS, PM |
| A.Carb-2871 | AD 4502 L2 | Active | Massive Carbonate | Costa Rica | CC |
| A.Carb-3460 | AD 4589 R8 | Active | Massive Carbonate | Costa Rica | TS |
| A.Carb-4588E3 | AD 4588E3 | Active | Massive Carbonate | Costa Rica | X, PP, CC |
| A.Carb-5152 | J2 593 E4B B24 | Active | Massive Carbonate | Hydrate Ridge | PP, CC, BV, $^{14}$C |
| L.Sed-2939 | AD 4504 PC3 3-6 cm | Low Activity | Sediment | Costa Rica | CC |
| L.Sed-5043 | J2 593 E1 PC2 0-12 cm | Low Activity | Sediment | Hydrate Ridge | CC, $^{14}$C, PM |
| L.Carb-2719 | AD 4256 G4 | Low Activity | Massive Carbonate | Eel River Basin | PP |
| L.Carb-2787 | AD 4258 G2 | Low Activity | Massive Carbonate | Eel River Basin | PP |
| L.Carb-2874 | AD 4502 S3 | Low Activity | Massive Carbonate | Costa Rica | X, TS, CC |
| L.Carb-3414 | AD 4629 E3B | Low Activity | Massive Carbonate | Hydrate Ridge | TS, PM |
| L.Carb-3604 | AD 4633 L1 | Low Activity | Massive Carbonate | Hydrate Ridge | X, CC, 16S |
| L.Carb-5028 | J2 593 E1A B12 | Low Activity | Massive Carbonate | Hydrate Ridge | PP, CC, $^{14}$C |
| L.Carb-5473 | J2 593 E10B B15 | Low Activity | Massive Carbonate | Hydrate Ridge | PP |

**Supplementary Table 1.2**. Porosity and permeability results from core plug analysis of several carbonate samples. Vuggy active porous carbonates were not testable with this method due to structural instability caused by macroscale voids.

| Sample | Sampling Location | Description | Porosity (%) | Permeability ($m^2$) |
|---|---|---|---|---|
| L.Carb-2787 | Eel River Basin | Low Activity Massive | 4.9 | $3x10^{-18}$ |
| L.Carb-5028 | Hydrate Ridge | Low Activity Massive | 8.9 | $4x10^{-18}$ |
| L.Carb-2719 | Eel River Basin | Low Activity Massive | 8 | $1.1x10^{-17}$ |
| L.Carb-5473 | Hydrate Ridge | Low Activity Massive | 16.6 | $3.5x10^{-17}$ |
| A.Carb-5152 | Hydrate Ridge | Active Massive | 34.4 | $1.7x10^{-15}$ |
| A.Carb-4588E3 | Costa Rica | Active Massive | 25 | $4.9x10^{-15}$ |

**Supplementary Table 1.3**. Cell counts from ten samples examined in this study. Values represent cumulative counts over 25 fields of view. Absolute cell count numbers are not directly comparable between samples, as different volumes of material were concentrated on filters for each sample; rather, the proportion of single cells can be compared among different samples.

| Sample | Aggregate-based Cells | Single Cells | Proportion of Single Cells |
|---|---|---|---|
| A.Sed-3098 | 2044 | 17 | 0.80% |
| A.Sed-5128 | 897 | 9 | 1% |
| A.Nod-2518 | 629 | 5 | 0.79% |
| A.Nod-3099 | 3138 | 26 | 0.83% |
| A.Carb-3439 | 1887 | 13 | 0.69% |
| A.Carb-5152 | 342 | 7 | 2% |
| L.Sed-2939 | 487 | 65 | 13.35% |
| L.Sed-5043 | 620 | 61 | 9.84% |
| L.Carb-2874 | 342 | 52 | 15.20% |
| L.Carb-3604 | 1002 | 143 | 14.27% |

**Supplementary Table 1.4**. $^{13}C$ and $^{15}N$ atom percent enrichment values for aggregates from labeled (2 mM $^{15}NH_4Cl$, 0.74 mM $^{13}CH_4$, and 0.74 mM $^{12}CH_4$) and unlabeled (2 mM $^{14}NH_4Cl$ and 1.48 mM $^{12}CH_4$) incubations of sample A.Carb-3439 at 4 °C for 27 months under anoxic conditions. Values represent full aggregate analyses, incorporating data from all nanoSIMS cycles within a defined region of interest that was informed by CARD-FISH biomass identifications. Aggregate 17 refers to the aggregate in panel c of Fig. 2, aggregate 25 to panel a, and aggregates 31a and b to cell aggregates seen on the left and right of panel b, respectively. *Clostridia* spores (n=5 in both cases) were added following experimental treatment and demonstrate consistent measurement conditions.

| $^{15}N$, $^{13}C$ Labeled Incubation Aggregates | | |
|---|---|---|
| | $^{13}C$ atm % | $^{15}N$ atm % |
| Aggregate 17 | 1.15 | 81.48 |
| Aggregate 25 | 0.87 | 81.31 |
| Aggregate 31a | 0.80 | 69.42 |
| Aggregate 31b | 1.03 | 69.51 |
| *Clostridia* spore avg | 0.77 | 0.37 |
| Unlabeled Incubation Aggregates | | |
| | $^{13}C$ atm % | $^{15}N$ atm % |
| Aggregate 16 | 0.48 | 0.35 |
| Aggregate 23 | 0.66 | 0.37 |
| Aggregate 24 | 0.51 | 0.33 |
| *Clostridia* spore avg. | 0.76 | 0.37 |

**Chapter 1 Supplementary Methods**

*Phylogenetic Analysis*

Polymerase chain reaction (PCR) was performed in order to amplify bacterial and archaeal 16S rRNA genes. Bacterial PCR used the 27F[1] (5'-AGAGTTTGATCCTGGCTCAG-3') / 1492R[2] (5'-GGYTACCTTGTTACGACTT-3') primers, while archaeal PCR used 8F[3] (5'-TCCGGTTGATCCTGCC-3') / 958R[2] (5'-YCCGGCGTTGAMTCCAATT-3') primers. New England BioLab's *Taq* DNA Polymerase (NEB, Ipswich, MA) was used in all PCRs. PCR was run on an Eppendorf Mastercycler Ep Gradient S thermocycler as follows: an initial denaturation of 2 minutes at 95 °C; 30 cycles of 15 seconds at 94 °C, 30 seconds at 54 °C, and 45 seconds at 72 °C; and a final 4 minute elongation at 72 °C.

Sequences were aligned with Mothur[4] and checked for chimeras with bellerophon, pintail, and slayer chimera check programs. Non-chimeric sequences were imported to ARB[5], aligned in accordance with the Silva 115 NR99 database.

*454 Sequencing*

PCR reactions (50 µl) for 454 sequencing were prepared with 20 ng of template DNA, 5 µl 10x buffer, 1 µl dNTP mix (10 mM each), 4 µl MgCl (25 mM), 1 µl forward primer (10 mM), 1 µl reverse primer (10 mM), 0.2 µl Taq polymerase and 1.5 µl BSA, and 1 µl (10 mM) of each of the universal primers targeting the V6-V8 region of the bacterial and archaeal 16S rRNA gene[6]: 926F (5'-AAACTYAAAKGAATTGRCGG-3') and 1392R (5'-ACGGGCGGTGTGTRC-3') modified on the 5' end to contain 454 sequencing adaptor sequences. The reverse primer also contained a 5–6 base sample-specific barcode sequence. The PCR program included one cycle at 95 °C for 3 minutes,

followed by 30 cycles at 95 °C for 30 seconds, 55 °C for 30 seconds, and 75 °C for 30 seconds, and then a final extension at 74 °C for 10 minutes. After amplification, amplicons were pooled and sequenced using the Roche 454 GS-FLX Titanium platform (Roche Diagnostics, Castle Hill, NSW, Australia) at the Australian Centre for Ecogenomics.

Amplicons derived from 454 sequencing were processed using the Quantitative Insights Into Microbial Ecology (QIIME) package[7]. Chimera detection was performed using UCHIME[8] against a modified Silva115 NR99 reference database[9]. The Silva 115 NR99 database had been filtered to include only those sequences with pintail value >75, and appended with 1197 high-quality, full-length sequences from the Orphan lab, increasing the database coverage of common methane seep taxa. This modified database, including taxonomies, is available upon request.

*CARD-FISH*

Domain and group-specific probes were used to visualize Archaea (Arch915[10] – Alexa green: 5'-GTGCTCCCCCGCCAATTCCT-3'), ANME-2 (ANME2-538[11] – Alexa green 5'-GGCTACCACTCGGGCCGC-3'), and *Desulfosarcina* / *Desulfococcus* (DSS658[12] – Alexa red: 5'-TCCACTTCCCTCTCCCAT-3'). 1 µl of probe was added to 300 µl of hybridization buffer (50% formamide by volume), and 20 µl of the mixture was placed on the sample surface. The amplification buffer mix was prepared by mixing 600 µl amplification buffer with 6 µl dilute $H_2O_2$ (200 µl PBS + 6 µl 30% $H_2O_2$), and 1 µl of the appropriate tyramide fluorochrome (Alexa green for Arch915 and ANME2-538, Alexa red for DSS658). Probe-free negative controls to test for endogenous peroxidases were also processed, and no fluorescence signal was observed using the same exposure

settings. ANME-1 FISH analysis was conducted as in Pernthaler et al.[13] and utilized the ANME-1 350 probe[14] Cy3 5'-AGTTTTCGCGCCTGATGC-3' with 40% formamide hybridization buffer.

*$^{14}CH_4$ Rate Measurements*

Radiolabeled methane (1 ml of $^{14}CH_4$ dissolved in seawater, corresponding to an activity of 52 kBq) was injected into each incubation bottle and samples were placed at 4 °C. At the designated time point (3 and 7 days for anaerobic incubations, 1.875 and 4 days for aerobic incubations), 2.5 ml of 2.5% (w/w) NaOH was injected to stop microbial activity. The relatively extended incubation durations likely encompass multiple stages of growth, with rates likely decreasing as methane was consumed. Thus, the reported average growth rates represent a potential underestimate of maximum growth rates under conditions of constant 2.2 mM methane supply. Each sample's headspace was purged with airflow through an 850 °C quartz tube furnace filled with Cu(II) oxide, combusting unused $^{14}CH_4$ to $^{14}CO_2$, which was collected in two sequential 23-ml scintillation vials pre-filled with 7 ml phenylethylamine and 1 ml 2-methoxyethanol. 10 ml of scintillation cocktail (Ultima Gold XR, PerkinElmer) was added, and the activity attributable to $^{14}CO_2$ was measured by scintillation counting 24 hours later (Beckman Coulter LS 6500 Multi-Purpose Scintillation Counter, 10 minute analysis per sample).

To quantify the $^{14}CO_2$ and $H^{14}CO_3^-$ produced during the incubation period, each sample was uncapped and the entire volume was transferred into a 250-ml Erlenmeyer flask along with 1 drop of antifoam. 5 ml of 6M HCl was added and the flask was immediately closed with a rubber stopper, two clamps, and parafilm to prevent gas escape. The flask was placed on a shaking table (60 rpm) at room temperature for 24

hours. A 7-ml scintillation vial, pre-filled with 1 ml of 2.5% NaOH and 1 ml of phenylethylamine, was suspended from the rubber stopper inside the flask to collect $^{14}CO_2$ generated by the acidification. 5 ml of scintillation cocktail was added, and the vial was measured by scintillation counting 24 hours later. This method has been shown to recover an average of 98% of $^{14}CO_2$[15].

Finally, six of the sterilized control incubations (four anaerobic, two aerobic) were set aside after $^{14}CH_4$ addition for gas chromatography to determine the initial concentration of methane gas. 400 µl was injected into a gas chromatograph (Shimadzu GC-2014), equipped with a packed stainless steel Supelco Custom Column (50/50 mixture, 80/100 Porapak N support, 80/100 Porapak Q column, 6 ft x 1/8 in) and a flame ionization detector. The carrier gas was helium at a flow rate of 30 ml $min^{-1}$. The column temperature was 60 °C. Results were scaled based on comparison with standards of known methane concentrations (10 and 100 ppm; Matheson Tri-Gas, Twinsburg, OH).

**Chapter 1 Supplementary References**


1. Lane, D. J. *et al.* Rapid determination of 16S ribosomal RNA sequences for phylogenetic analyses. *Proceedings of the National Academy of Sciences* **82,** 6955–6959 (1985).
2. DeLong, E. F. Archaea in coastal marine environments. *Proceedings of the National Academy of Sciences* **89,** 5685–5689 (1992).
3. Teske, A. *et al.* Microbial Diversity of Hydrothermal Sediments in the Guaymas Basin: Evidence for Anaerobic Methanotrophic Communities. *Applied and Environmental Microbiology* **68,** 1994–2007 (2002).
4. Schloss, P. D. *et al.* Introducing mothur: open-source, platform-independent, community-supported software for describing and comparing microbial communities. *Applied and environmental microbiology* **75,** 7537–7541 (2009).
5. Ludwig, W. *et al.* ARB: a software environment for sequence data. *Nucleic acids research* **32,** 1363–1371 (2004).
6. Engelbrektson, A. *et al.* Experimental factors affecting PCR-based estimates of microbial species richness and evenness. *The ISME journal* **4,** 642–647 (2010).
7. Caporaso, J. G. *et al.* QIIME allows analysis of high-throughput community sequencing data. *Nature methods* **7,** 335–336 (2010).

8. Edgar, R. C., Haas, B. J., Clemente, J. C., Quince, C. & Knight, R. UCHIME improves sensitivity and speed of chimera detection. *Bioinformatics* **27,** 2194–2200 (2011).
9. Quast, C. *et al.* The SILVA ribosomal RNA gene database project: improved data processing and web-based tools. *Nucleic acids research* **41,** D590–D596 (2013).
10. Stahl, D. Development and application of nucleic acid probes. *Nucleic acid techniques in bacterial systematics* (1991).
11. Treude, T., Knittel, K., Blumenberg, M., Seifert, R. & Boetius, A. Subsurface Microbial Methanotrophic Mats in the Black Sea. *Applied and Environmental Microbiology* **71,** 6375–6378 (2005).
12. Ravenschlag, K., Sahm, K., Knoblauch, C., Jørgensen, B. B. & Amann, R. Community Structure, Cellular rRNA Content, and Activity of Sulfate-Reducing Bacteria in Marine Arctic Sediments. *Applied and Environmental Microbiology* **66,** 3592–3602 (2000).
13. Pernthaler, J., Glöckner, F.-O., Schönhuber, W. & Amann, R. Fluorescence< i> in situ hybridization (FISH) with rRNA-targeted oligonucleotide probes. *Methods in microbiology* **30,** 207–226 (2001).
14. Boetius, A. *et al.* A marine microbial consortium apparently mediating anaerobic oxidation of methane. *Nature* **407,** (2000).
15. Treude, Boetius, Knittel, Wallmann & Jorgensen. Anaerobic oxidation of methane above gas hydrates at Hydrate Ridge, NE Pacific Ocean. *Mar Ecol Prog Ser* **264,** 1–14 (2003).

# Appendix 2:

## AUTOENDOLITHS: A DEISTINCT TYPE OF ROCK-HOSTED MICROBIAL LIFE

Jeffrey J. Marlow[1], Jörn Peckmann[2], Victoria J. Orphan[1]

[1]Division of Geological and Planetary Sciences, California Institute of Technology, Pasadena, CA
[2]Department of Geodynamics and Sedimentology, University of Vienna, Vienna, Austria

*Adapted from Marlow, J., J. Peckmann, and V. Orphan. "Autoendoliths: a distinct type of rock-hosted microbial life." Geobiology (2015).
DOI: http://doi.org/10.1111/gbi.12131

The continued exploration of Earth's biological potential has revealed a range of unexpected microbial habitats. The discovery of organisms inhabiting rock interiors, known as endoliths, was one such revelation that has altered our perspective of habitability, bioenergetics, and the relationship between biology and geology (Walker & Pace 2007).

Endolithic organisms were described during the early- to mid-1900s, but their detailed study was initiated largely by E. Imre Friedmann, who published reports of rock-hosted algae in the Negev Desert (Friedmann et al. 1967) and the Dry Valleys of Antarctica (Friedmann & Ocampo 1976). In an attempt to standardize terminology, Golubic et al. (1981) formalized rock-associated subdivisions, providing three distinct categories of endoliths (in contrast to exterior surface-associated organisms known as epiliths). The resulting description remains standard nomenclature to this day: "chasmoendoliths" inhabit fissures and cracks, "cryptoendoliths" live in structural cavities, and "euendoliths" actively penetrate into rock interiors (Fig. A2.1).

Here, we propose a fourth subdivision: the "autoendoliths" (using the Greek prefix for "self"), whose metabolism induces mineral precipitation, leading to the formation of a rock that remains inhabited by the same kind of organism (Fig. A2.1). Three criteria demarcate the autoendolithic lifestyle:

1) Microbial activity-dependent inducement of mineralization. This process may occur directly, when metabolic products precipitate as mineral phases, or indirectly, when a microbial matrix such as extracellular polymeric substances (EPS) promotes and structures localized mineralization.

2) The formation of rock (as opposed to poorly lithified precipitates) as a result of extensive biologically induced mineralization.

3) Continued metabolic activity within rock cavities.

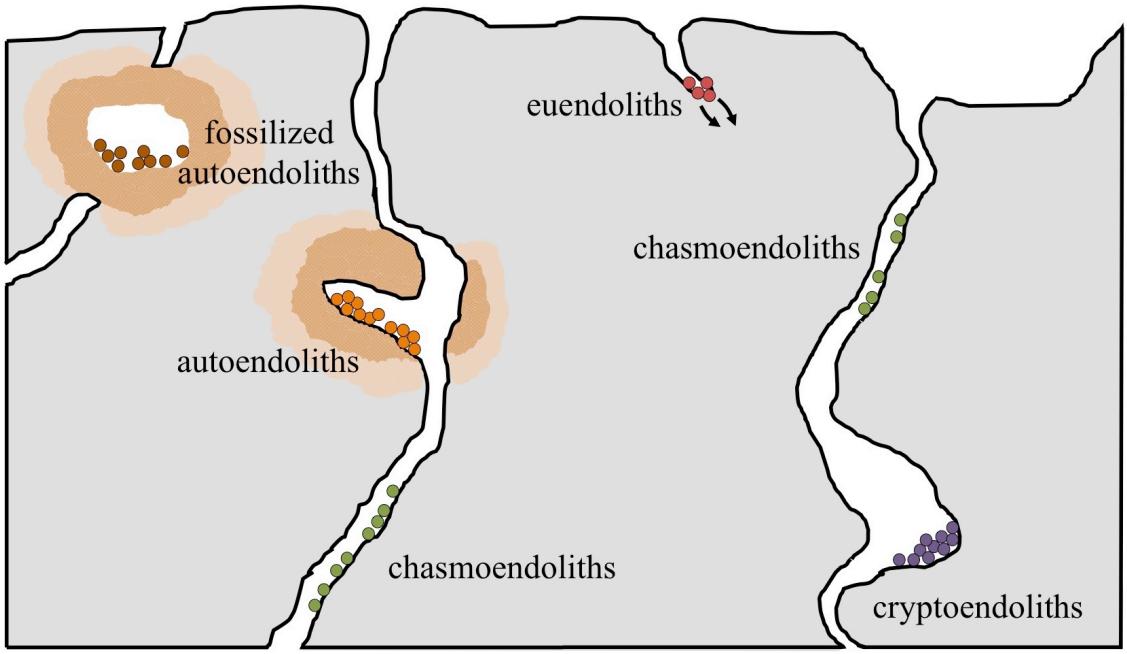


Fig. A2.1: A schematic diagram demonstrating relative locations and microbe-rock relationships of endolithic organisms. Gray shading represents previously formed solid rock, while white areas indicate conduits and pore spaces. The distinct types of endoliths are shown with colored circles, including the newly formalized autoendoliths, whose metabolism results in rock formation (indicated by the orange shading suggesting the integral role of metabolic by-products in rock precipitation). Autoendoliths retain activity when fluid conduits remain open; full self-entombment likely leads to the cessation of metabolic activity.

As with the Golubic et al. scheme, endolithic categorization retains its imprecision regarding functionality- and location-based parameters. Chasmoendoliths and cryptoendoliths are distinguished by their location within rock interiors, although their metabolic characteristics may vary widely, and their mode of mineral interaction is unspecified. Euendoliths and autoendoliths are not distinguishable by their relative

placements, but interact with their substrate in very different ways, through disintegration and construction, respectively.

We submit that autoendoliths represent a fundamentally distinct type of rock-hosted organism. Whereas the three previously named categories degrade rock or passively inhabit its cavities, seeking environmental stability or energy sources from the rock setting (Friedmann 1982; Walker & Pace 2007), autoendoliths construct the structures in which they reside, actively shaping their habitat and seemingly complicating future habitation prospects through pore space filling (Luff et al. 2004). Functionality- and location-based descriptors are not necessarily mutually exclusive; for example, pore occupying (cryptoendolithic) cyanobacteria in South African sandstone formations biochemically contribute to rock exfoliation (i.e., euendolithic behavior; Büdel et al. 2004). Thus, multiple terms may be needed to provide a precise indication of an organism's role and position within a lithified structure.

A model case of autoendolithic life is the carbonate rock-hosted anaerobic oxidation of methane (AOM) at marine methane seeps (Marlow, et al. 2014a). In accordance with the three criteria presented above, sulfate-coupled AOM metabolism is widely accepted to result in carbonate precipitation, as bicarbonate production increases local alkalinity and co-precipitates with dissolved cations to generate characteristically $^{13}C$-depleted seep carbonates (e.g., Ritger et al. 1987; Greinert et al. 2002). The resulting rock fabric is highly irregular, with semi-occluded cavities in which microbial aggregates persist (Fig. A2.2). Continued metabolic activity occurs within both porous carbonate rocks at actively seeping sites and more consolidated lithologies in settings with no or

little surface expression of methane seepage, which may reflect the latter stages of seepage and resultant self-entombment of AOM prokaryotes (Marlow et al., 2014a).

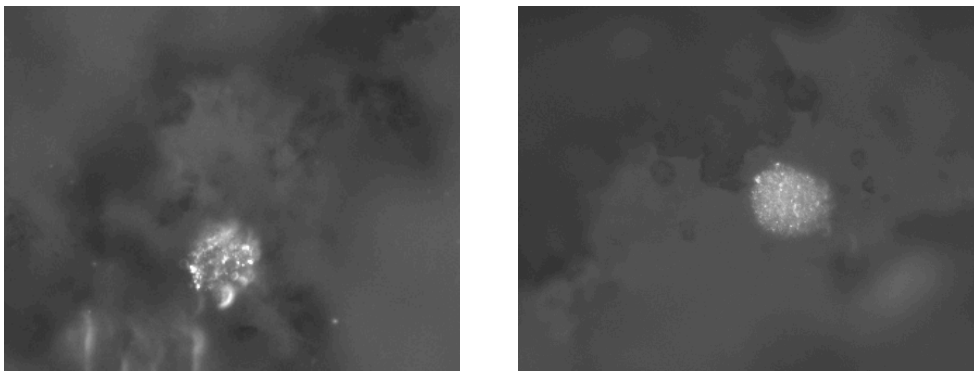

Fig. A2.2: DAPI-stained cell aggregates within authigenic carbonates from an active methane seep at Hydrate Ridge, OR. Similar aggregates from the same sample were identified as ANME-SRB consortia via fluorescence *in situ* hybridization and were shown to be actively performing AOM (Marlow et al., 2014a). Image acquired with an epifluorescence microscope at 40x magnification. Images are approximately 40 μm across.

Evidence for the successive nature of AOM-driven carbonate formation also comes from the analysis of ancient seep carbonate rocks, which archive a sequence of mineralization events. Among the $^{13}$C-depleted carbonate phases resulting from AOM are features that have been interpreted to represent fossilized biofilms that lined internal fractures crossing pre-existing methane-derived rock (Peckmann et al. 1999; Peckmann & Thiel 2004). Examples of such structures from the Miocene Marmorito seep deposit are shown in figures A2.3-A2.5, where putative autoendolithic biofilms are postulated to have precipitated dolomitic seams on internal surfaces of rock fragments that resulted from *in situ* brecciation prior to calcite cement infilling of the fractures. The fragmented microcrystalline rock matrix consists of $^{13}$C-depleted dolomite and contains $^{13}$C-depleted biomarkers of AOM-performing microorganisms. The observation that rock matrix and rock-hosted biofilms resulted from the same biogeochemical process indicates that AOM

activity persisted after initial rock formation (Peckmann et al. 1999; Hagemann et al. 2013). The mineral phases of such putative autoendolithic biofilms have been shown to contain more molecular fossils of AOM-associated microorganisms than other, similarly $^{13}C$-depleted mineral phases of the same seep deposits (Hagemann et al. 2013).

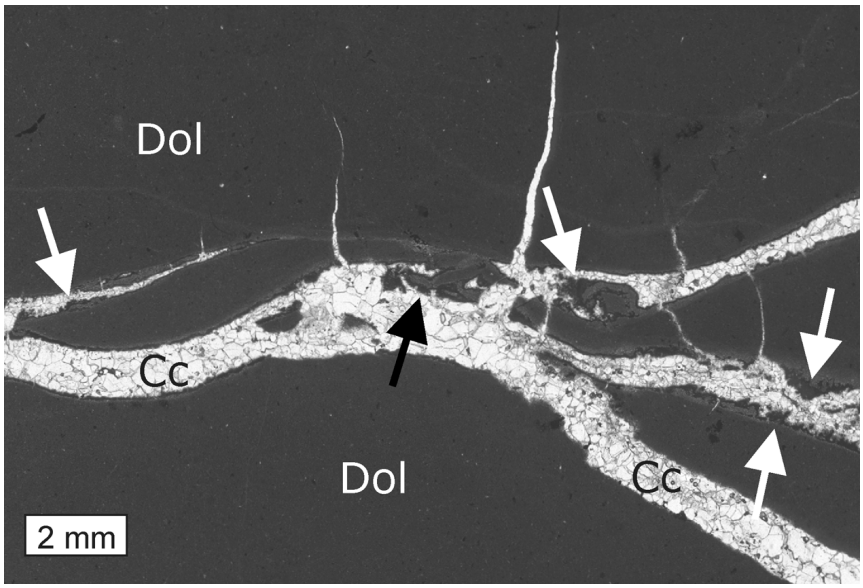


Fig. A2.3: Scanned thin section of fossilized endolithic biofilms of the Marmorito seep limestone, Miocene, northern Italy. The methane-derived dolomitic rock matrix (Dol) is cross-cut by veins subsequently filled with equant calcite cement (Cc). Fragmentation resulted from *in situ* brecciation at a methane seep, and rock matrix fragment surfaces are covered by microcrystalline, constructive seams of dolomite that are interpreted to represent fossilized biofilms of autoendolithic organisms (Peckmann *et al.*, 1999; Peckmann & Thiel, 2004). Arrows indicate most extensive dolomite seams; arrow on the far right indicates detail shown in Fig. A2.4.

Other mineralizing archaea and bacteria may fulfill some or all of the autoendolith requirements. Stromatolite-forming cyanobacterial mats trap and bind sediment and form carbonate rocks (Macintyre et al. 2000), with potential contribution from sulfate reducing bacteria (Visscher et al. 2000), although the extent to which microbial constituents remain active in lithified parts of a mat is unclear. Iron oxidizing bacteria such as *Gallionella* and *Leptothrix* precipitate minerals and retain activity, but the resulting iron

oxy-hydroxide precipitates fall short of the cohesive, macroscale deposits that would be considered a rock, at least on the timeline of a contiguous microbial community (e.g., Hallberg & Ferris 2004). Microorganisms have also been proposed to play a role in seeding manganese nodule (Wang et al. 2009) and phosphorite formation (Schulz & Schulz 2005; Crosby & Bailey 2012); biological colonization and continued activity may occur following rock formation (Berndmeyer et al. 2012), although this has not yet been observed in a modern system.

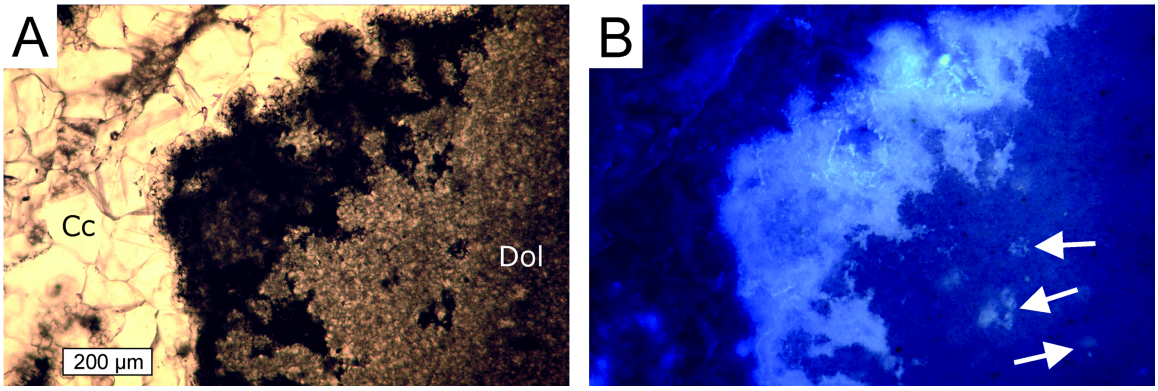


Fig. A2.4: Fossilized biofilms of the Marmorito limestone suggestive of autoendolithic activity. (A) The biofilm preserved as dolomitic seam (dark, center) overgrew a fragment of the dolomitic rock matrix (Dol) and is postdated by equant calcite cement (Cc); plane-polarized light image. (B) A fluorescence image showing the same feature as (A). The dolomitic seam exhibits an intense autofluorescence indicative of high organic matter content (e.g., Dravis & Yurewicz, 1985; Bertrand *et al.*, 1986). Some biofilm remains are engulfed in the methane-derived dolomitic rock matrix (arrows), indicating episodic precipitation and prolonged endolithic activity.

Determining whether a particular organism qualifies as an autoendolith is empirically challenging, although the application of contextual environmental and metabolic knowledge, stable isotope tracing experiments, and microscopic analysis can provide crucial information. For example, the observation of metabolisms facilitating the production of minerals found in a given environment (e.g., sulfate reduction for pyrite deposits or manganese oxidation in a birnessite-rich rock) could help reveal the role of

microbial activity in rock formation. Inferences from such observations can be used to develop laboratory-based microcosm experiments. To constrain the role of metabolic activity in mineral precipitation, one might provide isotopically labeled precursor substrate – both the element that is believed to enter the solid mineral phase as well as a general reporter of anabolic activity – to inhabited and killed control incubations. Measuring the isotopic composition of the resultant lithified material would reveal the role of biological activity in rock formation, while fluorescent *in situ* hybridization coupled with nanoscale secondary ion mass spectrometry (FISH-nanoSIMS) could constrain the phylogenetic identity of the organisms responsible (e.g., Dekas & Orphan 2011). Using this information alongside FISH-nanoSIMS and thin section light and electron microscopy of natural mineral deposits would complete the experimental cycle by linking process based empirical studies to the natural occurrence of the implicated organisms. The duration of continued autoendolithic viability can be assessed in part by long-term incubations or the use of rocks of various ages in incubation studies. Analyses of deposits from the rock record must rely on modern analogs for the first two aspects of this experimental approach, connecting ancient and contemporary processes through molecular or isotopic signatures.

The metabolism and precipitation balance sheet of autoendolithic life appears to represent a negative feedback mechanism in which metabolic activity creates conditions challenging to continued viability. However, self-generated physical substrate may confer an ecological advantage, such as a reduced threat of predation, and there are likely conditions under which long-term persistence is sustainable, as when a partially occluded conduit generates a steady-state advective flow sufficient to remove dissolved ions or

precipitated particles before nucleation (Zhao et al. 2007). Large-scale and highly irregular carbonate deposits with extensive internal surfaces likely provide a scaffold that traps and concentrates reactants, offering an opportunity for microbial descendants to persist and spread. The lithification process may seed structures with autoendolithic communities that can remain viable through periods of low seepage activity. Such communities may be resuscitated under the appropriate conditions (Marlow et al. 2014b) such as localized dissolution promoted by aerobic methanotrophy or sulfide oxidation, or the creation of new seepage conduits.

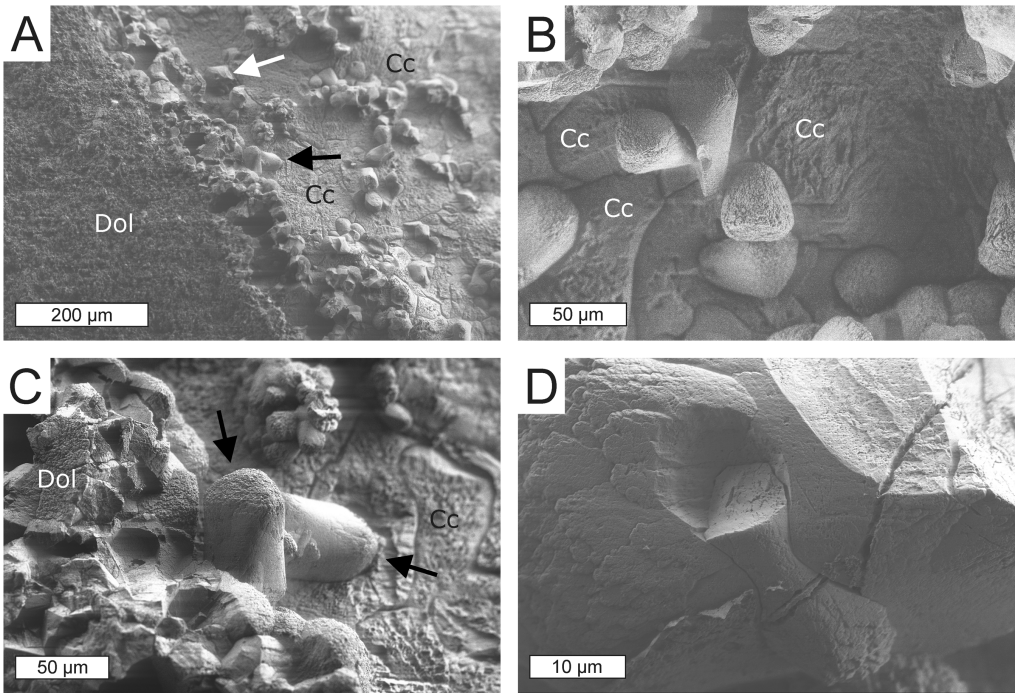


Fig. A2.5: Fossilized biofilms of the Marmorito limestone consists of crystal aggregates including hemispherical, rod-shaped, and dumbbell-shaped features that commonly result from microbially induced carbonate precipitation (Buczynski & Chafetz, 1991); field emission scanning electron microscopy images. (A) Dolomite crystal aggregates adhering to the dolomitic rock matrix (Dol) and encased by later equant calcite cement (Cc). Black arrow indicates the detail shown in (C), white arrow points to the detail shown in (D). (B) Pointed spherical (center) and rod-shaped crystal aggregates surrounded by later formed calcite spar (Cc). (C) Rod-shaped crystal aggregates with brush-like terminations (arrows) at the contact to the dolomitic rock matrix (Dol) and engulfed by calcite spar (Cc). (D) Dumbbell-shaped crystal aggregate preserved within a rod-shaped crystal aggregate.

Furthermore, a responsive balance between reactant concentration, advective flow, and metabolic rates could offer a sustainable existence in which precipitation directs fluid flow. At high ratios of fluid flow to mineral precipitation (a term that incorporates metabolic rate and precipitation kinetics), biogenic bicarbonate ions could be transported sufficiently far from the AOM reaction site as to not impinge upon continued viability. Moreover, autoendolithic communities may produce metabolites that could adaptively discourage mineral formation, similar to the calcium ion-scavenging EPS of cyanobacterial mats (Dupraz & Visscher 2005). Observations of silica-rich clay, rather than carbonate, templating onto the outer surface of AOM aggregates may suggest that the associated microenvironment is not immediately conducive to carbonate precipitation (Chen et al. 2014), which may impact nutrient flux. The type of carbonate mineral formed may also influence the niche of autoendolithic microorganisms in seep carbonates. The two most common phases – microcrystalline high Mg calcite and fibrous aragonite cement – pose different challenges and advantages to autoendoliths. The former mostly represents mineral formation in a matrix of fine sediment, where AOM activity will locally cease upon the occlusion of the pore space. The latter forms in rock cavities and fissures that are commonly up to several centimeters in width; in such endolithic environments, long-lasting AOM activity is more likely.

Autoendoliths represent a distinct category of rock-hosted life – one that merits inclusion in the categorization of endolithic organisms. Methane-oxidizing autoendoliths signify a type case of the group, but analogous lifestyles encompassing distinct metabolisms and lithologies may be common. The classification proposed herein broadens the scope of the microbial relationship with the geosphere from one of

opportunistic resident to a more intimate and nuanced role of geological constructor, offering geobiologists and microbial ecologists a new lens through which to view rock-hosted organisms.

References

Berndmeyer C, Birgel D, Brunner B, Wehrmann L, Jöns N, Bach W, Arning ET, Föllmi KB, Peckmann J (2012) The influence of bacterial activity on phosphorite formation in the Miocene Monterey Formation, California. *Palaeogeography, Palaeoclimatology, Palaeoecology* **317-318**, 171–181.

Bertrand P, Pittion J-L, Bernaud C (1986) Fluorescence of sedimentary organic matter in relation to its chemical composition. *Organic Geochemistry* **10**, 641–647.

Buczynski C, Chafetz HS (1991) Habit of bacterially induced precipitates of calcium carbonate and the influence of medium vicosity on mineralogy. *Journal of Sedimentary Petrology* **61**, 226–233.

Büdel B, Weber B, Kühl M, Pfanz H, Sültemeyer D, Wessels D. (2004). Reshaping of sandstone surfaces by cryptoendolithic cyanobacteria: bioalkalization causes chemical weathering in arid landscapes. *Geobiology* **2**, 261–268.

Chen Y, Li Y-L, Zhou G-T, Li H, Lin Y-T, Xiao X, Wang F-P (2014) Biomineralization mediated by anaerobic methane-consuming cell consortia. *Scientific Reports* **4**, 5696.

Crosby CH, Bailey JV (2012) The role of microbes in the formation of modern and ancient phosphatic mineral deposits. *Frontiers in Microbiology* **3**, 241.

Dekas AE, Orphan VJ. (2011). Identification of diazotrophic microorganisms in marine sediment via fluorescence in situ hybridization coupled to nanoscale secondary ion mass spectrometry (FISH–NanoSIMS). *Methods Enzymol* **486,** 281–305.

Dravis JJ, Yurewicz DA (1985) Enhanced carbonate petrography using fluorescence microscopy. *Journal of Sedimentary Petrology* **55**, 795–804.

Dupraz C, Visscher PT (2005). Microbial lithification in marine stromatolites and hypersaline mats. *Trends in Microbiology* **13**, 429–438.

Friedmann EI (1982) Endolithic microorganisms in the Antarctic Cold Desert. *Science* **215**, 1045–1053.

Friedmann I, Lipkin Y, Ocampo-Paus R (1967) Desert algae of the Negev (Israel). *Phycologia* **6**, 185–200.

Friedmann I, Ocampo R (1976) Endolithic blue-green algae in the Dry Valleys: Primary producers in the Antarctic Desert ecosystem. *Science* **193**, 1247–1249.

Golubic S, Friedmann I, Schneider J (1981) The lithobiontic ecological niche, with special reference to microorganisms. *Journal of Sedimentary Research* **51**, 475–478.

Greinert J, Bohrmann G, Elvert M (2002) Stromatolitic fabric of authigenic carbonate crusts: result of anaerobic methane oxidation at cold seeps in 4,850 m water depth. *Int J Earth Sci* **91**, 698–711.

Hagemann A, Leefmann T, Peckmann J, Hoffmann V, Thiel V (2013) Biomarkers from individual carbonate phases of an Oligocene cold-seep deposit, Washington State, USA. *Lethaia* **46**, 7–18.

Hallberg R, Ferris FG (2004) Biomineralization by *Gallionella*. *Geomicrobiology Journal* **21**, 325–330.

Luff R, Wallmann K, Aloisi G (2004) Numerical modeling of carbonate crust formation at cold vent sites: significance for fluid and methane budgets and chemosynthetic biological communities. *Earth and Planetary Science Letters* **221**, 337–353.

Macintyre IG, Prufert-Bebout L, Reid RP (2000) The role of endolithic cyanobacteria in the formation of lithified laminae in Bahamian stromatolites. *Sedimentology* **47**, 915–921.

Marlow JJ, Steele JA, Case DH, Connon SA, Levin LA, Orphan VJ (2014) Microbial abundance and diversity patterns associated with sediments and carbonates from the methane seep environments of Hydrate Ridge, OR. Frontiers in Marine Science 1.

Marlow, Steele JA, Ziebis W, Thurber AR, Levin LA, Orphan VJ (2014) Carbonate-hosted methanotrophy represents an unrecognized methane sink in the deep sea. *Nature Communications* **5**, 5094.

Peckmann J, Thiel V (2004) Carbon cycling at ancient methane–seeps. *Chemical Geology* **205**, 443–467.

Peckmann J, Thiel V, Michaelis W, Clari P, Gaillard C, Martire L, Reitner J (1999) Cold seep deposits of Beauvoisin (Oxfordian; southeastern France) and Marmorito (Miocene; northern Italy): microbially induced authigenic carbonates. *International Journal of Earth Sciences* **88**, 60–75.

Ritger S, Carson B, Suess E (1987) Methane-derived authigenic carbonates formed by subduction-induced pore-water expulsion along the Oregon/Washington margin. *Geological Society of America Bulletin* **98**, 147–156.

Schulz HN, Schulz HD (2005) Large sulfur bacteria and the formation of phosphorite. *Science* **307**, 416–418.

Visscher PT, Reid RP, Bebout BM (2000) Microscale observations of sulfate reduction: correlation of microbial activity with lithified micritic laminae in modern marine stromatolites. *Geology* **28**, 919–922.

Walker JJ, Pace NR (2007) Endolithic microbial ecosystems. Annual Reviews of Microbiology **61**, 331–347.

Wang X, Schröder H, Schloßmacher U, Müller WG (2009) Organized bacterial assemblies in manganese nodules: evidence for a role of S-layers in metal deposition. Geo-Marine Letters **29**, 85–91.

# Appendix 3: Supplementary Information for Chapter 3

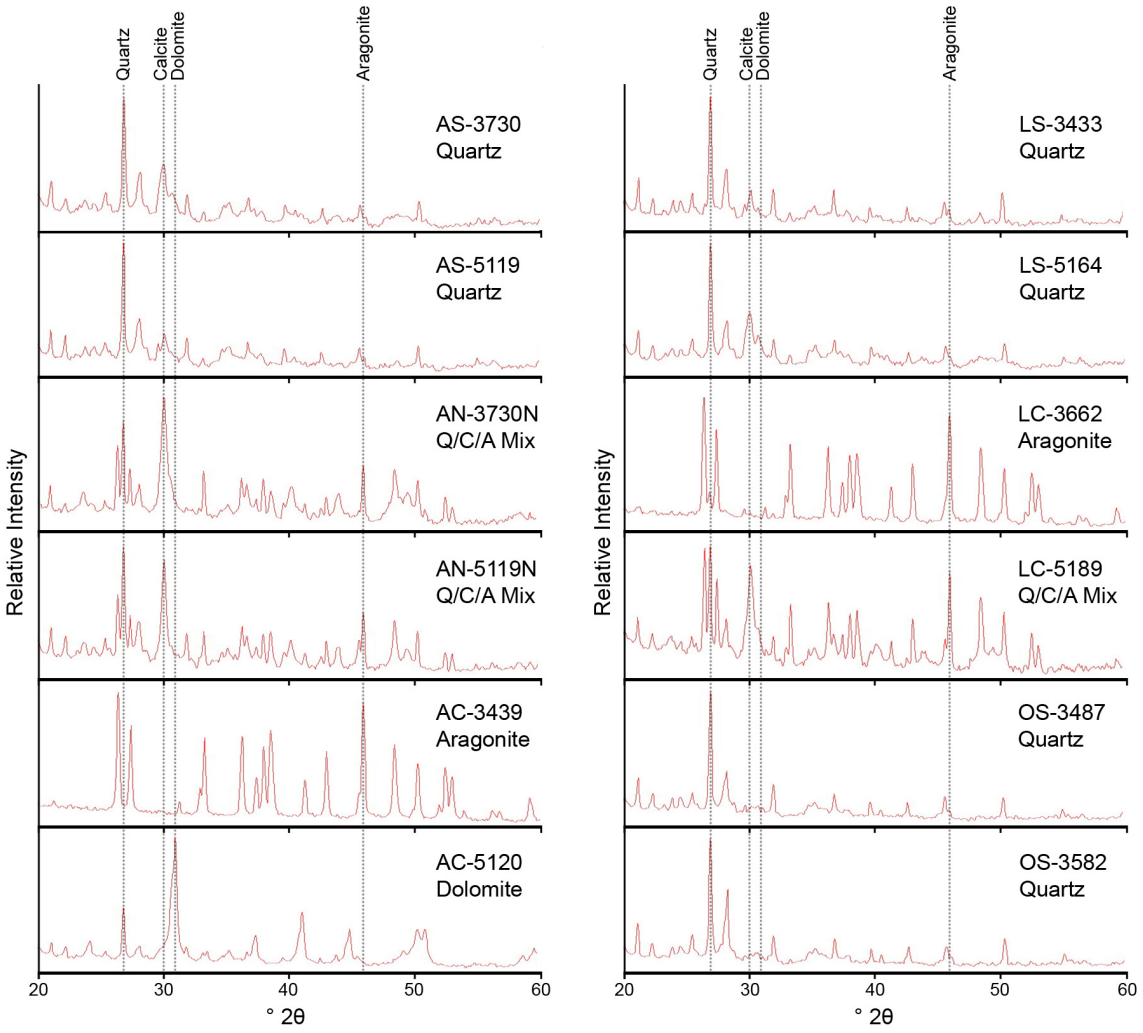


**Supplementary Figure 3.1**: X-ray diffraction data from the 12 samples analyzed in this study. Each panel shows an experimental spectrum and peak placements of the top database matches. Qualitative mineralogical assignments based on relative peak heights are provided below the sample identifier.

| | Archaea | | | Bacteria | | |
|---|---|---|---|---|---|---|
| **Sample** | Clones Sequenced | High Quality Sequences | Non-Chimeric Sequences Used in Analysis | Clones Sequenced | High Quality Full Length Sequences | Non-Chimeric Sequences Used in Analysis (One-Way) |
| AS-3730 | 33 | 29 | 29 | 96 | 79 | 73 |
| AS-5119 | 48 | 46 | 45 | 48 | 43 | 42 (3) |
| AN-3730N | 48 | 48 | 41 | 48 | 42 | 33 (1) |
| AN-5119N | 48 | 48 | 42 | 48 | 44 | 45 (3) |
| AC-3439 | 66 | 61 | 51 | 96 | 77 | 76 |
| AC-5120 | 48 | 48 | 43 | 48 | 42 | 38 (2) |
| LS-3433 | 48 | 47 | 35 | 48 | 31 | 38 (11) |
| LS-5164 | 48 | 47 | 41 | 48 | 44 | 39 (2) |
| LC-3662 | 48 | 45 | 43 | 48 | 40 | 42 (5) |
| LC-5189 | 57 | 53 | 50 | 48 | 46 | 39 |
| OS-3487 | 48 | 47 | 43 | 48 | 47 | 39 |
| OS-3582 | 48 | 46 | 44 | 48 | 47 | 36 |

**Supplementary Table 3.1**. The number of 16S rRNA gene sequences used for each sample at sequential steps of processing and analysis.

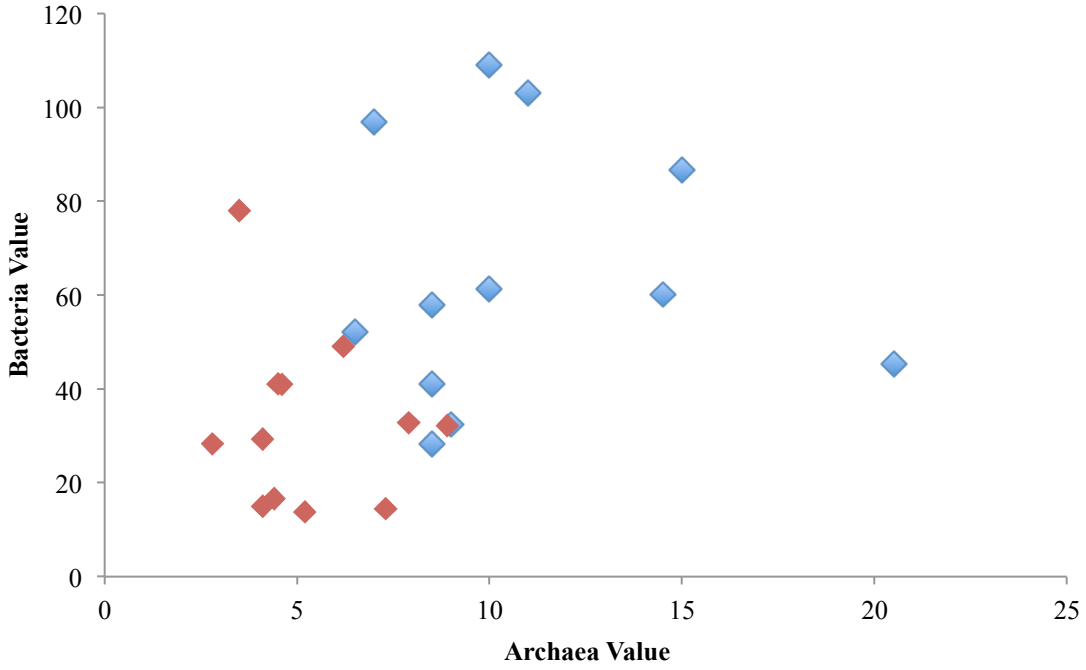


**Supplementary Figure 3.2**. Bacterial Chao-1 (blue) and Inverse Simpson (red) values vs. archaeal Chao-1 and Inverse Simpson values. The wide scatter of both blue and red points suggests no significant correlation between domain-level diversity indices. $R^2$ of the linear best fit is $2.8 \times 10^{-5}$ for Chao-1 and 0.029 for Inverse Simpson.

a)

| | Active | Low-Activity | Off-Seep |
|---|---|---|---|
| Active | | 0.2 (0.157) | 0.38 (0.107) |
| Low-Activity | 0.32 (0.057) | | -0.07 (0.533) |
| Off-Seep | 1 (0.036) | 1 (0.067) | |

b)

| | Sediment | Nodule | Carbonate |
|---|---|---|---|
| Sediment | | -0.14 (0.714) | 0.61 (0.01) |
| Nodule | -0.17 (0.786) | | 0.71 (0.067) |
| Carbonate | 0.03 (0.31) | 0.21 (0.267) | |

**Supplementary Table 3.2**. R level values for pairwise ANOSIM results on Bray-Curtis distances based on a) seep activity level or b) physical substrate type parameters. Green-shaded fields contain data from archaeal sequences; blue-shaded fields contain Bacteria-specific data. P values are in parentheses.

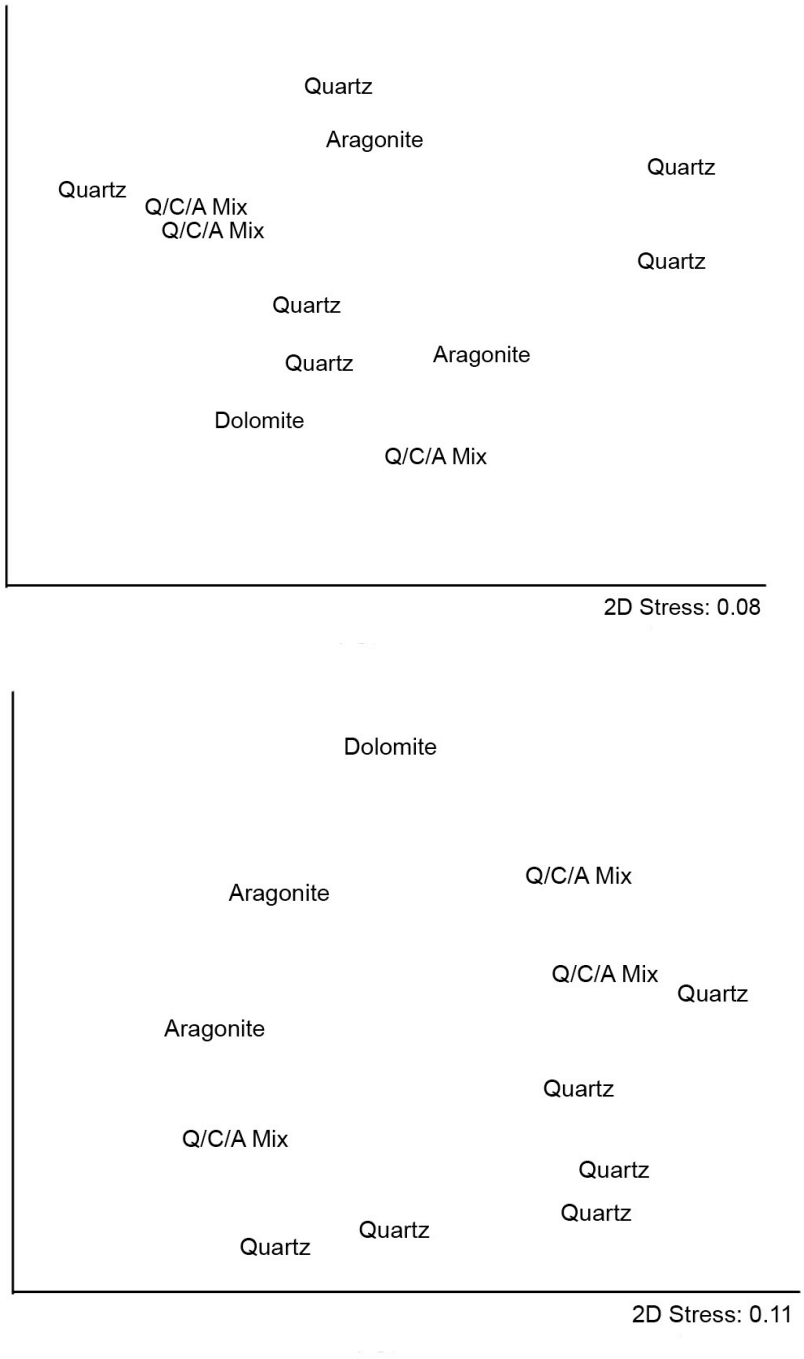


**Supplementary Figure 1.3.** Non-metric MDS results of a) archaeal, and b) bacterial communities, where samples are labeled by mineralogical type.

# Appendix 4: Supplementary Information for Chapter 4

**Supplementary Table 4.1**. Details of the constituents that comprise the metagenomic database used in this study.

| **In-house Metagenomes** | | | |
|---|---|---|---|
| **Metagenome Name** | **Source Material** | **Sequencing Platform** | **# of ORFs** |
| BC | Bead Capture from Hydrate Ridge Seep Sediment, E3A PC47, 0-9 cm | 454 | 25208 |
| V01 | Hydrate Ridge Seep Sediment, AD 4635 PC16, 0-6 cm | Illumina | 4599 |
| V02 | Hydrate Ridge Seep Sediment, E3A PC47, 0-9 cm | Illumina | 4841 |
| 3730 | Hydrate Ridge Seep Sediment, AD 4635 PC16, 0-6 cm | Illumina | 118384 |
| 5133 | Hydrate Ridge Seep Sediment, E3A PC47, 0-9 cm | Illumina | 78724 |
| 5579 | Hydrate Ridge Seep Sediment, E3A PC41, 0-12 cm | Illumina | 133690 |
| 3datasets | Combined assembly of 3730, 5133, 5579 | | 133255 |
| 5datasets | Combined assembly of 3730, 5133, 5579, VO1, VO2 | | 246534 |
| **Other Sequence Data** | | | |
| **Name** | **Source Material** | **Sequencing Platform** | **# of ORFs** |
| Hallam Fosmids[1] | Eel River Basin Seep Sediment | Sanger | 2219 |
| Meyerdierks Fosmids[2] | Black Sea Microbial Mats | Sanger | 3122 |
| ANME-2a[3] | Capt Aryutinov Mud Volcano | Illumina | 4031 |
| ANME-2d[4] | Sediment / Wastewater Sludge Enrichment | Illumina | 3427 |
| Cultured Organisms | NCBI Genome Repository | | 591976 |

**Supplementary Table 4.2:** Aggregate counts and sulfide concentration measurements for the incubations analyzed in this study.

| | #3731 | | | | #5133 | | | |
|---|---|---|---|---|---|---|---|---|
| | #3731 $^{14}N$ | | #3731 $^{15}N$ | | #5133 $^{14}N$ | | #5133 $^{15}N$ | |
| Days After Incubation Set-Up | Aggregate Counts (per mL) | Sulfide Concentration (mM) | Aggregate Counts (per mL) | Sulfide Concentration (mM) | Aggregate Counts (per mL) | Sulfide Concentration (mM) | Aggregate Counts (per mL) | Sulfide Concentration (mM) |
| 0 | $3.4 \times 10^6$ | 0.874 | $3.4 \times 10^6$ | 0.874 | $2.4 \times 10^7$ | | $2.4 \times 10^7$ | |
| 6 | | | | | | 1.192 | | 1.0324 |
| 17 | | 1.357 | | 1.954 | | | | |
| 20 | | | | | | 3.264 | | 3.837 |
| 65 | | 2.169 | | 1.563 | | 12.837 | | 13.029 |
| 160 | | | | | $3.4 \times 10^7$ | 14.323 | $4.1 \times 10^7$ | 17.863 |
| 326 | $2.7 \times 10^6$ | 4.188 | $7.9 \times 10^5$ | 3.029 | | | | |

**Supplementary Table 4.3**. The number of proteins identified in selected previous metaproteomic studies, using a variety of protein extraction, digestion, separation, MS, and search parameters. *1TP, 1UP proteins were only included when corresponding mRNA sequence was present. **Average from 27 samples; 3 MS/MS runs for each sample.

| Study | Sample | Protein Identifications | |
|---|---|---|---|
| | | 2TP 1UP | 1TP 1UP |
| Ram et al., 2005 | Acid Mine Drainage | 2033 | 5090 |
| Schulze et al., 2005 | Lake and Soil | | 513 |
| Kan et al., 2005 | Estuary | 3 | |
| Giovannoni et al., 2005 | Ocean | 1 | |
| Markert et al., 2007 | Riftia Symbionts | 220 | |
| Klaassens et al., 2007 | Infant GI Tract | | 1 |
| Lo et al., 2007 | Acid Mine Drainage | 3234 | |
| Lacerda et al., 2007 | Wastewater Treatment Reactor | 109 | |
| Benndorf et al., 2007 | Contaminated Soil / Groundwater | | 59 |
| Wilmes et al., 2008a | Sludge | 46 | |
| Wilmes et al., 2008b | Sludge | 2378 | |
| Park et al., 2008 | Sludge EPS | | 10 |
| Sowell et al., 2009 | Ocean | | 1042 |
| Denef et al., 2009 | Acid Mine Drainage | 2752** | |
| VerBerkmoes et al., 2009 | Human Gut | 2214 | |
| Dong et al., 2010 | South China Sea water column | 3035 | 505 |
| Pan et al., 2011 | Acid Mine Drainage biofilm | 815-2326 | |
| Liu et al., 2012 | Sponge symbiont community | 765 | |
| Stokke et al., 2012 | Nyegga Cold Seep | 356 | |
| Urich et al., 2014 | Trollveggen Hydrothermal Vent Field Microbial Mat | 1012 | 1408* |

**Supplementary Fig. 4.1**: $^{15}N$ enrichment distributions for all peptides identified in a) the #5133 15N and b) #3731 15N T2 incubations. In both cases, the precursor pool of $NH_4^+$ was 496 µM and 1 mM of $^{15}NH_4^+$ was added at the beginning of the incubation period.

a)

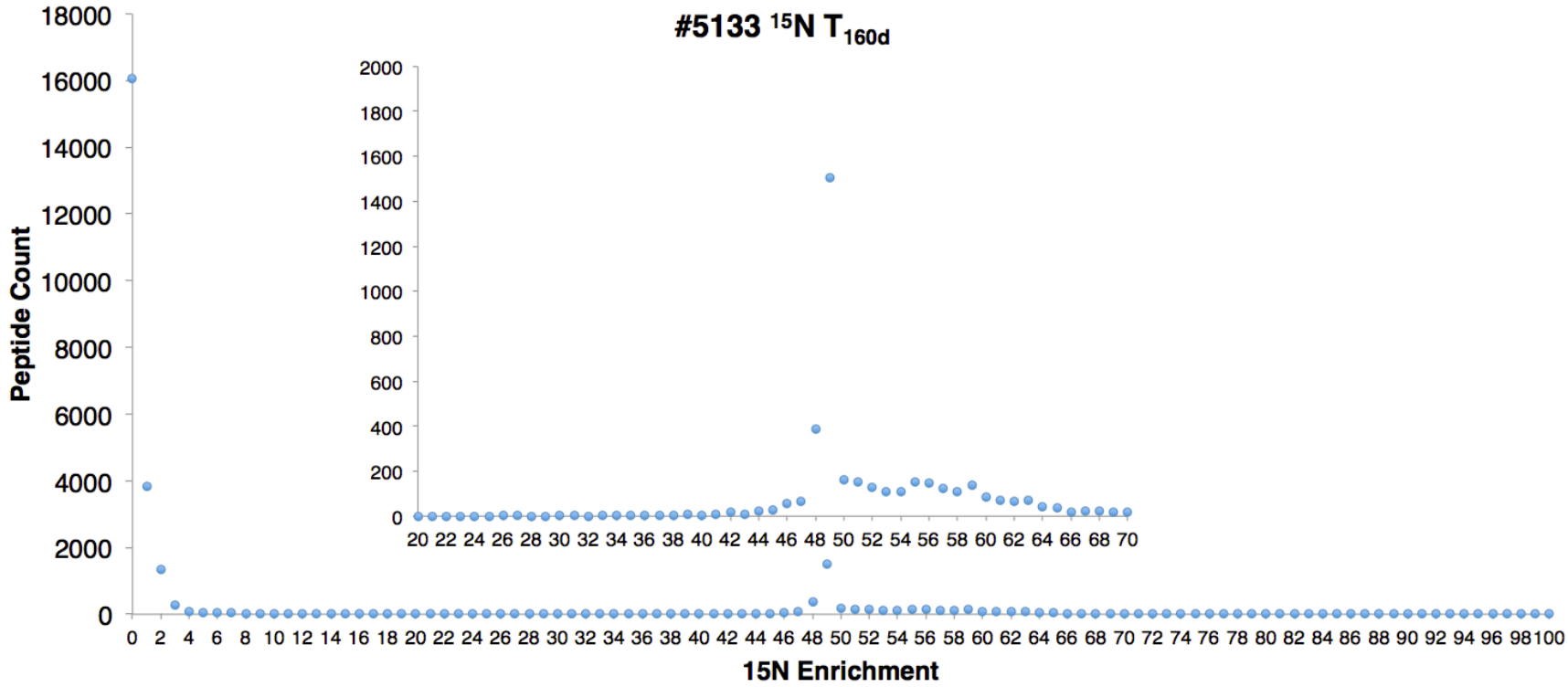

b)

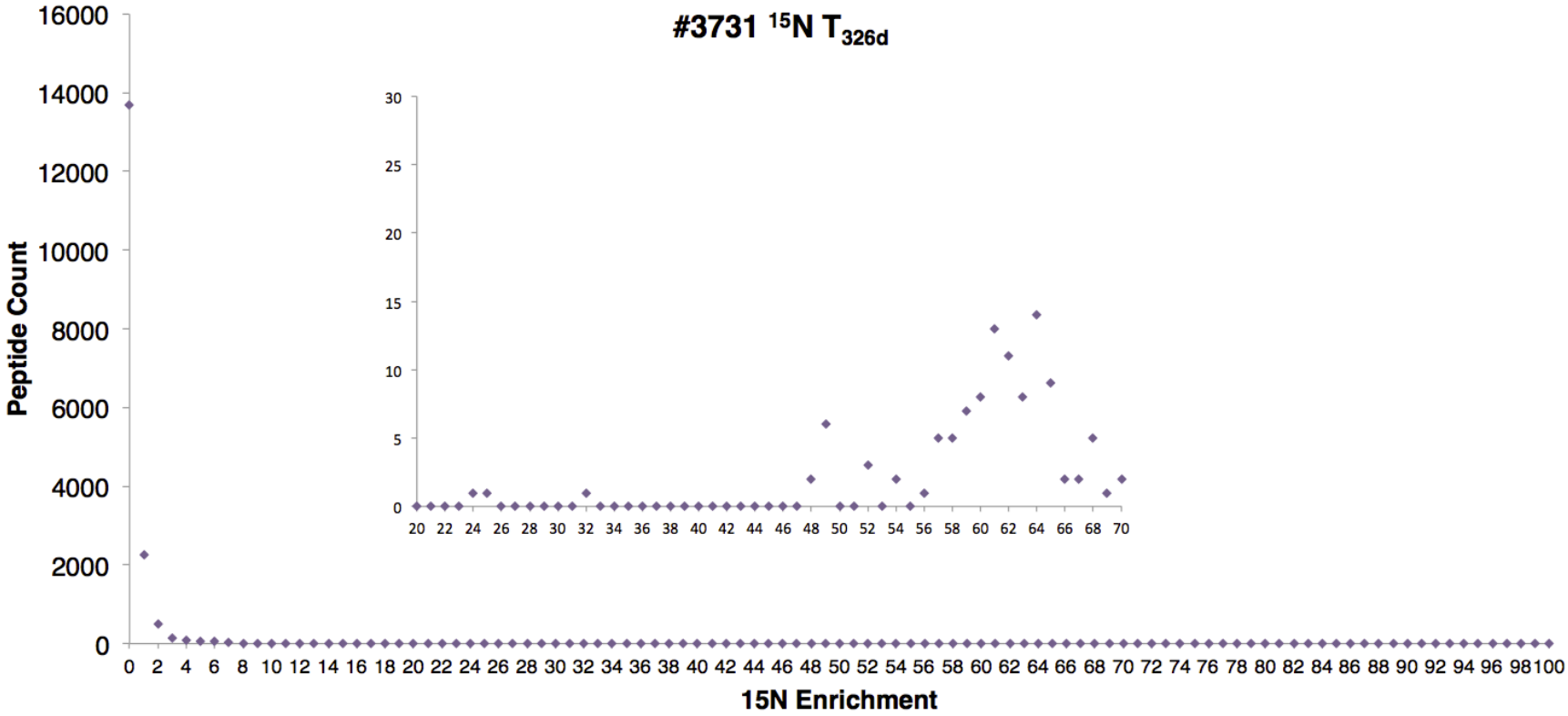
#3731 15N T326d
Peptide Count
15N Enrichment
0
2000
4000
6000
8000
10000
12000
14000
16000
0 2 4 6 8 10 12 14 16 18 20 22 24 26 28 30 32 34 36 38 40 42 44 46 48 50 52 54 56 58 60 62 64 66 68 70 72 74 76 78 80 82 84 86 88 90 92 94 96 98 100
0
5
10
15
20
25
30
20 22 24 26 28 30 32 34 36 38 40 42 44 46 48 50 52 54 56 58 60 62 64 66 68 70

**Supplementary Table 4.4**: UniProt and InterPro results for the 46 proteins that were detected in all six proteomes, enriched in #5133 15N, and were unannotated via KAAS and UniProt.

| ORF | UniProt Annotation | InterPro Annotation | Phylogenetic Assignment |
|---|---|---|---|
| | | | |
| BCs_pro_contig_00449_449_2 | Putative uncharacterized protein | | Uncultured archaeon |
| BCs_pro_contig_21403_21403_1 | Uncharacterized protein | | Uncultured bacterium |
| 3730_contig_546_3 | Putative uncharacterized protein | | Uncultured Desulfobacterium sp. |
| 3730_contig_2910_1 | Putative uncharacterized protein | Signal transduction | |
| 3730_contig_3529_6 | Putative uncharacterized protein | | Uncultured archaeon |
| 3730_contig_4042_9 | Uncharacterized protein | | |
| 3730_contig_5498_5 | Putative uncharacterized protein | | Uncultured Desulfobacterium sp. |
| 3730_contig_6405_2 | Uncharacterized protein | | Cand. Methanoperedens nitroreducens |
| 3730_contig_6723_4 | Putative uncharacterized protein | | Uncultured archaeon |
| 3730_contig_10399_1 | Uncharacterized protein | | Desulfonatronospira thiodismutans |
| 3730_contig_23750_5 | Hypothetical exported protein | | Syntrophus aciditrophicus |
| 3730_contig_26432_2 | Hypothetical protein | | Desulfatirhabdium butyrativorans |
| 3730_contig_27169_1 | Putative uncharacterized protein | | Uncultured archaeon |
| 3730_contig_30859_1 | Hypothetical protein | | Desulfuromonas sp. |
| 3730_contig_109916_2 | Uncharacterized protein | | Desulfonatronospira thiodismutans |
| 3datasets_contig_19395_3 | Putative uncharacterized protein | | Uncultured archaeon |
| 3datasets_contig_47745_1 | Hypothetical protein | Signal peptide | Desulfuromonas sp. |
| 3datasets_contig_52223_1 | Hypothetical secreted protein | Transmembrane domain | Uncultured archaeon |
| 3datasets_contig_56636_2 | Uncharacterized protein | Transmembrane domain | Desulfococcus oleovorans |
| 3datasets_contig_80833_1 | Uncharacterized protein | | |
| 3datasets_contig_128337_2 | Hypothetical secreted protein | Transmembrane domain | Uncultured archaeon |
| 5133_contig_2235_8 | Uncharacterized protein | | Cand. Methanoperedens nitroreducens |

| | | | |
|---|---|---|---|
| 5133_contig_14488_5 | Hypothetical exported protein | | Syntrophus aciditrophicus |
| 5579_contig_3535_1 | Putative uncharacterized protein | | Uncultured archaeon |
| 5579_contig_5937_4 | Putative uncharacterized protein | Signal transduction | |
| 5datasets_contig_13906_2 | Putative uncharacterized protein | | Uncultured Desulfobacterium sp. |
| 5datasets_contig_14875_4 | Uncharacterized protein | | Desulfococcus oleovorans |
| 5datasets_contig_26951_1 | Hypothetical protein | | Desulfosarcina sp. BuS5 |
| 5datasets_contig_34983_3 | Hypothetical protein | | Methylomarinum vadi |
| 5datasets_contig_41630_1 | Putative uncharacterized protein | Signal transduction | |
| 5datasets_contig_80150_1 | Hypothetical protein | | Longispora albida |
| 5datasets_contig_93287_2 | Putative uncharacterized protein | | Moorea producens |
| 5datasets_contig_110039_2 | Putative uncharacterized protein | | Desulfobulbus |
| 5datasets_contig_120508_2 | Hypothetical protein | | Desulfobulbus |
| 5datasets_contig_120634_2 | Hypothetical secreted protein | Transmembrane domain | Uncultured archaeon |
| 5datasets_contig_137335_2 | Putative uncharacterized protein | | Uncultured archaeon |
| 5datasets_contig_175666_3 | Hypothetical protein | | Thermodesulfatator atlanticus |
| 5datasets_contig_214909_1 | Putative uncharacterized protein | | Uncultured archaeon |
| 5datasets_contig_244181_2 | Uncharacterized protein | Transmembrane domain | Uncultured bacterium |
| 5datasets_contig_264150_1 | Putative uncharacterized protein | | Uncultured archaeon |
| 5datasets_contig_354507_3 | Putative uncharacterized protein | | Uncultured archaeon |
| 5datasets_contig_426791_2 | Putative uncharacterized protein | | Uncultured archaeon |
| VO1_contig_3180_1 | Putative uncharacterized protein | | |
| VO1_contig_16363_1 | Uncharacterized protein | | |
| VO1_contig_53771_3 | Putative uncharacterized protein | Signal transduction | |
| VO1_contig_140707_2 | Putative uncharacterized protein | | Uncultured archaeon |

**Supplementary Table 4.5**: Central reverse methanogenesis enzymes identified in metagenomic, metatranscriptomic, and metaproteomic analyses. Dark green = identified; light green = protein type identified, subunits unspecified; orange = not addressed; red = not identified. Proteins newly detected in seep environments during this study are highlighted in bold text. (McrABG subunits associated with ANME-2c derived fosmids were also detected; no other ANME-2c genes related to reverse methanogenesis were in the metagenomic database.)

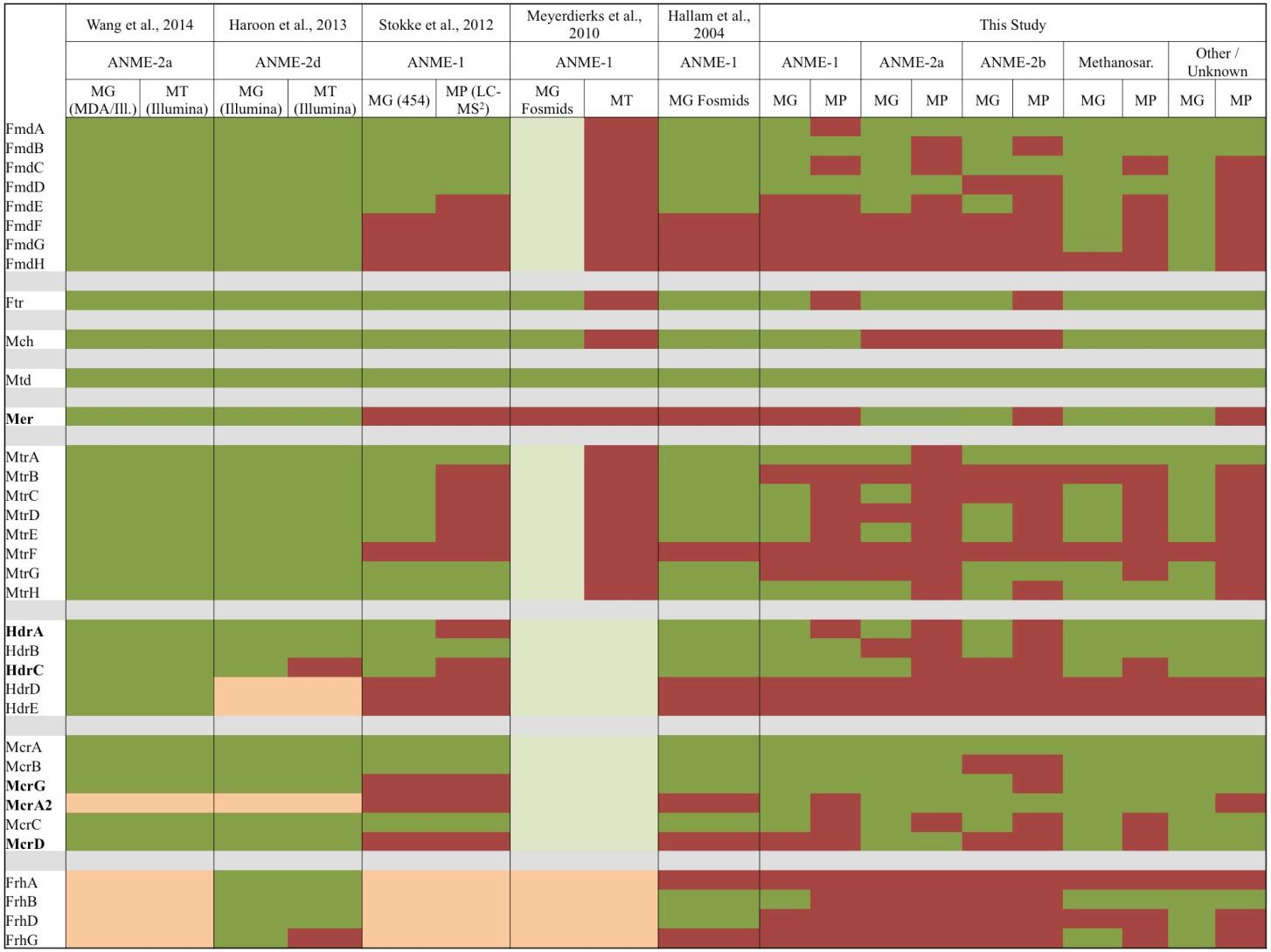
Wang et al., 2014
Haroon et al., 2013
Stokke et al., 2012
Meyerdierks et al., 2010
Hallam et al., 2004
This Study
ANME-2a
ANME-2d
ANME-1
ANME-1
ANME-1
ANME-1
ANME-2a
ANME-2b
Methanosar.
Other / Unknown
MG (MDA/Ill.)
MT (Illumina)
MG (Illumina)
MT (Illumina)
MG (454)
MP (LC-MS²)
MG Fosmids
MT
MG Fosmids
MG
MP
MG
MP
MG
MP
MG
MP
MG
MP
FmdA
FmdB
FmdC
FmdD
FmdE
FmdF
FmdG
FmdH
Ftr
Mch
Mtd
Mer
MtrA
MtrB
MtrC
MtrD
MtrE
MtrF
MtrG
MtrH
HdrA
HdrB
HdrC
HdrD
HdrE
McrA
McrB
McrG
McrA2
McrC
McrD
FrhA
FrhB
FrhD
FrhG

**Supplementary Table 4.6**: The order-level phylogenetic affiliations of sulfate reduction pathway enzymes detected in the cumulative metaproteome, given in percentage by enzyme.

| | **Sat** | **AprA** | **AprB** | **DsrA** | **DsrB** |
|---|---|---|---|---|---|
| Unclassified Proteobacteria | 0 | 2.4 | 0 | 0 | 0 |
| Proteobacteria // Betaproteobacteria // Hydrogenophilales | 0 | 4.9 | 0 | 0 | 0 |
| Proteobacteria // Deltaproteobacteria // Desulfobacterales | 20 | 19.5 | 15.8 | 7.1 | 30 |
| Proteobacteria // Deltaproteobacteria // Desulfovibrionales | 5 | 4.9 | 0 | 0 | 5 |
| Proteobacteria // Deltaproteobacteria // Desulfuromonadales | 0 | 4.9 | 0 | 0 | 0 |
| Proteobacteria // Deltaproteobacteria // Syntrophobacterales | 10 | 0 | 0 | 0 | 0 |
| Proteobacteria // Gammaproteobacteria // Chromatiales | 0 | 7.3 | 5.3 | 7.1 | 5 |
| Proteobacteria // Unclassified Deltaproteobacteria | 10 | 17.1 | 0 | 21.4 | 10 |
| Proteobacteria // Unclassified Gammaproteobacteria | 0 | 2.4 | 15.8 | 0 | 0 |
| Nitrospirae // Nitrospira // Nitrospirales | 0 | 2.4 | 0 | 0 | 0 |
| Unclassified Bacteria | 55 | 34.1 | 63.2 | 64.3 | 50 |

**Supplementary Table 4.7**: Data from various protein identification approaches, using the #5133 $^{14}N$ dataset.

| False Detection Rate | # Unique Peptides Required | # Total Peptides Required | # Proteins Identified |
|---|---|---|---|
| 1% | 0 | 1 | 12013 |
| 1% | 1 | 1 | 11166 |
| 1% | 1 | 2 | 2885 |
| 3% | 1 | 1 | 14134 |
| 3% | 1 | 2 | 3476 |

**Supplementary Figure 4.2**. Metaproteomic data for enzymes involved in the nitrogen metabolism.

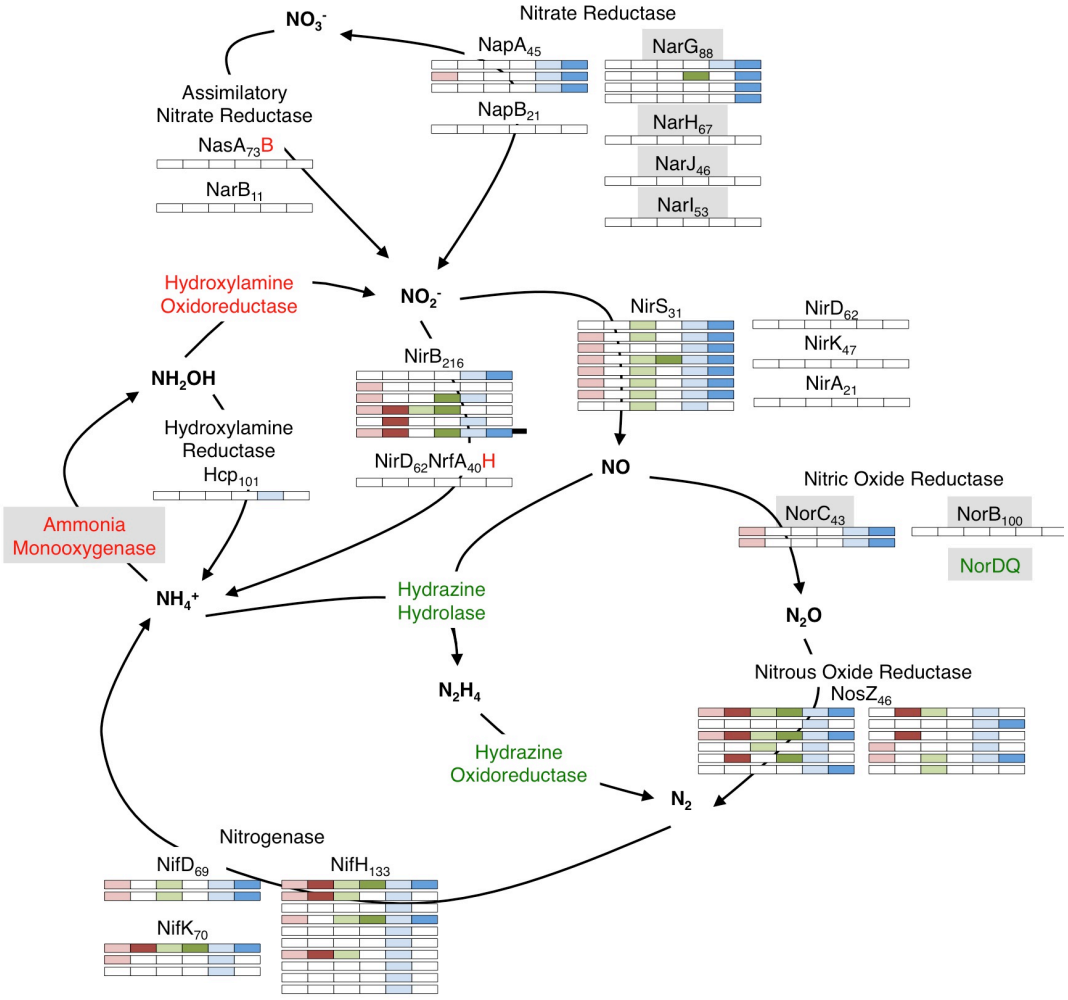

**Supplementary Figure 4.3**. Minimum net synthesis rates of proteins in sample #5133 $^{15}N$ with enriched unique peptides. Horizontal axis placement is arbitrary and connotes no information; red dots are indicative of reverse methanogenesis proteins, green dots signify sulfate reduction proteins, and blue dots are associated with all other proteins.

.

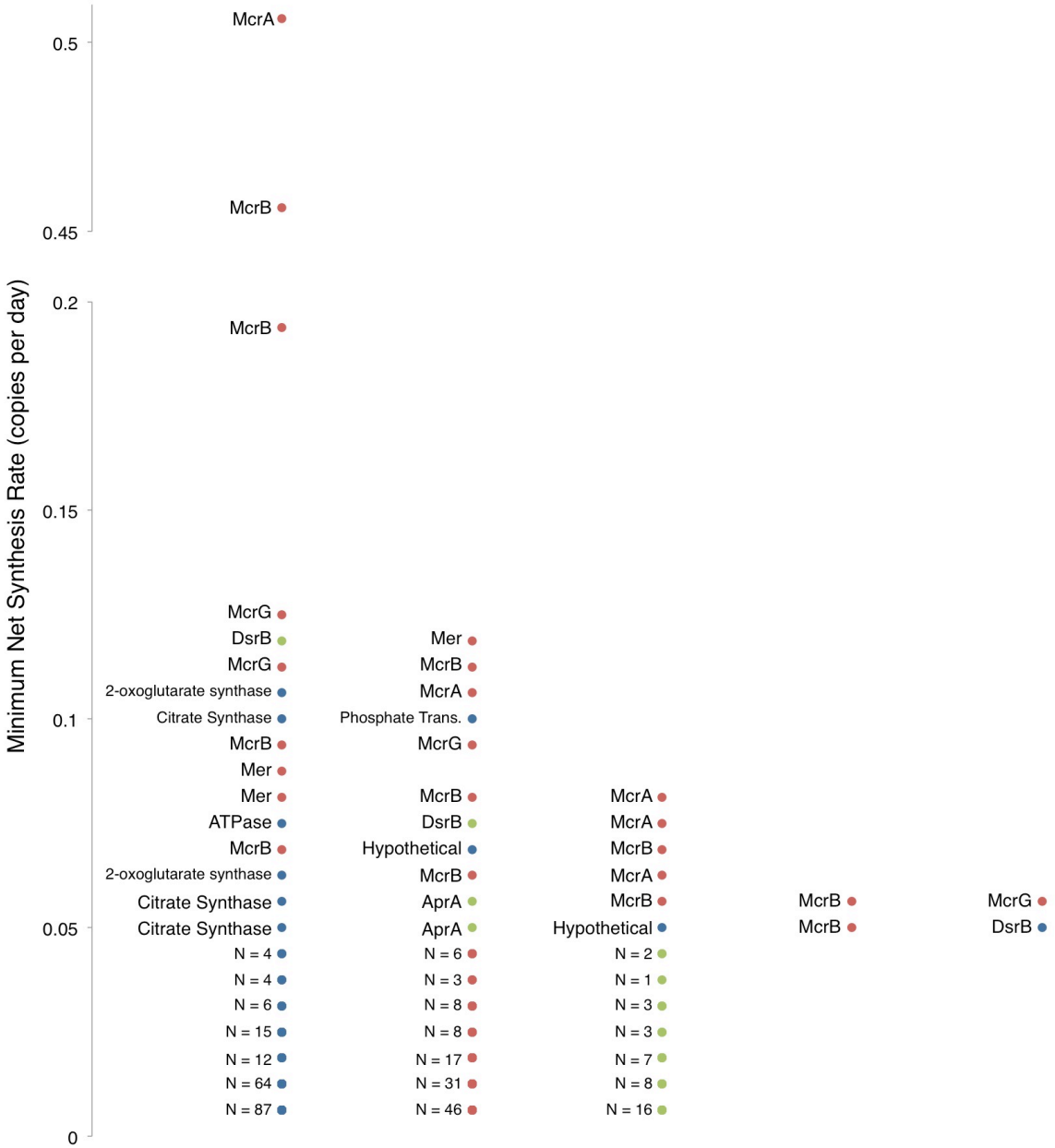

***Supplementary Methods***

*Sample Collection and Processing*

At Hydrate Ridge, the sulfate-methane transition zone occurs in the top several centimeters of seafloor sediment; within this horizon, microbial aggregate abundance, methane oxidation rates, and sulfate reduction rates are highest (Boetius et al. 2000; Boetius & Suess 2004). Methane concentrations at active seep sediments have been measured and modeled at values up to 70 mM (Boetius & Suess 2004) and 50 mM (Tryon et al. 2002), respectively; sulfate concentrations decrease with sediment depth, concomitant with augmented sulfide levels up to 26 mM (Sahling et al. 2002). On the seafloor, sediment was collected in push cores (35 cm long) deployed by the *ROV Jason* or *DSV Alvin*. #3730 and #3731 were both recovered from push core 16 from *Alvin* dive 4635 at Hydrate Ridge South, taken from an actively seeping site marked by clam beds, authigenic carbonates, and sparse white microbial mat. During the depressurization associated with ascent to the surface, supersaturated methane may have degassed, as suggested by occasional gas pockets in core tubes. Shipboard, push cores were immediately transferred to a 4 °C walk-in cold room and processed within several hours. To prepare sediment for future experimentation, compacted sediment was stored in anoxic, Ar-flushed mylar bags at 4 °C until use. Incubations prepared for metaproteomic analysis were amended with 1 mM of $^{14}NH_4^+$ or $^{15}NH_4^+$. Inhibition of microbial activity due to $^{15}NH_4^+$ was unlikely, as methanogen and sulfate reducing bacterial pure cultures, as well as methane seep sediment, showed no adverse effects when presented with $^{15}N$ ammonia ratios up to 100% (Krüger et al. 2008).

*16S rRNA Gene Tag Sequencing Processing Protocol*

Briefly, to process 16S rRNA gene tag data, paired Illumina MiSeq-derived reads were assembled into a single contig, trimmed to a minimum quality value of 30, and assigned to OTUs with uclust (Edgar et al. 2011) using a sequence similarity threshold of 99%. To run the protocol, place the makefile into the same directory as the raw sequencing reads, ensuring that qiime 1.8 and usearch are installed. The complete protocol can be run by typing "./orphanlab_itag_protocol.mk all" into the command prompt.

*Metagenome Database Construction and Annotation*

Bulk sediment metagenomes were derived from Illumina HiSeq data and processed as follows. Raw sequencing reads were quality trimmed (using a threshold of 0.05) and assembled using CLCBio genomics workbench 6.0. Sequencing reads from each metagenome were assembled individually and two assemblies were performed by combining sequencing reads from the three datasets. For each assembly, the raw sequencing reads from all datasets were aligned to contigs greater than 500bp with BWA 0.7.5a (Li 2013) using the 'mem' algorithm and converted into bam files using samtools 0.1.19 (Li et al. 2009). These bam files were used as input for GroopM 0.2 (Imelfort et al. 2014), which generated genome bins. The 'refine' command in GroopM was used to improve the genome bins manually by removing contigs with unusual coverage or tetramer frequencies. The completeness and contamination of genome bins was determined using CheckM 0.9.4 (Parks et al. 2014).

Bead capture metagenomes derived from 454 sequencing platforms generated ~25-145 Mb of sequence data per sample. Sequencing reads from all bead capture metagenomes were combined and assembled using Newbler. Open reading frames

(ORFs) were called using prodigal 2.5 (Hyatt et al. 2010) using the metagenome mode (command line 'prodigal –i <FILE> -p meta –a <translation.faa> -o <output.gbk>'). Only ORFs that were considered complete (contained both a start and stop codon) were considered for inclusion to the metagenomic database. This data set was supplemented with fosmid sequence from seep sediment and physiologically relevant genomes from cultured organisms. All ORFs were clustered at 100% identity using uclust (Edgar et al. 2011) to remove duplicates.

Functional annotations were derived from previously determined NCBI annotations (for cultured organism genomes) or the KEGG Automatic Annotation Server (KAAS; Moriya et al. 2007) for genes from the metagenomes. For cultured organisms, phylogenic affiliations of gene products were incorporated from NCBI annotations. For the metagenomes, the phylogeny of genome bins with low (< 10%) contamination was assessed using the CheckM parsimonious genome tree, and the proteins derived from that genome bin were all given the same taxonomy. For all other proteins derived from the metagenomes, individual genes were compared to the NCBI nr database using blastp 2.2.29+ (Camacho et al. 2009) and taxonomy was determined using the lowest common ancestor algorithm implemented by Blast2lca 0.600 (https://github.com/emepyc/Blast2lca). #5133 $^{15}$N enriched proteins that were annotated as "hypothetical proteins" by KAAS (n=319) were subjected to a secondary search process. Corresponding ORFs were blasted against UniRef 90 (Suzek et al. 2007) using the UniProt platform (UniProt Consortium 2008) and an e-value cutoff of $10^{-30}$. Annotations derived from this process were incorporated into the data analysis, while ORFs that remained "hypothetical" or "uncharacterized" were searched by hand against

the Interpro database (Mitchell et al. 2014) for putative functional domains. The subset of these proteins that was also present in all six proteomes (n=62) is discussed in the "Hypothetical Proteins" section of the main text.

Proteins involved in the reverse methanogenesis pathway were resolved to finer phylogenetic resolution to determine their ANME subtype affiliation. Proteins from the metagenomes were combined with proteins downloaded from the KEGG database and aligned using muscle 3.8.31 (Edgar 2004). A phylogenetic tree was built from the alignment using FastTree 2.1.7 (Price et al. 2010) and visualized with Archaeopteryx 0.9901 (https://sites.google.com/site/cmzmasek/home/software/archaeopteryx). ANME subtypes were determined by identifying monophyletic groups with known ANME-1, ANME-2a, ANME-2b and ANME-2c sequences and cross validating between genes from the same contigs to resolve inconsistencies in phylogenetic placement. The alignment shown in Fig. 4.3 was visualized in Jalview 2.8.2 (Waterhouse et al. 2009).

*Protein Extraction Protocol*

Environmental metaproteomics investigations have dealt most prominently with samples of relatively low community complexity and few mineralogical / geochemical complications (Wilmes & Bond 2009; Ram et al. 2005). As investigations moved into soils and sediments, difficulties arose due to high community diversity, soil matrix hydrophobicity, and protein degradation caused by humics (Bastida et al. 2009; Solaiman et al. 2007). In this study, proteins were isolated using an SDS-TCA-based protocol for direct protein extraction as outlined in Chourey et al., (2010).

To summarize, frozen sediment slurry was thawed, and 10g (#3731 T1 and T2) or 5g (#5133) of wet sediment were placed in a 100 mL glass Pyrex beaker with 20 mL of

lysis buffer (5% SDS, 50 mM Tris-HCl, pH 8.5, 0.15 M NaCl, 0.1 mM EDTA, 1 mM $MgCl_2$). The denaturing agent dithiothretiol (DTT) was added to a final concentration of 75 mM. The mixture was vortexed and immersed in a boiling water bath for 20 minutes, then allowed to cool for five minutes and transferred to a sterile 50 mL Falcon tube. A 10-minute centrifugation at 2500 x g separated soil particles and cellular debris from the whole cell lysate, which was retained in the supernatant. 1.5 mL of supernatant was pipetted into each of two 2-mL tubes, to which 100% trichloroacetic acid (TCA) was added to a final concentration of 25%. The tubes were vortexed and stored overnight at -20 °C to precipitate the extracted proteins. 200 µL of 6 M guanidine was added the next day, and following an overnight incubation at 4 °C, tubes were centrifuged for 1 minute at 2000 x g to collect any in-tube condensation and the contents were combined. DTT was added to a final concentration of 10 mM, and the solution was incubated at 37 °C for 60 minutes. To avoid trypsin deactivation, the mixture was diluted 1:6 with 50 mM Tris (with 10 mM $CaCl_2$ buffer) to achieve a guanidine concentration of 1 M. Trypsin was added in two separate doses of 20 µg each, separated by several hours of incubation at 37 °C; the second addition was allowed to incubate overnight. DTT was again added to a final concentration of 10 mM and allowed to incubate for 45 minutes at room temperature; this step was intended to linearize peptides prior to filtration. The peptide solution was de-salted using a $C_{18}$+ Sep-Pak solid phase extraction cartridges (Waters, Milford, MA). The column was initially wetted with acetonitrile and water; sample was then added, and the filtered flow-through was run through the column again. HPLC-grade $H_2O$ + 0.1% formic acid was introduced to remove soluble salts, and acetonitrile + 0.1% formic acid was used to elute the peptides. (Formic acid is used in on-line solvents in

order to protonate analytes for downstream electrospray ionization.) This elution was collected and placed in a Savant SpeedVac (ThermoFisher Scientific, Waltham, MA) to evaporate the solvent and concentrate the solute by approximately 10x. Tubes were stored at -20 °C overnight; the next day, contents were pooled with 500 μL $H_2O$ and dried with SpeedVac treatment to ensure full removal of acetonitrile. The resulting solution was stored at -80 °C prior to two-dimensional LC−MS/MS analysis.

*Peptide Separation and Analysis*

Two duplicate runs of LC-MS/MS analysis were conducted for each sample. Peptides were seppaked, solvent exchanged in acidified water ($H_2O$ with 0.1% formic acid) and ~75 μg peptides were pressure-loaded onto split-phase Reverse Phase (RP)-SCX column which was aligned with an in house RP-packed PicoFrit tip (New Objective, Woburn, MA). Peptides were eluted and chromatographically separated via a 24-hr Multi-Dimensional Protein Identification Technology (MuDPIT), using an 12-step salt gradient using liquid chromatography (LC) as described earlier (Brown et al, 2006 , Thompson et al., 2007, Sharma et al, 2012). Peptide analyte was introduced to the MS/MS system by electrospray ionization. Peptide separation, fragmentation and measurements were carried out using various high end mass spectrometers (Thermo Fisher Scientific, Germany) coupled to the Ultimate 3000 HPLC system (Dionex, USA) and operated in data dependent mode using the Thermo Xcalibur software V2.1.0. Each full scan was followed by individual microscans of the 20 most abundant parent ions, which were fragmented via collision-activated dissociation (CID) using 35% collision energy, a mass exclusion width of 0.2 m/z, and a dynamic exclusion duration of 60 s. A range of Orbitrap instruments was used for data collection in keeping with the rapid

development of the field's best available technology: #3731 $^{14}N$ $T_1$ and #3731 $^{15}N$ $T_1$ were analyzed on an LTQ Orbitrap Velos, #3731 $^{14}N$ $T_2$ on an LTQ Velos, #3731 $^{15}N$ $T_2$ on an LTQ Orbitrap Velos Pro, and #5133 $^{14}N$ and #5133 $^{15}N$ on an LTQ Orbitrap Elite.

*Protein Search Parameters*

When searching MS/MS data with the Sipros / ProRata 3.0 program (Wang et al. 2013), the metaproteomic database was predicted from the metagenomes and concatenated with its reverse complement to estimate its false positive detection rate (FDR) (Elias & Gygi 2007). The search results were filtered to achieve a specified FDR at the peptide level, and proteins were inferred from the identified peptides using parsimony rules (Nesvizhskii & Aebersold 2005).

Identifying peptides and determining precursor protein identifications required three parameters: the peptide-level FDR and the number of unique and total peptides matched to the protein in question. The most stringent settings, which have been used in several proteomics studies (e.g., Liu et al. 2012; Verberkmoes et al. 2009; Denef et al. 2009), are a 1% FDR, 2 total peptides, and 1 unique peptide (expressed with the notation [1%, 2TP, 1UP]). However, the [1%, 1TP, 1UP] approach has been promoted on statistical grounds (Gupta & Pevzner 2009), and with the acknowledgement that less stringent protein identification parameters result in lower confidence of a protein's presence, we examined the balance between FDR, UP, and TP requirements and the number of identified proteins. Using the #5133 $^{14}N$ data and the metagenomic database described in Table S4.1, five different Sipros search parameters were tested: [1%, 1TP, 0UP], [1%, 1TP, 1UP], [1%, 2TP, 1UP], [3%, 1TP, 1UP], and [3%, 2TP, 1UP] (Table S7).

We found that a relaxation of the FDR from 1% to 3% led to an average protein count increase of 23.5% (1TP, 1UP increase was 26.6%; 2TP, 1UP increase was 20.5%). Removing the requirement that the 1TP be a unique peptide resulted in a 7.6% increase in protein identifications. Shifting from a 2TP, 1UP requirement to 1TP, 1UP created the most substantial increase, resulting in an average of 297% more proteins (1% FDR increase was 287%; 3% FDR increase was 307%). Because of the large increase in protein identifications and the statistical validity of the 1TP, 1UP search parameter (Gupta & Pevzner 2009), we present both [1%, 1TP, 1UP] and [1%, 2TP, 1UP] results, clearly noting the provenance of each identification. Our 3% FDR and 1TP, 0UP searches resulted in relatively minor increases in the number of protein identifications but tripled the error rate and removed the protein-specificity requirement, respectively; thus, we believe these search parameters do not warrant inclusion in our analysis.

The following PTMs were dynamically searched in McrA analysis: oxidation of methionine; hydroxylation of proline and lysine; deamidation of asparagine and glutamine; citrullination of arginine; monomethylation of arginine, lysine, aspartic acid and glutamic acid; dimethylation of arginine and lysine; trimethylation of lysine; phosphorylation of serine, threonine, tyrosine, histidine and aspartic acid; acetylation of lysine; S-nitrosylation of cysteine; nitration of tyrosine; and methylthiolation of aspartic acid. PTMs were localized based on the DeltaP score as described in Li et al (2014).

*SIP Enrichment Threshold*

To set the $^{15}N$ value above which a peptide would be declared "enriched", multiple factors were considered. First, peptide $^{15}N$ distributions from each sample's $^{14}NH_4^+$ incubation were determined, and the value below which 99% of peptides fell set a

1% FDR for the declaration of enriched peptides. This value was 3% $^{15}N$ in #3731 $T_1$, 4% in #3731 $T_2$, and 5% in #5133.

Alternatively, we can consider the probability of unenriched peptides containing a range of $^{15}N$ values using the binomial distribution. Using the mean enrichment value of the corresponding $^{14}NH_4^+$ incubation as the baseline $^{15}N$ frequency (0.45% for #3731 $^{14}N$ $T_1$, 0.35% for #3731 $^{14}N$ $T_2$, and 0.49% for #5133 $^{14}N$), expected frequencies of N-length peptides containing X% $^{15}N$ can be calculated. Shorter peptides are more likely to yield a higher $^{15}N$ atom % value as a function of $^{15}N$ incorporation probability. For example, with a 6-residue peptide (the shortest peptide detected across all samples, which, with an average of 1.31 N atoms per amino acid as measured across all proteomic samples, has 8 N atoms), the probability of 1 $^{15}N$ atom given #5133 $^{14}N$'s isotopic frequency of 0.49% $^{15}N$ is 3.8%. Thus, there is a 3.8% chance of observing a 12.5% $^{15}N$ atom % value given $^{14}NH_4^+$ incubated sample material. When the probability of different $^{15}N$ atom % values was plotted based on the binomial distribution and a best fit curve was calculated ($R^2$ = 0.99924), the $^{15}N$ enrichment value corresponding to a 1% likelihood of natural occurrence (i.e., the $^{15}N$ value corresponding to a 99% confidence that it in fact was not enriched), was 0.1%. In a 53-residue peptide (the longest detected in this analysis), 70 N atoms are predicted; the likelihood of one $^{15}N$ atom incorporation is much higher (24.6%) but the atom % $^{15}N$ this represents is substantially lower (1.43%). There is a 4.2% chance of a 2.86% $^{15}N$ enrichment, and a 0.47% chance of a 4.29% enrichment.

Of these statistical tests, the most conservative 99% confidence interval surrounding an "enriched" designation is 5% $^{15}N$ (derived from the $^{15}N$ distribution in peptides recovered from the #5133 $^{14}N$ sample). This value therefore demarcates enriched

proteins in this study's analysis; the same enrichment level has been used as a threshold in other SIP studies (Justice et al. 2012; Pan et al. 2011).

*Protein Abundance*

Relative quantification was conducted using spectral counts, an approach that has been incorporated into previous studies of eukaryotic systems (Pan et al. 2011), cultured bacterial (Albrethsen et al. 2013), and environmental (Justice et al. 2012) proteomic profiles. Given the correlation between the amount of a protein and the number of tandem mass spectra associated with it (Liu et al. 2004), more spectral counts reveal a higher protein concentration. This label-free approach is advantageous because it permits simultaneous protein identification and quantification, a particularly useful trait in sample-limited experiments like the Hydrate Ridge sediment incubations. There is also evidence that label-free approaches offer a larger dynamic range than stable isotope approaches (Bantscheff et al. 2007) and offers the deeper proteome coverage than isobaric or metabolic labeling techniques (Li et al. 2011). However, the broad quantitative comparability of distinct peptides is limited by the dynamic exclusion of ions already analyzed by fragmentation limits accuracy for high-abundance peptides (Old et al. 2005), but enables higher overall peptide and spectral counts and a more reliable detection of low-abundance proteins (Zhang et al. 2009).

To facilitate semi-quantitative comparisons of individual proteins between experiments, the normalized balanced spectral count (NBSC) was calculated for each protein in a given experimental treatment (Li et al. 2011). Unique peptides' spectral counts were allocated to their associated protein, and spectral counts of shared peptides were distributed evenly between the proteins to which they matched. These "balanced"

spectral counts were then normalized by both run and experiment (most experiments had two technical replicate LC MS/MS "runs"). To determine the NBSC for a particular sample, total spectral counts for a given run were determined, ratioed between the two runs, and the resulting scaling factor was applied to the balanced spectral counts of the run with fewer total spectral counts. When proteins were identified in both runs, the two NBSCs were averaged. To normalize between all experiments, the same process was performed on each experiment's run-normalized balanced spectral count values, using a scaling factor calculated as the largest NBSC sum divided by the NBSC sum of the experiment in question. These normalization steps assume that equivalent quantities of peptide material are analyzed with each LC MS/MS run and allow for semi-quantitative comparisons of individual proteins between different experimental treatments.

## ***Supplementary Results & Discussion***

### *Protein Identifications*

Phylogenetic affiliations of detected proteins offer insight into lineages present in seep sediment material. Among Archaea, proteins linked with Methanosarcinaceae (27.8%), unclassified Methanomicrobia (12.6%), unclassified Methanosarcinales (12.3%), and ANME-1 (12.1%) were most abundant (all values in reference to 2TP, 1UP conditions). Bacterial proteins were most commonly identified as unclassified Bacteria (27.8%), Desulfobacteraceae (12.7%), unclassified Deltaproteobacteria (11.3%), and Geobacteraceae (5.9%; all data in Supplementary Data File 4.2).

Despite the large number of detected proteins, the quantitative recovery, detection, and characterization of all proteins is not technically feasible. The irreversible

adsorption of proteins to silicate minerals (Ding & Henrichs 2002) and complexation in organic aggregations (Nguyen & Harvey 2001) as well as the difficulty of solubilizing membrane-bound constituents (Tan et al. 2008) complicates extraction techniques, biasing instrument-bound peptides in favor of those derived from cytoplasmic proteins and proteins with fewer basic amino acids (Ding & Henrichs 2002). Humic substances in soils and sediments may complex preferentially with low molecular weight, hydrophobic proteins (Arenella et al. 2014), and mineral-complexed extracellular proteins may be preserved despite diminished physiological relevance (Giagnoni et al. 2012; Nannipieri 2006). For these and other reasons, proteome coverage is not well constrained, and it is therefore difficult to definitively rule out the presence of any particular protein.

*Metabolic Pathway Analyses*

*Sulfur Metabolism*

Sulfate reduction coupled to methane oxidation is discussed in the main text, but the sulfate-coupled oxidation of non-methane hydrocarbons can also play a substantial role in sulfur metabolic processing at hydrocarbon seeps (Bose et al. 2013). This process is typically attributed to the DSS clade, with additional contributions from non-DSS Desulfobacteraceae, Desulfobulbaceae, Syntrophobacteraceae, and Desulfurellales (Kleindienst et al. 2014; Widdel et al. 2010). It is difficult to attribute the presence of these organisms exclusively to higher-order alkane oxidation, but Sat enzymes linked to Syntrophobacteraceae were detected, and all of the above lineages were represented in the 16S rRNA gene tag data (Supplementary Data File 4.1a). 90 (1TP, 1UP) proteins – 89 of which did not correspond with previously annotated proteins – demonstrated closest

homology to the Desulfosarcina strain BuS5, the only pure culture organism known to degrade short chain alkanes (Kniemeyer et al. 2007).

*Nitrogen Metabolism*

Methane oxidizing environments are intimately linked with nitrogen metabolisms, as revealed through AOM coupled to nitrate and nitrite reduction (Raghoebarsing et al. 2006; Haroon et al. 2013) and nitrogen fixation by ANME within consortia (Dekas et al. 2009). Components of all enzymes involved in reductive nitrogen metabolisms such as dissimilatory nitrate reduction, denitrification, and nitrogen fixation are present within the cumulative metaproteome (Fig. S4.1); in contrast, no nitrogen metabolism enzymes were reported from the Nyegga seep (Stokke et al. 2012). Detected proteins include membrane-bound NarG and NorC, a cytochrome-containing nitric oxide reductase subunit that processes the toxic NO intermediate into $N_2O$ (Mesa et al. 2002). NorB, NorD and NorQ were also shown to be essential for anaerobic growth in mutational analyses of various nitrate reducers (De Boer et al. 1996; Mesa et al. 2002); our lack of detection of these subunits is likely attributable to their membrane-bound subcellular location and the potential disuse and breakdown of nitrogen-processing machinery. Indeed, of all nitrogen metabolism enzymes, only one copy of NirB was in the enriched fraction of the #5133 $^{15}N$ proteome. The lack of proteins involved in the assimilatory reductive pathway (NasAB, NarB) suggests that the seep sediment system is not limited for bioavailable nitrogen (if the proteins were never present) or NasAB and NarB breakdown occurred before protein extraction. Nitrogenase is well represented, with 10 NifH, two NifD, and three NifK orthologs identified across all samples. Nitrogen fixation

is an energetically demanding undertaking, which may explain the lack of enriched Nif proteins generated under conditions of abundant bioavailable $NH_4^+$.

The detection of substantial portions of nitrate reducing, denitrifying, and nitrogen fixing pathways, coupled with the recovery of almost no newly synthesized proteins, suggests that nitrogen-based metabolisms – particularly among Epsilon- and Gammaproteobacteria – may be important in seep sediments, but that our methane- and ammonium-rich incubation conditions rendered such metabolisms unnecessary or energetically untenable.

*SIP Analysis*

*Peptide Enrichment Distributions*

From the samples exhibiting $^{15}N$ enrichment, 1.48% of #3731 $^{15}N$ $T_2$ peptides and 18.06% of #5133 $^{15}N$ peptides were enriched (i.e., >5% $^{15}N$). Peptide enrichments in #3731 $^{15}N$ $T_2$ and #5133 $^{15}N$ revealed a bimodal distribution with the vast majority of peptides exhibiting no $^{15}N$ incorporation and nearly all enriched peptides found between 45%-70% (Fig. S4.1). When peptides were assigned to proteins following the single unique peptide rule, 2.44% and 17.5% of identified proteins in #3731 $^{15}N$ $T_2$ and #5133 $^{15}N$ were enriched, respectively; with the two peptide requirement, these values were 1.8% and 29.8%, respectively.

Given that the precursor $NH_4^+$ pool for both $^{15}N$ incubations was 67% $^{15}N$ (496 μM $NH_4^+$ at natural $^{15}N$ abundance in the filtered bottom water, supplemented with 1 mM $^{15}NH_4Cl$), the peak value and spread of the peptide enrichment distributions (Fig. S4.1) are noteworthy. Enriched peptides recovered from #5133 $^{15}N$ are found most frequently at 49% $^{15}N$, which suggests a preferential incorporation of $^{14}N$ into newly synthesized

amino acids. The magnitude of this bias is far larger than potential kinetic isotope effects (Ohkouchi et al. 2015), and may be reflective of "indirect" nitrogen incorporation into amino acids (Von Bergen et al. 2013). For example, the mobilization of ~500 μM nitrogen from sediment inoculum, processed to the level of free amino acids or their precursors, would "re-set" the $^{15}N$ precursor pool to ~50% $^{15}N$; such dramatic degradation of the native community, particularly given the subsequent nanoSIMS-derived growth rates, is difficult to explain. The spread of peptide enrichment values is not consistent with a binomial expansion centered around the $^{15}N$ abundance of the N precursor pool, which would be expected in the combinatorial process of amino acid synthesis (Doherty & Beynon 2006). The narrow distribution observed in Fig. S4.1a would therefore suggest a widespread metabolic process that offers a stringent selectivity of N incorporation. Alternatively, both of these unanticipated distribution parameters, the peak value and the spread, could be attributable to instrumental or computational errors, though no abnormalities in the sample processing metadata or Sipros output were observed.

The $^{15}N$ distribution of the #3731 $^{15}N$ $T_2$ peptides is more consistent with a binomial distribution centered at 67% $^{15}N$. The curve's peak retains some of the irregularities mentioned above (the distribution's center is approximately 63% $^{15}N$, and the abundance of peptides at 49% is incongruous), but the discrepancies are less severe, and a substantially lower number of overall peptides predisposes the distribution to scatter.

*Protein Net Synthesis Rates*

In order to calculate a protein's synthesis (S) and degradation (D) rates, four supporting data points must be known in the context of a SIP experiment: the initial abundance ($A_{U,0}$), the final abundance of both unenriched ($A_{U,T}$) and enriched ($A_{E,T}$) protein, and the elapsed time (T; see eq. 4.1, 4.2).

$$(S - D) * T = A_{E,T} \quad \text{Eq. 4.1}$$

$$A_{U,0} - (D * T) = A_{U,T} \quad \text{Eq. 4.2}$$

Sample #5133 has just one time point of data; as a result, $A_{U,0}$ is not known and full kinetic evaluation of the sample's proteins is not possible. However, a "minimum net synthesis rate," (MNSR) which is equivalent to the daily rate of protein synthesis minus the rate of degradation (S – D), can be determined (eq. 4.1). To do so, only unique peptides recovered from the #5133 $^{15}N$ sample were considered. The number of enriched (≥5% $^{15}N$) spectral counts (each of which corresponds to a newly synthesized corresponding protein) was divided by T (160 days) to give the MNSR. The degree of enrichment above the 5% threshold was not considered. Given the expectation of incomplete peptide detection and variable ionization efficiencies, the resulting values should be viewed as minima that are not directly comparable. Nonetheless, we believe that stark differences and broad trends warrant discussion.

MNSR values of unique peptides with spectra indicative of $^{15}N$ enrichment are shown in Fig. S4.2. Two Mcr subunits, both most closely associated with ANME-2a contigs, generated at least 0.51 (McrA, contig ANME2a_02350) and 0.46 (McrB, ANME2a_02354) copies per day, on average, over the course of the 160-day incubation period. Despite these relatively high values, the majority of these McrA- and McrB-linked peptides – 73.8% and 68.5%, respectively – were unenriched, indicating that these

proteins were likely abundant prior to incubation set-up and were not synthesized exclusively in response to high-methane, high-ammonium conditions. Proteins involved in the reverse methanogenesis pathway appear to exhibit higher MNSRs than those associated with sulfate reduction, a result that is consistent with the higher mean $^{15}N$ enrichment values of peptides unique to reverse methanogenesis. This potential trend may imply a higher stability of sulfate reduction pathway enzymes, faster sulfate reduction kinetics, and/or a non-stoichiometric coupling of methanotrophy and sulfate reduction, suggestive of non-methane electron donors in native seep sediment (Joye et al. 2004).

Of the newly synthesized unique peptides, 48 were found exclusively in their enriched form, indicating high degradation rates (thereby erasing any signal of pre-incubation copies) and/or up-regulation during the experimental period. The vast majority (95%) of the phylogenetically annotated peptides from this subset were bacterial, possibly suggesting that a more substantial shift in metabolism was required among bacterial representatives than archaeal organisms during the incubation period that likely saw increasingly sulfidic and energy limited conditions. The two highest MNSR-value peptides among this group were associated with the same *Desulfuromonadales* linked 2-oxoglutarate synthase. Other enzymes with multiple unique peptides drawn from the exclusively enriched subset include citrate synthase and acetyl-CoA hydrolase from the *Geobacteraceae* family, a *Desulfobulbus* succinate dehydrogenase subunit, a *Desulfuromonadales* aldehyde:ferredoxin oxidoreductase, and two distinct *Desulfuromonadales* 2-oxoglutarate synthases.

Intriguingly, all of these enzymes are involved in carbon metabolism. Aldehyde:ferredoxin oxidoreductase is a component in the primarily anabolic pentose phosphate pathway, acetyl-CoA hydrolase is active in central carbon metabolism, citrate synthase and succinate dehydrogenase are oxidative TCA cycle constituents, and 2-oxoglutarate synthase is found in both the energy-yielding TCA cycle in heterotrophs and the carbon fixing reductive-TCA cycle known to occur in some proteobacterial lineages (Hügler & Sievert 2011). Substantial quantities of carbon, whether in the form of AOM-generated bicarbonate or remineralized biomass, may have become newly available under incubation conditions.

**References**

Albrethsen J, Agner J, Piersma SR, Højrup P, Pham TV, Weldingh K, et al. (2013). Proteomic Profiling of Mycobacterium tuberculosis Identifies Nutrient-starvation-responsive Toxin–antitoxin Systems. Molecular & Cellular Proteomics 12:1180–1191.

Arenella M, Giagnoni L, Masciandaro G, Ceccanti B, Nannipieri P, Renella G. (2014). Interactions between proteins and humic substances affect protein identification by mass spectrometry. Biology and fertility of soils 50:447–454.

Bantscheff M, Schirle M, Sweetman G, Rick J, Kuster B. (2007). Quantitative mass spectrometry in proteomics: a critical review. Anal Bioanal Chem 389:1017–1031.

Bastida F., Moreno JL, Nicolás C, Hernández T, García C. (2009). Soil metaproteomics: a review of an emerging environmental science. Significance, methodology and perspectives. European Journal of Soil Science 60:845–859.

Von Bergen M, Jehmlich N, Taubert M, Vogt C, Bastida Felipe, Herbst F-A, et al. (2013). Insights from quantitative metaproteomics and protein-stable isotope probing into microbial ecology. The ISME journal 7:1877–1885.

De Boer APN, Van Der Oost J, Reijnders WNM, Westerhoff HV, Stouthamer AH, Van Spanning RJM. (1996). Mutational Analysis of the Nor Gene Cluster which Encodes Nitric-Oxide Reductase from Paracoccus denitrificans. European Journal of Biochemistry 242:592–600.

Boetius A, Suess E. (2004). Hydrate Ridge: a natural laboratory for the study of microbial life fueled by methane from near-surface gas hydrates. Chemical Geology 205:291–310.

Bose A, Rogers DR, Adams MM, Joye SB, Girguis PR. (2013). Geomicrobiological linkages between short-chain alkane consumption and sulfate reduction rates in seep sediments. Frontiers in microbiology 4.

Camacho C, Coulouris G, Avagyan V, Ma N, Papadopoulos J, Bealer K, et al. (2009). BLAST+: architecture and applications. BMC bioinformatics 10:421.

Chourey K, Jansson J, VerBerkmoes N, Shah M, Chavarria KL, Tom LM, et al. (2010). Direct Cellular Lysis/Protein Extraction Protocol for Soil Metaproteomics. J. Proteome Res. 9:6615–6622.

Dekas A, Poretsky RS, Orphan VJ. (2009). Deep-Sea Archaea Fix and Share Nitrogen in Methane-Consuming Microbial Consortia. Science 326:422–426.

Denef VJ, VerBerkmoes NC, Shah MB, Abraham P, Lefsrud M, Hettich RL, et al. (2009). Proteomics-inferred genome typing (PIGT) demonstrates inter-population recombination as a strategy for environmental adaptation. Environmental Microbiology 11:313–325.

Ding X, Henrichs SM. (2002). Adsorption and desorption of proteins and polyamino acids by clay minerals and marine sediments. Marine Chemistry 77:225–237.

Doherty MK, Beynon RJ. (2006). Protein turnover on the scale of the proteome.

Edgar RC. (2004). MUSCLE: multiple sequence alignment with high accuracy and high throughput. Nucleic acids research 32:1792–1797.

Edgar RC, Haas BJ, Clemente JC, Quince C, Knight R. (2011). UCHIME improves sensitivity and speed of chimera detection. Bioinformatics 27:2194–2200.

Elias JE, Gygi SP. (2007). Target-decoy search strategy for increased confidence in large-scale protein identifications by mass spectrometry. Nature methods 4:207–214.

Giagnoni L, Magherini F, Landi L, Taghavi S, Van der Lelie D, Puglia M, et al. (2012). Soil solid phases effects on the proteomic analysis of Cupriavidus metallidurans CH34. Biology and Fertility of Soils 48:425–433.

Gilchrist A, Au CE, Hiding J, Bell AW, Fernandez-Rodriguez J, Lesimple S, et al. (2006). Quantitative Proteomics Analysis of the Secretory Pathway. Cell 127:1265–1281.

Gupta N, Pevzner PA. (2009). False Discovery Rates of Protein Identifications: A Strike against the Two-Peptide Rule. J. Proteome Res. 8:4173–4181.

Haroon MF, Hu S, Shi Y, Imelfort M, Keller J, Hugenholtz P, et al. (2013). Anaerobic oxidation of methane coupled to nitrate reduction in a novel archaeal lineage. Nature 500:567–570.

Hügler M, Sievert SM. (2011). Beyond the Calvin cycle: autotrophic carbon fixation in the ocean. Marine Science 3.

Hyatt D, Chen G-L, LoCascio PF, Land ML, Larimer FW, Hauser LJ. (2010). Prodigal: prokaryotic gene recognition and translation initiation site identification. BMC bioinformatics 11:119.

Imelfort M, Parks D, Woodcroft BJ, Dennis P, Hugenholtz P, Tyson GW. (2014). GroopM: an automated tool for the recovery of population genomes from related metagenomes. PeerJ 2:e603.

Joye SB, Boetius A, Orcutt BN, Montoya JP, Schulz HN, Erickson MJ, et al. (2004). The anaerobic oxidation of methane and sulfate reduction in sediments from Gulf of Mexico cold seeps. Chemical Geology 205:219–238.

Justice NB, Pan C, Mueller R, Spaulding SE, Shah V, Sun CL, et al. (2012). Heterotrophic Archaea Contribute to Carbon Cycling in Low-pH, Suboxic Biofilm Communities. Applied and Environmental Microbiology 78:8321–8330.

Kleindienst S, Herbst F-A, Stagars M, Von Netzer F, Von Bergen M, Seifert J, et al. (2014). Diverse sulfate-reducing bacteria of the Desulfosarcina/Desulfococcus clade are the key alkane degraders at marine seeps. ISME J 8:2029–2044.

Kniemeyer O, Musat F, Sievert SM, Knittel Katrin, Wilkes H, Blumenberg M, et al. (2007). Anaerobic oxidation of short-chain hydrocarbons by marine sulphate-reducing bacteria. Nature 449:898–901.

Krüger M, Wolters H, Gehre M, Joye SB, Richnow H. (2008). Tracing the slow growth of anaerobic methane-oxidizing communities by 15N-labelling techniques. FEMS microbiology ecology 63:401–411.

Li H. (2013). Aligning sequence reads, clone sequences and assembly contigs with BWA-MEM. arXiv preprint arXiv:1303.3997.

Li H, Handsaker B, Wysoker A, Fennell T, Ruan J, Homer N, et al. (2009). The sequence alignment/map format and SAMtools. Bioinformatics 25:2078–2079.

Li Z, Adams RM, Chourey K, Hurst GB, Hettich RL, Pan C. (2011). Systematic Comparison of Label-Free, Metabolic Labeling, and Isobaric Chemical Labeling for Quantitative Proteomics on LTQ Orbitrap Velos. J. Proteome Res. 11:1582–1590.

Liu H, Sadygov RG, Yates JR. (2004). A Model for Random Sampling and Estimation of Relative Protein Abundance in Shotgun Proteomics. Anal. Chem. 76:4193–4201.

Liu M, Fan L, Zhong L, Kjelleberg S, Thomas T. (2012). Metaproteogenomic analysis of a community of sponge symbionts. ISME J 6:1515–1525.

Mesa S, Velasco L, Manzanera ME, Delgado MJ, Bedmar EJ. (2002). Characterization of the norCBQD genes, encoding nitric oxide reductase, in the nitrogen fixing bacterium Bradyrhizobium japonicum. Microbiology 148:3553–3560.

Mitchell A, Chang H-Y, Daugherty L, Fraser M, Hunter S, Lopez R, et al. (2014). The InterPro protein families database: the classification resource after 15 years. Nucleic acids research gku1243.

Moriya Y, Itoh M, Okuda S, Yoshizawa AC, Kanehisa M. (2007). KAAS: an automatic genome annotation and pathway reconstruction server. Nucleic acids research 35:W182–W185.

Nannipieri P. (2006). Role of Stabilised Enzymes in Microbial Ecology and Enzyme Extraction from Soil with Potential Applications in Soil Proteomics. In:Nucleic Acids and Proteins in Soil, Nannipieri, P & Smalla, K, eds (ed). Soil Biology Vol. 8, Springer Berlin Heidelberg, pp. 75–94. http://dx.doi.org/10.1007/3-540-29449-X_4.

Nesvizhskii AI, Aebersold R. (2005). Interpretation of shotgun proteomic data the protein inference problem. Molecular & Cellular Proteomics 4:1419–1440.

Nguyen RT, Harvey HR. (2001). Preservation of protein in marine systems: Hydrophobic and other noncovalent associations as major stabilizing forces. Geochimica et Cosmochimica Acta 65:1467–1480.

Ohkouchi N, Ogawa NO, Chikaraishi Y, Tanaka H, Wada E. (2015). Biochemical and physiological bases for the use of carbon and nitrogen isotopes in environmental and ecological studies. Progress in Earth and Planetary Science 2:1–17.

Old WM, Meyer-Arendt K, Aveline-Wolf L, Pierce KG, Mendoza A, Sevinsky JR, et al. (2005). Comparison of Label-free Methods for Quantifying Human Proteins by Shotgun Proteomics. Molecular & Cellular Proteomics 4:1487–1502.

Pan C, Fischer CR, Hyatt D, Bowen BP, Hettich RL, Banfield JF. (2011). Quantitative Tracking of Isotope Flows in Proteomes of Microbial Communities. Molecular &

Cellular Proteomics 10. http://www.mcponline.org/content/10/4/M110.006049.abstract.
Parks DH, Imelfort M, Skennerton CT, Hugenholtz P, Tyson GW. (2014). CheckM: assessing the quality of microbial genomes recovered from isolates, single cells, and metagenomes. PeerJ PrePrints.
Price MN, Dehal PS, Arkin AP. (2010). FastTree 2–approximately maximum-likelihood trees for large alignments. PloS one 5:e9490.
Raghoebarsing AA, Pol A, Van de Pas-Schoonen KT, Smolders AJP, Ettwig KF, Rijpstra WIC, et al. (2006). A microbial consortium couples anaerobic methane oxidation to denitrification. Nature 440:918–921.
Ram RJ, VerBerkmoes NC, Thelen MP, Tyson GW, Baker BJ, Blake RC, et al. (2005). Community Proteomics of a Natural Microbial Biofilm. Science 308:1915–1920.
Ravenschlag K, Schubert CJ, Rickert D, Widdel Friedrich, Gieseke A, Amann R, et al. (2000). A marine microbial consortium apparently mediating anaerobic oxidation of methane. Nature 407:623–626.
Sahling H, Rickert D, Lee RW, Linke P, Suess E. (2002). Macrofaunal community structure and sulfide flux at gas hydrate deposits from the Cascadia convergent margin, NE Pacific. Marine Ecology Progress Series 231:121–138.
Sardiu ME, Cai Y, Jin J, Swanson SK, Conaway RC, Conaway JW, et al. (2008). Probabilistic assembly of human protein interaction networks from label-free quantitative proteomics. Proceedings of the National Academy of Sciences 105:1454–1459.
Solaiman Z, Kashem M, Matsumoto I. (2007). Environmental Proteomics: Extraction and Identification of Protein in Soil. In:Advanced Techniques in Soil Microbiology, Varma, A & Oelmüller, R, eds (ed). Soil Biology Vol. 11, Springer Berlin Heidelberg, pp. 155–166. http://dx.doi.org/10.1007/978-3-540-70865-0_10.
Stokke R, Roalkvam I, Lanzen A, Haflidason H, Steen IH. (2012). Integrated metagenomic and metaproteomic analyses of an ANME-1-dominated community in marine cold seep sediments. Environmental microbiology 14:1333–1346.
Suzek BE, Huang H, McGarvey P, Mazumder R, Wu CH. (2007). UniRef: comprehensive and non-redundant UniProt reference clusters. Bioinformatics 23:1282–1288.
Tan S, Tan HT, Chung MCM. (2008). Membrane proteins and membrane proteomics. Proteomics 8:3924–3932.
Tryon M., Brown K., Torres M. (2002). Fluid and chemical flux in and out of sediments hosting methane hydrate deposits on Hydrate Ridge, OR, II: Hydrological processes. Earth and Planetary Science Letters 201:541–557.
UniProt Consortium. (2008). The universal protein resource (UniProt). Nucleic acids research 36:D190–D195.
Verberkmoes NC, Russell AL, Shah M, Godzik A, Rosenquist M, Halfvarson J, et al. (2009). Shotgun metaproteomics of the human distal gut microbiota. The ISME journal 3:179–189.
Wang Y, Ahn T-H, Li Z, Pan C. (2013). Sipros/ProRata: a versatile informatics system for quantitative community proteomics. Bioinformatics 29:2064–2065.

Waterhouse AM, Procter JB, Martin DM, Clamp M, Barton GJ. (2009). Jalview Version 2—a multiple sequence alignment editor and analysis workbench. Bioinformatics 25:1189–1191.

Widdel F., Knittel K., Galushko A. (2010). Anaerobic Hydrocarbon-Degrading Microorganisms: An Overview. In:Handbook of Hydrocarbon and Lipid Microbiology, Timmis, K, ed (ed)., Springer Berlin Heidelberg, pp. 1997–2021. http://dx.doi.org/10.1007/978-3-540-77587-4_146.

Wilmes P, Bond PL. (2009). Microbial community proteomics: elucidating the catalysts and metabolic mechanisms that drive the Earth's biogeochemical cycles. Current Opinion in Microbiology 12:310–317.

Zhang Y, Wen Z, Washburn MP, Florens L. (2009). Effect of Dynamic Exclusion Duration on Spectral Count Based Quantitative Proteomics. Anal. Chem. 81:6317–6326.

Appendix 5: Supplementary Metaproteomic Study of Alternative Electron Acceptors in the Anaerobic Oxidation of Methane

**Introduction**

The biological anaerobic oxidation of methane (AOM) is mediated by sulfate reduction in marine sulfate-methane transition zones (SMTZs)[1,2]. This metabolism (eq. 1) enables the mutualistic relationship between anaerobic methanotrophic (ANME) archaea and sulfate reducing bacteria (SRB)[3,4]. However, methane oxidation coupled to iron (eq. 2) or manganese (eq. 3) reduction appears to be an energetically more attractive option: oxidized forms of these elements have higher redox potentials than that of sulfate, and would thereby generate more negative Gibbs energy values per methane molecule oxidized[5,6].

Eq. 1: $CH_4 + SO_4^{2-} \rightarrow HCO_3^- + HS^- + H_2O$ $\Delta G = -14$ kJ/mol

Eq. 2: $CH_4 + 8Fe(OH)_3 + 15H^+ \rightarrow HCO_3^- + 8Fe^{2+} + 21H_2O$ $\Delta G = -270.3$ kJ/mol

Eq. 3: $CH_4 + 4MnO_2 + 7H^+ \rightarrow HCO_3^- + 4Mn^{2+} + 5H_2O$ $\Delta G = -556$ kJ/mol

Despite this seemingly exergonic metabolism – and the previously established oxidation of higher hydrocarbons with metal oxides[7] – AOM directly coupled to iron or manganese reduction remains one of the few outstanding metabolisms involving abundant redox pairs[8]. Several efforts have explored the potential linkage between iron and manganese reduction and methane oxidation, depending upon geochemical and isotopic signatures to demonstrate the presence or absence of metal-induced methane oxidation in laboratory based incubations and environmental samples[6,9–14].

One of the most challenging complications in demonstrating the immediate coupling of methane oxidation to metal reduction is the possibility of cryptic sulfur

cycling, whereby reduced sulfur species abiotically reduce metal oxides, generating sulfate in the process and allowing AOM to proceed biologically using sulfate as an electron acceptor [9]. Under low-sulfate conditions, oxidized metals can be required to drive methane oxidation, while aqueous chemistry can be marked by reduced metals, methane depletion, and sulfur species below detection limits, masking the biological process that maintains sulfate-based AOM.

In support of an effort examining the role of metal oxides in the methane oxidizing potential of methane seep sediment from Hydrate Ridge, OR, this study broadens the effort through a stable isotope probing (SIP) metaproteomics approach. For the purposes of this document, the data set bolsters the growing repository of seep environment proteins, revealing which products are common to such settings, and which may be induced by distinct electron acceptors.

**Methods**

Marine sediment was recovered by the ROV *Jason* during R/V *Atlantis* leg AT18-10, Dive J2-593 from Hydrate Ridge, Oregon, a convergent tectonic margin that has been well-characterized as a site of methane seepage and AOM[10–12]. The sediment analyzed in this study was collected in push core (PC) 41 on elevator 3, which retained a 15-cm vertical transect of sediment. The sampling site exhibited common manifestations of active methane seepage including microbial mats and clam beds. Shipboard, cores were immediately transferred to a 4 °C walk-in cold room and processed within a few hours. Sediment from PC 41 was placed into sterile gas-tight bags and flushed for five minutes with Ar gas to maintain anoxic conditions.

In the laboratory, PC 41 sediment was reconstituted in a sterile 1L glass bottle with $CH_4$ headspace to a final slurry composition of 1:2 v/v sediment : filter-sterilized seawater collected from the seafloor at Hyrdrate Ridge. In an effort to remove aqueous phase sulfate from the incubation, the sediment was washed ten times, removing the liquid and replenishing with sulfate-free artificial seawater[13]. The resulting slurry was shown to contain sulfate and sulfide levels below detection.

16 experimental incubations were set up to track the seep sediment community's response to methane availability in the presence of different potential electron acceptors. All incubations were prepared in 120 mL serum bottles and received 60 mL sediment slurry (homogenized by shaking prior to distribution) and 60 mL methane headspace. One of four potential electron acceptor conditions was provided: bottles #1, #2, #9, and #10 received 10 mM $Na_2SO_4$, bottles #3, #4, #11, and #12 received 10 mM $Fe(OH)_3$, bottles #5, #6, #13, and #14 received 10 mM $MnO_2$, and bottles #7, #8, #15, and #16 received no added acceptor (NAA). Bottle numbers and their corresponding contents are shown in Table S5.1.

| Bottle # | Methane | Nitrogen | Electron Acceptor | Autoclaved Control? |
|---|---|---|---|---|
| 1 | $CH_4$ | $^{14}NH_4Cl$ | $SO_4^{2-}$ | No |
| 2 | $CH_4$ | $^{15}NH_4Cl$ | $SO_4^{2-}$ | No |
| 3 | $CH_4$ | $^{14}NH_4Cl$ | $Fe(OH)_3$ | No |
| 4 | $CH_4$ | $^{15}NH_4Cl$ | $Fe(OH)_3$ | No |
| 5 | $CH_4$ | $^{14}NH_4Cl$ | $MnO_2$ | No |
| 6 | $CH_4$ | $^{15}NH_4Cl$ | $MnO_2$ | No |
| 7 | $CH_4$ | $^{14}NH_4Cl$ | -- | No |
| 8 | $CH_4$ | $^{15}NH_4Cl$ | -- | No |
| 9 | $CH_3D$ | $^{15}NH_4Cl$ | $SO_4^{2-}$ | No |
| 10 | $CH_3D$ | $^{15}NH_4Cl$ | $SO_4^{2-}$ | Yes |
| 11 | $CH_3D$ | $^{15}NH_4Cl$ | $Fe(OH)_3$ | No |
| 12 | $CH_3D$ | $^{15}NH_4Cl$ | $Fe(OH)_3$ | Yes |
| 13 | $CH_3D$ | $^{15}NH_4Cl$ | $MnO_2$ | No |
| 14 | $CH_3D$ | $^{15}NH_4Cl$ | $MnO_2$ | Yes |
| 15 | $CH_3D$ | $^{15}NH_4Cl$ | -- | No |
| 16 | $CH_3D$ | $^{15}NH_4Cl$ | -- | Yes |

Table S5.1: A description of incubation bottles involved in this study.

Bottles destined for SIP metaproteomics (#1-8) were provided with $CH_4$ headspace as the light isotopologue would not interfere with SIP analyses; the remaining bottles (#9-16) received $CH_3D$ headspace to track methane consumption activity (see Chapter 2). Among metaproteomics sample pairs with a given electron acceptor condition, one bottle received 1 mM $^{14}NH_4^+$ and the other received 1 mM $^{15}NH_4^+$. Among non-metaproteomics pairs (#9-16), one bottle was autoclaved to serve as a killed control. All samples were stored at 4 °C and sampled periodically throughout the experimental process. Methane oxidation rates were measured via the deuterated methane approach presented in Chapter 2; SIP metaproteomics procedures can be found in Chapter 4.

**Results & Discussion**

*Methane Consumption Rates*

Quantification of the aqueous D/H ratio in methane-consuming systems incubated with $CH_3D$ provides a measure of methane activation rates and exhibits direct proportionality to more established methods of full methane oxidation rate values (see Chapter 2). Methane consumption values were determined over the course of the 965-day incubation period (Fig. S5.1), and rates were calculated for both the first 92 days of the incubation – a "growth phase" corresponding to maximal rates for all samples – as well as the full 965-day experiment. The sulfate incubation consumed methane at a rate of 95.7 nmol $day^{-1}$ $cm^{-3}$ sediment for the first 92 days and 16.2 nmol $day^{-1}$ $cm^{-3}$ sediment over the course of the entire experiment. Using the appropriate scaling factor for anoxic marine sediment, the corresponding methane oxidation rates were calculated to be 47.9 and 8.1 nmol $day^{-1}$ $cm^{-3}$ sediment, respectively. This growth phase value is consistent

with previously reported methane oxidation values from active seep sediment at Hydrate Ridge[10,14], the North Sea[15], the Gulf of Mexico[16], and slightly higher than those from inner continental shelves[2,17].

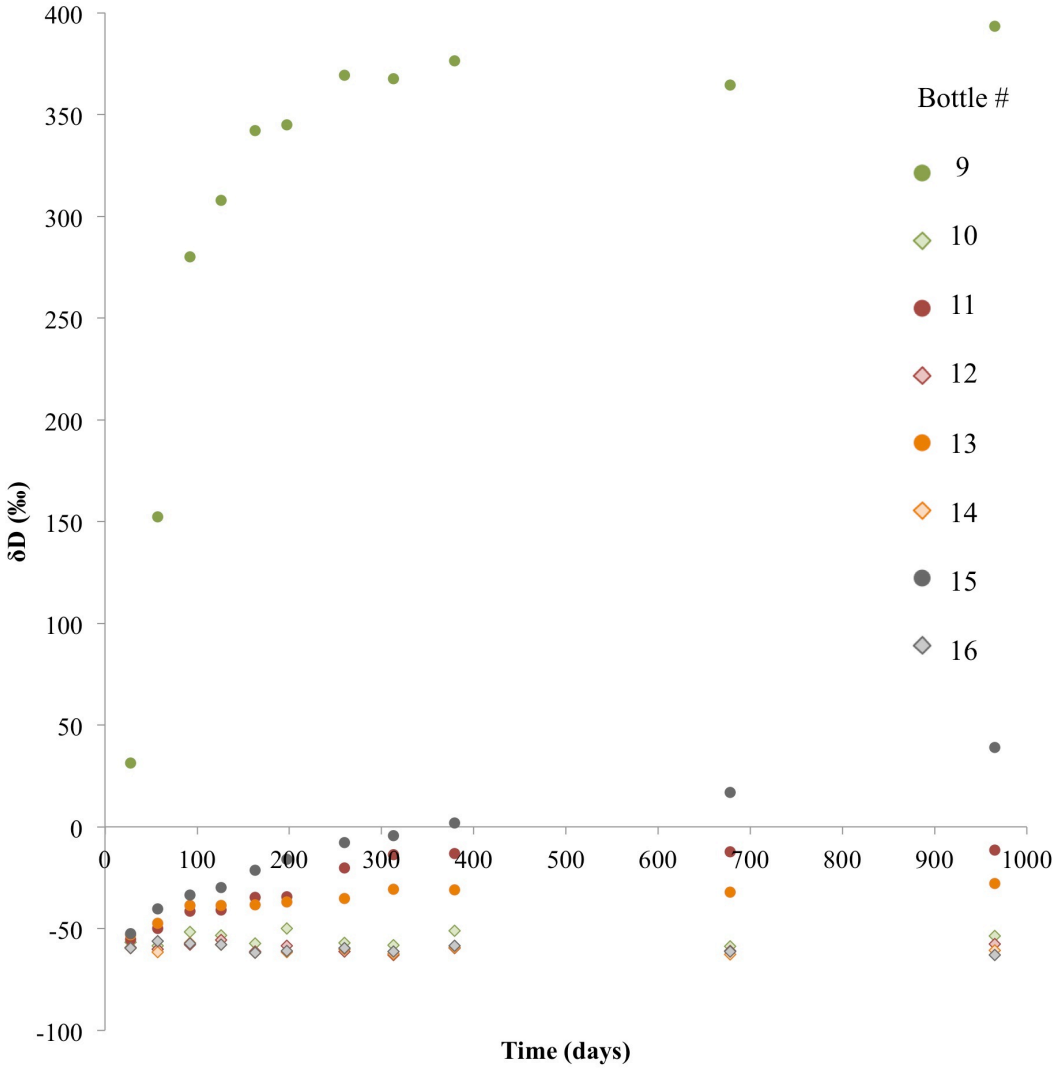


Fig. S5.1: δD values from bottles 9-16 throughout the course of the incubation period.

Methane consumption was also observed in incubations containing $Fe(OH)_3$, $MnO_2$, and no added electron acceptor, at rates analogous to sulfate-coupled AOM in low-activity seepage environments[14]. Surprisingly, the NAA incubation exhibited faster

methane consumption rates than either metal-based incubation over both time periods considered. A similar result was reported by Beal et al. (2009), who found that while birnessite and ferrihydrite enhanced methane oxidation rates above the live control, ferric oxyhydroxide led to lower rates. Furthermore, the degree of methane consumption rate decrease calculated over the full 965-day incubation period, compared with that derived from the 92-day growth phase, was substantially less for the NAA incubation than for all three other conditions. For the NAA sample, the full-experiment methane consumption rate was 47% of the rate exhibited during the growth phase; analogous values of methane consumption retention were 17% for $SO_4^{2-}$, 33% for $Fe(OH)_3$, and 19% for $MnO_2$. This finding suggests that the limiting factors that slowed methane consumption in the $SO_4^{2-}$, $Fe(OH)_3$, and $MnO_2$ samples – factors that likely differed between each treatment – were less prevalent or more readily overcome in the NAA incubation.

*SIP Metaproteomics*

Metaproteomics analysis offers a view of microbial community function that circumvents imprecise relationships between gene presence, transcript copy number, and protein abundance to provide a more appropriate understanding of metabolic reality[18]. Incorporating a stable isotope label such as $^{15}N$ into media allows users to isolate proteins synthesized during an experimental period[19].

SIP metaproteomic analysis revealed low relative abundances of isotopically enriched proteins under all electron acceptor conditions, though distinct patterns of functional and phylogenetic homology distinguished the different conditions. Overall protein identifications were highest for the sulfate $^{14}N$ sample (3169 proteins identified), and substantially lower in the $Fe(OH)_3$ (1874 proteins) and $MnO_2$ (1725 proteins)

samples. The sample with no added electron acceptor contained an intermediate number of recovered proteins (2307 identifications). Inhibition of microbial activity due to $^{15}NH_4^+$ is unlikely: pure cultures of *Methanosarcina mazei* and *Desulfobacter autotrophicum* exhibited no changes in cell abundance or activity with ammonia ratios up to 100% $^{15}N$, and the same study found that rates of AOM in seep sediment incubations did not change significantly when exposed to fully labeled $NH_4^+$ pool[20].

In contrast to a previous SIP metaproteomics study of Hydrate Ridge methane seep sediment (Chapter 4), the proportion of enriched proteins detected in this study is relatively low given analogous methane consumption rates, particularly with the sulfate sample. Using a 5% 15N threshold, 122 proteins were enriched in the sulfate incubation, while 25, 29, and 44 were enriched in the $Fe(OH)_3$, $MnO_2$, and NAA samples, respectively. These low relative levels of enrichment may reveal a shift toward a more catabolism-centric use of energetic resources or a preferential recycling of previously-synthesized amino acids. Increasing D/H ratios, as well as increasing numbers of cell aggregates (Fig. S5.2), suggest that the community was active and biosynthesis did occur, making bulk die-off unlikely unless newly synthesized material was preferentially degraded after aggregate abundances peaked partway through the experiment. Given the energetic costs of amino acid production[21], recycling and reuse would be advantageous, and biosynthesis pathways leading to many amino acids have not been identified in seep sediment metaproteomes (data not shown).

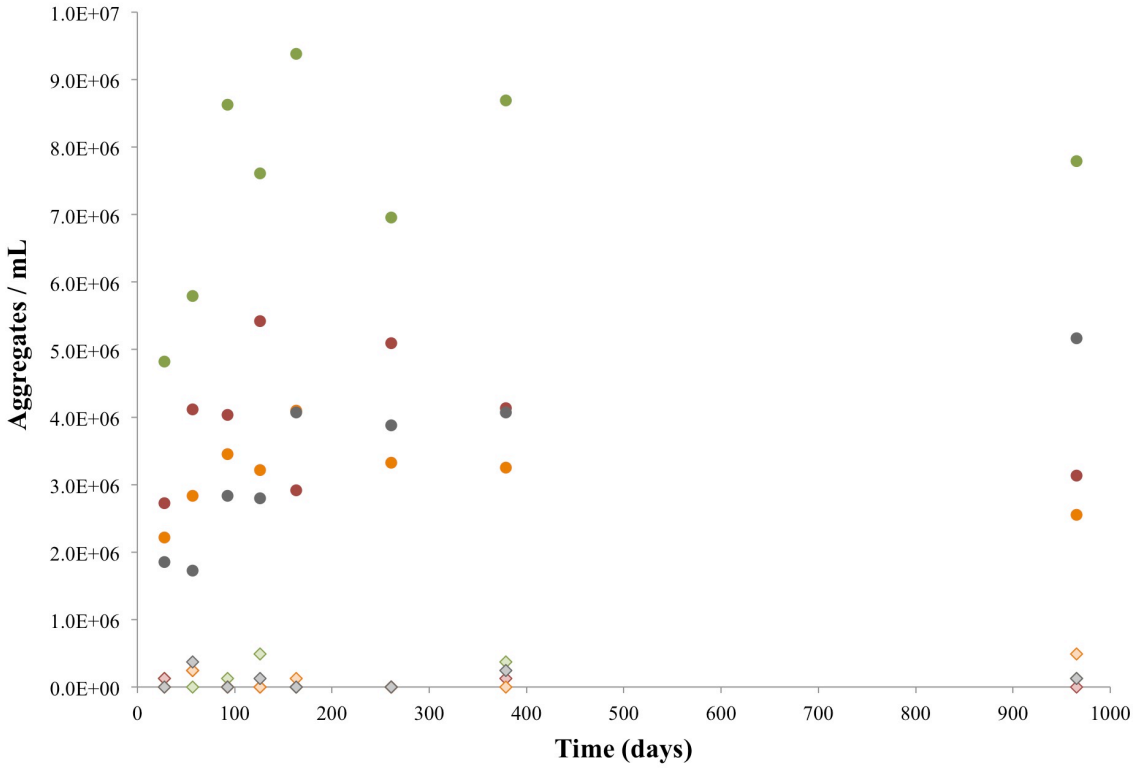


Fig. S5.2: Counts of DAPI-active cell aggregates during the course of the experiment. See Fig. S5.1 for a figure legend.

The number of enriched proteins recovered in this analysis demonstrates a relatively robust concordance with methane consumption activity: with both metrics, the sulfate incubation was most active, the metal-based incubations were similar to each other and substantially less active, while the NAA incubation occupied an intermediate position. In this context, SIP metaproteomics serves as a relatively reliable reporter of activity, though its strategic strength likely lies more in detecting low-level distributed activity among particular constituents rather than bulk behaviors (see chapter 4).

*Methane Seep Metaproteome*

The metaproteomes reported in this study can be incorporated into a growing compilation of seep-derived protein data, offering a new perspective on biomolecules and metabolic capabilities that may be central to the functioning of that ecosystem. Because

coverage levels of diverse systems are relatively low[22,23], multiple replicates are required to develop an accurate understanding of the protein complement. Relatedly, proteins that appear in multiple metaproteomic analyses are interpreted to be common, though differential ionization proclivities can bias MS/MS detections[24]. An analysis of the eight metaproteomic datasets collected here, as well as the six collected in the study presented in chapter 4, revealed 116 open reading frames (ORFs) that were present in all samples. These putative proteins can be categorized by function or by phylogeny, and the results are provided in tables S5.2 and S5.3, respectively.

| Protein Annotation | Relative Abundance |
|---|---|
| Hypothetical Protein | 58.5 |
| McrB | 8.6 |
| McrA | 6.9 |
| McrG | 6 |
| AprA | 4.3 |
| Mtd | 3.4 |
| DsrB | 3.4 |
| Mer | 2.6 |
| MotB (chemotaxis protein) | 1.7 |
| Elongation factor 1α | 1.7 |
| Glutamine synthase | 1.7 |
| MtrA | 1.7 |
| $Fe^{2+}$ transport protein A | 0.9 |
| Ftr | 0.9 |
| HdrA | 0.9 |
| Mch | 0.9 |
| Nitrous oxide reductase | 0.9 |
| Proteasome α | 0.9 |
| Putative Ni-responsive regulator | 0.9 |
| Sat | 0.9 |
| DsrA | 0.9 |

Table S5.2: Functional annotations of the 116 putative protein products identified in all metaproteomic analyses.

| Family-Level Phylogenetic Assignment | Relative Abundance |
|---|---|
| Archaea;Unclassified Archaea | 31 |
| Archaea;GZFosmids;ANME-2c | 8.6 |
| Unclassified | 7.8 |
| Archaea;GZFosmids;ANME-1 | 7.7 |
| Bacteria;Unclassified Bacteria | 6.8 |
| Bacteria;Proteobacteria;delta/epsilon subdivisions;Deltaproteobacteria | 5.2 |
| Archaea;Euryarchaeota;Methanomicrobia;Methanosarcinales | 4.3 |
| Archaea;Euryarchaeota;Methanomicrobia;Methanosarcinales;Methanosarcinaceae | 3.5 |
| Archaea;Euryarchaeota;Methanomicrobia;Methanosarcinales;Unclassified Methanosarcinales | 3.5 |
| Archaea;GZFosmids;ANME-2b | 2.6 |
| Archaea;GZFosmids;ANME-2a | 1.7 |
| Archaea;Euryarchaeota;Methanomicrobia | 1.7 |
| Archaea;Euryarchaeota;Methanomicrobia;Methanocellales;Methanocellaceae | 1.7 |
| Archaea;Euryarchaeota;Methanomicrobia;Methanosarcinales;Candidatus Methanoperedenaceae | 1.7 |
| Archaea;Euryarchaeota;Methanomicrobia;Methanosarcinales;Methanosaetaceae | 1.7 |
| Bacteria;Proteobacteria;delta/epsilon subdivisions;Deltaproteobacteria;Desulfobacterales;Desulfobacteraceae | 1.7 |
| Bacteria;Proteobacteria;delta/epsilon subdivisions;Deltaproteobacteria;Desulfobacterales;Desulfobulbaceae | 1.7 |
| Bacteria;Proteobacteria;delta/epsilon subdivisions;Deltaproteobacteria;Desulfuromonadales;Geobacteraceae | 1.7 |
| Archaea;Euryarchaeota;Methanobacteria;Methanobacteriales;Methanobacteriaceae | 0.9 |
| Bacteria;Actinobacteria;Actinobacteria;Actinobacteridae;Actinomycetales;Micromonosporineae | 0.9 |
| Bacteria;Cyanobacteria;Oscillatoriophycideae | 0.9 |
| Bacteria;Fibrobacteres/Acidobacteria group;Acidobacteria;Solibacteres;Solibacterales;Solibacteraceae | 0.9 |
| Bacteria;Proteobacteria;delta/epsilon subdivisions;Deltaproteobacteria;Desulfovibrionales;Desulfohalobiaceae | 0.9 |
| Bacteria;Proteobacteria;delta/epsilon subdivisions;Epsilonproteobacteria;Campylobacterales | 0.9 |

Table S5.3: Phylogenetic affiliations of the 116 putative protein products identified in all metaproteomic analyses.

These common identifications reveal the central importance of the methane oxidizing and sulfate reducing capabilities and their anticipated attendant microbial constituents. The reverse methanogenesis and sulfate reduction pathways account for 41.4% of the universally-identified proteins. In particular, the prevalence of multiple Mer orthologs, which have proven challenging to recover in genetic, transcript, or protein form[25,26], suggests that the proposed mer work-around pathway[27] is not highly relevant in seep settings. MotB chemotaxis proteins attributed to Deltaproteobacteria suggest that environmental sensing and adaptation, potentially through motility, could be a critical component of aggregates' sulfate-reducing partners or free-living organisms. Proteins responsive to iron and nickel highlight the importance of these metals in methane metabolisms[28,29], while proteasome presence suggests a dynamic protein pool that may be primed for recycling. Most strikingly, however, is the abundance of unannotated

hypothetical proteins, which constitute 58.5% of the universally-detected metaproteome. Of these, 65.5% are annotated as archaeal and 25.5% are bacterial, with half of those demonstrating closest phylogenetic affiliation with *Desulfobacterales*. These poorly-characterized products represent potential high-value targets for future biochemical investigation that may help disentangle some of the metabolic mysteries of methane seep environments.

**Conclusion**

Metaproteomics represents a powerful analytical tool for characterizing the functionally relevant state of microbiological communities, both in applied comparative contexts and as a discovery tool. This brief report of the most frequent detections distills the thousands of protein products from several seep sediment metaproteomic experiments, revealing targets of particular perceived importance and substantial future potential.

**References**


1. Iversen, N. Anaerobic methane oxidation rates at the sulfate-methane transition in marine sediments from Kattegat and Skagerrak (Denmark). *Limnol. Oceanogr* **30,** 944–955 (1985).
2. Hoehler, T. M., Alperin, M. J., Albert, D. B. & Martens, C. S. Field and laboratory studies of methane oxidation in an anoxic marine sediment: Evidence for a methanogen-sulfate reducer consortium. *Global Biogeochemical Cycles* **8,** 451–463 (1994).
3. Boetius, A. *et al.* A marine microbial consortium apparently mediating anaerobic oxidation of methane. *Nature* **407,** (2000).
4. Orphan, V. J., House, C. H., Hinrichs, K.-U., McKeegan, K. D. & DeLong, E. F. Methane-Consuming Archaea Revealed by Directly Coupled Isotopic and Phylogenetic Analysis. *Science* **293,** 484–487 (2001).
5. Nealson, K. H. & Saffarini, D. Iron and manganese in anaerobic respiration: environmental significance, physiology, and regulation. *Annual Reviews in Microbiology* **48,** 311–343 (1994).
6. Beal, E. J., House, C. H. & Orphan, V. J. Manganese-and iron-dependent marine methane oxidation. *Science* **325,** 184–187 (2009).
7. Canfield, D. E. *et al.* Pathways of organic carbon oxidation in three continental margin sediments. *Marine Geology* **113,** 27–40 (1993).
8. Raghoebarsing, A. A. *et al.* A microbial consortium couples anaerobic methane oxidation to denitrification. *Nature* **440,** 918–921 (2006).
9. Holmkvist, L., Ferdelman, T. G. & Jørgensen, B. B. A cryptic sulfur cycle driven by iron in the methane zone of marine sediment (Aarhus Bay, Denmark). *Geochimica et Cosmochimica Acta* **75,** 3581–3599 (2011).
10. Treude, Boetius, Knittel, Wallmann & Jorgensen. Anaerobic oxidation of methane above gas hydrates at Hydrate Ridge, NE Pacific Ocean. *Mar Ecol Prog Ser* **264,** 1–14 (2003).
11. Suess, E. *et al.* Gas hydrate destabilization: enhanced dewatering, benthic material turnover and large methane plumes at the Cascadia convergent margin. *Earth and Planetary Science Letters* **170,** 1–15 (1999).
12. Tryon, M. ., Brown, K. . & Torres, M. . Fluid and chemical flux in and out of sediments hosting methane hydrate deposits on Hydrate Ridge, OR, II: Hydrological processes. *Earth and Planetary Science Letters* **201,** 541–557 (2002).
13. Kester, D. R., Duedall, I. W., Connors, D. N. & Pytkowicz, R. M. PREPARATION OF ARTIFICIAL SEAWATER1. *Limnology and Oceanography* **12,** 176–179 (1967).
14. Marlow, J. J. *et al.* Carbonate-hosted methanotrophy represents an unrecognized methane sink in the deep sea. *Nature Communications* (2014).
15. Wegener, G. *et al.* Biogeochemical processes and microbial diversity of the Gullfaks and Tommeliten methane seeps (Northern North Sea). *Biogeosciences Discussions* **5,** 971–1015 (2008).
16. Joye, S. B. *et al.* The anaerobic oxidation of methane and sulfate reduction in sediments from Gulf of Mexico cold seeps. *Chemical Geology* **205,** 219–238 (2004).

17. Hansen, L. B., Finster, K., Fossing, H. & Iversen, N. Anaerobic methane oxidation in sulfate depleted sediments: effects of sulfate and molybdate additions. *Aquatic Microbial Ecology* **14,** 195–204 (1998).
18. Maier, T., Güell, M. & Serrano, L. Correlation of mRNA and protein in complex biological samples. *FEBS letters* **583,** 3966–3973 (2009).
19. Seifert, J. *et al.* Protein-based stable isotope probing (protein-SIP) in functional metaproteomics. *Mass spectrometry reviews* **31,** 683–697 (2012).
20. Krüger, M., Wolters, H., Gehre, M., Joye, S. B. & Richnow, H. Tracing the slow growth of anaerobic methane-oxidizing communities by 15N-labelling techniques. *FEMS microbiology ecology* **63,** 401–411 (2008).
21. Akashi, H. & Gojobori, T. Metabolic efficiency and amino acid composition in the proteomes of Escherichia coli and Bacillus subtilis. *Proceedings of the National Academy of Sciences* **99,** 3695–3700 (2002).
22. VerBerkmoes, N. C., Denef, V. J., Hettich, R. L. & Banfield, J. F. Systems biology: functional analysis of natural microbial consortia using community proteomics. *Nature Reviews Microbiology* **7,** 196–205 (2009).
23. Schneider, T. & Riedel, K. Environmental proteomics: analysis of structure and function of microbial communities. *Proteomics* **10,** 785–798 (2010).
24. Li, Z. *et al.* Systematic Comparison of Label-Free, Metabolic Labeling, and Isobaric Chemical Labeling for Quantitative Proteomics on LTQ Orbitrap Velos. *J. Proteome Res.* **11,** 1582–1590 (2011).
25. Hallam, S. J. *et al.* Reverse methanogenesis: testing the hypothesis with environmental genomics. *Science* **305,** 1457–1462 (2004).
26. Stokke, R., Roalkvam, I., Lanzen, A., Haflidason, H. & Steen, I. H. Integrated metagenomic and metaproteomic analyses of an ANME-1-dominated community in marine cold seep sediments. *Environmental microbiology* **14,** 1333–1346 (2012).
27. Meyerdierks, A. *et al.* Metagenome and mRNA expression analyses of anaerobic methanotrophic archaea of the ANME-1 group. *Environmental Microbiology* **12,** 422–439 (2010).
28. Thauer, R. K., Kaster, A.-K., Seedorf, H., Buckel, W. & Hedderich, R. Methanogenic archaea: ecologically relevant differences in energy conservation. *Nat Rev Micro* **6,** 579–591 (2008).
29. Glass, J. B. *et al.* Geochemical, metagenomic and metaproteomic insights into trace metal utilization by methane-oxidizing microbial consortia in sulphidic marine sediments. *Environmental microbiology* **16,** 1592–1611 (2014).

# Appendix 6: Supplementary Information for Chapter 5

## Fluid Composition

The concentrations of chemical species for the 7 fluids considered in this study are listed in Table 2. In cases where AOM-relevant species were not given in the literature, concentrations from similar environments were used to approximate these values for the fluid in question. Specific instances include the following.

*Reduced Sulfur*

Sulfide concentrations for Fluids 1 and 4 were determined by calculating the ratios of the five most abundant ions ($Na^+$, $K^+$, $Mg^{2+}$, $SO_4^{2-}$, and $Cl^-$) to sulfide in Fluid 2, which has a similar acid-sulfate geochemistry. The mean of these analogous ratios was used to back-calculate a sulfide concentration from the fluid's other ions. The sulfide concentration in Fluid 2 was also used for Fluid 3, due to the solutions' chemical similarities. The sulfide value for Fluid 5 was obtained from Seyfriend and Bischoff (1981), whose data come from similarly sourced Icelandic groundwater. An upper limit for sulfide in Fluid 7 is derived from Alt and Shanks (2006), who characterize a serpentinization system in the Mariana forearc.

*Oxidized Carbon*

Dissolved inorganic carbon (DIC, including $CO_2$ (aq), $HCO_3^-$, or $CO_3^{2-}$, depending on the pH) concentrations were only provided in primary sources for Fluids 1, 4, 5, 6, and 7. The inclusion of specific $CO_2$ concentrations from atmospheric approximations (see main text) provided DIC for all fluids. For Fluids 1, 4, 5, 6, and 7, the higher of the reported and atmospheric values was used.

RTM Parameters

Specific values for boundary conditions and reaction parameters were taken from similar studies reported in the literature, as delineated below.

*Porosity*

Martian crust porosity was approximated by the mean value of porosities measured in 14 martian meteorites. In a compilation of data that uses 100x magnification images to quantify pore space, Coulson et al. (2007) report a mean porosity of 0.049 (and a standard deviation of 0.03). This value is on the lower range of those given for terrestrial fractured basalts (0.05 - 0.5) as tabulated by Freeze and Cherry (1979) and may represent a conservative treatment of porosity, nutrient flow, and the spatial extent of exergonic conditions.

*Concentrations*

Dirichlet boundary conditions were used for all chemical species. Initial molal concentrations of dissolved chemical species were obtained from relevant published reports and supplemented as described above. Dissolved methane was kept constant at the lower boundary of the simulated rock column at 2 mM. This value is commonly observed at sites of AOM on Earth (e.g., Joye et al., 2004; Alperin et al., 1988) and is producible through serpentinization (Bradley & Summons, 2010; Brazelton et al., 2006), but represents a conservative concentration given analogous studies (Boetius et al., 2000; Gibson et al., 2005). Maintaining up to 2 mM dissolved methane in aqueous solution is possible at shallow depths due to lithostatic pressure (Zatsepina & Buffett, 1997). The top-of-column methane concentration remained at 0 mM throughout each model run.

*Diffusion Coefficients*

Temperature dependent molecular diffusion coefficients for $CO_2$, $H_2S$, $HS^-$, $HCO_3^-$, and $SO_4^{2-}$ were obtained from Tivey and McDuff (1990), who modify the Einstein-Stokes equation to better fit experimental data. Values for $CH_4$ were obtained from a second degree polynomial fit to data from Oelkers (1991).

*Advection Velocity*

Any estimates of groundwater advection rates on ancient Mars would be largely speculative given the uncertainties of flow paths, water sources, heat sources, and the localized plumbing configuration. Advection may derive from buoyant flow due to hotter fluids at depth and/or other gravity- or pressure-driven mixing dictated by local geologic circumstances. This study uses four different advection rates: 0, 1, 2, and 3 m/day, offering a range of values sufficient for demonstrating the effect of advection rate on the modeled AOM system.

*$V_{max}$ for AOM*

The maximum rate of AOM is an important parameter that determines the speed of the reaction when methane is not limiting. The value of 1.89 mol / $m^3$ day is obtained from Dale et al. (2008), who use in situ data and a kinetic-bioenergetic model (Dale et al., 2006) to estimate reaction rates in the Skagerrak, Denmark.

*Temperature*

Temperatures used in the model are as shown in Table 2; these parameters allow for the geochemical speciation used as thermodynamic input and are all feasible values for putative microbial niches on ancient Mars.

*Half Saturation Constants*

The $K_m$ for $CH_4$ in AOM is relatively high, possibly because the first step in reverse methanogenesis would generate a destabilizing methyl radical (Kruger et al., 2003, Hallam et al., 2004, Shima and Thauer, 2005). The model uses 5 mM, a value obtained from an experimental treatment of seep sediment from multiple field sites (Wegener & Boetius, 2009) and one that is in keeping with other findings (Nauhaus et al., 2007; Orcutt and Meile, 2008). For $SO_4^{2-}$, a Km of 500 μM was used (Van Cappellen et al., 2006; Wegener & Boetius, 2009).

*Membrane Potential*

A ΔΨ value of 120 mV was selected because it has been shown to be the optimal physiological potential for ATP production in multiple species (Dimroth et al., 2003; Kadenbach, 2003; Toei et al., 2007). The standing membrane potential of three methanogenic organisms was found to be 118 mV (Daniels et al., 1984), and LaRowe et al. (2012) report that experimental data is best approximated in model thermodynamic calculations when 120 mV is used.

*Growth Yield and Maximum Biomass*

A microbial growth yield of 600 mg cell dry weight per mol of $CH_4$ consumption was measured by Nauhaus et al. (2007) in their 24-month incubation of Hydrate Ridge seep sediment. This value corresponds to a 1% contribution of catabolic AOM throughput to anabolism. The upper biomass limit of $3\times10^6$ mg/m$^3$ was calculated from the maximum cell count value of $3\times10^9$ cells/ml, measured by Orcutt et al. (2005) at a Gulf of Mexico seep, and an average microbial cell mass of $1\times10^{-12}$ g (Kubitschek, 1986). This value is similar to other maximum biomass estimates, such as investigations

at Hydrate Ridge by Boetius et al. (2000), which revealed a maximum of $7\times10^7$ 300-cell aggregates per $cm^3$, corresponding to $2.1\times10^6$ $mg/m^3$.

*Decay Constant*

The environmental destruction rate of AOM organisms is a poorly constrained parameter, as long term *in situ* studies on standing stocks of biomass have not been conducted, and predation (which is not included in our model) is an important component in terrestrial systems (Thurber et al., 2012). Our model uses an estimate of a predation-independent decay term in a sulfate-reducing, hydrocarbon-oxidizing system of $10^{-9}$ $s^{-1}$ (Bethke, 2008). This is a low value relative to the rate of production; thus, biomass decay does not strongly influence RTM output.

References

All references for Appendix 5 can be found in the main text, Chapter 5.